Theses and Dissertations--Pharmacy   College of Pharmacy

2022

Investigating the Physical Stability of Amorphous Pharmaceutical Formulations

Travis W. Jarrells

University of Kentucky, tw.jarrells@gmail.com

Author ORCID Identifier:

 https://orcid.org/0000-0002-9372-3595

Digital Object Identifier: https://doi.org/10.13023/etd.2022.194

Right click to open a feedback form in a new tab to let us know how this document benefits you.

INVESTIGATING THE PHYSICAL STABILITY OF AMORPHOUS
PHARMACEUTICAL FORMULATIONS

_____

DISSERTATION

_____

A dissertation submitted in partial fulfillment of the
requirements for the degree of Doctor of Philosophy in the
College of Pharmacy
at the University of Kentucky

By
Travis Wayne Jarrells

Lexington, Kentucky

Director: Dr. Eric Munson, Professor of Pharmaceutical Sciences

Lexington, Kentucky

2022

ABSTRACT OF DISSERTATION

INVESTIGATING THE PHYSICAL STABILITY OF AMORPHOUS
PHARMACEUTICAL FORMULATIONS

Amorphous formulations, including amorphous solid dispersions (ASDs), consisting of the active pharmaceutical ingredient (API) intimately mixed in a polymeric matrix, are an attractive formulation approach to improve drug delivery, dissolution, and solubility. However, an amorphous API in an ASD is in a higher energy state compared to the crystalline drug and results in most ASDs being inherently unstable. The polymer helps to stabilize the amorphous drug against crystallization such that the resulting homogenous mixture maintains its solubility advantage relative to the crystalline form. One challenge of ASDs is that the presence of impurities including crystals or residual solvent, variations in the ingredients, or changes in storage conditions can all affect physical stability and bioavailability. There is a clear need for advanced analytical techniques that can both detect, characterize, and quantify the components of amorphous formulations, especially ASDs. This research focuses on methods to detect and quantify crystallinity, ensure consistency between manufactured lots of amorphous formulations, and predict shelf life and drug substance properties. Poorly soluble model drug compounds such as nifedipine, indomethacin, and patiromer were studied using multiple analytical techniques including solid-state nuclear magnetic resonance (SSNMR) spectroscopy. First, SSNMR was used to develop a method to quantify the monomeric makeup of an insoluble polymeric API which can be used to demonstrate API sameness during generic drug development. Second, crystallinity was detected, quantified, and compared using a variety of analytical techniques with SSNMR and powder X-ray diffraction being used to predict drug-polymer solubility form the first time. Third, an extensive investigation into the effect of hydrogen bonding, drug loading, and storage temperature on crystallization tendency was conducted around the glass transition temperature (T_g) and found that hydrogen bonding plays a particularly important role in stability near T_g. Lastly, the impact of multiple absorbed solvents on the physicochemical properties of pharmaceutical polymers was investigated using dynamic vapor sorption. In conclusion, this research proposes new methods and new applications of existing analytical techniques for the advanced characterization of pharmaceutical amorphous formulations. The results provide an improved understanding of the factors affecting the physical stability of ASDs and should aid in their successful formulation.

Travis Wayne Jarrells

04/06/2022
Date

INVESTIGATING THE PHYSICAL STABILITY OF AMORPHOUS
PHARMACEUTICAL FORMULATIONS

By

Travis Wayne Jarrells

Eric J. Munson, Ph.D.
Director of Dissertation

David J. Feola, Ph.D.
Director of Graduate Studies

04/06/2022
Date

To Sarah and to my parents

ACKNOWLEDGEMENTS

First and foremost, I want to thank my advisor, Dr. Eric Munson, for the opportunity to conduct research under your guidance for the last five years. I am incredibly grateful to have had an advisor who cares about both my professional growth as a scientist and personal growth outside the lab. He has given me the opportunity to pursue my own scientific interests while providing the scientific expertise needed to collectively advance our research. I recognize that my graduate career may not have been typical, and I am indebted to him for his patience with me both in and outside of the lab.

I also want to thank my committee members Dr. Dan Pack, Dr. Thomas Dziubla, Dr. Joseph Chappell, and Dr. Patrick Marsac. Your insightful comments and guidance were always appreciated and went a long way to helping me become a successful scientist by thinking outside of the box. In particular, thank you to Dr. Patrick Marsac for serving as my co-advisor as well as allowing me to begin my graduate research in your lab. You took a personal interest in my scientific advancement and went out of your way to help me develop a deep understanding of the research problem which was especially helpful.

I would also like to thank the past and present members of the Munson and Marsac labs: Dr. Sean Delaney, Dr. Kanika Sarpal, Dr. Ashley Lay, Dr. Julie Calahan, Dr. Nico Setiawan, Dr. Jonas Alin, Dr. Sadegh Poozesh, Dr. Matt Defrese, Freddy Arce, Heather Campbell, Daniel DeNeve, Cole Tower, and Ophelia Zhang. You have all been wonderful colleagues and I have learned so much from each of you.

In addition to my daily colleagues, I am indebted to the countless support staff who helped make my graduate career run smoothly. To Catina Rossoll, thank you for keeping track of all the requirements of the department and making sure I get them done on time.

To Tonya Vance, thank you for your tireless work organizing the CPD meetings and my travel for various academic conferences. To Kristi Moore and Todd Sizemore, thank you for helping to keep me safe in the lab and ensuring I had all the equipment needed to conduct daily research. Moving to Purdue would not have been possible without the help of Mary Ellen Hurt and Nancy Cramer. You both were instrumental to answering my many questions about beginning research at Purdue and helped get me settled.

While I did not have the privilege of working with some people every day, there were many who helped make my time in graduate school very enjoyable. I especially want to thank Dr. Matt Nethercott for his tireless help with teaching me solid-state NMR as well as our friendship. He was incredibly patient and repeatedly went out of his way to help diagnose, fix, and analyze my research. To Dr. Mike Hanrahan, thank you for the help with the dual solvent quantitation project and your expertise in explaining the results of 2D NMR experiments. To Mario Incitti, thank you for your work in getting our new spectrometer operational and always being available to help troubleshoot during installation.

I also want to thank the various professors and teachers over the years that led me to where I am today and helped make learning enjoyable along the way. Thank you to Mr. Zach Matson, my high school chemistry teacher who helped spur my interest in science and engineering while making learning fun. In particular, I also must thank Dr. Brad Anderson for his teaching and focus on the fundamentals. I feel that your teaching in the Rate Processes and Thermodynamics courses were some of the most beneficial courses during graduate school and helped me appreciate the complexity of many of the research projects we face.

Lastly, and perhaps most importantly, I want to thank my family. In particular, thank you to my wonderful wife, Sarah, for her continued support throughout my time in graduate school. The last five years have been more than either of us could have bargained for: Two children, a move to Purdue, and a pandemic have made the last five years more than either of us could have ever bargained for. You've patiently been there every step of the way with me, and I can't express how lucky I am to have had you supporting me. To my daughters, Palmer and Marlee, you are the reason I go to work every day and keep going. All the sleepless nights are worth it when I'm reminded that you don't see me as a scientist, but as your dad. You both kept me grounded and are each truly a blessing. Mom and Dad, I can't begin to describe how lucky I am to have had you as my parents. You were my first fans and instilled in me a work ethic that I know helped get me though the struggles of grad school. Thank you for always believing in me and encouraging me to pursue my dreams, even if that included moving away to finish my degree. I also want to thank my in-laws, Chuck and Jennifer. You have both always been incredibly encouraging in my career pursuits and I am so grateful to be a part of your family.

TABLE OF CONTENTS

LIST OF FIGURES

xii

CHAPTER 1: INTRODUCTION

1.1   Pharmaceutical Development

The vast majority of drugs are formulated as an oral solid dosage form, typically a tablet or capsule. As of 2017, 62% of marketed drugs were taken orally (1). There are many reasons why oral dosage forms dominate the pharmaceutical landscape. From a patient compliance point of view, taking a tablet is often preferable to an injection especially as tablets are easy to store and transport. Similarly, tablets are often much easier and cheaper to product from a manufacturing standpoint. Despite the simplicity of a tablet, the route it takes to deliver the drug to the site of action is often extremely difficult. Once swallowed, the drug typically must survive the stomach's acidic environment before disintegrating and dissolving in the gastrointestinal fluid of the small intestine. Even then, a sufficient amount of drug must remain soluble long enough to be absorbed across the intestinal membrane and survive hepatic clearance in the liver before reaching systemic circulation to reach the site of action. Each of the aforementioned steps contribute to the oral bioavailability. Perhaps most importantly, the success or failure of an oral solid dosage form is dependent on two properties: solubility and permeability, from which the biopharmaceutical classification system (BCS) is based (2).

The BCS system, shown in Figure 1.1, divides drugs into four categories based on their solubility and permeability. Ideally, drugs are BCS class I (high solubility and permeability) and easily deliver efficacious amounts of drug. More commonly, however, many drugs suffer from poor solubility and fall under BCS classes II (low solubility/ high permeability) or IV (low solubility and permeability). A recent survey by Di et al. found that 40% of marketed drugs are poorly soluble while at least 75% of drug candidates in the

development pipeline suffer from poor solubility (3, 4). This is likely a result of the hydrophobic interactions which mediate drug-receptor binding as well as an increased use of high throughput screening in non-aqueous or mixed solvent media (5). These findings are particularly striking for two reasons. First, they demonstrate that low solubility is a current problem broadly impacting the pharmaceutical industry. Second, and more importantly, poorly soluble compounds will continue to plague the drug development process for years to come. Each highlights the need for new and improved formulation strategies that will be required to solubilize and deliever the majority of new drugs in the near future.

Class III *High permeability, low solubility* • Immediate release formulation with absorption enhancer	**Class I** *High permeability and solubility* • Immediate release formulations
Class IV *Low permeability and solubility* • Class II approaches and absorption enhancer	**Class II** *Low permeability, high solubility* • Immediate release formulation with surfactant • Crystal modifications • Particle size reduction • Amorphous solid dispersions • Cyclodextrin complexation • Lipid formulations • pH modification

Solubility (vertical axis) — **Permeability** (horizontal axis)

Figure 1.1. Biopharmaceutical Classification System (BCS) and typical formulation approaches. Adapted from refs. (2) and (6).

Figure 1.1 highlights some of the typical formulation approaches based on the BCS class of the drug. For the purposes of this dissertation, most drugs of interest fall into BCS class II or IV indicating the main challenge for a successful formulation is overcoming a slow dissolution rate and low solubility (7). There are many ways to improve the

dissolution rate and apparent solubility of a drug including many which have already received FDA approval. This includes the use of co-solvents, salts, surfactants, cyclodextrin complexation, particle size reduction, polymorphic changes, lipid-based systems, co-crystals, prodrugs, and amorphous solid dispersions. Without a formulation to deliver therapeutic amounts of drug, all of the prior work in discovering, synthesizing, and characterizing the drug candidate is wasted.

1.2   Pharmaceutical Solids

Pharmaceutical solids can be broadly classified into two categories: crystalline and amorphous. The two states vary broadly in both their physicochemical properties, stability, prevalence, and application in drug development.

1.2.1   The Crystalline State

The crystalline state has a defined rigid structure in which molecules are highly ordered resulting in both short- and long-range order. The molecules are held together though non-covalent interactions including hydrogen bonding, ionic bonding, and pi-stacking. The rigid order and intramolecular bonds result in the crystal being the most thermodynamically stable solid form of a given molecule (5). The thermodynamic stability of crystalline solids often comes at the cost of aqueous solubility. The increased prevalence of poorly solubility drugs has led to the need for alternative formulation strategies other than standard crystalline solids (5).

1.2.1.1   Polymorphism

The same compound can exist in more than one crystalline structure, a phenomenon known as polymorphism. For instance, diamond and graphite are both polymorphs of

carbon. Diamond forms a cubic crystal structure whereas graphite is hexagonal (8, 9). In addition, pseudopolymorphs can exist, typically as hydrates or solvates where one or more water or solvent molecules are incorporated into the crystal structure, respectively.

As a rule of thumb, "the number of known polymorphic forms for a given compound is proportional to the time and energy spent in research on that compound" (10). However, over half of molecules in the Cambridge Structural Database have only a single known crystal structure, while 5-methyl-2-((2-nitrophenyl)amino)3-3 thiophenecarbonitrile (ROY) has at least eleven confirmed polymorphic forms (11, 12). Different packing arrangements in polymorphs may result in varying physicochemical properties including solubility, hardness, density, and crystal shape (13). A metastable polymorph may be chosen during the formulation process to exploit its unique physicochemical properties and improve drug product performance (i.e., bioavailability). For example, equivalent doses of chloramphenicol palmitate polymorphs resulted in a seven-fold increase in maximum blood serum concentration for form B relative to form A (14). Provided that the polymorph of interest can remain stable over the shelf-life of the drug, varying the polymorphic form drug product may be a viable formulation approach. However, at a particular temperature and pressure, only one polymorph is the most stable (i.e., it has the lowest free energy). All other polymorphs at those conditions are metastable polymorphs and have the potential to convert to the stable form. Thus, there is always significant risk when using a metastable polymorphic form. Perhaps most notably is the example of ritonavir. Ritonavir was marketed as an anti-HIV drug in the late 1990's. The crystalline form of ritonavir used in the formulation (Form I) was assumed to be thermodynamically stable but after two years of production, a previously unknown,

thermodynamically more stable form appeared during the manufacturing process (Form II). Form I was up to 5.6x more soluble than Form II leading to the repeated failing of dissolution testing (15). Ritonavir was eventually pulled from the market until a process was developed to control the formation of Forms I and II. Hence, the ritonavir example underscores the importance for controlling polymorphism during production and its potential impacts on product performance.

The relative stability of polymorphs at constant pressure can vary as a function of temperature. A pair of polymorphs which have the same relative stability across all temperatures below each melting point are known as monotropic. On the other hand, the relative stability of enantiotropic polymorphs varies as a function of temperature with a transition occurring somewhere below the melting point of each form. Burger and Ramberger developed various rules which help to predict the stability-temperature relationship of different polymorphs including the heat of fusion rule, heat of transition rule, density rule, and the infrared rule (16). Figure 1.2 illustrates the temperature relationship for monotropic and enantiotropic polymorphs.
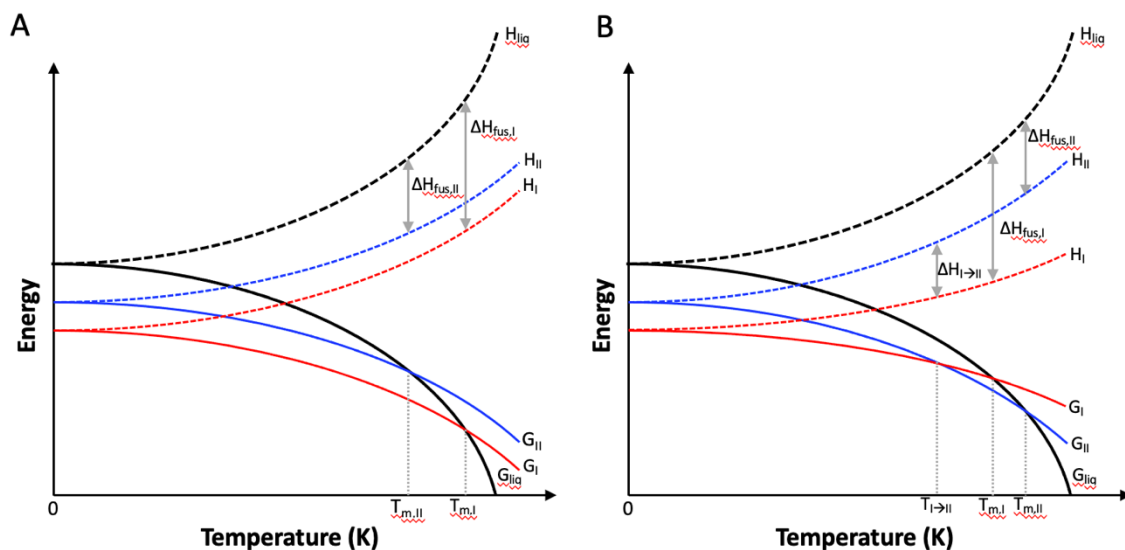
Figure 1.2. Energy-temperature diagrams for two hypothetical polymorphs (forms I and II) showing a (A) monotropic and (B) enantiotropic relationship. Adapted from ref. (16). G_I, G_{II}, and G_{liq} are the Gibbs free energy of polymorphs I, II, and the liquid, respectively while H_I, H_{II}, and H_{liq} are the enthalpy of polymorphs I, II, and the liquid, respectively. $\Delta H_{fus,I}$ and $\Delta H_{fus,II}$ are the heat of fusion for forms I and II which occur at their respective melting points $T_{m,I}$ and $T_{m,II}$. $\Delta H_{I \rightarrow II}$ is the enthalpy change of the polymorphic transition from form I to form II occurring at the transition temperature, $T_{I \rightarrow II}$.

1.2.1.2 The Amorphous State

It is easiest to describe the amorphous state relative to the crystalline state. Contrary to the crystalline state, the amorphous state lacks long-range order but still may possess short-range molecular ordering with immediately adjacent molecules (i.e., on the order of a few angstroms) (17). The amorphous state is also thermodynamically unstable and wants to revert back to the stable crystalline state. Despite its inherent instability, amorphous solids are widely used in the pharmaceutical industry. Many compounds including peptides, proteins, and some polymers are naturally occurring amorphous forms.

Additionally, the fact that amorphous drugs are more soluble than their crystalline counterparts make amorphous formulations a desirable approach for improving the bioavailability of poorly soluble drug candidates.

The amorphous state is often defined by the glass transition temperature (T_g). The glass transition is a pseudo second order phase transition characterized by a dramatic increase in viscosity and decrease in molecular mobility (18). Depending on the temperature relative to T_g, the amorphous state takes on different forms and has different properties. Above T_g, the amorphous solid can be viewed as an extension of the liquid phase. More specifically, the amorphous solid is a supercooled liquid or rubber. Below T_g, the amorphous state is classified as a glass and behaves more like a solid. A detailed illustration of the thermodynamic relationship of crystalline and amorphous compounds is shown in Figure 1.3.
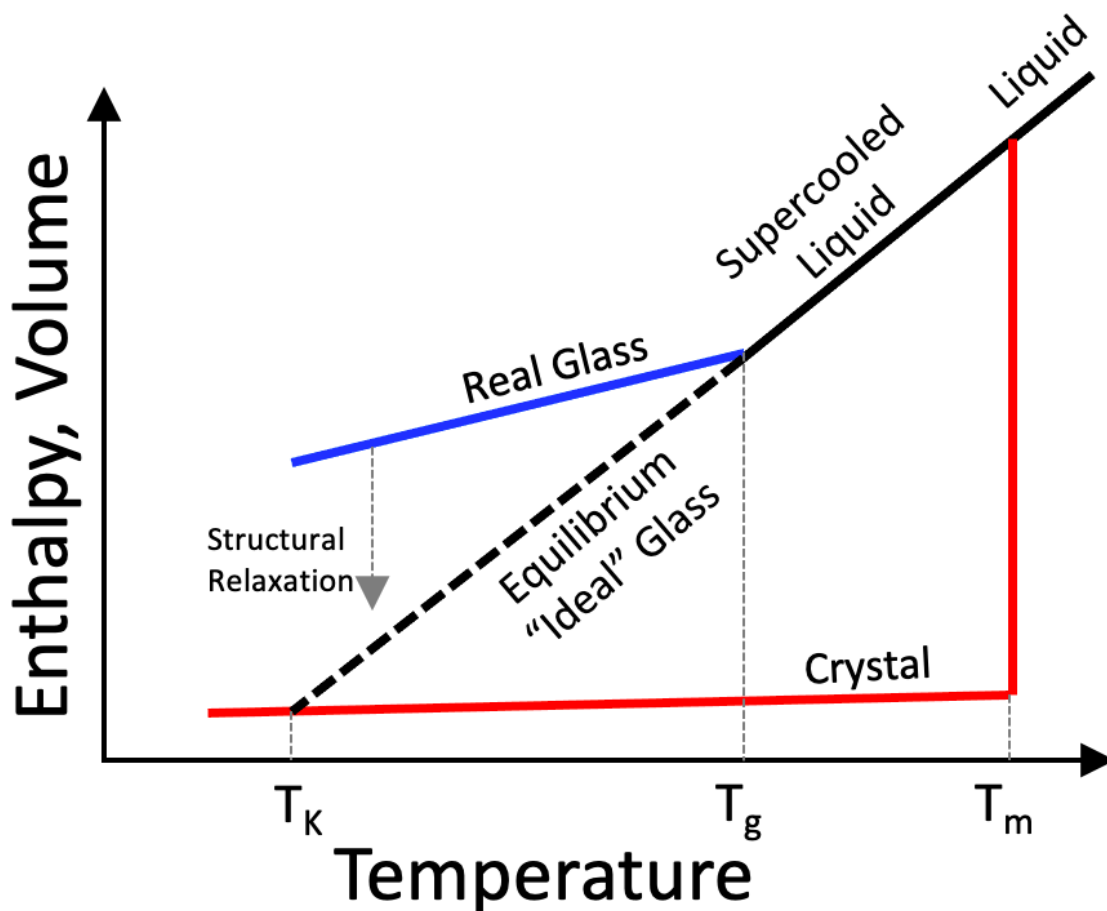
Figure 1.3. Illustration of the enthalpy and volume relationship with temperature in amorphous and crystalline solids.

When a crystalline or amorphous drug is heated above the melting point (T_m), the liquid is at equilibrium and the original state cannot be discerned. Crystallization typically occurs upon cooling below T_m as the molecules have sufficient time to reorganize into a thermodynamically stable point in a crystal lattice (19). This is a first order phase transition leading to a step decrease in H and V as the ordering of molecules into a defined crystal lattice results in densification and a decrease the system energetics. However, if upon cooling below T_m, crystallization does not occur, the drug enters the supercooled liquid

state and no discontinuity in H or V is observed. At this point, the system is still in equilibrium and is also referred to as the rubbery state. The molecular mobility further decreases, and viscosity increases with continued cooling. Eventually, molecular mobility decreases to the point where molecules are no longer able to sufficiently rearrange on the experimental timescale and the system falls out of equilibrium. The temperature at which this pseudo second order phase transition occurs is the T_g and results in a change in slope of the H or V as a function of temperature. It is important to note that the glass transition is a kinetic phenomenon and the exact temperature (T_g) at which it occurs is heavily influenced by many factors including heating/ cooling rate, moisture content, thermal history, etc.

Further cooling through T_g enters the non-equilibrium glassy state. At this point, viscosity has increased ($> 10^{12}$ Pa·s) to the point where molecular mobility occurs on > 100 s timescales and the drug is kinetically stabilized against crystallization (20). Molecular mobility continues to decrease with decreasing temperature to the point at which it becomes insignificant. This is known as the Kauzmann temperature (T_K) and hypothetically occurs at the temperature where the supercooled liquid line intersects with the crystalline line. At this point, configurational entropy (the difference in entropy between the crystalline and amorphous phase) would become negative and violate the third law of thermodynamics (21). Thus, this point cannot be reached before the system falls out of equilibrium. However, it is estimated that $T_K \approx T_g - 50°C$ is sufficient for molecular motions to become negligible (20).

The amorphous drug will relax towards the equilibrium supercooled liquid state upon storage below T_g. This relaxation is structural in nature, resulting in a lower energy,

densified glass. The enthalpy lost to relaxation is recovered upon heating through T_g and is observed as an enthalpic recovery endotherm.

Various types of relaxation contribute to the reduction in free energy of a glassy API. α-relaxation is the cooperative motion of multiple molecules and mainly contributes to the glass transition and crystallization above T_g (22). This cooperative motion results in a large activation energy. Below T_g, the timescales of alpha-relaxations become increasing long and cooperative or diffusive motions are quickly inaccessible. At this point, secondary β or Johari-Goldstein (β_{JG}) relaxations occurring on much shorter timescales become increasingly important. β_{JG} relaxations correspond to noncooperative single molecule motions with lower activation energies than α-relaxations (23). These β_{JG} motions are thought to occur in 'islands of mobility' where hindered rotational motions of the whole molecule are possible (24). β_{JG} motions often serve as the precursors to cooperative α-motion and therefore contribute to the physical stability of glassy solids. Additional secondary relaxations (gamma, delta, etc.) exist in the glassy state including side-chain rotations or bond vibrations (25). However, secondary motions aside from β_{JG} are not thought to contribute to the instability of amorphous solids (26).

1.3   Amorphous Drug Instability

The greater free energy and molecular mobility in amorphous drugs often leads to improved dissolution and solubility relative to the crystalline form. However, this comes at the cost of chemical and physical instability and is the biggest issue with the use of amorphous formulations. This disadvantage must be accounted for during the formulation, manufacture, and storage of the drug to inhibit any instability that is detrimental to

bioavailability (25). Just as tablets containing crystalline API are formulated with a variety of excipients, amorphous drug substances are also formulated with other molecules including polymers and surfactants to help stabilize the API from physicochemical degradation. Chemical stability is defined as changes in chemical composition that occur as a result of chemical reactions within the drug substance or drug product. Regarding amorphous solid dispersions, physical stability is defined as the ability of the drug to remain amorphous and prevent crystallization.

1.3.1 Chemical Instability

Chemical stability is the main concern of crystalline drug products since they are the most physically stable form. However, chemical stability is often overlooked in the amorphous state yet is still critically important and will briefly be considered. Chemical degradation may simply cause changes in physical appearance such as discoloration. Often, however, the results of chemical degradation are more severe and may include the loss of therapeutic potency or the production of toxic degradation byproducts (25).

Reactions in the solid state are proposed to follow a four-step process (27). 1) Loosening of molecules at the reaction site; 2) molecular change; 3) solid solution formation; and 4) separation of the product phase. In particular, the first step requires sufficient molecular mobility to occur. For example, chemical degradations in crystalline solids occur preferentially at crystalline defects where molecular mobility is increased relative to the bulk crystal. Since the amorphous state has enhanced molecular mobility relative to the crystalline state, it follows that chemical reactions may be especially prevalent in amorphous solids.

The most common chemical degradation reactions in the solid state include thermal decomposition, photodegradation, hydrolysis, oxidation, or rearrangement reactions (cyclization, isomerization, etc.) (28, 29). The enhanced mobility in amorphous solids often results in increased degradation rates relative to the same crystalline drug. For instance, the rate of spirapril HCl cyclization was over 25-fold faster in the amorphous solid than its crystalline form (30).

Chemical reactivity can be minimized or prevented entirely over the shelf life of an amorphous drug product by storage below the T_g where molecular mobility is restricted. Solid-state reactions typically do not follow Arrhenius reaction kinetics as in the solution state which complicates the extrapolation of accelerated stability or stress testing to relevant storage temperatures (25). Instead, more complex models are needed to predict the chemical stability of amorphous solids (31, 32). Clearly, the chemical stability of amorphous drugs is very important and must be considered during the design, production, and storage of an amorphous drug product. However, the work of this dissertation focuses on the physical stability of amorphous pharmaceuticals and will be discussed in more detail.

1.3.2   Physical Instability

Physical instability is a concern in the formulation of any drug product however, it is particularly important any time a metastable phase is used such as a metastable crystal polymorph or an amorphous solid. While the focus of this dissertation is on the physical instability of small molecule APIs (namely, crystallization), it is important to note another source of physical instability in the amorphous state. Lyophilization is often used to stabilize peptides, proteins, or other large molecules in the amorphous state. Specifically,

rather than preventing protein crystallization, it is important to sufficiently stabilize proteins in their native state to prevent aggregation and preserve their activity upon reconstitution and administration.

Recrystallization represents one of the biggest hurdles to the widespread use of amorphous pharmaceuticals to overcome the poor solubility of many drug candidates (17). The higher free energy of the amorphous state makes it metastable relative to the crystal form which is the most stable state at any temperature. The free energy difference between the amorphous and crystalline form represents a thermodynamic driving force to revert to the stable crystalline form through crystallization. Figure 1.4 illustrates the different energetics of the crystalline and amorphous states.
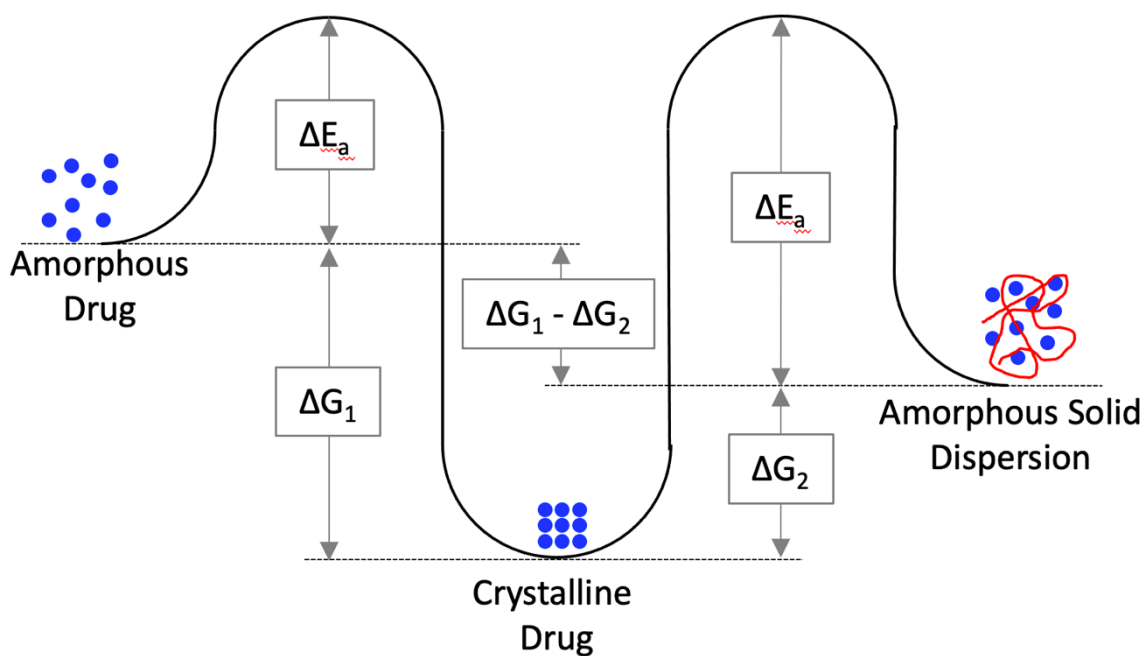
Figure 1.4. Energy diagram for various solid-state forms. Adapted from ref. (33).

1.3.2.1   Crystallization from the Amorphous State

Crystallization is a two-step process involving nucleation and crystal growth. The rate and extent of crystallization is dependent on temperature and governed by two

competing processes: thermodynamic driving force (supersaturation or supercooling) and molecular mobility. Supercooling is defined as the difference in temperature between the melting point, T_m, and the temperature, T, of the amorphous system. Decreasing temperature (increasing supercooling) increases the thermodynamic driving force for crystallization. At the same time, decreasing temperature also reduces the molecular mobility as the thermal barrier to translational/ diffusional motion decrease. The decrease in mobility is observed as a decrease in diffusivity or an increase in viscosity. Figure 1.5 illustrates the competing forces of supercooling and molecular mobility and their effect on the overall crystallization rate.
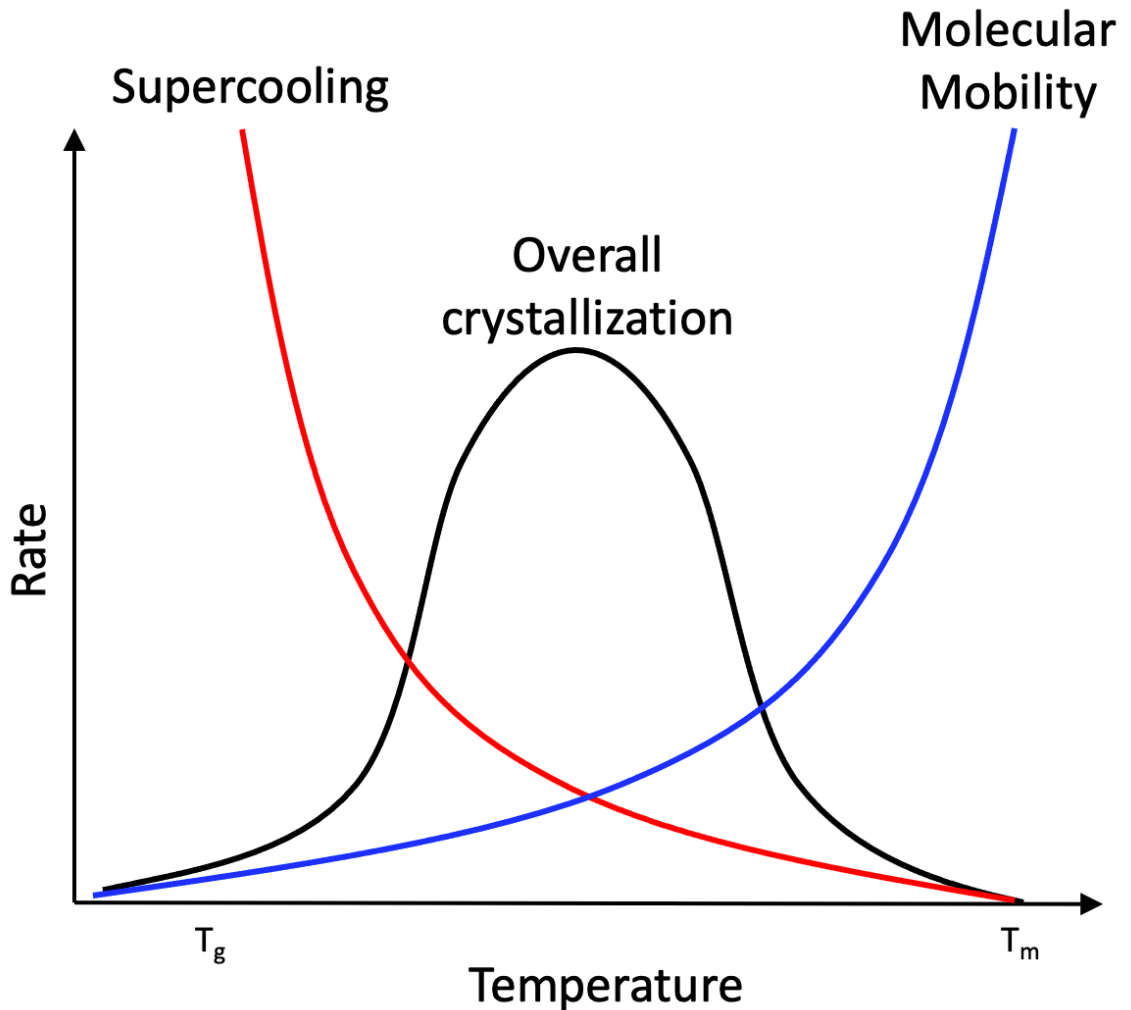
Figure 1.5. Overall crystallization rate from the amorphous state as a function of temperature and the relative importance of thermodynamic and kinetic factors. Adapted from ref. (34).

The maximum rate of crystallization is expected to occur at a temperature intermediate to the glass transition and melting point. The specific temperature of maximum crystallization rate is dependent on the molecule as well as the polymorphic form (35, 36). Note that while the effects of supercooling reach zero at T_m, molecular mobility still contributes to crystallization below T_g. Although translational mobility is

significantly inhibited in the glassy state, molecules still possess rotational and vibrational motion which can spur nucleation and crystal growth (25).

While Figure 1.5 provides a good picture of crystallization from the amorphous state, the reality is more complex. As noted earlier, crystallization consists of nucleation followed by crystal growth. The rate of each process varies with temperature and may operate in different temperature regimes. The temperature dependence of the rates of crystal nucleation and growth are illustrated in Figure 1.6.
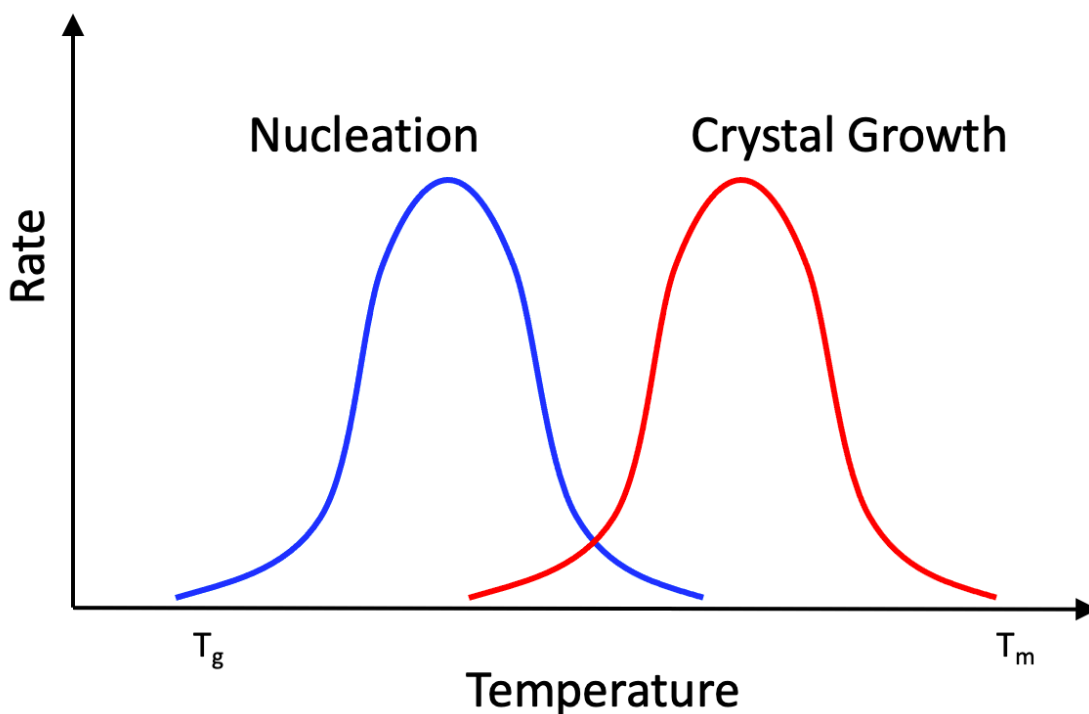
Figure 1.6. Nucleation and temperature growth regimes as a function of supercooling. Adapted from refs. (37) and (38).

The exact temperature range, shape, and relative magnitude of each rate may change based on the amorphous molecule observed. It is also important to note that the presence of excipients, such as in polymeric ASDs, does not change the maximum temperatures during isothermal crystallization (39). Rather, the magnitude of each regime

will likely change if the polymer functions to slow nucleation and/ or crystal growth. A thorough understanding of the API-specific crystallization kinetics displayed in Figures 1.5 and 1.6 is required to avoid temperature regimes during the manufacture and storage that are conducive to crystallization.

The relative position of each regime has also been related to the glass forming ability (GFA) of the drug molecules (40). Drugs with significant overlap of the two zones are typically poor glass formers as the rate of each process is relatively high at the same temperature. Crystal nuclei that form are then able to immediately grow to measurable sizes. On the other hand, compounds with well-resolved nucleation and crystal growth temperature ranges are typically better glass formers as amorphous molecules do not have sufficient mobility to diffuse to the nuclei formed at lower temperatures and thus hinder crystal growth. Figure 1.6 also helps to explain the observation that crystallization is more likely to occur in freshly prepared amorphous materials during reheating rather than during cooling (40). Despite first traversing the temperature range favoring growth upon cooling, it is unlikely that any nuclei have formed. Reheating the same sample from the glassy state traverses the nucleation zone and the likelihood of crystal nuclei existing is now greater and serves as a starting point for crystal growth upon heating.

It is important to note that crystallization from the amorphous state is slightly different than crystallization from the liquid or in the presence of solvent. Nonetheless, classical nucleation and crystal growth theory can be used to provide a general understanding of the factors affecting crystallization.

1.3.2.1.1 Classic Nucleation Theory

Nucleation can be divided into two broad categories: primary and secondary nucleation. Secondary nucleation occurs on preexisting crystal surfaces which act as nucleation sites for further crystal growth. Primary nucleation occurs without preexisting crystal surfaces and can be subdivided into heterogeneous nucleation, which is induced by dissolved impurities, and homogenous nucleation. Heterogeneous nucleation is nearly always observed in practice as it is nearly impossible to eliminate all impurities and surfaces which may act as nucleation sites. Therefore, homogeneous nucleation is extremely rare in practice, yet it forms the basis of classical nucleation theory (41). A more detailed discussion of homogeneous and heterogeneous nucleation follows as well was the impact of each on amorphous drug stability.

Homogeneous nucleation results from local solute concentration fluctuations in a supersaturated solution. Increased local concentrations can create ordered clusters which form by an additive mechanism (42, 43). Nucleation is a balance of competing energetic forces which determine whether a stable nucleus forms or redissolves. The free energy change of forming a new phase, $\Delta G(r)$, is shown in Equation 1.1 where ΔG_v and ΔG_s are the bulk free energy difference between the crystalline and amorphous/ liquid state, and the free energy required to create a new surface, respectively.

$$\Delta G(r) = \Delta G_v + \Delta G_s \qquad (1.1)$$

The liquid or amorphous state is metastable relative to the crystalline state so crystallization is exothermic and ΔG_v is negative. Surface tension (γ) opposes the creation of new surfaces so ΔG_s is positive. Equation 1.2 shows the balance between the energy

18

gain associated with forming a solid phase and the energy penalty of creating a new crystal surface.

$$\Delta G(r) = -\frac{4}{3}\pi r^3 \Delta G_v + 4\pi r^2 \gamma \qquad (1.2)$$

Initially, the radius of a molecular clusters is very small and high surface tension makes nucleation unfavorable. Eventually, the growing cluster reaches a critical size (r*) where the additional volume of forming crystal nucleus outweighs the effects of surface tension and nucleation becomes energetically favorable. The nucleus now continues to grow into an observable crystal. Figure 1.7 illustrates the competition between ΔG_v and ΔG_s during nucleation as a function of radius where the critical nucleus (r*) the corresponding energy barrier it must overcome (ΔG^*) are calculated in Equations 1.3 and 1.4.

$$r^* = \frac{2\gamma}{\Delta G_v} \qquad (1.3)$$

$$\Delta G^* = \frac{16\pi\gamma^3}{3\Delta G_v^2} \qquad (1.4)$$
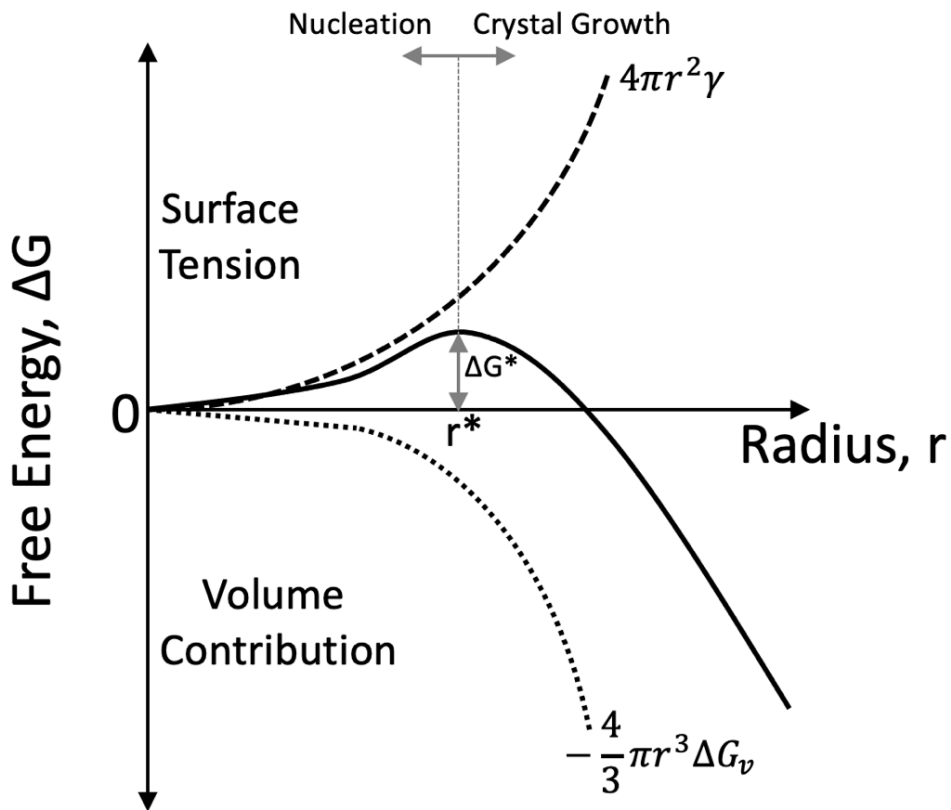
Figure 1.7. Free energy as a function of crystal nucleus radius. Adapted from ref. (37).

ΔG_v, or the free energy difference between the crystalline and amorphous state, can be estimated by the Hoffman equation (Equation 1.5) which uses the degree of supercooling ($T_m - T$) and the heat of fusion (ΔH_{fus}) of pure drug to estimate the free energy change during crystallization (44).

$$\Delta G_v = \Delta H_{fus} \frac{(T_m - T)T}{T_m^2} \qquad (1.5)$$

This relationship assumes that enthalpy varies linearly with temperature for both the supercooled liquid and crystal (44). Therefore, it can only be applied to supercooled liquids between T_g and T_m. The growth of the critically sized clusters is governed by the Gibbs-Thompson equation where S is the supersaturation ratio, v is the molecular volume,

and k is the Boltzmann constant (Equation 1.6) (25). Combining Equations 1.6 and 1.4 when r = r* to yield energy barrier in terms of supersaturation and temperature (Equation 1.7).

$$\ln S = \frac{2\gamma v}{k_B T r} \tag{1.6}$$

$$\Delta G^* = \frac{16\pi\gamma^3 v^2}{3(k_B T \ln S)^2} \tag{1.7}$$

Equation 1.8 shows that the nucleation rate (I) follows an Arrhenius type expression where A is a preexponential constant. Substituting Equation 1.7 into Equation 1.8 provides a more detailed picture of the various parameters that affect nucleation (Equation 1.9).

$$I = A exp\left(-\frac{\Delta G^*}{k_B T}\right) \tag{1.8}$$

$$I = A exp\left[-\frac{16\pi\gamma^3 v^2}{3(k_B T)^3 (\ln S)^2}\right] \tag{1.9}$$

Temperature and the supersaturation ratio have the largest effects on nucleation rate. Increasing concentration and/ or supercooling in the amorphous state should exponentially increase nuclei formation. While this is true for increasing concentration, nucleation rate increases then decreases with decreasing temperature. Clearly, there is an additional factor affecting nucleation that is not accounted for in Equation 1.9. Decreasing temperature results in a reduction in molecular motion which is observed as an increase in viscosity (45). This was shown above in Figure 1.5. The viscous free energy, ΔG_{visc}, was therefore incorporated as Equation 1.10 and better predicts the nucleation behavior from the amorphous state (46).

$$I = A exp\left[-\frac{16\pi\gamma^3 v^2}{3(k_B T)^3 (\ln S)^2} + \frac{\Delta G_{visc}}{k_B T}\right] \tag{1.10}$$

The equations above represent the ideal case of homogeneous primary nucleation. In reality, homogeneous nucleation is rarely observed, and heterogeneous nucleation is

more common. The presence of foreign materials or surfaces is typically found to reduce the free energy of nucleation which poses a particular challenge for stabilizing amorphous drugs (41). Similarly, secondary nucleation is also a particular concern in amorphous formulations as preexisting 'parent crystals' catalyze further nucleation and subsequent crystal growth (41).

Furthermore, measuring nucleation rate is rarely done by measuring the time at which at which a nucleus forms because nuclei are extremely small and difficult to detect until they grow into larger crystals. Rather, nucleation rates are estimated by measuring the induction time, t_{ind}, which is defined as the elapsed time between creation of supersaturation and the formation of a new phase (41). The new crystalline phase can be detected visibly or through a change in a property of the solution. Therefore, the induction time contains both the time for nucleation to occur as well as the time for the nucleus to grow to a detectible size (Equation 1.11).

$$t_{ind} = t_n + t_g \qquad (1.11)$$

Here, t_n is the steady-state nucleation time and t_g is the time to grow to a detectible size.

1.3.2.1.2 Crystal Growth

The second step in crystallization is crystal growth whereby additional molecules add to a stable nucleus and grow to an observable size. Crystal growth can occur either in the bulk or on the surface of amorphous solids. Surface crystallization is observed to be faster due to enhanced molecular mobility at the surface, however both must be inhibited to fully physically stabilize an amorphous formulation (47). The normal crystal growth rate (u) from the amorphous state can be described by Equation 1.12 (48).

$$u = \frac{k}{\eta}\left[1 - exp\left(-\frac{\Delta G_c}{RT}\right)\right] \qquad (1.12)$$

22

Here, k is a constant, η is the supercooled liquid viscosity, ΔG_c is the free energy difference between the amorphous and crystalline states, and R is the ideal gas constant. Similar to Equation 1.10 that described nucleation rate, Equation 1.12 also describes the competing contributions of thermodynamics and molecular mobility. $[1 - \exp(-\Delta G_c/RT)]$ describes the thermodynamic driving force where increased supercooling also increases ΔG_c and the crystal growth rate. Conversely, the molecular mobility contribution, $1/\eta$, shows that increasing viscosity slows the growth rate. Other factors including intermolecular interactions, polymeric additives, and humidity can also impact the crystal growth rate of amorphous pharmaceuticals (37, 49).

Crystal growth is normally diffusion-controlled whereby the rate of molecular addition to the growing crystal surface is limited by the rate at which molecules diffuse to the crystal-liquid (amorphous) interface. The crystal growth rate is directly proportional to diffusivity and is observed over a wide range of supercoolings (50). However, this relationship breaks down in some molecular systems near T_g and an abrupt increase in growth rate is observed relative the predicted diffusion-controlled rate (51-53). The positive deviation from diffusion-controlled crystal growth rate near T_g is termed diffusionless or glass-crystal (GC) crystal growth. Diffusionless crystal growth is not observed in all systems leading to potential issues modeling the stability of amorphous pharmaceuticals. The origin of this anomaly is debated in the literature and will be discussed further in chapter 5 (52, 54, 55).

1.3.2.1.3 Factors Affecting Crystallization Tendency

Configurational properties are a measure of the difference between the thermodynamic properties of the crystalline and amorphous state and have been used to

explain the thermodynamic driving force for crystallization from the amorphous state. Configurational properties are typically measured using differential scanning calorimetry (DSC) and rely on an accurate measurement of the difference in heat capacity ($C_{P,config}$) between the pure amorphous ($C_{P,amorph}$) and crystalline ($C_{P,crystal}$) phases. Figure 1.8 shows the reversing heat capacity of indomethacin and the corresponding configurational heat capacity.
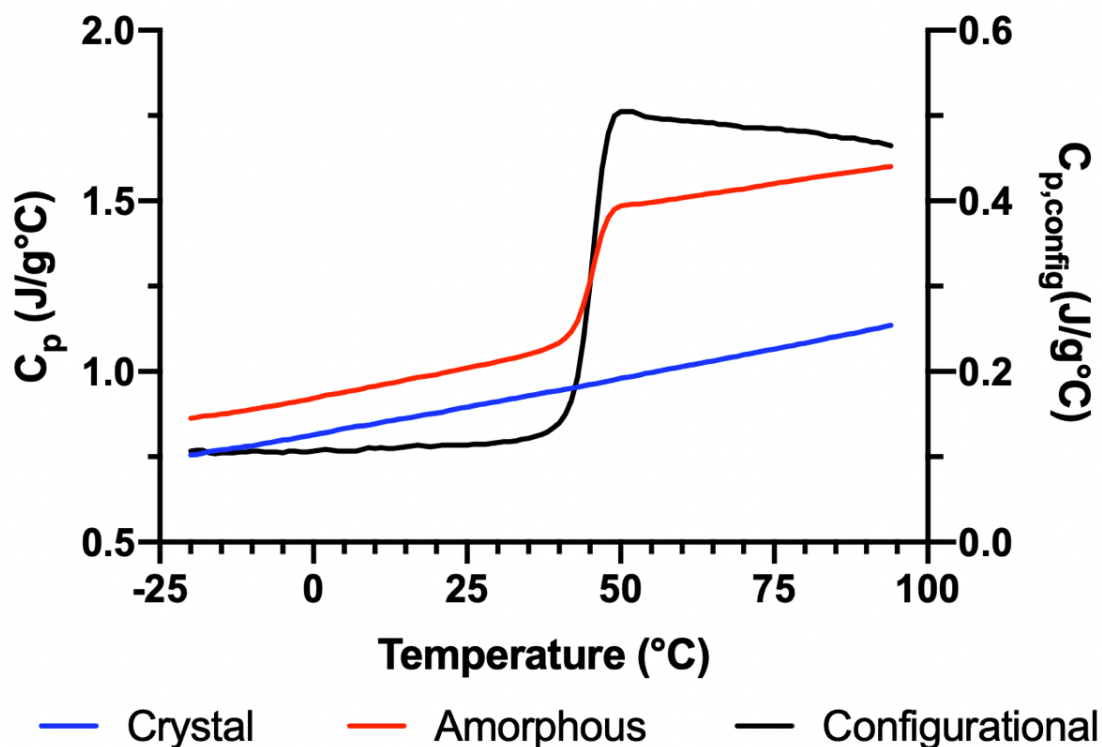
Figure 1.8. Crystalline, amorphous, and configurational heat capacity of indomethacin.

The change in $C_{P,config}$ with temperature (T) is used to measure configurational enthalpy, entropy, and free energy (H_{config}, S_{config}, and G_{config}, respectively). Equations 1.13 – 1.16 show how each configurational property is calculated from heat capacity data.

$$C_{P,config} = C_{P,amorph} - C_{P,crystal} \tag{1.13}$$

$$H_{config} = \Delta H_m - \int_T^{T_m} C_{P,config}\, dT \tag{1.14}$$

$$S_{config} = \Delta S_m - \int_T^{T_m} \frac{C_{P,config}}{T} dT \qquad (1.15)$$

$$G_{config} = \Delta H_{config} - T\Delta S_{config} \qquad (1.16)$$

Here, ΔH_m is the heat of fusion, T_m is melting temperature, and ΔS_m (= $\Delta H_m/T_m$) is the entropy of fusion. Configurational free energy is the same value used in Equations 1.5 and 1.12.

The importance of configurational properties has been discussed previously by Zhou et al. (56). Briefly, the thermodynamic driving force for crystallization can be enthalpic or entropic based. Since the crystal form is more stable than the amorphous state, crystallization is expected to be exothermic. Larger values for the heat of fusion or configurational heat capacity are directly related to the energy dissipated to the surroundings during crystallization. Conversely, there is an entropic energy penalty during crystallization as the crystal packs in a well-defined lattice whereas the amorphous form lacks long-range order. The configurational entropy can be thought of the degree of different configurations that molecules can exist in between the amorphous and crystalline states (57). The number of configurations in the crystal state is well defined by the crystal state of a particular polymorph. However, the lack of long-range order in the amorphous state allows molecules to orient in more configurations which may be dissimilar to the crystal structure. Therefore, configurational entropy is inversely related to the probability that molecules in the amorphous state are properly oriented for nucleation and crystal growth (56). Configurational entropy has been used to predict physical stability as compounds with greater configurational entropy values are generally found to possess superior physical stability however certain exceptions have been observed (56-58). While

the configurational entropy has predicted relative physical stability rather well, configurational enthalpy and free energy generally do not correlate well with stability (56).

1.4   Amorphous Solid Dispersions

The enhanced dissolution and greater solubility of the amorphous state relative to the crystalline state provide an opportunity to overcome the poor solubility of many drug candidates. However, it was shown above that the main drawback to an amorphous formulation is its inherent physical instability and propensity to recrystallize. The amorphous form must be stabilized during manufacturing and storage and, ideally, should also resist crystallization during dissolution in vivo.

In order to better stabilize the drug in the amorphous state it can be intimately mixed with an excipient, typically a polymer. The resulting molecular mixture is known as an amorphous solid dispersion (ASD) and helps maintain a solubility advantage relative to the crystalline state while having enhanced physical stability relative to the pure amorphous drug (Figure 1.4). While the focus of this dissertation is on the physical stability of ASDs during shelf life, their stability and performance during dissolution must briefly be considered.

Dissolution of a crystalline compound must overcome the crystal packing energy by disrupting the crystal lattice and removing individual molecules into solution (59). This is an energy intensive process and often limits the solubility of crystalline drugs. However, amorphous drugs do not have to break the crystalline lattice which often results in their rapid dissolution and high aqueous solubility. Ideally, an amorphous formulation provides a "spring and parachute" effect where a supersaturated solution is quickly generated and

the concentration is maintained for longer periods of time to maximize exposure to the drug (Figure 1.9). The spring is a result of the increased free energy of the amorphous state and its rapid dissolution. Since the resulting solution is supersaturated, the dissolved amorphous drug is thermodynamically unstable must be stabilized by the polymeric component of the ASD. If the parachute fails, the solubility advantage of the ASD is not realized, and the concentration dissolved equals the crystalline solubility (C_x).
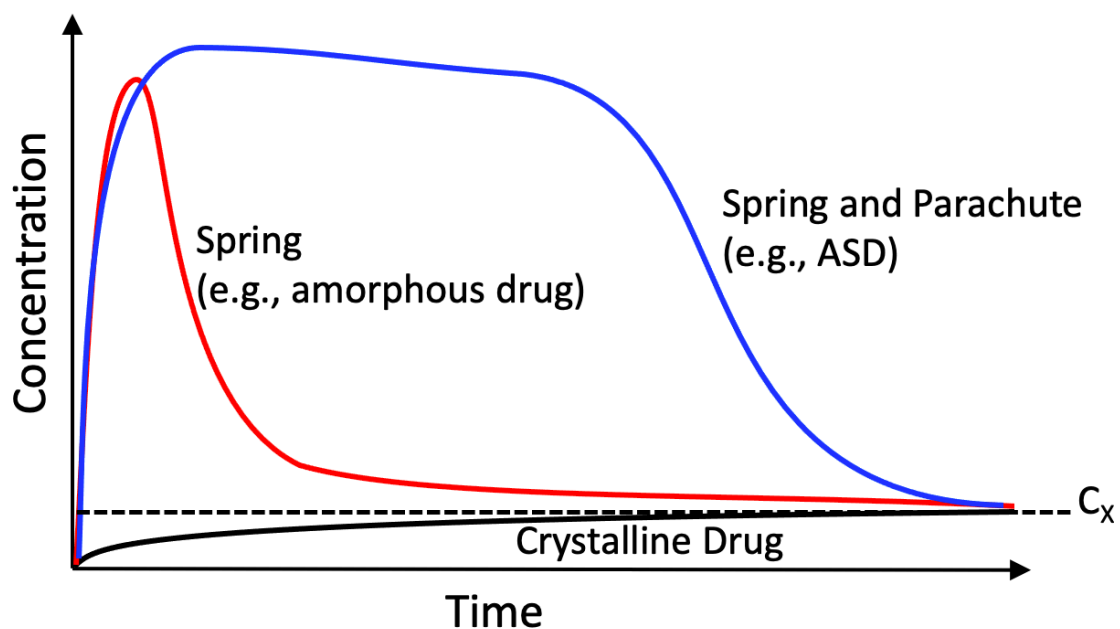
Figure 1.9. Spring and parachute dissolution profile where CX is the crystalline solubility. Adapted from ref. (59).

BCS class II and IV are ideal candidates for formulation as an ASD. The choice of polymer is dependent on the physicochemical properties of the API. However, only a few classes of polymers are used in most marketed formulations. This includes vinylpyrrolidone-based (PVP, PVPVA), cellulose-based (HPC, HPMC, HPMCAS), polyethylene glycol, and methacrylate/ methacrylic acid (Eudragit) (60, 61). The polymer usually acts to physically stabilize the amorphous drug and/ or improve dissolution.

Ternary ASDs may also be formulated with a surfactant or multiple polymers to better control the dissolution rate and stability.

In order to take advantage of the combined drug-polymer properties relative to the individual components on an ASD, the drug and polymer must be intimately mixed to form a miscible single-phase system (25). Miscibility is determined both by the drug-polymer combination their relative ratio. Miscibility is expected when the free energy change upon mixing is negative ($\Delta G_{mix} < 0$), as expressed by the Gibbs-Helmholtz equation (Equation 1.17).

$$\Delta G_{mix} = \Delta H_{mix} - T\Delta S_{mix} \tag{1.17}$$

The free energy change is controlled by either the enthalpy (ΔH_{mix}) or entropy (ΔS_{mix}) of mixing at a given temperature, T. There is greater disorder in a mixture relative to the individual components so entropic changes are typically favorable to mixing ($\Delta S_{mix} > 0$). Higher temperatures further favor mixing when ΔS_{mix} is negative such that the magnitude of the entropic contribution is greater.

There is no enthalpy change in an ideal mixture (i.e., $\Delta H_{mix} = 0$) and miscibility is determined by entropy. However, real mixtures often have enthalpic contributions due to specific interactions between the drug and polymer. The enthalpy of mixing is determined by the number and strength of interactions between the drug and polymer. Exothermic mixing occurs when adhesive drug-polymer interactions are more favorable than the cohesive drug-drug and polymer-polymer interactions ($\Delta H_{mix} < 0$). Conversely, mixing is endothermic when $\Delta H_{mix} > 0$.

The thermodynamics of mixing in solid systems are usually described by the Flory-Huggins (FH) lattice theory (62). FH theory was developed to calculate the change in free

energy upon mixing two polymers in the absence of any specific interactions and takes the difference in size of the polymeric units into account by using volume fractions of drug and polymer rather than mole fractions. Despite hydrogen bonding in many drug-polymer systems, FH lattice theory is often sufficient for modeling the mixing of a small molecule API with a relatively large polymer (Equation 1.18).

$$\Delta G_{mix} = RT(n_1 ln\phi_1 + n_2 ln\phi_2 + n_1\phi_2\chi) \qquad (1.18)$$

Here, R is the ideal gas constant, n_1 and n_2 are the moles of drug and polymer, respectively. Φ_1 and Φ_2, are the volume fractions of drug and polymer, respectively, and χ is the Flory-Huggins drug-polymer interaction parameter. The left-hand portion of the FH equation describes the entropic contributions to mixing (Equation 1.19) whereas the enthalpic contribution is described by the right-hand portion of the FH equation (Equation 1.20) (63).

$$\Delta S_{mix} = -R(n_1 ln\phi_1 + n_2 ln\phi_2) \qquad (1.19)$$

$$\Delta H_{mix} = RTn_1\phi_2\chi \qquad (1.20)$$

χ provides a numerical measure of miscibility where negative values indicate miscibility and positive values suggest immiscibility. χ can be determined by Hildebrand solubility parameters, melting point depression, or drug-polymer dissolution/ crystallization data (64-66). Chapter 4 demonstrates the use of recrystallization data to determine χ in a nifedipine-polyvinylpyrrolidone ASD.

1.4.1 Causes of Instability

Amorphous solid dispersions are still plagued by many of the problems facing a pure amorphous drug in addition to new issues that arise by the addition of a polymeric excipient. Most notably, the polymers used are often hygroscopic and may absorb significant amounts of water which can lead to phase separation and/ or drug crystallization

(67). The possibility also exists for chemical interactions or degradation between the drug and polymer including hydrolysis, oxidation, acid-base reactions, or Maillard reactions (25). However, despite the issues mentioned above and the stabilizing effects of the polymeric excipient, the biggest stability concern to ASDs is recrystallization or phase separation. Most pharmaceutically relevant drug loadings result in formulations which are still metastable relative to the crystalline form. Formulation of low drug loadings and storage at low temperatures (below T_g) are the most common ways in which ASDs can be further stabilized against recrystallization.

1.4.1.1 Drug-in-Polymer Solubility

The physical stability of an amorphous drug in an ASD is ultimately determined by its drug loading relative to its polymer-specific solubility. Just as every drug has an aqueous solubility, it also has a solubility in the polymer used in the ASD however the polymer now acts as the solvent. The stability of the ASD depends on both the drug loading and storage temperature. Figure 1.10 shows an example temperature-composition phase diagram.
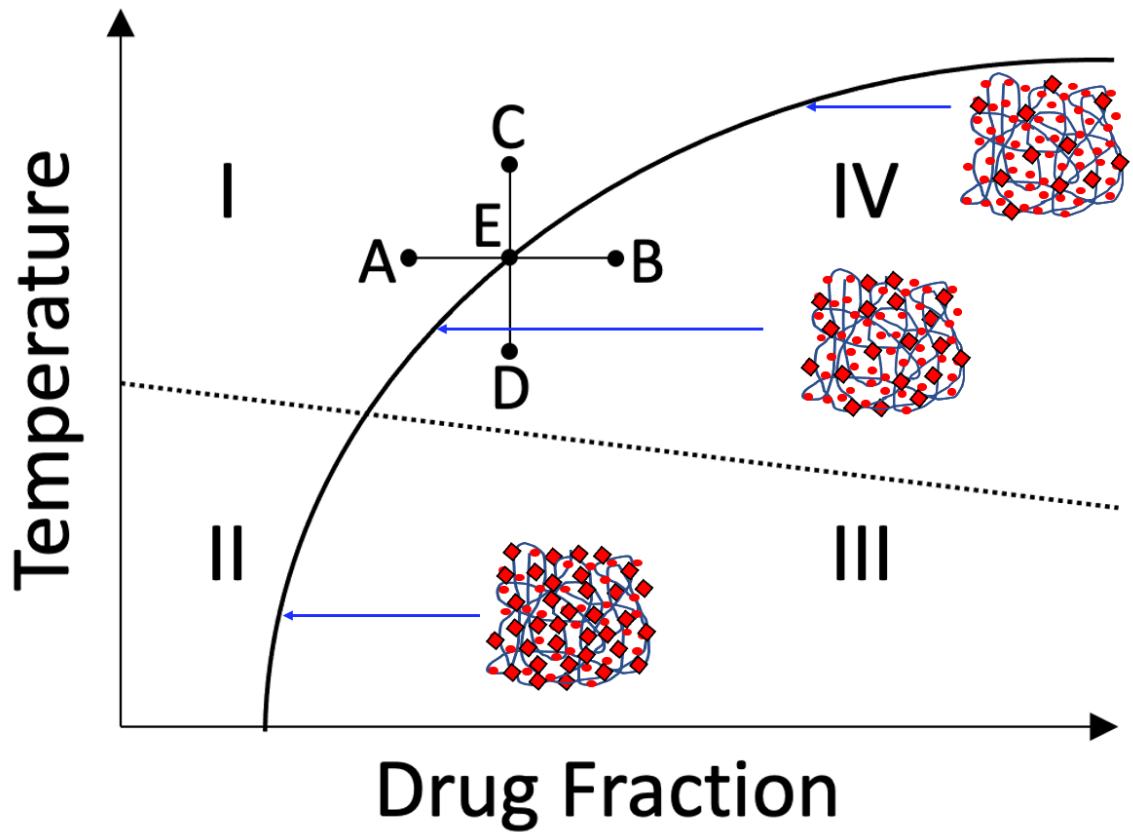
Figure 1.10. Theoretical two-component phase diagram. Adapted from ref. (66). An illustration of the changing drug-polymer system is overlaid where dark blue lines represent the polymer, red circles represent amorphous drug, and red diamonds represent crystalline drug. At high temperatures, the crystalline drug solubility is high and little drug will recrystallize whereas at low temperatures, solubility is low and only a small fraction of drug remains amorphous.

The solid line in Figure 1.10 is the solid-liquid equilibrium curve and represents the equilibrium solubility of crystalline drug in a polymer matrix at a specific temperature. Above the curve, the polymer is undersaturated with drug and will remain physically stable. Below the solubility curve, the ASD is supersaturated and drug will eventually crystallize. Drug will continue to crystallize until the composition of the remaining ASD reaches the

concentration governed by the equilibrium solubility curve at a given temperature. At this point, crystallized drug will exist in equilibrium with the saturated ASD (63). Figure 1.10 can be divided into four regions based on tendency to crystallize using the T_g of the amorphous mixture. Regions 1 and 2 are undersaturated and physically stable at all temperatures with region 1 an undersaturated melt and region 2 an undersaturated glass. Regions 3 and 4 are both supersaturated and, therefore, thermodynamically unstable. Below T_g, region 3 is a kinetically stabilized glass while above T_g, region 4 is both a kinetically and thermodynamically unstable melt. Consequently, the four regions can be ordered by the increasing risk of crystallization: $I = II < III < IV$.

Designing an undersaturated ASD may or may not be feasible depending on the solubility of the drug in the polymer at storage temperature. Many BCS class II and IV drugs also have relatively low solubility in polymers typically used for ASD formulations (68). Therefore, apart from highly potent APIs, formulation of an undersaturated ASD may not provide an efficacious dose of drug and a supersaturated dispersion may be required. Samples in region 3 are kinetically stabilized against crystallization due to the decreased molecular mobility in the glassy state, however the degree to which the system is stabilized is dependent on a variety of factors including any specific drug-polymer interactions and the supersaturation ratio. Extensive stability testing is required as the ASD still must remain stable over the shelf life of the drug. Samples in region 4 pose the greatest risk of crystallization as they have no kinetic stability. The only stability offered in this region comes from specific drug-polymer interactions, yet crystallization is often observed to occur quickly in region 4. Nonetheless, storage in this region should be avoided to help ensure product stability over the shelf life of the drug.

Despite the importance of drug-polymer solubility as a formulation parameter, its determination is non-trivial and often a time-consuming process. The tie lines in Figure 1.10 indicate the four ways in which equilibrium solubility can be approached and are described in detail by Sun et al (66). Briefly, path AE follow the dissolution of crystalline drug into an undersaturated solution at a constant temperature. Path BE is also an isothermal approach which follows crystallization out of a supersaturated ASD. Path CE begins with an undersaturated solution and measures the temperature at which crystallization occurs upon cooling. Path DE is opposite to CE and measures the dissolution temperature or melting point depression upon heating a supersaturated ASD. Despite approaching equilibrium from different directions, each path should provide a thermodynamically equivalent measure of solubility.

The solubility of a drug should ideally be measured at the temperature of interest (i.e., storage or room temperature). This is not an issue for aqueous solubility measurements as the liquid solvent (water) is not viscous and excess solute (drug) can quickly precipitate out to form a saturated solution. However, the inverse relationship of temperature and viscosity complicates drug-polymer solubility measurements as most pharmaceutically relevant polymers are sufficiently viscous or even solid at ambient temperatures. Increased viscosity slows the kinetics of dissolution or crystallization required to achieve equilibrium between a crystalline drug and a saturated ASD to the point where the required experimental time may become unreasonably long (69).

Because of the difficulties in measuring drug-polymer solubility highlighted above, solubility measured at elevated temperatures must be extrapolated to relevant temperatures using a suitable equation of state. Flory-Huggins (FH) theory has been used for this purpose

most frequently as it is relatively easy to experimentally measure the interaction parameter

(χ) using thermal analysis methods. Equation 1.21 is the Flory-Huggins equation:

$$\frac{\Delta H_m}{R}\left(\frac{1}{T_m} - \frac{1}{T}\right) = ln(v_1) + \left(1 - \frac{1}{\lambda}\right)(1 - v_1) + \chi(1 - v_1)^2 \qquad (1.21)$$

where ΔH_m is the heat of fusion, R is the ideal gas constant, T_m is the melting point, v_1 is

the drug volume fraction, λ is the molar volume ratio of the polymer and drug, and χ is the

Flory-Huggins/ drug-polymer interaction parameter. As discussed previously, the FH

equation assumes there are no significant interactions between drug and polymer (62).

However, this often does not hold true for pharmaceutical systems where drug-polymer

interactions, such as hydrogen bonds, are associated with enhanced physical stability (70).

The limitations of FH theory have been recognized and additional predictive methods have

been proposed to better account for specific interactions which usually exist in ASDs (71).

There have been many modifications of the FH theory for modeling ASDs. In

particular, the Kyeremateng and perturbed chain statistically associated fluid theory (PC-

SAFT) methods have been applied for drug-in-polymer solubility measurements. The

Kyeremateng method uses an empirically derived equation to predict the temperature at

which a specific drug loading is solubilized using the pure drug melting point and a

measure of drug-polymer interactions (72). PC-SAFT was developed by Gross and

Sadowski to measure the residual Helmholtz energy of a binary drug-polymer mixture

based on repulsion, dispersion, and association interaction contributions (73).

While drug-in-polymer solubility is an important formulation parameter, it is

important to note that it measures the crystalline solubility which is typically very low for

most drug-polymer combinations. For example, nifedipine's solubility in

polyvinylpyrrolidone is around 2% (w/w). This shows that most reasonable formulations

are thermodynamically unstable and must be kinetically stabilized by storage below T_g or sufficient drug-polymer interactions to inhibit crystallization over the shelf life of the drug product. Further, the polymer molecular weight does not have a significant impact on the drug's solubility (74). Therefore, the solubility of an ASD may be improved by changes to the polymer used rather than varying the polymer molecular weight.

Chapter 4 further examines the difficulties of measuring drug-in-polymer solubility using the recrystallization method. Specifically, new methods to quantify crystallinity and approach equilibrium are discussed.

1.4.2 Stability Mechanisms

Depending on the polymer used and its concentration in the ASD, it can act in different ways to stabilize the amorphous drug. In general, the drug is stabilized against crystallization through antiplasticization/ reduced mobility, the formation of specific drug-polymer interactions, and/ or dilution effects. The result is typically an increased crystallization activation energy by the inhibition or slowing of nucleation and/ or subsequent crystal growth (61).

1.4.2.1 The Glass Transition Temperature and Reduced Mobility

The high degree of molecular mobility in the amorphous state relative to the crystal contributes to its instability. The glass transition temperature is a rough measure of molecular mobility where a larger value of T_g indicates a reduction in mobility. Most polymers have a T_g significantly higher than the API. In a phase separated system, two separate T_gs equal to each individual T_g are expected (25). However, a single T_g, intermediate to the T_g of pure drug and polymer, should be observed in intimately mixed ASDs.

By raising the T_g of the ASD, the polymer acts as an antiplasticizer and confers its relatively restricted mobility onto the drug. Conversely, the drug, having a lower T_g, acts as a plasticizer and lowers the mixture T_g relative to the polymer. Other low molecular weight additives such as water plasticize amorphous systems and may negate the stabilizing effects of the polymer through higher mobility and/ or phase separation that may result in crystallization (67).

The glass transition is likely the most important property of an ASD as it is used to estimate the physical stability and set storage conditions (75). Therefore, its measurement and prediction are critically important. The most common way to predict the glass transition temperature of an ASD is the Gordon-Taylor (GT) equation (76). The glass transition temperature of the mixture ($T_{g,mix}$) is predicted in Equation 1.22 using the properties of each pure component weighted to account for their relative concentrations in the ASD.

$$T_{g,mix} = \frac{X_1 T_{g,1} + K X_2 T_{g,2}}{X_1 + K X_2} \qquad (1.22)$$

Here, X_1 and X_2 are the weight fractions of the drug and polymer while $T_{g,1}$ and $T_{g,2}$ are the pure drug and polymer T_gs, respectively. The GT equation was originally developed for copolymers and assumes the two components are roughly the same size (molecular volume) and do not interact (e.g., hydrogen bond) with one another. Deviations from the GT-predicted T_g may be a result of specific drug-polymer interactions (75). The effect of drug-polymer interactions on ASD stability will be discussed in the following section. The constant, K, is related to the individual properties of each component. The Simha-Boyer rule (Equation 1.23) uses the density (ρ) and T_g while Couchman-Karasz (Equation 1.24) measures the change in heat capacity (C_p) at T_g (77, 78).

$$K = \frac{\rho_1 T_{g,1}}{\rho_2 T_{g,2}} \qquad\qquad (1.23)$$

$$K = \frac{\Delta c_{p,1}(T_g)}{\Delta c_{p,2}(T_g)} \qquad\qquad (1.24)$$

It is typically assumed that an amorphous solid should be stored at $T_g - 50°C$ or below to totally inhibit α- and β- motions contributing to crystallization on a pharmaceutically relevant timescale (i.e., shelf life ~ 2 years) (20). However, indomethacin has been observed to nucleate in less than five months at 55°C below its T_g (79). Hence, even storage far into the glassy state may be insufficient to stabilize an amorphous drug. Increasing concentrations of polymers with a relatively high T_g have been shown to increase viscosity and suppress the α-relaxations and possibly the β-relaxations involved in nucleation and crystallization (80).

1.4.2.2 Specific Interactions

Specific interactions including between the drug and polymer may exist based on the structure of each molecule and the state of mixing in the multicomponent system. These interactions include hydrogen bonding, ionic bonding, dipole-dipole interactions, and Van der Waals interactions. The presence of adhesive drug-polymer interactions is known to contribute to the physical stability of ASDs where the polymer interrupts cohesive drug-drug interactions which are also found in the crystalline state (81). The polymer accomplishes this through a reduction in mobility which can inhibit nucleation and/ or prevent subsequent crystal growth (61).

It is typically assumed that stronger and more numerous interactions confer greater resistance to crystallization in ASDs. Table 1.1 describes the bond strength of each type of specific interaction. Ionic bonds form the strongest drug-polymer interactions and typically

confer the greatest physical stability to the amorphous drug. For example, ketoconazole (KET) forms ionic and hydrogen bonds with PAA and PHEMA, respectively while only interacting with PVP through dipole-dipole interactions. It was found that the interaction strength trended with crystallization resistance where, in order of increasing resistance to crystallization: KET-PVP < KET-PHEMA < KET-PAA (70). However, hydrogen bonds are observed most often in ASDs and the hydrogen bond strength is also related to physical stability. Compared to HPMCAS and PAA, nifedipine formed stronger hydrogen bonds with PVP which reduced α-mobility and slowed crystallization kinetics (82).

Table 1.1. Strength of various drug-polymer interactions. Adapted from ref. (83).

Type of Interaction	Bond Energy (kJ/mol)
van der Waals	~ 1
Dipole-dipole	2 – 8
Hydrogen bonding	50 – 170
Ionic bonding	850 – 1700

The effectiveness of drug-polymer interactions in stabilizing ASDs is modulated by the degree of mixing between the drug and the polymer. Just because hydrogen bond donator and acceptor groups exist between the two components does not mean hydrogen bonds will be formed, nor does it mean the system will be sufficiently stable. For example, physical mixtures of indomethacin and PVP show no spectroscopic evidence of drug-polymer hydrogen bonds whereas ASDs prepared by solvent evaporation showed direct interactions between the indomethacin carboxylic acid and PVP amide (84). Furthermore, the relative concentrations of drug and polymer play a large role in the extent of hydrogen

bonding and miscibility. For instance, nifedipine-PVP ASDs were only partially miscible at high drug loadings where drug-polymer hydrogen bonding was limited compared to lower drug loads where nifedipine was extensively hydrogen bonded with PVP and the system was miscible (85). The examples above highlight the importance of specific interactions, in ASDs against crystallization. Both the drug-polymer combination, concentration, and the formulation/preparation method must be considered to help ensure stabilizing drug-polymer interactions form.

Lastly, environmental factors including temperature and humidity impact the ability of hydrogen bonds to stabilize the amorphous drug. Hydrogen bond strength decreases at higher temperatures, therefore the ability of polymers to stabilize the drug at high temperatures is diminished (86). The presence of moisture at elevated relative humidity can cause phase separation and crystallization by replacing drug-polymer hydrogen bonds with drug-water or polymer-water bonds. In addition, the hygroscopic nature of many pharmaceutical polymers can lead to extensive water sorption and plasticization resulting in an additional stability risk (87, 88). It was suggested that the strength of drug-polymer interactions affect the extent to which phase separation and crystallization occur in PVP-containing ASDs (67). Thus, the polymer partially loses its drug-stabilizing ability, and it is easier for crystallization to proceed.

1.4.2.3 Dilution Effects

Even in situations where the drug and polymer do not form specific interactions, the polymer may still be able to stabilize low concentrations of amorphous drug. High concentrations of polymer physically separate drug molecules in the amorphous matrix and act as a barrier to their translational motion required for nucleation and crystal growth. For

instance, the indomethacin (IND) carboxylic acid dimer is the dominant hydrogen bonding species found in γ-IND and is also present in α-IND. In polystyrene ASDs with 5% or less indomethacin, Yuan et al. observed increasing amounts of free (unbound) indomethacin (89). In addition, lowering the concentration of drug also lowers its supersaturation ratio in the polymer. Therefore, the thermodynamic driving force for crystallization is also reduced.

1.4.3 Formulation Approaches

The formation of an amorphous drug or ASD is usually a top-down method in which a crystalline drug is transformed into an amorphous drug system. While a vast number of methods exist for both lab- and commercial-scale production, ASD formulation can broadly be classified into two categories: fusion based or solvent based (90). The desired end product is an ASD which is stable over the shelf-life of the drug and offers improved dissolution performance relative to the crystalline drug (75).

1.4.3.1 Fusion Based

Fusion based methods were first proposed by Sekiguchi and Obi and begin with the crystalline drug or a physical mixture of crystalline drug and polymer. The mixture is heated above the melting point of the drug, allowed time for molecular mixing of drug and polymer to occur, then solidified by cooling (91). Fusion based techniques are easy to implement as they do not involve the use of a solvent. However, fusion-based applications are often limited to drug-polymer combinations that are miscible at high temperatures in order to ensure homogeneous mixing occurs. Phase separation may result if the drug and polymer are immiscible or cooled at exceedingly slow rates (92). The drug and polymer should also thermally stable at the temperature chosen or else degradation may occur (93).

1.4.3.1.1 Hot Melt Extrusion

In its most basic form, the fusion technique can be applied by melting a mixture of drug and polymer in an oil bath prior to quench-cooling in liquid nitrogen. Similarly, heating and cooling in a differential scanning calorimeter can produce small amounts of an amorphous solid dispersion. On a pharmaceutical production scale, the most commonly applied fusion-based method is hot melt extrusion (HME). Figure 1.11 shows a simplified schematic of a twin-screw hot melt extruder.
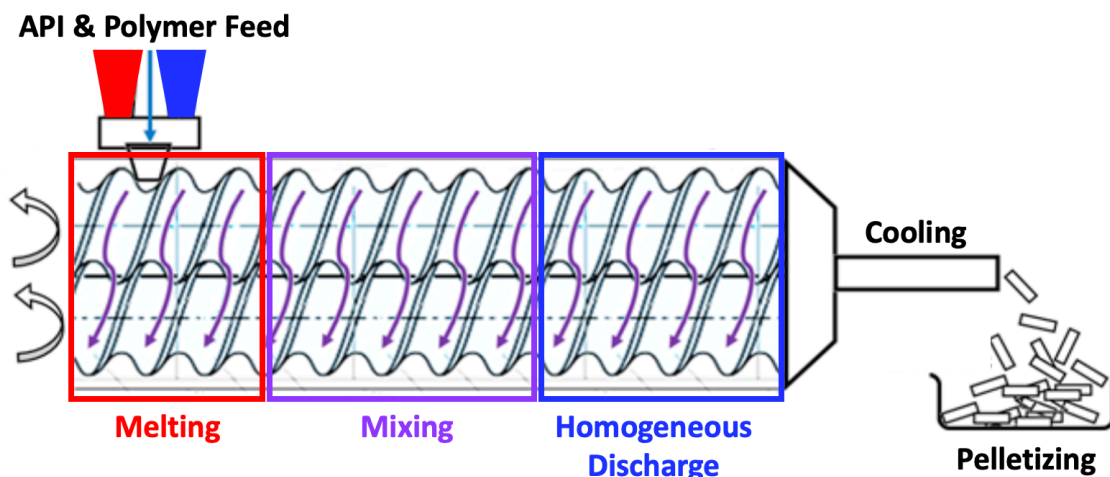
Figure 1.11. Simplified twin screw hot melt extruder diagram. Adapted from ref. (94).

In HME, a powdered physical mixture is introduced into the extruder which simultaneously heats and mixes the combination until a molten phase is formed. The mixture if conveyed along a barrel by a single or double screw system. The temperature and screw speed can be adjusted to tailor the mixture to the desired final properties and/ or ensure a crystalline-free ASD is formed. Aside from being solvent-free, HME is widely used in the pharmaceutical industry as it can be operated as either a batch or continuous process, is high-throughput and easily scalable throughout the drug development process (95). HME also minimizes processing steps by providing the opportunity to extrude the

ASD into the shape of the final dosage form including tablets or pellets (96). HME has been used extensively in the literature as a convenient way to create ASDs (90). HME has also been successfully used for the commercial manufacturing of Intelence, Isoptin SR, Kaletra, Norvir, Noxafil, Onmel, and Rezulin (60).

1.4.3.2 Solvent Based

Solvent based methods are often used for thermolabile drugs to avoid the possibility thermal degradation. Typically, a drug and polymer are dissolved in a common solvent prior to evaporative drying at low temperatures. Molecular mixing of drug and polymer is much more efficient in a liquid solution relative to the molten state and should exist after rapid solvent removal through drying. Solvent based methods include spray drying, freeze drying, spray freeze drying, rotary evaporation, electrospinning, and supercritical solvation or anti-solvation (97). The two main limitations of solvent-based methods are finding a suitable solvent and the removal of solvent below acceptable levels.

Finding a suitable solvent where both the hydrophobic drug and hydrophilic polymer are sufficiently soluble can be difficult due to differences in polarity. In this case, a cosolvent system may be used or a surfactant added. However, Baghel et al. point out that surfactants used in this manner often concentrate in the final dosage form, potentially lessening drug loading or leading to toxicity issues (90). Even after the initial solvent removal, residual solvent may remain which may pose health risks to the patient. The International Council of Harmonization (ICH) has set guidelines for solvent-specific concentrations of residual solvent that may remain in a final formulation. Removal of residual solvent to ICH-acceptable levels is system-dependent and may prove difficult even with secondary drying steps (59). In addition, the residual solvent can act as a plasticizer

with potentially negative impacts to both chemical and physical stability (98). Solvent removal also tends to be relatively expensive due to the use of large volumes of organic solvents. The evaporation of large volumes of organic solvent may, in turn, also pose an environmental concern. However, despite the many risks of solvent-based formulation techniques, it is extensively used in the pharmaceutical industry especially during early-stage development as it is applicable to most compounds and material sparing at small-scale (99, 100).

1.4.3.2.1 Spray Drying

Spray drying is the most popular solvent-based production method in the pharmaceutical industry and has been widely used for API production, micro-particles or -capsules, nanoparticles, controlled release particles, liposomes, and ASDs (100, 101). Broadly, spray drying transforms a crystalline drug into an amorphous drug or ASD through a multistep process. First, a feed solution containing dissolved drug and polymer is atomized by spraying through a nozzle to form a stream of droplets. The discharged droplets contact the surrounding drying fluid (hot air) at which point a heat and mass transfer reaction occurs on the droplet surface. The rapid solvent removal causes a sharp increase in viscosity, trapping drug molecules within an amorphous polymer matrix (90). Dried particles are removed from the drying chamber and collected using a cyclone. A simplified schematic of the spray drying process is shown below in Figure 1.12.
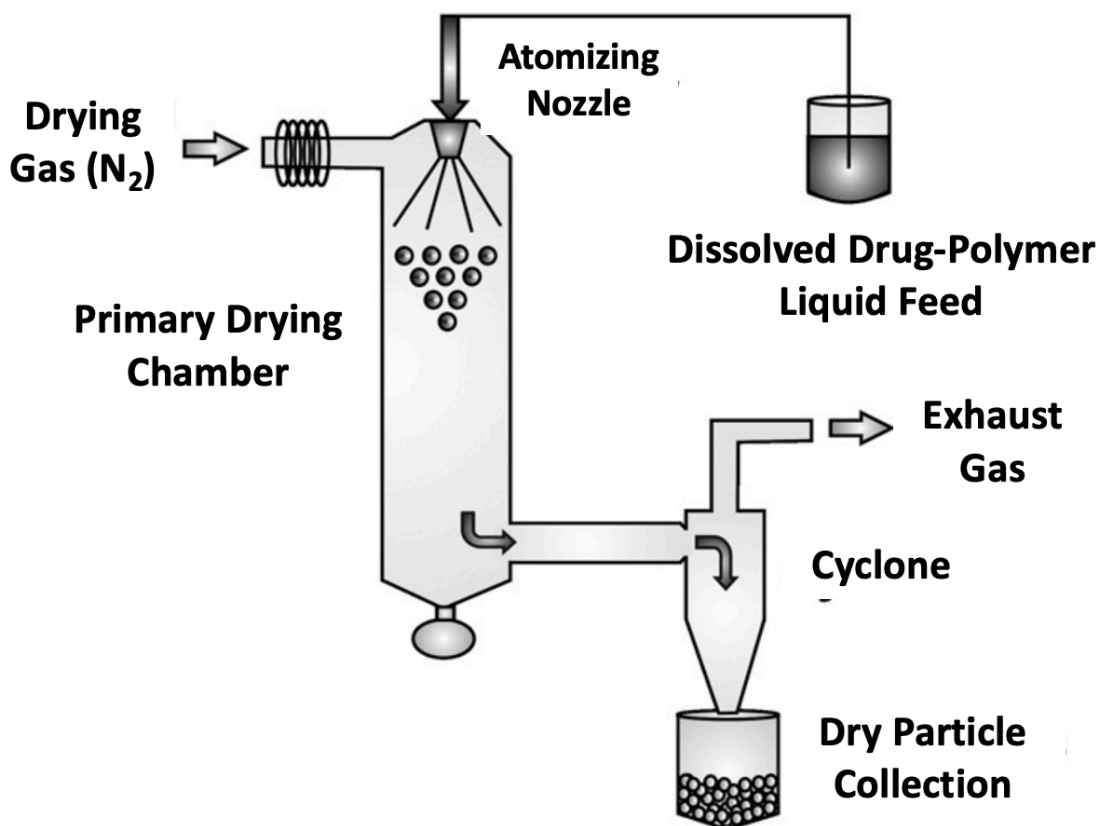
Figure 1.12. Simplified spray drying schematic. Adapted from ref. (102).

Figure 1.12 notes various experimental and processing parameters which may be changed to modify the physical properties of the final product. This includes the inlet and outlet conditions, nozzle type, air flow rate and orientation, and cyclone dimensions (100). However, modification of processing conditions alone is not enough to generate a non-phase separated amorphous system as Mahlin et al. and Baird et al. showed the drug and polymer physicochemical properties also play a significant role (103, 104). Nonetheless, spray drying offers better process control than other solvent-based techniques and is easily scalable during the development process. It has been successfully employed in the production of Crestor, Fenoglide, Incivek, Intelence, Kalydeco, Lozanoc, Noxafil, and Sporanox (60).

1.4.3.2.2 Co-precipitation

Another less commonly used solvent-based method is co-precipitation, which takes advantage of drug-polymer-solvent immiscibility rather than miscibility in common solvent. Co-precipitation dissolves a drug and polymer in a common solvent before adding an anti-solvent in which both the drug and polymer are insoluble. The anti-solvent is miscible with the first solvent yet causes immediate precipitation of drug and polymer. The precipitated particles are filtered, washed, and dried to yield ASDs. Filtration and washing of the precipitated particles yield an ASD. Dong et al. found that drug-HPMCAS precipitates were more porous and dissolved faster than similar ASDs produced by HME (105). The unique physical properties of co-precipitated dispersions may allow for its application as an alternative to spray drying or HME. To date, Zelboraf and Certican are the only commercially available coprecipitated ASDs (60).

1.4.4 Characterization Techniques

Perhaps just as important as formulating an ASD is the ability to adequately characterize the ASD. The full characterization of ASDs is vital from both a research and regulatory perspective to achieve a qualitative and quantitative understanding of the drug product physicochemical properties, stability, and performance upon dosing. Luckily, a myriad of characterization techniques and are often used in conjunction with one another to effectively characterize amorphous drug formulations. Of particular interest to ASDs is the detection and characterization of crystallinity, physical properties (chemical structure, T_g, T_m, pK_a, etc.), drug-excipient interactions, degree of mixing, phase behavior/ transformations, molecular mobility, moisture content, physical stability, and dissolution performance. While the in vivo performance is also of paramount importance, the

characterization techniques discussed herein will be restricted to the characterization of physicochemical properties and some in vivo performance.

1.4.4.1 Differential Scanning Calorimetry

Differential scanning calorimetry (DSC) is perfectly suited for the measurement of many of the thermal properties of ASDs including the all-important T_g. DSC is widely available and used in both academic and industrial settings as part of the standard analytical toolbox used for ASD characterization and drug development (106). Standard DSC heats both an empty and sample-filled aluminum pan at a linear heating rate and records the difference in heat flow required to maintain an equal temperature between the two pans. Thermally induced transitions occurring in the sample require the input of more heat flow or less heat flow to the sample pan (relative to the reference pan) to maintain its linear increase in temperature. For example, crystallization is exothermic which requires less heat flow to maintain the temperature. Similarly, the endothermic heat of fusion upon melting will require more heat flow in order to continue raising the temperature linearly. However, simultaneously occurring thermal events cause overlapping heat flow signals, complicating the analysis of many pharmaceutical materials. Modulated DSC (mDSC) was developed to help overcome this by imposing a sinusoidal heating rate upon the linear/ underlying heating rate of standard DSC. The modulated heating rate deconvolutes total heat flow (Q_{tot}) into two components: reversing (Q_{rev}) and non-reversing (Q_{nonrev}) which are described by Equations 1.25 and 1.26:

$$Q_{tot} = Q_{rev} + Q_{nonrev} \qquad (1.25)$$

$$\frac{dH}{dt} = C_p \frac{dT}{dt} + f(T,t) \qquad (1.26)$$

where dH/dt is the total heat flow, C_p is the reversing heat capacity calculated from just the modulated heat flow, and dT/dt is the measured heating rate. C_pdT/dt is the reversing heat flow component and f(T,t) is the kinetic component of total heat flow calculated from the difference between the total signal and heat capacity (reversing) component. The reversing heat flow measures transitions that respond to the instantaneously changing heating rate including the heat capacity, glass transition, and most melting (75, 106). The non-reversing heat flow signal corresponds to kinetic processes such as enthalpic relaxation, evaporation, melting, crystallization, curing, and decomposition (106).

As was previously mentioned, the T_g is a defining property of the amorphous state and is often used as a rough indicator of physical stability. Therefore, the T_g is often the first thermal property measured and, fortunately, T_g is straightforward using the mDSC reversing heat flow signal. The T_g corresponds to the change in heat capacity between glassy and rubbery state and is typically measured as the midpoint or half-height of the step-change in the reversing heat flow signal (75). However, the T_g is a kinetic event and the exact location of T_g is heavily dependent on the sample's thermal history and water/ solvent content as well as the linear heating rate (107). An example of a typical mDSC heating scan is shown in Figure 1.13 where the T_g (-0.43°C), crystallization onset (T_c = 65.9°C), and melting point (T_m = 90.5°C) are shown for indomethacin methyl ester.
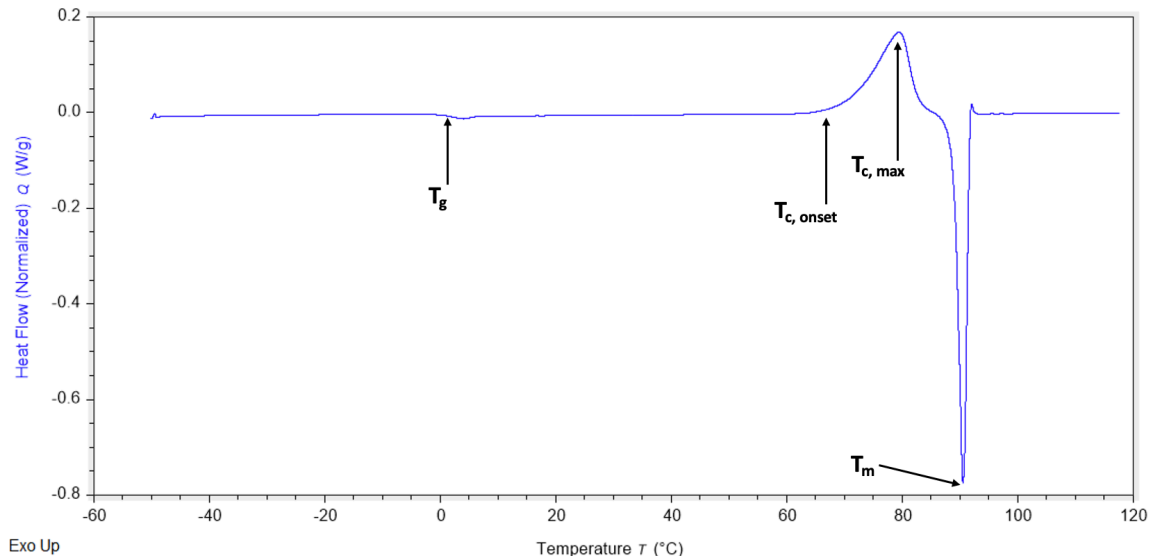
Figure 1.13. Standard DSC scan for indomethacin methyl ester showing the glass transition, crystallization, and melting.

DSC is also particularly suited for the measurement of molecular mobility. T_g is a rough measure of the temperature at which molecular mobility drastically changes and can be measured as described above. From a physical stability perspective, crystallization is the main challenge facing an ASD formulation. Crystallization is a two-step process of nucleation and crystal growth, both of which require varying levels of molecular mobility to occur (75). DSC can monitor enthalpic relaxation which is a measure of molecular mobility below the T_g. Below T_g, the amorphous system is in the non-equilibrium glassy state and has excess volume and enthalpy relative to the equilibrium crystalline state. The rate of relaxation towards equilibrium is temperature and time dependent and can be measured by DSC. After storage below T_g, the enthalpy or volume 'lost' to relaxation is regained through reheating the sample through T_g and measured as an enthalpic relaxation endotherm at T_g. The integrated enthalpic relaxation endotherms can be fit to the various equations as a function of storage time to yield relaxation times which indicate molecular

mobility (108-112). Most often, the Adam-Gibbs-Vogel (AGV) or Kohlrausch-Williams-Watts (KWW) equations are used to model relaxation in the glassy state whereas the Vogel-Tammann-Fulcher (VTF), Adam-Gibbs (AG), Williams-Landell-Ferry (VLF) equations predict relaxation times above T_g (75).

Most often, however, DSC measurements use the KWW equation to predict relaxation times below T_g as it accounts for a wide range of individual relaxation times occurring simultaneously. Shamblin and Zografi first applied the structural relaxation method to sucrose mixtures using the KWW equation (113). Since then, variations of the method have been applied to a wide range of pharmaceutical systems. Marsac et al. partially attributed different physical stability characteristics to differences in the relaxation times of nifedipine- and felodipine-PVP ASDs (58). Bhugra et al. also used KWW relaxation times in conjunction with dielectric spectroscopy to predict crystallization onset in various BCS class II drugs (114).

DSC has also been employed to help characterize amorphous solid dispersions through their thermodynamic and kinetic properties and crystallization propensity. Two particularly important studies conducted using DSC were by Zhou et al. and Baird et al (40, 56). Zhou et al. determined the configurational properties of five different drugs and related the configurational entropy amorphous stability (56). The importance of configurational properties as a screening tool for stability has been investigated further although the results have been contradictory at times (57, 58, 115). Baird et al. related the stability of a glass to their glass forming ability (GFA) as measured by their crystallization tendency during cooling and heating from the melt (40). The GFA of a drug has since been shown to directly correlate with a drug's stability in an ASD (116).

1.4.4.2 Thermogravimetric Analysis and Vapor Sorption

Thermogravimetric analysis (TGA) is often used in conjunction with DSC as a secondary thermal analysis method. The experimental set up is very simple as only a microbalance suspended inside a furnace is required. A sample is placed on the balance and the mass change is recorded as a function of time and/ or temperature during heating in a controlled atmosphere. As with DSC, TGA can measure kinetic events and absolute values measured are highly heating rate dependent (117). TGA is operated in isothermal, quasi-isothermal (multiple isothermal steps), or dynamic (linear heating rate) modes to study solvent loss, desolvation kinetics, or thermal degradation in ASDs (13). For example, Bhujbal et al. estimated the initial water content in lumefantrine ASDs from mass loss upon heating while Calahan et al. found that differences in the water content of different magnesium stearate forms partially explained differences in lubrication efficiency, tabletability, and dissolution (118, 119). Furthermore, Ben Osman et al. investigated ASD thermal stability found that PVP can either stabilize or destabilize indomethacin or felodipine ASDs to chemical degradation, respectively (120).

TGA is frequently used in tandem with a spectroscopic technique such as Fourier-transform infrared radiation spectroscopy (TGA/FTIR) or mass spectroscopy (TGA/MS) for the evolved gas analysis of hydrates or solvates. The volatile compounds evolved during heating have unique FTIR or MS spectra which may be used to identify evolved species and better characterize the thermal transitions in the TGA thermogram (25). For example, Rodriguez and Bugay used TGA-FTIR to reveal water and butyl acetate are sequentially evolved from a hypercholesterolemia drug upon heating (121).

1.4.4.3 Dynamic Vapor Sorption

Water vapor sorption is a useful tool for the analysis of sample hygroscopicity. More broadly, dynamic vapor sorption (DVS) can describe the uptake or water and/ or other solvents in a controlled environment. Both the chemical and physical stability of a drug or formulation are affected by exposure to elevated levels of moisture. Therefore, the ability to characterize the moisture uptake behavior of a solid is a necessary part of drug development.

Sorption broadly encompasses both adsorption (on the surface) and absorption (penetration into the bulk of the sample). Each mechanism can be observed and, in some cases separated, using DVS. In prior iterations, samples were stored in sealed desiccators over saturated salt solutions. Individual samples were analyzed at periodic timepoints for mass change or water content using TGA or Karl Fisher titration, respectively. Currently, the DVS process is automated and mixes water-saturated and dry gas streams in varying proportions to achieve any relative humidity (RH).

A typical DVS experiment records the equilibrium mass uptake at multiple RH stages at a constant temperature. The amount of water sorbed by the solid as a function of temperature is referred to as an isotherm. The extent of water uptake decreases with increasing temperature, a result of the exothermic nature of absorption. Therefore, the activation energy of absorption can be determined by recording isotherms at various temperatures. Figure 1.14 illustrates differences in uptake between a crystalline and amorphous material.
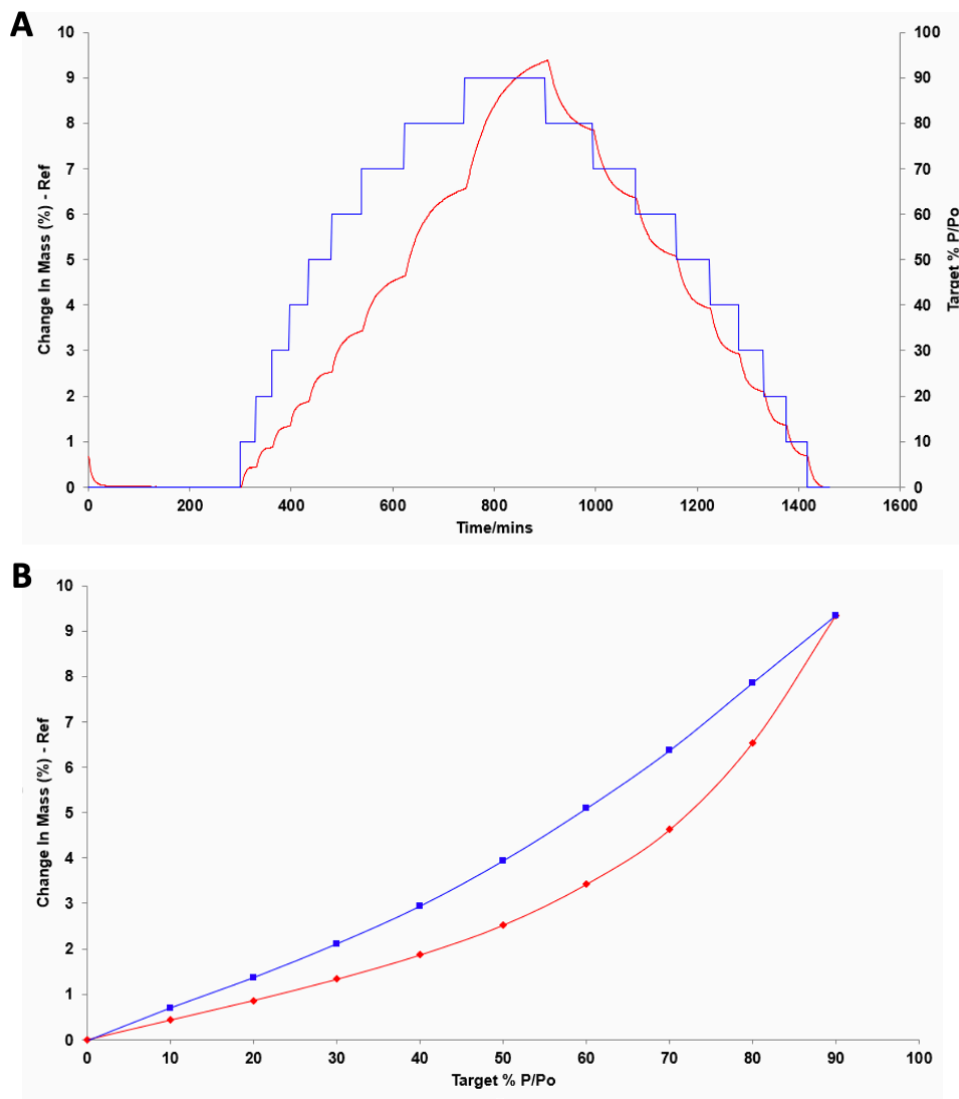
Figure 1.14. Dynamic vapor sorption of HPMCAS (HF grade) at 25°C. (A) Water uptake as a function of relative humidity (blue is % relative humidity, red is % change in mass). (B) Sorption (red) and desorption (blue) isotherms.

It is often difficult or unreasonable to maintain completely dry (nearly 0% RH) conditions. Since it was established that water typically negatively impacts the stability of pharmaceutical solids. Therefore, establishing the uptake behavior of a solid is necessary to ensure stability over the shelf-life of the formulation. Depending on the material, the

state of the material, and the RH, different phenomena may occur. The consequences of water uptake are often physical (plasticization, crystallization, deliquescence, or solvate transformations) but may also include chemical reactions such as hydrolysis. DVS can monitor or induce moisture-related transformations. Knowledge of the RH at which these transformations occur can inform manufacturing or storage conditions to avoid said transformations.

Most crystalline drugs formulated suited for ASD formulation are hydrophobic and do not absorb much water. The crystalline lattice is generally impenetrable to diffusing solvent molecules (122). Rather, surface adsorption is the dominant uptake mechanism in most crystalline solids except for hydrates or solvates. For significantly polar solids, deliquescence may occur whereby excessive surface adsorption forms liquid water which then dissolves the sample (123). For example, sodium chloride (table salt) deliquesces above 75% RH.

Conversely, the lower density and excess free volume of amorphous solids typically allows greater uptake than the corresponding crystalline phase and may be further aided by the formation of hydrogen bonds between the solid and solvent (124). Some pharmaceutical polymers such as PVP have been shown to absorb nearly 40% of their weight in water (125). Significant amounts of absorbed solvent further increase the free volume and molecular mobility of the system thereby plasticizing the amorphous solid. Moisture-induced plasticization manifests as a reduction in T_{g} (126). In some cases, the T_g may be depressed below ambient conditions thus pushing a previously glassy system into the rubbery state. The plasticization of a system can be monitored by DVS and DSC used in tandem.

A second moisture-induced transformation of concern is crystallization. The enhanced mobility imparted by absorbed moisture can either cause direct crystallization or amorphous-amorphous phase separation prior to crystallization (67). In either case, the physical stability has been compromised. DVS can monitor the moisture-induced crystallization of drug from an ASD. An increasing mass is recorded as the ASD continually absorbs moisture. However, a sudden decrease in mass at constant or increasing RH indicates crystallization. Water is not able to incorporate into the predefined crystal lattice (except for solvates) and the excess water is desorbed from the system. The RH at which an ASD crystallizes can help to better inform recommended storage conditions for the final dosage form.

In addition to generating isotherms and helping to characterize moisture-induced transformations, DVS can also be used to quantify crystallinity. Despite their methodological differences, multiple research groups successfully quantified amorphous content in a sufficiently crystalline system (127-129). While there were slight methodological differences, all took advantage of the different uptake characteristics of the crystalline and amorphous state and/ or the effect of water content on other physical properties such as T_g.

Ultimately, DVS uptake measurements can be used to predict product stability. Transformations such as crystallization or plasticization can typically be measured quickly in DVS and may be used to predict long-term stability. For instance, Marsac et al. and Rumondor et al. have used DVS with DSC and infrared radiation to investigate the physical stability of ASDs. It was found that the additional physical stability imparted by increasing polymer contents outweighed the increased moisture uptake (67, 130). Futhermore, DVS

54

has been used to monitor crystallization kinetics of amorphous solids or ASDs at varying temperature and humidity conditions (131, 132).

1.4.4.4 Powder X-ray Diffraction

Powder X-ray diffraction (PXRD) is often considered the most definitive method for detecting crystallinity and has been used extensively for the analysis of ASDs and other pharmaceutical solids. It is a variation of single-crystal X-ray diffraction and better suited for pharmaceuticals as PXRD can be performed with small amounts of material, is non-destructive, and can provide both qualitative and quantitative phase information. X-rays are scattered upon impinging on an object with the diffracted intensity governed by the Bragg equation (Equation 1.27).

$$n\lambda = 2dsin\theta \tag{1.27}$$

The Bragg equation states that, for an incident angle (θ), a multiple (n) of the wavelength (λ) must equal twice the distance (d) between diffraction planes (13). In other words, constructive interference is only observed when the additional distance travelled by X-rays between two planes, is an integer multiple of the wavelength at a particular incident angle.

A typical PXRD experiment measures a sample's diffraction pattern across all θ. Incident angles which satisfy Bragg's condition result in constructive interference. This occurs within a crystalline lattice and sharp diffraction peaks are observed. Angles which do not satisfy Bragg's condition result in destructive interference and a broad background signal is observed. This is common in amorphous solids where there is a lack of long-range molecular order. The broad background signal is therefore often called an amorphous halo.

Although PXRD definitively detects crystallinity, it cannot confirm a sample is totally amorphous. Rather, samples void of diffraction peaks may be considered 'X-ray

amorphous' (20). PXRD typically has limits of detection and quantitation of 1% and 5%, respectively (133, 134). PXRD is frequently applied for monitoring process-induced phase transformations and can detect multiple polymorphic forms (135). ASDs are often analyzed by PXRD for residual crystallinity or the detection of crystallinity during stability studies (136). Crystallinity can be quantified using a variety of integration methods including internal or external standards and whole powder pattern fitting (137). Additionally, in-situ monitoring of crystallization kinetics can be monitored using variable temperature or variable humidity PXRD.

The utility of PXRD to analyze ASDs has recently been expanded through a pair distribution function (PDF) (138). Simply put, a PDF is the inverse Fourier-transformed total scattering pattern and provides the probability of the spacing of atoms over lengths of a few angstroms (139). PDF has been used to monitor drug-polymer miscibility in ASDs and has shown that small changes in polymer structure can significantly impact drug dissolution (140, 141).

1.4.4.5 Vibrational Spectroscopy

Absorption of infrared radiation (IR) causes the vibration of chemical bonds. Changes to the dipole moment or polarizability of the bond can be observed and form the basis of vibrational spectroscopy. Vibrational spectroscopy encompasses all spectral regions in the infrared range including near-IR (12500-400 cm^{-1}), mid-IR (4000-400 cm^{-1}), and far-IR (400-20 cm^{-1}). All three regions are frequently used to characterize ASDs (134).

The frequency of absorbed radiation depends molecular structure and the atoms forming the chemical bond. The resonant or vibrational frequency is governed by Hooke's Law (Equation 1.28):

$$\nu = \frac{1}{2\pi}\sqrt{\frac{k}{u}} \qquad (1.28)$$

where k is the force constant and u is the reduced mass ($u=m_1m_2/(m_1+m_2)$). The force constant reflects bond strength as carbon-carbon double and triple bonds resonate at higher wavenumbers than single carbon-carbon bonds. Similarly, the reduced mass increases with molecular mass (m_i). Therefore, chemical bonds containing heavier atoms resonate at lower wavenumbers (e.g., C-H and C-Cl bonds vibrate at 3000 cm^{-1} and 800 cm^{-1}, respectively).

Overlapping overtones and complicated vibrational combinations have limited the limited the widespread use of near-IR spectroscopy (142). However, it is finding increased use in the pharmaceutical industry as a process analytical technology and is being applied as an in- or on-line monitoring tool during manufacturing (143). Similarly, far-IR (terahertz) spectroscopy has not reached its fully potential in the pharmaceutical industry. Recently, however, terahertz spectroscopy has seen limited use the advanced characterization of final dosage forms (144).

Mid-IR spectroscopy broadly encompasses all types of IR between 4000 cm^{-1} and 400 cm^{-1} including transmission, attenuated total reflectance (ATR), diffuse reflectance, etc. (25). It is the most frequently used form of vibrational spectroscopy for the analysis of ASDs and provides insight into any intra- and intermolecular bonds present. Moreover, Fourier transform infrared (FTIR) spectroscopy is typically used for this purpose and is the gold standard for the detection of hydrogen bonding. Specific interactions, such as

hydrogen bonds, between a drug and polymer are observed as a peak shift to a lower wavenumber or peak broadening (84). FTIR is regularly used to confirm the presence or absence of intermolecular interactions (70). Additionally, FTIR can monitor phase separation (67), detect crystallization (58), and aid in polymorph identification (145, 146).

Whereas FTIR results from the absorbed radiation changing the dipole moments of bonds, Raman spectroscopy is a result of a change in polarizability due to inelastic scattering of infrared radiation. Raman spectroscopy is often used as a complementary technique to FTIR and offers the advantages of rapid analysis time, minimal sample preparation, and can more easily provide quantitative phase data (147). Comparison of FTIR and FT-Raman spectra have been used to aid in the assignment of individual hydrogen bonding species in ASDs (84). Raman also provides the additional advantage of being using shorter wavelengths than FTIR. The spectral region of 150-50 cm^{-1} corresponds to lattice vibrations characteristic of unique crystal structures (84). Therefore, Raman spectroscopy is uniquely suited for polymorphic determination in regions not visible to mid-IR spectroscopy. Recently, confocal Raman spectroscopy has combined the advantages of Raman with microscopy to provide a non-invasive analytical tool with applications to drug discovery, drug delivery, and quality control of final dosage forms (148).

1.4.4.6 Microscopy

Microscopy provides the only way to directly visualize the pharmaceutical system of interest and can provide insights not available through other analytical techniques. Broadly speaking, microscopy is used to correlate particle features on the micro-scale to bulk physicochemical properties observed on the macro-scale (13). In its most basic sense,

optical microscopy can view surface details invisible to the naked eye (< 1 mm). Reflected and transmitted light microscopes are commonly used for observation on a micron-scale (25).

An optical microscope is perhaps most useful in a pharmaceutical sense when equipped with a polarizer (polarized light microscopy, PLM). In short, the polarizer converts visible light into plane-polarized light which interacts differently with isotropic and anisotropic materials (13). Liquids and amorphous materials, among others, are isotropic and are invisible under polarized light. Most crystals, however, are anisotropic and the refracted polarized light appears as colorful shapes with high background contrast. The diffraction of polarized light in anisotropic materials is called birefringence.

Polarized light microscopy (PLM) has been extensively used for confirming amorphicity or the detection of crystallinity and can discriminate between the different crystal shapes of polymorphs or crystals grown under varying conditions (149). In addition, nucleation and crystal growth kinetics can be monitored at different temperatures using a hotstage (58, 150). A digital camera and imaging software are often used to continuously record the crystallization process and measure crystal features including particle size.

In addition to PLM, other forms of microscopy can be used in pharmaceutical analysis. Scanning electron microscopy (SEM) and atomic force microscopy (AFM) have found the most success in the analysis of ASDs. SEM uses electrons and an electromagnetic field rather than polarized light and optical lenses to magnify images and offers higher resolution (on the order of 10's of nanometers) compared to PLM (25). SEM has been used extensively with ASDs with applications including, crystallization onset, particle size distribution and morphology, as well as the homogeneous distribution of drug in polymeric

dispersions (138, 151, 152). AFM offers resolution on the nanometer-scale and can actually be used to manipulate atomic level features in addition to imaging (25). Hence, AFM has the potential observe the initial stages of phase separation and crystallization in ASDs at previously unattainable length scales (153).

1.4.4.7 Chromatography

Chromatography encompasses a wide range of methods used for the separation, identification, and purification of target compounds from complex mixtures. Chromatographic methods used much more regularly in synthetic or medicinal chemistry than formulation and drug product development. Reaction products must be purified repeatedly during synthesis to yield an API or other pharmaceutical ingredient of acceptable purity. However, there are a few instances where liquid chromatography is useful for the formulation of ASDs which are highlighted below. Thin layer chromatography (TLC) was used in this thesis work while high performance liquid chromatography (HPLC) has had limited usage in the literature.

TLC has been used as a quick and qualitative measure of reaction product purity during synthesis of drug analogues. For example, the methyl ester of indomethacin (INDME) has been used as a structural analogue of indomethacin (IND) to investigate how changes in hydrogen bonding affect ASD physical stability (154). INDME was synthesized by an acid catalyzed reflux reaction of IND in methanol. Different affinities for the mobile phase result in different retention factors between IND, INDME, and reaction byproducts. TLC was used to confirm the conversion of IND to INDME and its subsequent purification.

Many types of HPLC have been used for the extensive characterization of drug candidates during the drug development process including normal phase, reverse phase,

gel permeation/ size exclusion, and ion exchange (155). HPLC has served two primary purposes for the examination of ASDs: detection of chemical degradation and solubility measurements. Aso et al. used HPLC to monitor for thermally-induced chemical degradation after the storage of ASDs at high temperatures (156). Marsac et al. and Knopp et al. proposed a shake-flask method to determine the solid-state solubility of the drug in a polymer using a low molecular weight analogue or monomer. Excess crystalline drug is equilibrated in the liquid analogue, filtered, and assayed using reverse phase HPLC. Drug remaining in solution is then quantified using UV-vis spectroscopy (68, 157). A similar HPLC-based solubility procedure was proposed using drug and polymer solubilized in a suitable solvent (158). Despite being a liquid-based technique, HPLC has shown promise for solid-state pharmaceutical analysis.

1.4.4.8 Nuclear Magnetic Resonance Spectroscopy

Nuclear magnetic resonance (NMR) spectroscopy provides molecular-level information into the specific nuclei present in a sample as well as its surrounding environment. Solution-state NMR has been used extensively in drug development for structural elucidation and identification. However, as most drugs exist as solids, solid-state nuclear magnetic resonance (SSNMR) spectroscopy provides an advanced in-situ analysis tool for pharmaceutical solids. Chapter 2 provides an in-depth discussion into the theory of SSNMR as well as its use in the analysis of amorphous solid dispersions.

1.5   Thesis Outline

1.5.1   Chapter 1

Chapter 1 briefly describes the solubility issues facing the drug development process and introduces the amorphous state. The manufacture, analysis, and stability of amorphous solid dispersions are discussed. The goal of the introduction was to provide a basic understanding of challenges facing the development of ASDs and the analytical methods used to investigate and better characterize their physical stability.

1.5.2   Chapter 2

Chapter 2 introduces solid-state nuclear magnetic resonance (SSNMR) spectroscopy as an analytical technique for the advanced characterization of pharmaceutical solids, specifically amorphous solid dispersions. The basic theory and pulse sequences used for pharmaceutical analysis are discussed with an added emphasis on aspects of data acquisition and processing to ensure quantitative data is acquired.

1.5.3   Chapter 3

Chapter 3 expands upon the quantitative aspects of SSNMR with a case study using patiromer (Veltassa®). By accounting for cross polarization dynamics, applying fundamental relaxation analyses, and manipulating the spin speed, a new method is proposed and validated for determining the block copolymer composition of the insoluble amorphous polymer, patiromer. The proposed method may be used for the analysis of other insoluble block copolymers or for ensuring API sameness during the development of generic drugs containing polymeric APIs.

1.5.4   Chapter 4

Chapter 4 investigates the thermodynamics of ASDs using a model nifedipine-polyvinylpyrrolidone (NIF-PVP) system. Annealing studies were conducted to determine equilibrium crystallinity at various temperatures. The ability of different analytical techniques to accurately quantify crystallinity were compared at multiple drug loadings. It was found that typical DSC methods may not provide an accurate measure of crystallinity in ASDs, but more sensitive analytical techniques can be applied to measure crystallinity. In addition, for the first time, PXRD and SSNMR were applied to measure drug-in-polymer solubility. The results of the crystallinity and solubility study in chapter 4 expand the options available to a pharmaceutical scientist during formulation.

1.5.5   Chapter 5

As chapter 4 focuses primarily on the thermodynamic considerations of ASD stability, chapter 5 investigates stability from a kinetic perspective using indomethacin-and indomethacin methyl ester-PVP ASDs. The impact of drug loading, storage temperature, and hydrogen bonding on preventing crystallization is explored through an expansive stability study. Differences in crystallization trends between the two structurally similar molecules, as well as a previously undetected mode of crystallization, will be discussed.

1.5.6   Chapter 6

Chapter 6 provides a high-level summary of the work completed in this dissertation and its place within the scientific literature. A better understanding of the impact on hydrogen bonding on physical stability and new methods for the quantitation of crystallinity and drug product composition should help to better analyze and formulate amorphous solid dispersions. While this research helped to answer many questions, the

physical stability of ASDs is still a very complex topic. Therefore, chapter 6 also includes research questions which were unanswered and the possible next steps to further the research in chapters 3, 4, 5, and Appendix A.

1.5.7   Appendix A

Chapters 4 and 5 each investigated the thermodynamic and kinetic stability of ASDs under dry conditions as to eliminate the effects of water. Appendix observes the moisture sorption and desorption behavior of different pharmaceutical polymers in the presence of water and/ or acetone. DVS was used to acquire isotherms under different conditions representative of manufacturing/ processing steps. In addition, the desorption behavior was used to provide a better understanding of solvent removal during spray drying.

CHAPTER 2: SOLID-STATE NMR SPECTROSCOPY

2.1   Introduction

Nuclear magnetic resonance (NMR) spectroscopy was first measured in 1938 by Rabi using molecular beams (159). In 1946, Bloch and Purcell each observed the phenomena for the first time in liquids and solids, respectively (160, 161). Soon after, it was discovered that changes in the Larmor frequencies of materials were caused by changes in the chemical bonding state of the atoms (162). Hence, NMR spectroscopy was born as a way to identify and/ or analyze various materials. Since then, NMR has been applied across a wide range of industries. Solution NMR has become one of the most powerful analytical techniques for structure elucidation, chirality/ purity analysis, protein dynamic studies, and cellular metabolism. However, as the majority of marketed drugs are solid dosage forms, solid-state NMR (SSNMR) spectroscopy has become an especially powerful analytical technique for the solid-state characterization of marketed drugs and drug candidates.

Despite its discovery over 80 years ago and similarities to solution NMR, the adoption of SSNMR has been much slower in the pharmaceutical industry. Complexities unique to the solid state make acquiring a high-resolution SSNMR spectrum more difficult relative to solution NMR. However, techniques now exist to significantly improve spectral quality and enable high quality SSNMR data acquisition.

This chapter highlights the general theory, techniques, advantages, and limitations of solid-state NMR spectroscopy as well as its application in characterizing crystalline and amorphous pharmaceuticals. More comprehensive reviews of SSNMR, including the

theory, experimental setup, and its pharmaceutical applications exist in the literature (163-166).

2.2 NMR Spectroscopy Basics

Spectroscopy is the interaction between matter and electromagnetic radiation. A given state of matter will vary in its interaction with different regions of the electromagnetic spectrum. In the case of NMR spectroscopy, nuclei (more specifically, nuclear spins) interact with the radiofrequency region (< 30 GHz) of the electromagnetic spectrum.

All nuclei have a nuclear spin quantum number I, with values of 0, ½, 1, 3/2, etc. however only nuclei with non-zero nuclear spins are observable via NMR. Whereas ^{1}H, ^{13}C, and ^{15}N are all I=1/2 and NMR-active, some highly abundant isotopes (e.g., ^{12}C and ^{16}O) are unable to be seen with NMR. The work herein will consider only the I=1/2 nuclei of ^{1}H and ^{13}C.

Non-zero spin number nuclei possess angular momentum and, in the presence of a static (external) magnetic field (B_0), generate an induced magnetic field or magnetic moment, μ, shown in Equation 2.1:

$$\mu = \frac{\gamma I h}{2\pi}$$

(2.1)

where γ is the gyromagnetic ratio for a specific nucleus, I is the nuclear spin, and h is Planck's constant. The gyromagnetic ratio is a nuclei-specific constant relating magnetic moment to the nuclear spin number. B_0 also causes nuclei that have a magnetic moment (I ≠ 0) to precess around their z-axis at a defined rate known as the Larmor or resonance frequency ($\nu = \gamma B_0/2\pi$). The Larmor frequency is proportional to the external field strength.

For example, in a 9.4 Tesla external field strength, ^{1}H nuclei resonate at approximate 400 MHz while ^{13}C nuclei resonate at approximately 100 MHz.

^{1}H and ^{13}C (each spin-½ nuclei) can exist in either of two energy states ($I = \pm1/2$). In the absence of a magnetic field, the two spin states are degenerate (equal energy). However, when placed in a static magnetic field, the Zeeman interaction between the magnetic moment of the nucleus and the external field causes a separation of nuclear spins where the energy state of the nucleus changes bases on its alignment with respect to B_0. Spins aligning with the magnetic field (α-state) are in a lower energy state than spins aligning against (β-state) the external magnetic field. Figure 2.1 illustrates the different spins state for spin-1/2 nuclei.
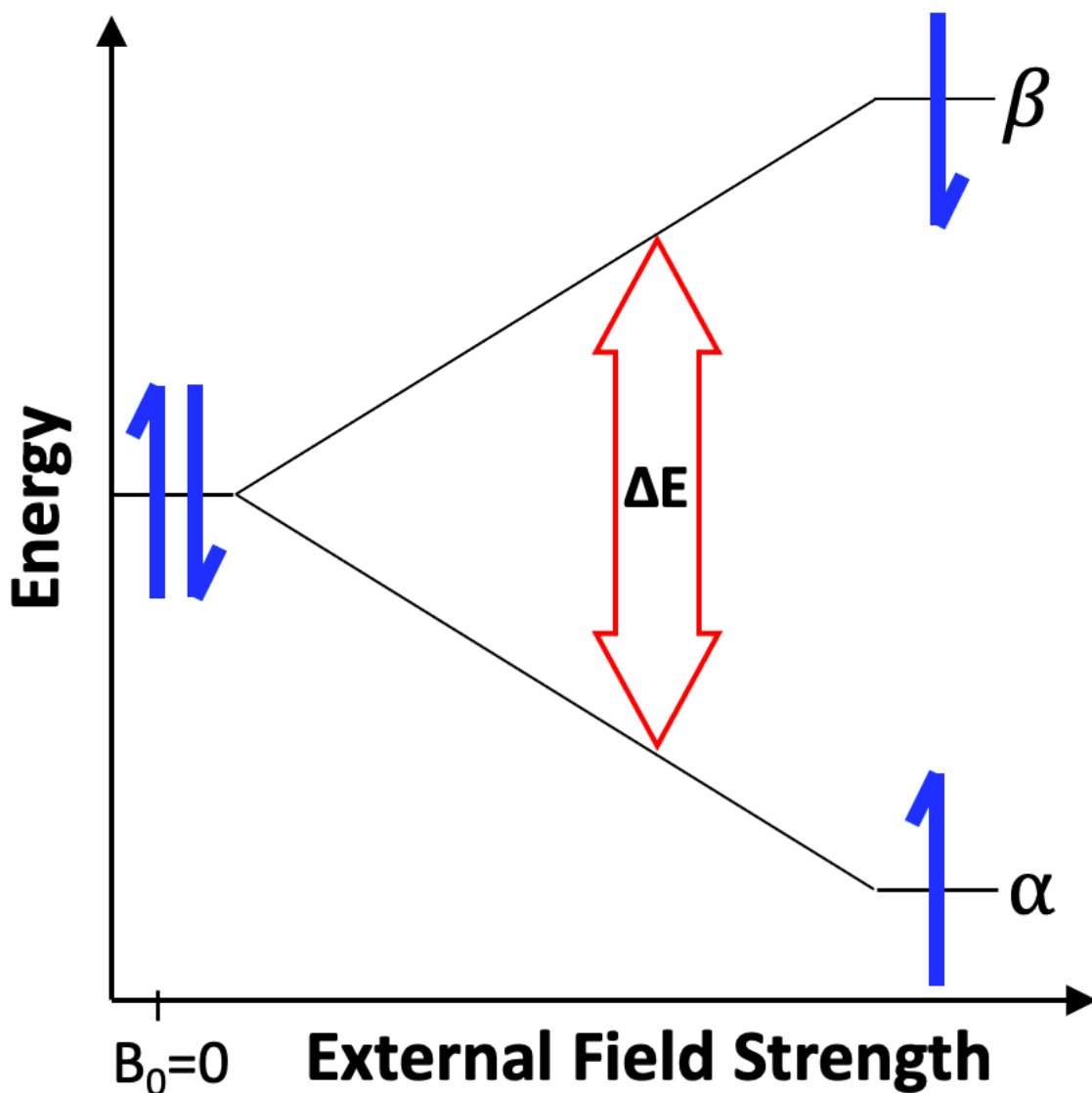
Figure 2.1. The splitting of nuclear spin states for I = 1/2 nuclei in an external magnetic field. Increasing B_0 also increases the population difference between the two energy states.

The observed NMR signal intensity is proportional to the population difference ($\Delta n_0 = n_\alpha - n_\beta$) of spins between α- and β-states. This population difference is governed by the Boltzmann distribution (Equation 2.2) where k is the Boltzmann constant, T is absolute temperature, and n_α and n_β are the number of spins in the α- and β-states, respectively.

$$\frac{n_\beta}{n_\alpha} = e^{-\frac{\Delta E}{kT}} \qquad\qquad (2.2)$$

The spin states are separated by an energy difference (ΔE) directly proportional to the strength of B_0 and gyromagnetic ratio, or, by extension, the resonance frequency, ν (Equation 2.3).

$$\Delta E = \frac{\gamma h B_0}{2\pi} = h\nu \qquad\qquad (2.3)$$

At room temperature, the spin population difference, Δn_0, is very small relative to the total number of nuclei present in a sample, N. Using Equations 2.2 and 2.3, it is shown that for a 400 MHz ^{1}H field (9.4 Tesla) at room temperature, approximately only 1 in every 125,000 protons contribute to the population difference and, therefore, the NMR signal. While signal intensity may be improved through stronger magnetic fields and lower temperatures, it now is easy to see why NMR suffers from poor sensitivity.

Modern NMR spectroscopy has three main components: the superconducting magnet, the probe, and the spectrometer. All data is acquired and analyzed at a computer which is connected the spectrometer. Figure 2.2 provides a schematic of a typical NMR spectrometer setup. Radiofrequency (RF) pulses of varying intensity, duration, and phase are programmed on the computer and sent to the spectrometer which contains the hardware necessary to create such pulses. The spectrometer also contains amplifiers to increase the intensity of outgoing pulses and incoming NMR signals. The pulses travel through wires connected to a cylindrical probe. At the end of the probe, the sample is housed within a copper coil which ultimately exposes the sample to the RF pulses generated in the spectrometer.
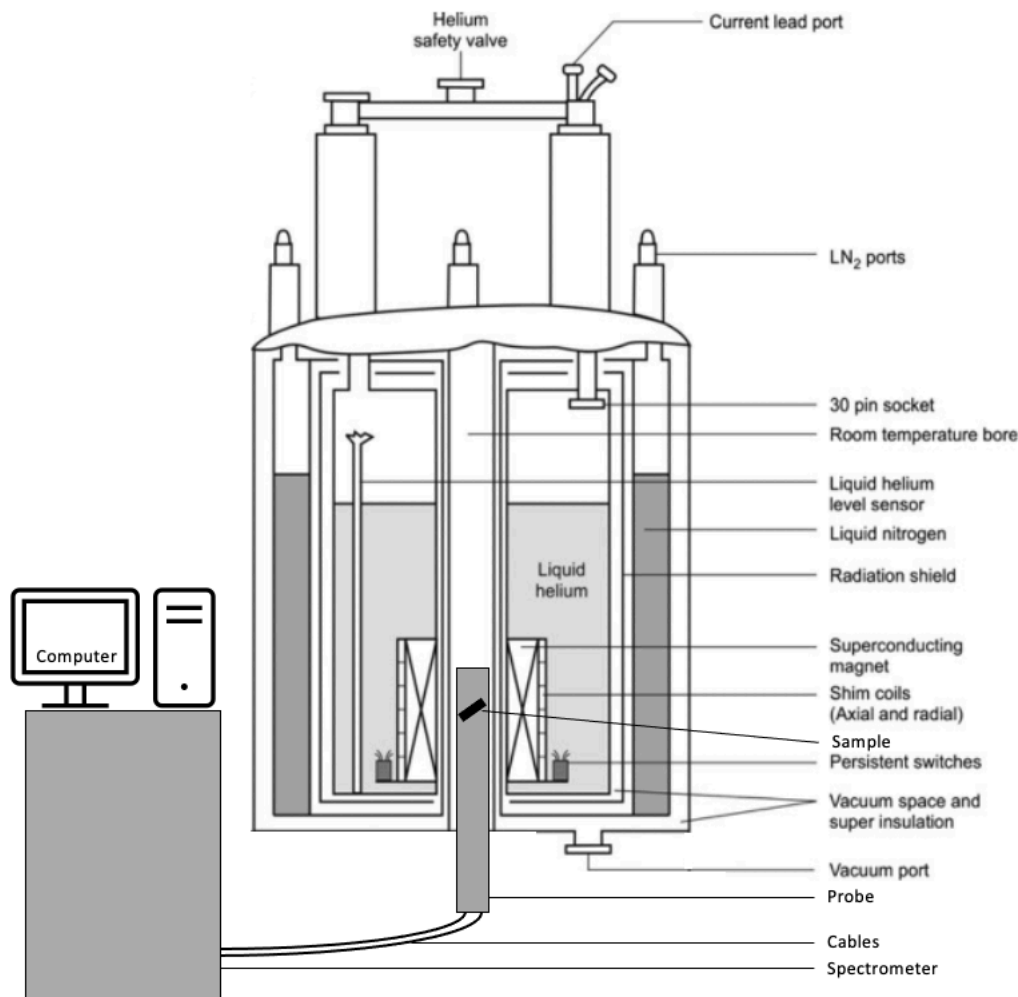
Figure 2.2. Simplified schematic showing the layout of the cryostat, sample probe, spectrometer, and computer. Modified from reference (167).

The superconducting magnet is a solenoid wound with niobium alloy wire immersed in a liquid helium bath (-269°C) to achieve superconducting conditions (166). This is further insulated by multiple radiation shields and a liquid nitrogen bath to maintain the solenoid at -269°C while minimizing helium boil off. The housing of the solenoid, liquid cryogen baths, and all insulation layers is known as the cryostat. The sample probe sets inside the bore of the solenoid and is positioned such that the sample is located in the center of the magnetic field generated by the solenoid (B_0).

2.2.1 Theory and the Chemical Shift

SSNMR can be thought of as a three-dimensional coordinate system (Figure 2.3) where the magnetic fields are represented by vectors (i.e., magnetization vectors). The external or static magnetic field is applied parallel to the z-axis or perpendicular to the x,y-plane. While the external magnetic field alone is enough to separate nuclei into different spin states, no NMR signal can be measured as no magnetization is in the x,y-plane. The applied magnetic field (B_1) is an additional magnetic field applied as a pulse of RF radiation perpendicular to B_0. When B_1 is applied at the Larmor frequency, the net magnetization is pushed from the z-axis and is allowed to precess in the x,y-plane (Figure 2.3).
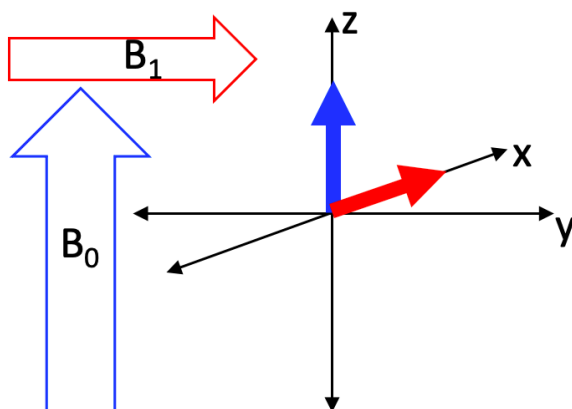
Figure 2.3. Three-dimensional coordinate system showing the net magnetization vector due to the external magnetic field (blue) and immediately after excitation by an applied magnetic field (red).

The return of the net magnetization to equilibrium creates an alternating current which is detected in a coil surrounding the sample. Changes in the current with time is collected as the NMR signal as a free induction decay (FID). The FID is Fourier transformed into the frequency domain to yield the NMR spectrum. This process is

repeated multiple times and FIDs are summed together until a spectrum of adequate signal-to-noise ratio is acquired.

Up to this point, only the nucleus has been discussed. However, all nuclei (except protons) are surrounded by electrons. The density of electrons surrounding the nucleus depends both on the nucleus itself and the local environment near the atom. When placed in a magnetic field, electrons begin circulating which creates an induced magnetic field opposing B_0. The strength of the induced magnetic field varies between chemically inequivalent nuclei due to differences in electron density at the nuclei of interest. Electron donating groups increase electron density around a nucleus causing a stronger induced field. This 'shielding' decreases the resonance frequency of the nucleus as it is exposed to a slightly weaker magnetic field. Conversely, electron withdrawing groups (e.g., F, OH, Cl, etc.) 'deshield' and decrease the electron density around a nucleus, weakening the induced field. This ultimately exposes the nucleus to a stronger magnetic field which resonate at higher frequencies. The different frequencies at which chemically inequivalent nuclei resonate are known as chemical shifts (δ). After the signal is Fourier transformed, chemical shifts are plotted on the x-axis with parts per million (ppm) units.

Not only is the chemical shift affected by directly bonded adjacent nuclei, but it is also impacted by the chemical environment surrounding the nuclei of interest (a through-space interaction). Therefore, changes in concentration, acidity, solvation, temperature, and/ or the presence of excipients can all impact the chemical shift. This includes the formation of hydrogen bonds which deshields the ^{1}H or ^{13}C of interest, resulting in a downfield shift. Hydrogen bonds are of particular interest as they are critical to the stability

of many pharmaceutical compounds including both intramolecular hydrogen bonds in protein formulations and/ or intermolecular drug-excipient interactions (70, 168).

2.3 Solid-state NMR Spectroscopy

Acquiring high quality solid-state NMR data presents unique challenges not encountered in the solution state. Most of the challenges stem from reduced molecular motion in the solid state relative to the solution state. In the solution state, anisotropic interactions are averaged to zero due to rapid molecular tumbling. Molecules are locked in a rigid structure in the solid state leading to a variety of interactions between nuclei which broaden peaks and reduces the resolution and sensitivity of SSNMR. This includes the Zeeman interaction, dipolar interactions, chemical shift interactions, and scalar interactions (13).

2.3.1 Chemical Shift Anisotropy and Magic Angle Spinning

Electronic shielding within a magnetic field is three-dimensional phenomenon, meaning the orientation of a molecule within the field will affect its chemical shift (13). Thus, while the static magnetic field is homogeneous, the shielding produced by the electrons is orientation dependent and non-homogeneous within the sample creating microenvironments where otherwise identical nuclei experience magnetic fields of slightly different strengths. This phenomenon, known as chemical shift anisotropy (CSA), creates broad peaks which greatly reduce the resolution of SSNMR.

Rapid molecular tumbling in liquids eliminates CSA in solution state NMR. However, reduced molecular motion in the solid state means that individual molecules spend different amounts of time in the x-, y-, and z-axis with respect to the applied magnetic

field. The shape of the resulting peak is defined by the chemical shielding tensor, σ, which combines the isotropic (σ_{iso}) and anisotropic (σ_{aniso}) components. Together, σ_{iso} and σ_{aniso} are defined in Equation 2.4 and represent the orientation dependence of the chemical shift where θ is the angle of the sample relative to the applied magnetic field.

$$\sigma = \sigma_{iso} + (3cos^2\theta - 1)\sigma_{aniso} \tag{2.4}$$

By spinning the sample at θ = 54.74°, $(3cos^2\theta - 1) = 0$ and effectively eliminates the anisotropic component (169). This known as magic angle spinning (MAS). Simply spinning the sample at the magic angle is not sufficient to completely eliminate CSA. When spinning at a rate less than the width of the CSA, spinning sidebands (SSBs) appear as spurious peaks flanking the isotropic peak at intervals equal to the MAS speed (170). Eliminating SSBs solely by spinning at very fast rates is not always feasible due to rotor material limitations or bearing capabilities. In this case, the total suppression of spinning sidebands (TOSS) pulse sequence may be used (see sections 2.3.5 and 2.5.2) (171).

2.3.2 Dipolar Coupling and High-power Proton Decoupling

Dipolar coupling results from the dipole-dipole interaction between the magnetic dipoles of nearby nuclei. Dipolar coupling can be homogeneous (^{13}C-^{13}C or ^{1}H-^{1}H) or heterogeneous (^{13}C $^{-1}$H). Due to their high natural abundance and prevalence in organic molecules and pharmaceuticals, ^{1}H-^{1}H homonuclear coupling is very prevalent and causes significant peak broadening. Conversely, as ^{13}C is only 1.1% naturally abundant, the probability of finding two ^{13}C nuclei close enough together to couple is extremely low. Therefore, ^{13}C-^{13}C homonuclear coupling does not contribute significantly to SSNMR linebroadening.

^{13}C-^{1}H heteronuclear coupling interactions are very common and result in broad ^{13}C SSNMR line shapes. By applying high-power ^{1}H decoupling (a high decoupling field at the ^{1}H Larmor frequency), ^{1}H spins rapidly flip between the α- and β-states. This averages the interaction of ^{1}H nuclei with ^{13}C nuclei, effectively averaging the dipolar interaction to zero (165).

2.3.3 Relaxation

Relaxation is the process by which a material property returns to its equilibrium state after being perturbed by an external stimulus. In the case of SSNMR, the property is equilibrium magnetization, and the stimulus is a radiofrequency (RF) pulse. There are multiple types of relaxation in SSNMR, each affecting different portions of experimental set up and acquisition. The three relaxation parameters of interest for designing experiments and acquiring data are spin-lattice relaxation in the laboratory frame (T_1), spin-spin relaxation (T_2), and spin-lattice relaxation in the rotation frame ($T_{1\rho}$). Figure 2.4 shows the difference in each magnetization vector after a 90° pulse.
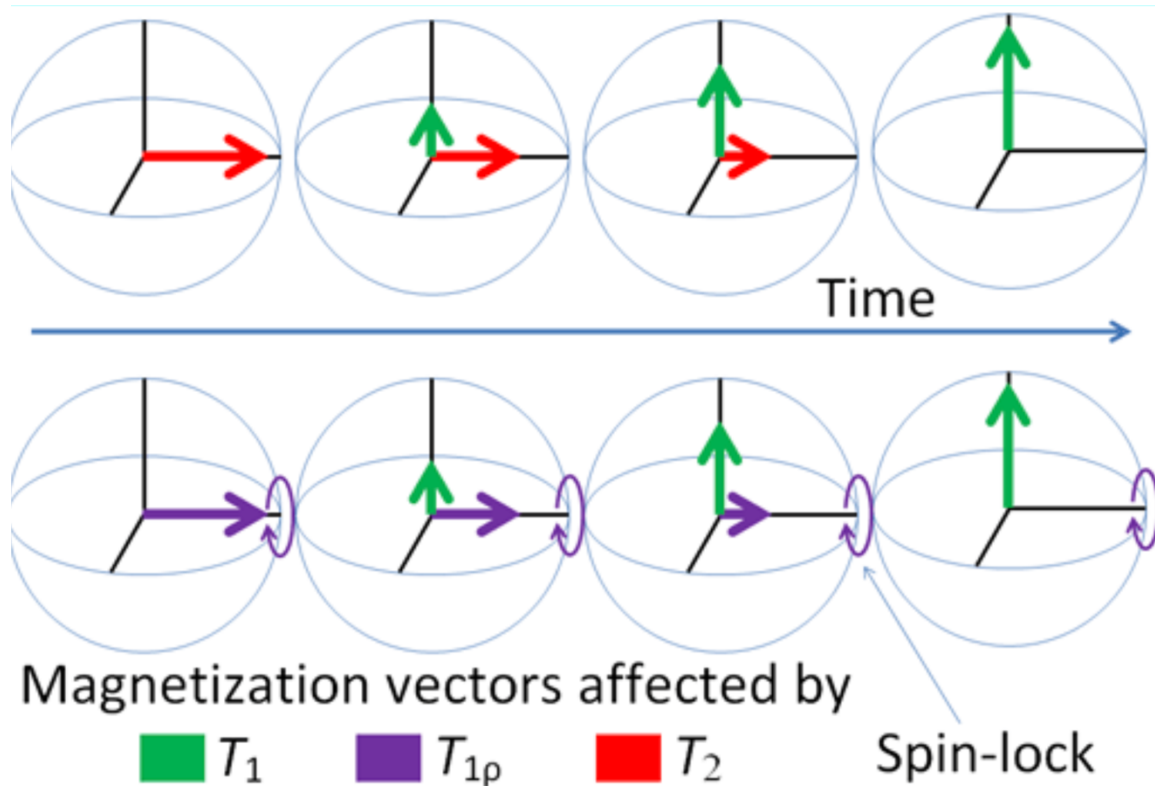
Figure 2.4. Time evolution of relaxation vectors after a 90° pulse. T_1 (green), T_2 (red), and $T_{1\rho}$ (purple) Adapted from ref. (172).

After a 90° pulse, all magnetization has been pushed from the z-axis to the x,y-plane. The return to thermal equilibrium is governed by the T_1 and T_2 relaxation times. Exchange of energy between the excited nucler spins and the lattice results in the return of magnetization to the z-axis and is known as the T_1 (spin-lattice or longitudinal) relaxation (165). The longitudinal return of magnetization (M) is an exponential process defined by Equation 2.5:

$$\frac{M}{M_0} = e^{-\left(\frac{\tau}{T_1}\right)}$$
(2.5)

where M_0 is the equilibrium magnetization and τ is the recovery/ pulse delay time (161). Practically, the experimental pulse delay (and experimental time) is determined based on

the T_1. Selecting $\tau = 5T_1$ effectively ensures all magnetization (99.3%) has returned to equilibrium and maximum signal intensity is observed. While slow, this is often necessary for acquiring truly quantitative data. Alternatively, a pulse delay of $\tau = 1.26T_1$ allows for collecting the highest signal-to-noise for a given time period and may be preferable when quantitative data is not required (173).

The magnetization vector in the x,y-plane after the 90° pulse is really the observed sum of all individual spin vectors. While initially coherent, the spins quickly lose coherence as the magnetization vector begins to precess at the Larmor frequency. The loss of coherence is a result of spin-spin interactions without energy transfer to the lattice and is known as T_2 (spin-spin or transverse) relaxation (165). In contrast to the T_2 relaxation which occurs after the 90° pulse is switched off, $T_{1\rho}$ relaxation can occur if the phase of the 90° pulse is changed by 90°. An applied RF field about 50 – 100 kHz in strength (or three orders of magnitude lower than the static magnetic field strength) changes the magnetization vector phase from the positive x-direction to the y-direction. The magnetization vector is now spin-locked (locked in place) and will relax to the lattice in the rotating frame (165). In practice, the T_2 relaxation time affects the length of time the free induction decay (amount of signal) can be acquired while $T_{1\rho}$ informs the choosing of an appropriate contact time and provides information about molecular mobility in the kHz regime.

2.3.4 Low Sensitivity and Cross Polarization

As the NMR signal is directly proportional to the number of distinct nuclei present in the sample, NMR analysis of low naturally abundant nuclei (e.g., ^{13}C and ^{15}N) is plagued by low sensitivity resulting in extremely long analysis times. Owing to its almost 100%

natural abundance and high gyromagnetic ratio, protons present in a sample can be used to improve the sensitivity and reduce the experimental time of ^{13}C SSNMR through cross polarization (CP) (174). When CP is used for ^{13}C SSNMR, the ^{1}H:^{13}C ratio of natural abundances (100:1.1), coupled with an approximately 4:1 ratio of gyromagnetic ratios results in a 3.6-fold increase in sensitivity.

The invention of CP by Pines et al. in 1973, followed by its application with MAS by Schaefer and Stejskal in 1976 ushered in the modern era SSNMR spectroscopy (174, 175). CP transfers the bulk magnetization from the abundant (^{1}H) spins to the dilute (^{13}C) spins through spin-locking once the Hartmann-Hahn condition is met. Spin-locking polarizes the magnetization in the direction of the applied pulse so that it relaxes in the rotating frame (165). Equation 2.6 shows the Hartmann-Hahn condition where γ_H and γ_C are the gyromagnetic ratios of ^{1}H and ^{13}C, respectively. The magnetic field frequency experienced by each nuclei is given by $B_{1,i}$.

$$\gamma_H B_{1,H} = \gamma_C B_{1,C} \tag{2.6}$$

^{1}H and ^{13}C nuclei normally precess at different frequencies equal to the product of their respective gyromagnetic ratio and the static magnetic field frequency, B_0. By adjusting the frequency experienced by the individual nuclei ($B_{1,i}$) the precession frequency of each nuclei can be tuned. The Hartmann-Hahn condition is met when ^{1}H and ^{13}C each precess at the same frequency. Nuclei in close proximity to one another now experience strong heteronuclear dipolar coupling and can exchange magnetization through energy-conserving spin-spin magnetization transfer from ^{1}H to ^{13}C (176). The transfer of magnetization from ^{1}H to ^{13}C is governed by two time constants: T_{CH} and $T_{1\rho}$. T_{CH} describes the initial buildup of ^{13}C magnetization and $T_{1\rho}$ represents the decay of

magnetization to the lattice. The amount of time that CP is allowed to occur is known as the contact time (CT). The importance and effects of T_{CH}, $T_{1\rho}$, and contact time are described further in section 2.5.1. It is important to note that CP efficiency is inversely related molecular mobility (177). Therefore, as molecules gain mobility at higher temperatures, the transfer of magnetization becomes less efficient and direct polarization of ^{13}C nuclei may be required.

^{13}C T_1 relaxation times are extremely long relative to ^{1}H T_1 to the point that multi-pulse direct polarization ^{13}C SSNMR experiments rarely used. However, in addition to the benefits described above, CP further improves experiment time as it uses ^{1}H relaxation times rather than ^{13}C. Spin-locked ^{1}H magnetization decays minimally during the ^{13}C free induction decay (FID) allowing for the process to be quickly repeated and an additional ^{13}C FID to be acquired (165). This allows for many more acquisitions in a given time period ultimately improving the signal-to-noise ratio and reducing the time required to acquire a well-resolved ^{13}C spectrum. The effect of each spectral enhancement technique discussed in sections 2.3.1, 2.3.2, and 2.3.4 are shown in Figure 2.5.
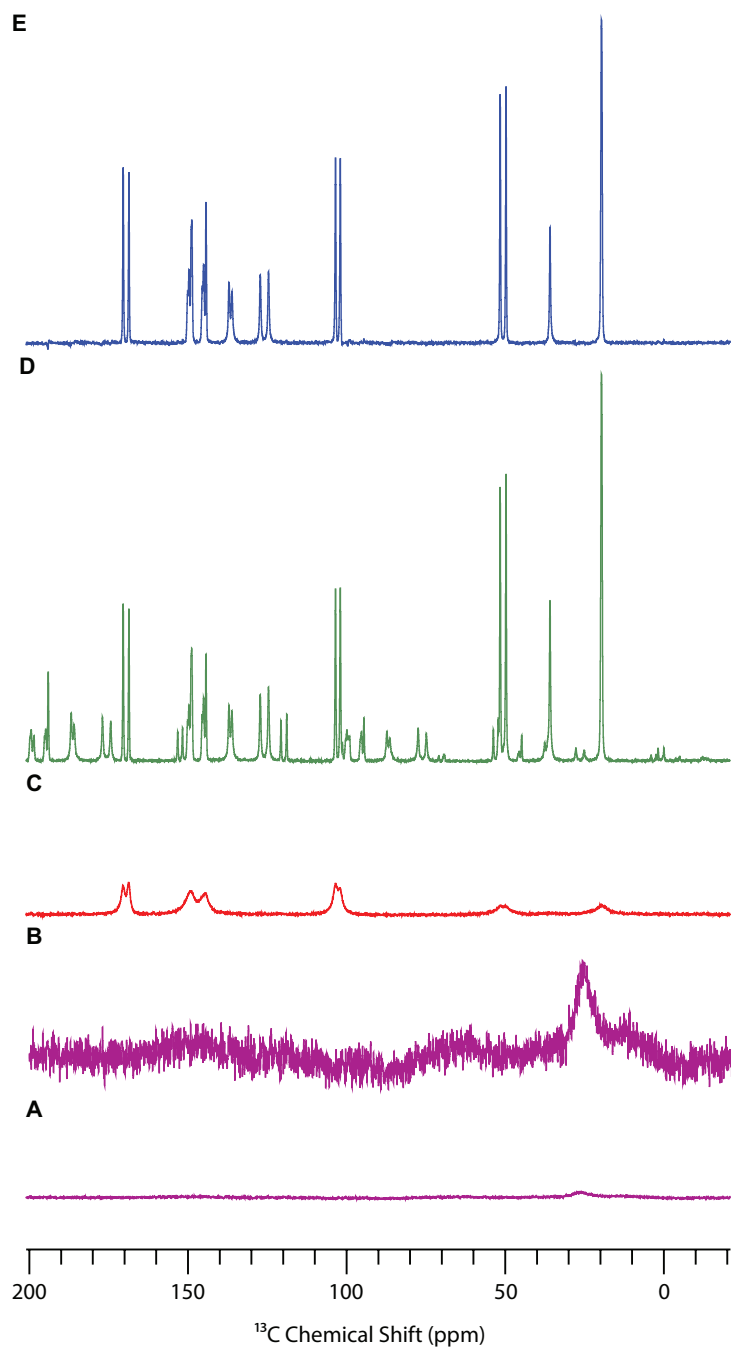
Figure 2.5. ^{13}C SSNMR spectra of nifedipine acquired using different spectral enhancement techniques. (A) Static (MAS = 0 kHz) CP with high power ^{1}H decoupling (1x vertical scaling), (B) Static (MAS = 0 kHz) CP with high power ^{1}H decoupling (16x vertical scaling), (C) CP MAS with TOSS and no ^{1}H decoupling, (D), CP MAS with high

power ^{1}H decoupling and no TOSS, and (E) CP MAS with TOSS and high power ^{1}H decoupling.

2.3.5 Pulse Sequences

The various methods discussed in sections 2.3.1, 2.3.2, and 2.3.4 are used to address the difficulties associated with SSNMR spectroscopy through the application of different pulse sequences. Due to the low natural abundance (1.1%), low gyromagnetic ratio, and long relaxation times of ^{13}C, direct polarization of ^{13}C is rarely used except in cases of highly mobile species. Similarly, strong ^{1}H-^{1}H homonuclear coupling results in broad featureless peaks in the solid state ultimately limiting the use of ^{1}H SSNMR. The direct polarization pulse sequence is shown in Figure 2.6, however only CP will be discussed further as it is the predominate pulse sequence used in SSNMR.

Figure 2.7 demonstrates the basic CP sequence as a 90° pulse is applied on the ^{1}H channel to transfer all magnetization from the z-axis to the x,y-plane. Once the Hartmann-Hahn condition is met, spin-locking is applied perpendicular to the direction of the 90° pulse allowing the transfer of ^{1}H magnetization to ^{13}C. As ^{1}H magnetization is transferred to ^{13}C, the ^{13}C magnetization is pushed from the z-axis to the x,y-plane. The amount of time CP is allowed to occur is the contact time. After CP, high power proton decoupling is applied to the ^{1}H channel while the signal (free induction decay, FID) is observed in the ^{13}C channel.
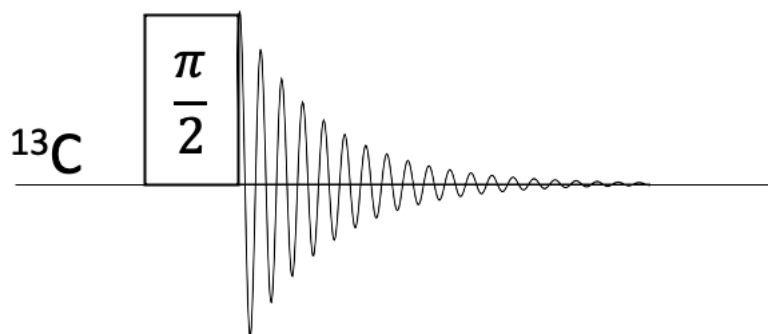
Figure 2.6. Direct polarization pulse sequence.
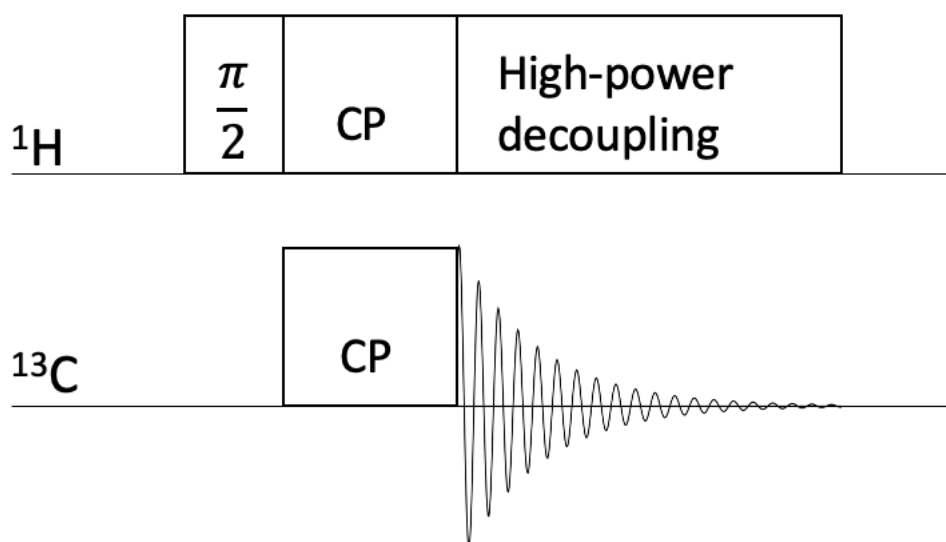
Figure 2.7. Cross polarization pulse sequence.

While CP MAS is the workhorse experiment in ^{13}C SSNMR, MAS alone is often insufficient to spin out chemical shift anisotropy at most feasible spinning speeds. To fully resolve most peaks in the spectrum, CP TOSS is used to suppress spinning sidebands and improve peak resolution. Figure 2.8 shows a typical CP TOSS sequence.
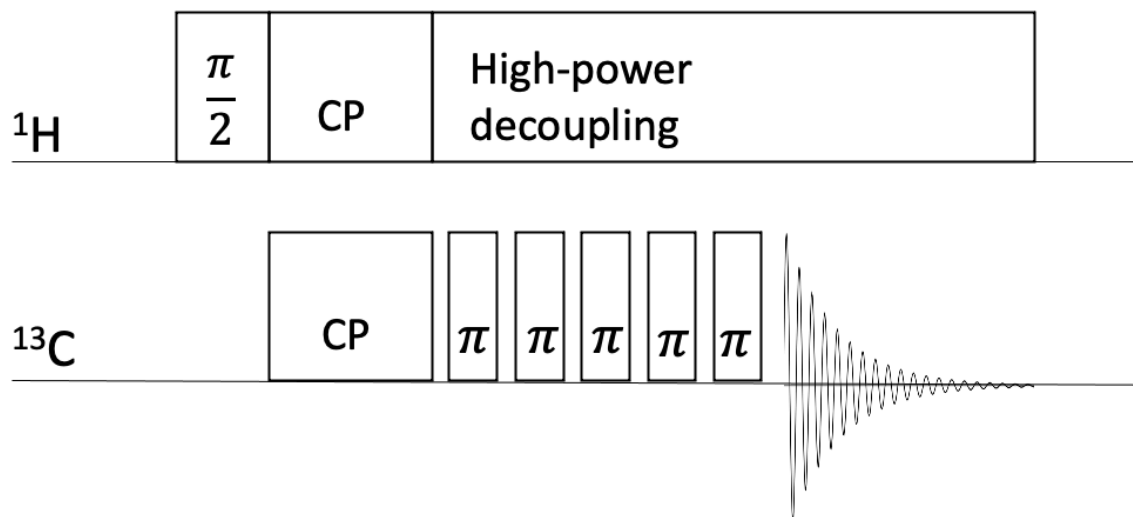
Figure 2.8. Cross polarization with total suppression of spinning sidebands.

The CP TOSS experiment begins exactly the same as a normal CP experiment with a 90° pulse to the ^{1}H channel and a spin-lock applied to transfer magnetization to ^{13}C nuclei. During high power proton decoupling, multiple 180° (π) pulses are applied to the ^{13}C channel at intervals defined by the MAS rate (171). This serves the randomize the phases of the SSBs ultimately cancelling out their intensity with minimal impact on the isotropic peak. The ^{13}C spectrum is then observed while decoupling continues.

Just as one-dimensional CP experiments are used to acquire a ^{13}C SSNMR spectrum, similar pulse sequences can be used to measure relaxation times through various pseudo two-dimensional experiments. Most commonly this includes ^{1}H T_1 and ^{1}H $T_{1\rho}$ experiments. Each will be discussed further in section 2.4.1.

2.4 Solid-state NMR of Pharmaceuticals and Amorphous Solid Dispersions

Solution NMR has long been used for structural identification pharmaceutical analysis, however the adoption of SSNMR in the pharmaceutical industry has been much slower. Only in the last few decades has SSNMR begun to be widely used for

pharmaceutical solids analysis as it has been realized how ideally suited SSNMR is for analyzing complex drug products. In particular, SSNMR has found extensive application in the analysis of amorphous solid dispersions as an emerging formulation strategy (178). SSNMR can simultaneously analyze all components of a formulated drug product (179).

2.4.1 Miscibility, Proton Relaxation Times, and Molecular Mobility

Section 2.3.3 described the main relaxation processes occurring after excitation of nuclear spins in a SSNMR experiment. Aside from being used to correctly design a pulse sequence and acquire the desired spectrum, relaxation times can provide useful data for the system of interest. While T_2 has found greater utility for solution NMR and magnetic resonance imaging, ^1H T_1 and $T_{1\rho}$ can be used extensively for the advanced analysis of ASDs.

^1H T_1 and $T_{1\rho}$ both offer a measure of molecular mobility on different timescales. T_1 provides information on rapidly occurring motional processes on the order of 10's or 100's of MHz such as methyl group rotations. ^1H T_1 relaxation times have been used as an estimator of the physical stability of amorphous pharmaceutical systems (178). $T_{1\rho}$, on the other hand, provides information on motions in the 10's of kHz region (165). In the case of ASDs, T_1 and $T_{1\rho}$ can also provide a measure of the degree of mixing or homogeneity in a sample as each value is affected by the process of spin diffusion. Spin diffusion, driven by dipolar coupling (typically ^1H-^1H), is the spontaneous exchange of magnetization between nuclei in close proximity (180). Therefore, differences in ^1H magnetization can be averaged over a given distance through spin diffusion if the sample is homogeneous while differences will remain if the system is heterogeneous. The length scale of spin diffusion (L) is given by Equation 2.7:

$$L = \sqrt{6Dt} \qquad\qquad (2.7)$$

where D is the coefficient of spin diffusion (estimated between 0.8×10^{-11} and 1×10^{-11} cm^2/s) (180, 181) and t is the relaxation time (either T_1 or $T_{1\rho}$). Spin diffusion experiments have been used to estimate homogeneous domain sizes in both polymer blends (180, 182) and ASDs (85, 183).

The radius over which spin diffusion can average magnetization differences is determined by the ^1H T_1 and $T_{1\rho}$ relaxation times of the various components of the system and their degree of mixing/ homogeneity. In the case of ASDs, this refers to the amorphous drug and polymer. Assuming typical amorphous pharmaceutical ^1H T_1 times between 1 and 5 s and typical $T_{1\rho}$ times between 2 and 20 ms, homogenous domain sizes can be determined (85). Common relaxation times are observed in the system is intimately mixed or homogeneous. Therefore, if the drug and polymer each have common ^1H T_1 and $T_{1\rho}$ times, the system is homogeneous on an approximately 2-5 nm length scale. Similarly, a homogenous domain size of 5-20 nm is predicted for similar T_1 times but different $T_{1\rho}$ times while different T_1 and $T_{1\rho}$ times are observed for a system homogeneous only down to 3.5-11 nm. The comparison of relaxation times is commonly used to measure miscibility in drug-polymer mixtures. The intimate mixing of drug and polymer is thought to be a requirement for forming a physically stable system. Therefore, domain sizes measured by SSNMR may be used as a possible indicator of ASD stability and shelf life (85).

^1H T_1 is easily measured by monitoring the return of magnetization to equilibrium after perturbation by a RF pulse. This is commonly accomplished through a saturation recovery experiment. Figure 2.9 illustrates a saturation recovery pulse sequence for measuring T_1. Alternatively, an inversion recovery sequence may be used by replacing the

90° pulse with a 180° pulse. Here, the return of magnetization to equilibrium is initially at its maximum in the -z direction, decreases through zero, then increases back to equilibrium. The inversion recovery experiment may be useful in determining small differences in relaxation behavior of multi-component systems such as ASDs (183). Additional methods to measure T_1 exist in the literature which may be useful in cases where significant spectral artifacts exist (184).
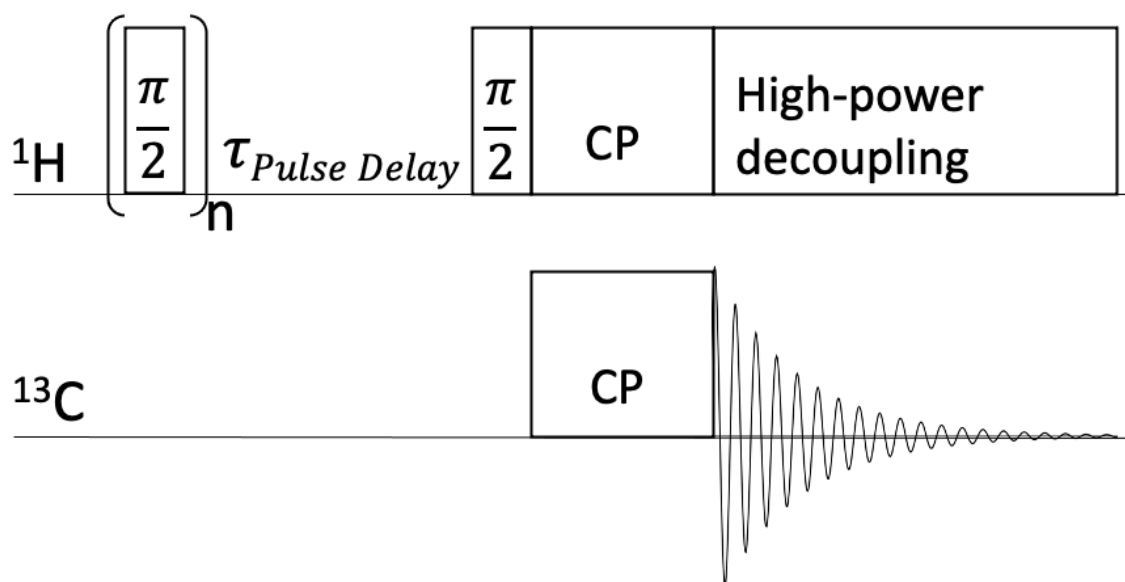
Figure 2.9. Spin-lattice relaxation (^1H T_1) pulse sequence. For simplicity, the TOSS component is not shown.

Graphically, the measured signal intensity for a given nucleus is plotted as a function of pulse delays. Ideally, a range of pulse delays from nearly zero to greater than 5-times the estimated T_1 are used. Figure 2.10 overlays the progression of longitudinal relaxation with the graphical results of a T_1 experiment.

Increasing the duration of the pulse delay increases the fraction of net magnetization that returns to the z-axis. In turn, there is a greater amount of magnetization

pushed to the x,y-plane by a subsequent 90° pulse, of which the magnitude is directly proportional to the measured NMR signal intensity.
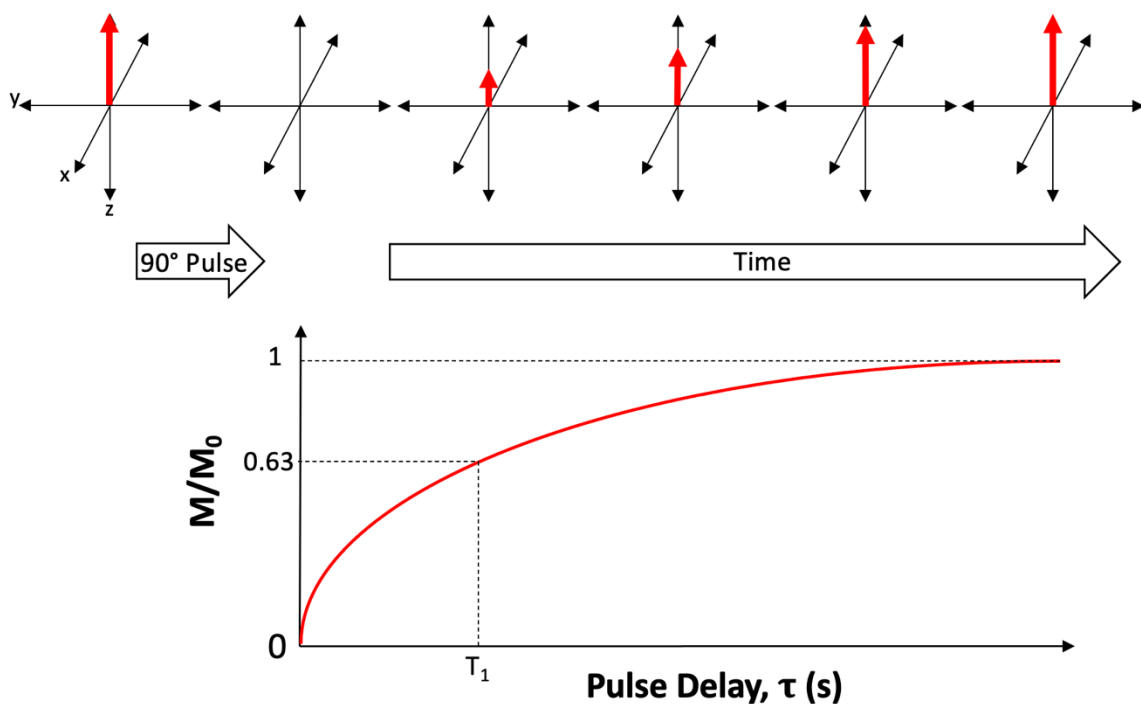
Figure 2.10. Schematic and graphical representation of the evolution of net magnetization during longitudinal (T_1) relaxation.

The concept of measuring $T_{1\rho}$ is nearly the same as for T_1 except the spin-lattice relaxation is now measured in the rotating frame rather than the laboratory frame. A similar pulse sequence is used (Figure 2.11) to measure the decay of magnetization (M) with

increasing spin-lock times. The decay is described by Equation 2.8 where (M_0) is equilibrium magnetization and τ is the spin-lock time.

$$M = M_0 e^{-\frac{\tau}{T_{1\rho}}} \qquad (2.8)$$
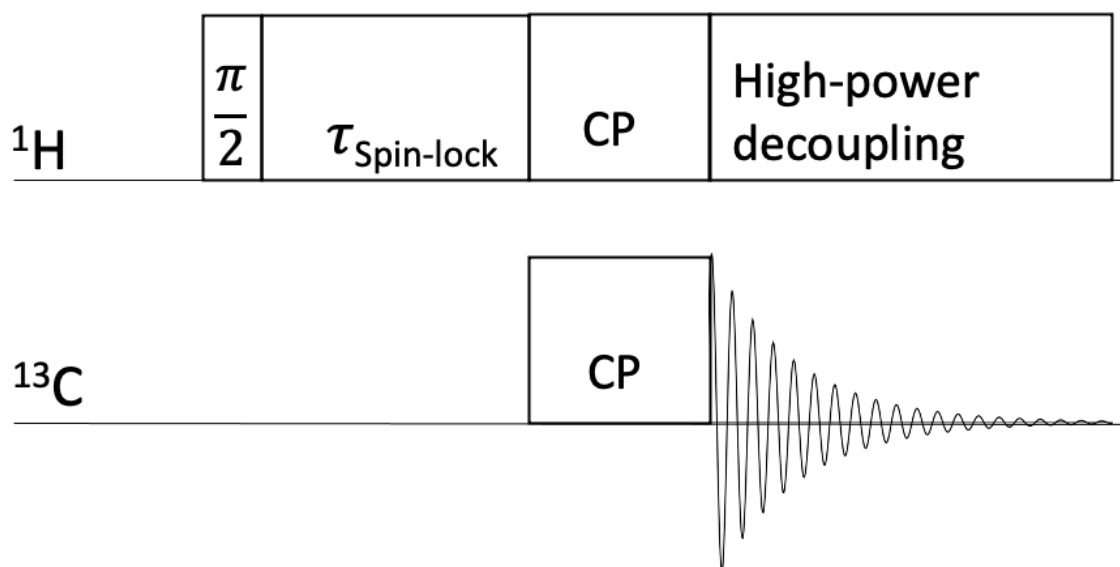
Figure 2.11. Pulse sequence for measuring spin-lattice relaxation in the rotating frame (^{1}H $T_{1\rho}$). For simplicity, the TOSS sequence is excluded.

2.5   Quantitative Solid-state NMR

NMR signal intensity is dependent on a variety of factors including the sample mass (m), nuclei present (gyromagnetic ratio, γ), magnetic field strength (B_0), number of scans (N), RF pulse intensity (B_1), and temperature (T), among others (165). The relationship between signal intensity and each of these factors is shown in Equation 2.9.

$$I = \frac{\gamma^4 B_0^2 N B_1 g(v) m}{T} \qquad (2.9)$$

Equation 2.9 shows that NMR is an inherently quantitative technique as the signal intensity is directly proportional to the number of distinct nuclei present in a sample. However, it is generally assumed that components of many SSNMR pulse sequences, such as CP and TOSS, are non-quantitative. While these pulse sequences make acquiring quantitative data more difficult, properly accounting for experimental parameters still yields quantitative data.

As was previously mentioned, SSNMR is particularly suited for the analysis of pharmaceuticals. More so than other analytical techniques, SSNMR provides the advantage of being able to provide quantitative data on a multicomponent system such as a formulated drug product. There are many examples in the literature of how SSNMR has been used to quantitatively analyze a pharmaceutical system. Briefly, SSNMR has shown its utility to quantify polymorphic forms (185), amorphous phases, homogeneous domain sizes (183), hydrogen bonding distributions (89), crystallinity, copolymer composition (186), particle size distributions (187), and water content (188). It is important to note that this list is by no means comprehensive and was meant only to provide an overview of pharmaceutically relevant analyses performed via SSNMR.

2.5.1 Cross Polarization Dynamics

When CP is applied to a sample spinning at the magic angle, the transfer of magnetization from ^{1}H to ^{13}C is time dependent and governed by two time constants. The initial buildup of magnetization in ^{13}C is controlled by the CP rate constant, T_{CH}. Simultaneously, however, ^{13}C magnetization decreases as it dispersed to the lattice. This rate of decay is controlled by the proton spin-lattice relaxation in the rotating frame (^{1}H

$T_{1\rho}$). The ^{13}C magnetization profile can be visualized by plotting the observed peak intensity or area as a function of contact time in which the initial rapid increase in magnetization (T_{CH}) is followed by a relatively slow decay with time ($T_{1\rho}$) (Figure 2.12). Further complicating things is the fact that the CP rate constants vary both intermolecularly between different molecular species present in the sample but also intramolecularly between nuclei in the same molecule. For example, CP to a methyl carbon is inefficient due to the high mobility of the methyl group whereas magnetization transfers more efficiently from protons to secondary carbons relative to tertiary carbons due to the increased number or ^{1}H directly bound to ^{13}C. In other words, magnetization does not transfer uniformly to each nucleus. Therefore, the rate constants must be experimentally determined for each nucleus of interest to ensure quantitative data is acquired. If CP dynamics are not properly accounted for, relative peak intensities of distinct nuclei will not be proportional to the amount of each component present (unless T_{CH} and $T_{1\rho}$ are equal between each form) (189).

In order to measure T_{CH} and $T_{1\rho}$, a variable contact time (VCT) experiment is needed. A VCT experiment varies the contact time (time that cross polarization is allowed to occur) in successive CP or CP TOSS experiments. Peak area or intensity (I) is plotted as a function of contact time (τ) and fit to the biexponential Equation 2.10.

$$I = \frac{I_0\left(\frac{\gamma_H}{\gamma_C}\right)\left[exp\left(-\frac{\tau}{T_{1\rho}}\right) - exp\left(-\frac{\tau}{T_{CH}}\right)\right]}{1 - \left(\frac{T_{CH}}{T_{1\rho}}\right)} \qquad (2.10)$$

Here, I_0 is the thermal equilibrium magnetization intensity, and γ_H and γ_C are the gyromagnetic ratios of ^{1}H and ^{13}C, respectively. The results of a VCT experiment on patiromer are shown in Figure 2.12.
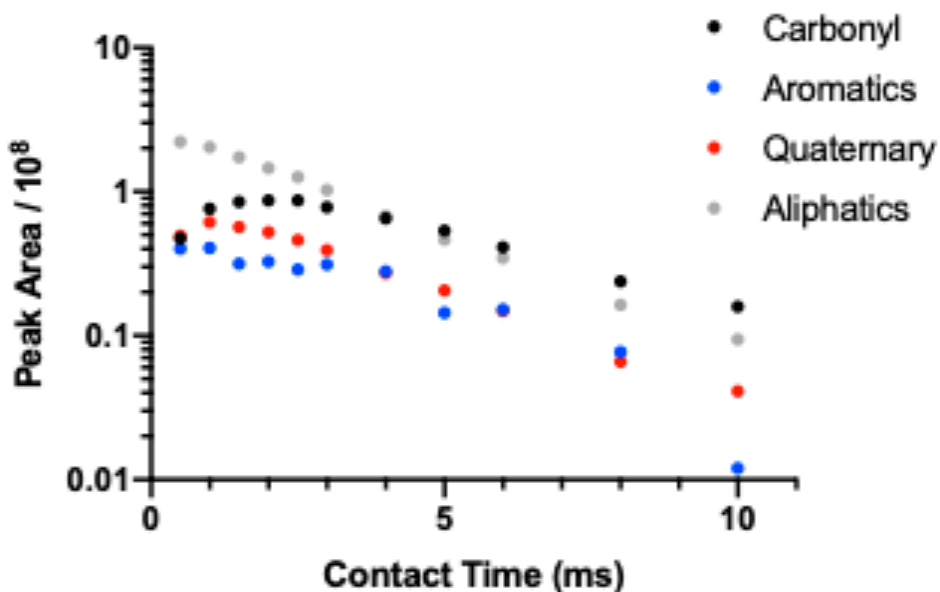
Figure 2.12. Results of a variable contact time experiment showing the cross polarization dynamics for the various functional groups in patiromer. Adapted from ref. (186).

T_{CH} and $T_{1\rho}$ can be determined by fitting experimental VCT data to Equation 2.10. Alternatively, $T_{1\rho}$ can be solved for through a ^1H $T_{1\rho}$ experiment (section 2.4.1 and Figure 2.11). Figure 2.12 illustrates the importance of a properly selected contact time for acquiring quantitative data. At short contact times, signal intensity has yet to reach its maximum value while at longer contact times, $T_{1\rho}$ relaxation causes a decrease in the observed signal. Again, the contact time at maximum signal is not necessarily the same between different nuclei due to non-uniform CP dynamics. To remedy this, signal intensity in Figure 2.12 is extrapolated back to zero-contact time to approximate an instantaneous CP process and yield the true intensity for a nucleus. Despite the complex nature of CP dynamics, there are many examples in the literature of SSNMR being used to quantify pharmaceutical systems. Offerdahl et al. demonstrated the proper characterization of CP dynamics for the quantitation of multiple neotame polymorphs and an amorphous form

(185). Through a similar procedure, Jarrells et al. quantified the relative proportions of different monomer units in the block copolymer, patiromer (186).

2.5.2   Total Suppression of Spinning Sidebands

Total Suppression of Spinning Sidebands (TOSS) is commonly used in acquiring SSNMR data, particularly for slow spinning speeds or complex spectra. Despite its relative ease of implementation, TOSS-simplified spectra can still have quantitative issues. TOSS eliminates the intensity of SSBs leaving only the intensity of the isotropic peak to be integrated. Thus, the integrated isotropic peak does not account for all signal associated with a distinct nucleus. The problem lies in that the CSA pattern may not be consistent between different nuclei. In other words, varying proportions of signal are contained in the SSBs for different nuclei potentially leading to significant error if only the isotropic peak is used for integration.

Ideally, using TOSS can be avoided entirely by spinning the sample fast enough to eliminate all SSBs. In this case, fast CP MAS is sufficient to 'spin out' all SSBs. However, this is not possible for most samples due to the reduced signal intensity caused by using smaller rotors that contain less sample. As a result, the SSBs for distinct nuclei must also be integrated to yield truly quantitative data. This often proves challenging as SSBs may overlap with other isotropic peaks or SSBs. Repeating a CP MAS experiment at multiple spinning speeds may be necessary to accurately isolate and integrate all SSBs (185, 186).

2.5.3   Relaxation Time Correction

The magnetization or signal intensity increases exponentially towards the equilibrium or maximum intensity according to Equation 2.8. Theoretically, as signal intensity asymptotically approaches its maximum value (see Figure 2.10), an infinite pulse

delay (τ) is needed avoid saturation and truly achieve quantitative data. Therefore, observed signal intensity (I) must be corrected to account for incomplete relaxation between successive NMR acquisitions. This is shown in Equation 2.11 where I_{corr} is the true/ corrected signal intensity.

$$I_{corr} = \frac{I}{1-e^{-\frac{\tau}{T_1}}} \qquad (2.11)$$

In practice, using $\tau = 5T_1$ approaches equilibrium (99.32%) and is the time typically chosen for acquiring quantitative data but results in long experimental times. In the interest of time however, $\tau \leq 2.5T_1$ and correction with Equation 2.11 will often suffice. It is important to note that, in the case of a multicomponent system with varying ^{1}H T_1 values, $\tau = 5T_1$ refers to the T_1 of the component with the longest T_1. Otherwise, quantitative data will be acquired for the faster relaxing components (short T_1's) while the slowest relaxing component (longest T_1) will be underestimated.

2.5.4 Deconvolution

Due to the various linebroadening contributors discussed in section 2.3, many SSNMR spectra often contain overlapping peaks which may complicate spectral analysis. Various pulse programs have been devised to help avoid overlap and identify individual peaks including isotopically labelled spectral subtraction (89, 190, 191), $T_{1\rho}$-filtering, interrupted decoupling (192), and two-dimensional SSNMR. However, in many cases, peak deconvolution is still needed to better analyze a SSNMR spectrum. Deconvolution typically refers to the separation of observed overlapping peaks into separate peaks attributed to different nuclei or species present such that the sum of all individual peaks equals the total shape and intensity of the observed peak(s). The chemical shift of the contributing individual peaks may be identified by the methods mentioned above and held

constant in a fitting procedure to minimize differences between the observed and predicted spectrum. A representative example is shown in Figure 2.13 for the deconvolution of the crystalline and amorphous components of nifedipine. The chemical shift and lineshape of the amorphous and crystalline peaks were determined from a crystalline-free ASD containing nifedipine and a $T_{1\rho}$-filtering experiment, respectively.
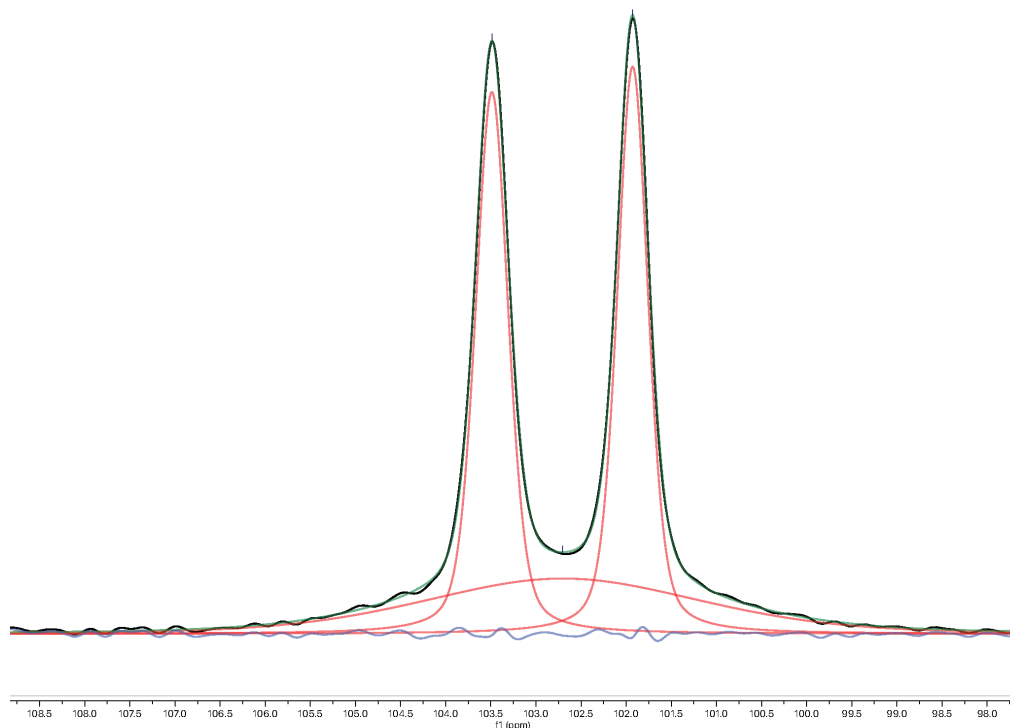
Figure 2.13. Deconvolution of overlapping crystalline/ amorphous nifedipine peaks in an 80-20 nifedipine-PVP ASD. The experimental spectrum is shown in black, individual peaks are shown in red, the predicted spectra is shown in green, and the difference between the experimental and predicted spectra is shown in blue.

Deconvolution can also be used to acquire semiquantitative data from a multi-component T_1 saturation recovery curve. Just as in a typical single component ^1H T_1 experiment, the intensity or area under the curve for the peak of interest is plotted as a

function of the pulse delay (τ), however in this case, the peak is composed of different components. For example, this procedure may be applied to peaks containing both crystalline and amorphous drug or when there is a bi-modal particle size distribution (187). Fitting the relaxation data to Equation 2.6 would yield a single T_1 time albeit a poor fit to the data. In this case, a biexponential T_1 curve (Equation 2.12) is needed to accurately fit the magnetization (M) data and yield the T_1 of each component.

$$M = M_{0,1}e^{-\frac{\tau}{T_{1,1}}} + M_{0,2}e^{-\frac{\tau}{T_{1,2}}} \tag{2.12}$$

Here, $M_{0,i}$ and $T_{1,i}$ represent the equilibrium magnetization and ^1H T_1 time for each component (drug and polymer), respectively. The equilibrium magnetization of each component can also be used to estimate the relative amount of each system component (187). This is shown in Equations 2.13 and 2.14.

$$\% \ Component \ 1 = 100 \times \frac{M_{0,1}}{M_{0,1}+M_{0,2}} \tag{2.13}$$

$$\% \ Component \ 2 = 100 \times \frac{M_{0,2}}{M_{0,1}+M_{0,2}} \tag{2.14}$$

While the deconvolution of a T_1 relaxation time curve can provide useful data for each component, it is necessary to provide good initial guesses such that the line fitting is performed on only two components (both $T_{1,i}$ or both $M_{0,i}$) at a time rather than four components (all $T_{1,i}$ and $M_{0,i}$) simultaneously. For example, Dempah et al. used dicumarol samples with uniform particle size distributions to determine initial T_1 estimates for bimodal mixtures of unknown composition (187).

2.6 Conclusions

The general theory of NMR was discussed and some of the key differences highlighted between solution-state and solid-state NMR. The intricacies of SSNMR were examined with an emphasis on ensuring quantitative data is acquired. The various applications for the advanced analysis of amorphous pharmaceuticals were also surveyed. Chapter 2 has shown not only the complexity of SSNMR but also the incredible potential it possesses, particularly for the analysis of amorphous and other complex pharmaceutical systems.

CHAPTER 3: QUANTIFICATION OF MONOMER UNITS IN INSOLUBLE POLYMERIC ACTIVE PHARMACEUTICAL INGREDIENTS USING SOLID-STATE NMR SPECTROSCOPY

3.1 Introduction

Polymers with desirable pharmacological properties are used in some drug formulations as the active pharmaceutical ingredient (API) rather than their traditional role as an inactive excipient or drug-delivery vehicle (193-201). The macromolecular size of polymers, advances in polymerization techniques, and an improved understanding of ligand-receptor interactions have increased the potential for polymers to be used as the API (193). Multivalent insoluble polymers have found the most success as sequestrants, whereby the polymer is typically used to bind excess ions, bile acids, **or** other unwanted moieties in the gastrointestinal (GI) tract (202-207). Patiromer (Veltassa®), sevelamer (Renagel® and Renvela®), and colesevelam (Welchol®) have all been approved by the FDA as polymeric APIs for treating hyperkalemia, hyperphosphatemia, and hypercholesterolemia, respectively, through binding in the GI tract (208-211). Polymeric APIs have also been investigated as potential antiviral (212) and antimicrobial drugs (213-215), as well as potential cancer treatments (216, 217).

Pharmaceutical polymers often contain some level of variation. This may come in the form of molecular weight or chain-length (74), tacticty (218), crystallinity (219), and/ or side-chain substitution (219, 220) and can vary between chemical suppliers (221). The

aforementioned variations in polymers may result in batch-to-batch variations which could affect drug performance (222). However, when the polymer itself is the API, extensive care must be taken to control batch-to-batch variability of the polymer (223).

A pharmaceutical manufacturing process is typically monitored for quality control during or post-production. During manufacture of the API, process analytical technologies (PAT) are used for in-line, on-line, or at-line analysis techniques to monitor and control critical parameters to ensure a consistent drug product. Post-production, critical quality attributes of a drug substance or intact drug product can be analyzed to ensure it is within acceptable limits. The ability to characterize a formulation across multiple lots or batches of different dosage strengths is critical for ensuring product uniformity. Similarly, the ability to conduct a detailed characterization of a drug product is necessary to demonstrate API sameness in generic drug development. As polymeric APIs do not strictly fit into a small molecule or biologic drug category, their analysis and characterization pose a significant regulatory and development challenge (202, 224).

Complex insoluble polymers and polymeric APIs are particularly difficult to analyze compared to soluble polymers as typical solution-based analytical methods often cannot be used (225). Fourier transform-infrared (FTIR) spectroscopy and Raman spectroscopy are used to identify the presence of different functional groups. Peak shifts in FTIR spectra can indicate changes in drug product composition but is semiquantitative at best. Near infrared (NIR) spectroscopy has been successfully implemented for PAT monitoring due to its quick analysis times and little-to-no sample preparation (226, 227). It has been used for determining copolymer composition (228) and the quantitation of certain functional groups in pharmaceuticals (229). However, use of NIR for quantitation

often relies on a reference or calibration standard and/or the use of chemometric methods (143). Different mass spectrometry (MS) techniques have been used for polymer analysis. Matrix assisted laser desorption/ionization time-of-flight (MALDI TOF) MS has been successfully used for the determination of molecular weight distribution and copolymer composition of poorly soluble and insoluble polymers (230, 231). Despite these successes, MALDI TOF sample preparation requires the use of a matrix additive while the use of chain statistics and model optimization is necessary to analyze results (232, 233).

Solid state nuclear magnetic resonance (SSNMR) spectroscopy is a non-destructive and sensitive analytical technique which can be used to provide information about structure (190), physical form (179), molecular mobility, miscibility (85), and molecular interaction (89). Most importantly, SSNMR is an inherently quantitative technique as the signal intensity is directly proportional to the number of a distinct nuclei present in the sample that resonate at a given frequency (185). This provides a significant advantage over many other solid state analytical techniques in that no pure standards are needed nor is a calibration curve required (234). Cross polarization (CP) is used to increase the sensitivity of SSNMR by transferring polarization from abundant spin (^{1}H) to dilute spin (^{13}C) nuclei (174). CP dynamics are governed by two time constants, T_{CH} and $T_{1\rho}$, which correspond to the transfer of magnetization from ^{1}H to ^{13}C nuclei and the subsequent decay of magnetization back to equilibrium, respectively. Because CP is not an instantaneous process, T_{CH} and $T_{1\rho}$ must be experimentally determined when CP is used in quantitative SSNMR. Failure to do so can result in misleading quantitation outcomes if the dynamics vary between distinct nuclei (185, 189). When CP dynamics are properly accounted for, SSNMR has been used in the quantitation of different polymorphic forms and amorphous

content (185), drug-polymer hydrogen bonding configurations (89), as well as block copolymer domain sizes and diffusivity measurements (180). SSNMR can therefore be used to answer a variety of questions even in complicated formulations.

Patiromer (Veltassa®) is an FDA-approved drug currently marketed for the treatment of hyperkalemia (235). It is an amorphous insoluble polymer which is administered orally by suspending in water and works by binding free potassium ions in the gut. Patiromer is not systemically absorbed and is eliminated, along with the bound potassium, through fecal excretion (208, 235). The drug product is a block copolymer consisting of three monomer units and a calcium-sorbitol counterion (Figure 3.1). Per the package insert, the potassium-binding portion of the drug, 2-fluoro-2-propenoate monomer (m-block), makes up 91% of the formulation. The remaining 9% is a combination of the crosslinking groups diethenylbenzene (n-block) and octa-1,7-diene (p-block). Two grams of calcium-sorbitol counterion is also included for each gram of patiromer in the formulation (208). The amount of crosslinker present is used to control the swelling ratio of patiromer when exposed to water or gastrointestinal fluid while the relative amount of each crosslinker used presumably helps to fine-tune the amount of swelling for a given amount of m-block (223, 236). Patiromer was chosen for analysis as a model polymeric drug product which currently has no approved generic equivalent. Analysis of patiromer may serve as a model for the analysis of other FDA-approved polymeric APIs, multiple polymeric APIs in development, as well as for demonstrating API sameness in generic drug development.
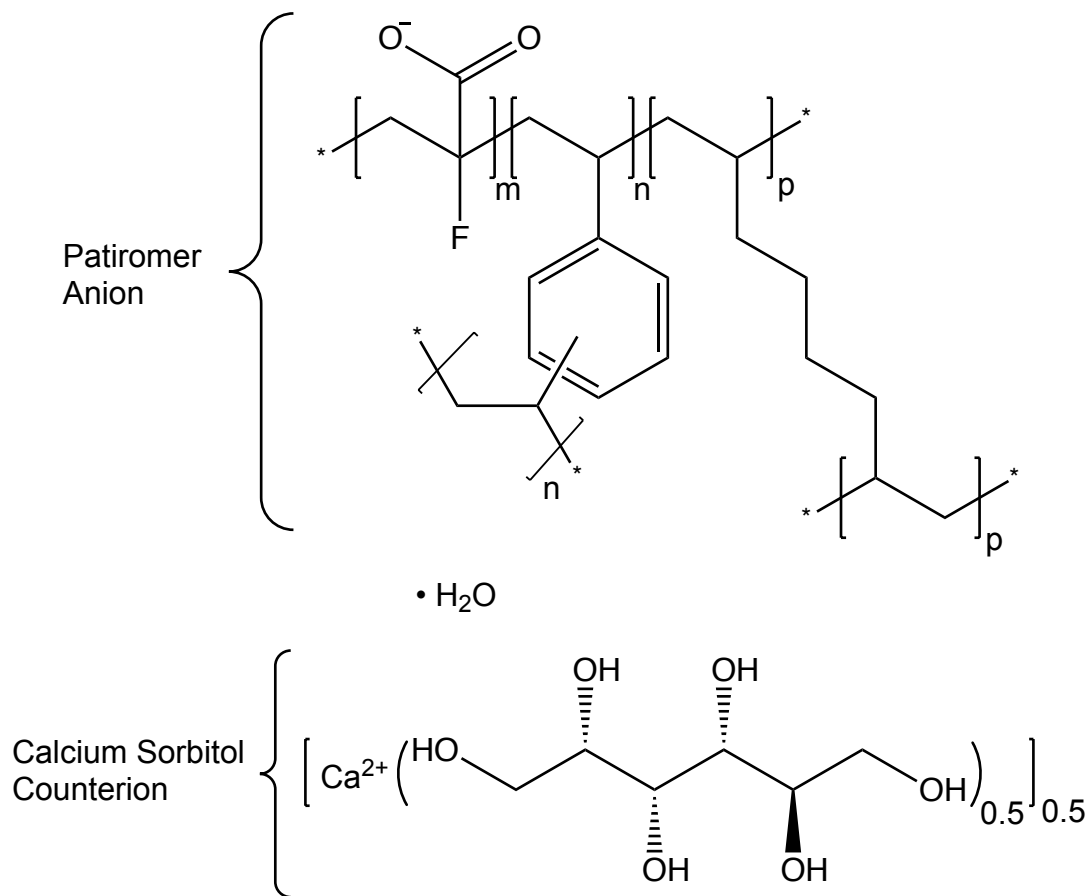
Figure 3.1. Patiromer chemical structure. m=2-fluoro-2-propenoate groups, n = diethenylbenzene groups, p = octa-1,7-diene groups. The extended polymeric network is indicated by the asterisk (*) and •H2O indicates associated water.

The specific goal of this work was to develop a method to quantify the relative amounts of each type of monomeric units present in the copolymer patiromer. The method can be applied as a process analytical technique for quality control between batches during manufacturing as well as a discriminating tool for demonstrating API sameness for generic drug development. SSNMR is perfectly suited to meet the goals of this method development and was used to analyze various patiromer lots. This was done by first identifying, evaluating, and quantifying the carboxylate, aromatic, and aliphatic groups in the drug molecule using a variety of ^{13}C-SSNMR techniques. This included accounting for the CP dynamics to ensure quantitative data. When compared to published values, the newly developed SSNMR method successfully quantified the amount of carboxylate groups present in intact patiromer while also providing the previously unknown relative amounts of aromatic and aliphatic monomer groups. The relative monomer ratios in different lots of patiromer were then compared to investigate lot-to-lot variations and further validate the new method. Development of new analytical methods, such as the SSNMR methodology presented herein, make the advanced characterization of complex polymeric API possible.

3.2   Materials and Methods

In total, seven lots of patiromer were analyzed. These samples included three dosage strengths (8.4 g, 16.8 g, and 25.2 g) and samples that had previously expired (Table 3.1). Lots A, B, and C were purchased from the Purdue University pharmacy (West Lafayette, IN) while four expired lots (lots D, E, F, and G) were also obtained and

evaluated. All samples were shipped to the University of Kentucky College of Pharmacy (Lexington, KY) for analysis.

Table 3.1. Properties of analyzed patiromer lots.

Lot	Dose Strength (g)	Expiration Date
A	8.4	2021
B	16.8	2021
C	25.2	2020
D	8.4	2017
E	8.4	2018
F	16.8	2018
G	25.2	2017

3.2.1   Solid-state NMR

All SSNMR experiments were acquired using a Tecmag Redstone HF3 2RX spectrometer (Tecmag, Inc., Houston, TX) operating at 75.48 MHz for ^{13}C. All experiments were acquired using cross polarization (174), magic angle spinning (MAS) (169), SPINAL64 decoupling (237) with a ^{1}H decoupling field of approximately 64kHz, and, unless otherwise noted, performed using a 7.5 mm double-resonance MAS probe (Varian, Palo Alto, CA) at 20°C. An external standard, 3-methylglutaric acid, was used to optimize the spectrometer parameters. The methyl peak was referenced to 18.84 ppm (238). Approximately 350 mg of patiromer was packed into a 7.5 mm rotor with Teflon or Kel-f endcaps.

The spin-lattice relaxation time (^{1}H T_1) was measured using a saturation-recovery pulse sequence through ^{13}C observation, with 4096 scans collected, each containing 512

acquisition points. A peak (typically carboxylate) in the Fourier-transformed spectra was integrated and plotted against recovery delay times according to Equation 3.1.

$$M = M_o\left(1 - e^{-\tau/T_1}\right) \tag{3.1}$$

M is the integrated peak intensity and τ is the recovery delay time (234). M_o is obtained from the fitting procedure and T_1 is the spin-lattice relaxation time. TNMR (version 3.3.9) software was used to plot and analyze the data.

When a solid sample is spun at the magic angle in a solid-state NMR spectrometer, magnetic field inhomogeneities often exist within the sample and result in the presence of spurious peaks known as spinning sidebands (SSBs) (170). In order to acquire a basic patiromer spectrum free of SSBs, a sample (lot A) was spun at the magic angle using a CP with total sideband suppression (TOSS) pulse sequence (171). A 3 ms contact time (CT) was used and, based on the ^1H T_1 of the sample, a 10 s pulse delay (PD). A total of 4096 scans with 512 acquisition points were obtained with the data zero-filled to 4096 points and no line broadening applied.

A variable contact time (VCT) experiment was conducted to determine the CP dynamics and select an appropriate CT. A series of CP TOSS experiments spinning at 4 kHz varied the CT from 0.5 to 10.0 ms and the integrated signal intensity of each peak was plotted on a logarithmic scale as a function of CT. The integrated signal intensity is extrapolated to zero-CT and used as the true intensity for each functional group.

The spin-lattice relaxation time in the rotating frame (^1H $T_{1\rho}$) and CP rate constant (T_{CH}) were determined through the VCT experiment by fitting the signal intensity as a function of CT to Equation 3.2 (234).

$$M = \frac{M_o\left(\frac{\gamma_H}{\gamma_C}\right)\left[\exp\left(\frac{-\tau}{T_{1\rho}}\right)-\exp\left(\frac{-\tau}{T_{CH}}\right)\right]}{1-\left(\frac{T_{CH}}{T_{1\rho}}\right)} \qquad (3.2)$$

M is the peak area for each contact time (τ) and M_o is the thermal equilibrium

magnetization. γ_C and γ_H are the gyromagnetic ratios for ^{13}C and ^1H, respectively.

$T_{1\rho}$ can also be determined through a ^1H $T_{1\rho}$ experiment. The same patiromer sample (lot

A) as in the VCT experiment was used in which 512 scans and 512 acquisition points were

collected using a 10 s PD and 3 ms CT. TNMR and Microsoft Excel (version 16.26) were

used to plot and analyze the data.

To further aid in assigning peaks to each functional group, interrupted decoupling

was used. An interrupted decoupling spectrum was acquired identically to the CP TOSS

spectrum only with a 50 µs dipolar dephasing time at the beginning of signal acquisition

to identify the number of protons directly bound to each ^{13}C atom.

To prevent any signal intensity from being lost due to using TOSS (189) or from

SSBs that are located underneath (at the same chemical shift) as other peaks, CPMAS

spectra without TOSS were acquired at varying spin speeds. All CP spectra were acquired

using the same rotors and endcaps as listed previously. Again, 4096 scans each containing

512 acquisition points were collected with a 10 s pulse delay (PD), 3 ms CT, and 64 kHz

proton decoupling field. The MAS frequencies ranged from 3 kHz to 12.5 kHz with 6 kHz

being used for quantitative analysis.

CP efficiency is inversely related to molecular mobility (177). A low temperature

CP TOSS spectrum was acquired to identify and resolve any mobility issues that may exist

in patiromer. Lot A was run at -20°C with TOSS parameters identical to other CP TOSS

spectra acquired. Compressed air gas was diverted through a copper coil that was

submerged in a liquid nitrogen dewar before being directed towards the spinning rotor. Once the outlet temperature reached -20°C, the sample was equilibrated for 15 minutes prior to spectral acquisition.

The calcium-sorbitol counterion was washed out of some patiromer samples to investigate if the presence of sorbitol in the drug product was affecting the NMR signal intensity of other functional groups. Two 8.4 g samples of lot A were each dissolved in 100 mL of deionized water, stirred at 400 rpm for four hours, and vacuum filtered through a P5 filter. One sample was dried at 40°C overnight while the other was dried under 25 in Hg at 20°C overnight. Samples were packed in 7.5 mm zirconia rotors and scanned by SSNMR (CP, T_1, and $T_{1\rho}$) using the conditions previously described. The resulting spectrum showed a small peak present between 55 and 80ppm indicating that the counterion was nearly completely washed from the patiromer (Figure 3.2). Minimal changes in the intensities of other peaks were detected.
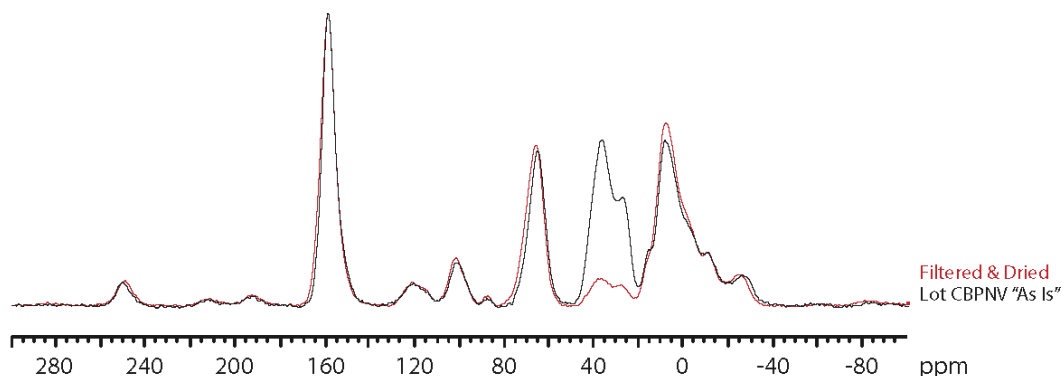
Figure 3.2. Overlaid ^{13}C CP spectra at 6.5 kHz MAS before and after washing in water, filtering, and drying to remove sorbitol.

It was not possible to formulate standard samples of patiromer to use in method validation. Therefore, calculations were performed on theoretical standard samples

containing known amounts of n- and p-block crosslinking groups. Additionally, monomer compositions of seven different patiromer lots were successfully quantified and served to help validate proposed SSNMR method.

3.2.2 Data Processing

All quantitative SSNMR spectra were phased identically using TNMR 'Phase Adjustment.' The downfield carboxylate SSB peak (approximately 257 ppm) was phased using zero-order phasing. Where necessary, minimal first-order phasing was used to phase the rest of the spectrum.

The baseline of each quantitative CPMAS SSNMR spectrum was corrected using TNMR 'Baseline Fix.' A 14-point spline was applied to the previously-phased spectrum. Care was taken to avoid fixing the baseline on any SSB. Multiple points were applied far upfield and far downfield of the spectrum with only two points applied in the chemical shift range of interest (approximately at 118 and 158 ppm).

3.3 Results and Discussion

3.3.1 Initial SSNMR Acquisitions of Patiromer

3.3.1.1 ^{1}H T_1 Relaxation Time

The proton spin-lattice relaxation time (^{1}H T_1) was determined using a saturation-recovery pulse sequence. This measured the return of magnetization to equilibrium as a function of different pulse delays and was used to determine the appropriate pulse delay for the study of patiromer. The initial lot A sample was spun at 4 kHz MAS for 512 scans and 1024 acquisition points and the results were fitted to Equation 3.1. The ^{1}H T_1 for the carboxylate was found to be 3.20 ± 0.09 s.

3.3.1.2   CP TOSS Spectrum at 4kHz MAS

Based on the 3.20 s ^{1}H T_1 collected, a pulse delay of 10 s was selected for the initial acquisition of a patiromer spectrum (173, 234). The same patiromer sample was used to acquire a CP spectrum. TOSS was used so that SSBs would not complicate the spectrum nor the subsequent assignment of peaks to each functional group. Based on the reported chemical structure (Figure 3.1) and literature values, it was expected that the main signals would resonate at 20 – 50 ppm (aliphatic), 60 – 80 ppm (sorbitol), 80 – 100 ppm (quaternary), 120 – 140 ppm (aromatic), and 170 – 180 ppm (carboxylate).

Figure 3.3 shows the CP TOSS spectrum of patiromer lot A acquired at 4 kHz MAS and 1.5 ms CT. As expected, resonances appear in each of the chemical shift regions of interest. The most intense peak at 177 ppm was assigned to the carboxylate carbon in the m-block carboxylate group. Similarly, the m-block also contains the quaternary/ α-carbon which is directly bound to fluorine at 95 ppm. The two peaks at 127 and 144 ppm were both assigned to aromatic carbons. Presumably, as the n-block can have meta- or para-linkages, the peak at 127 ppm has a bound proton while the peak at 144 ppm has no bound protons. The broad aggregate of peaks centered at 45 ppm is assigned to all aliphatic carbons in patiromer. This includes all of the p-block as well as the backbone aliphatic carbons in the m- and n-blocks. The remaining broad peak between 60 and 80 ppm is assigned to the three distinct carbons in sorbitol. The bound hydroxyl groups act to deshield each carbon and resonate farther downfield than the aliphatic nuclei.
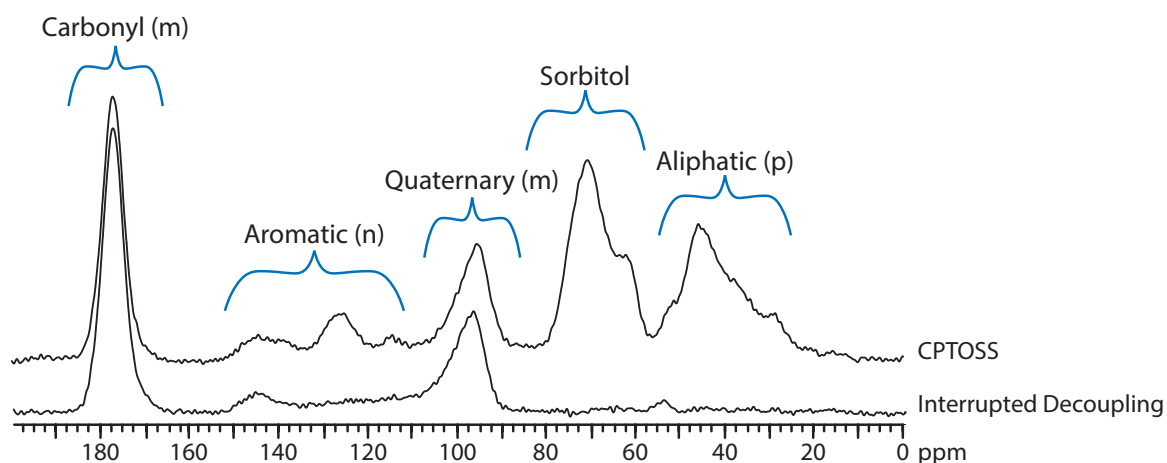
Figure 3.3. Initial CPTOSS spectrum acquired at 4 kHz MAS with labeled functional group ranges (top) and interrupted decoupling CP TOSS spectrum (bottom). (m, n, and p correspond to the patiromer polymer block in which each functional group is found).

As an additional check to confirm the peak assignments were correct, a CP spectrum was acquired using interrupted decoupling. For a short time prior to signal acquisition, the proton decoupler was turned off and ^{13}C nuclei strongly coupled to protons (-CH- and -CH$_2$) rapidly dephased. The dephased peaks were expected to show reduced or no signal relative to the CP TOSS spectrum (Figure 3.3). The peak at 127 ppm disappears in the interrupted decoupling spectrum which confirmed its assignment as the aromatic carbon with a bound proton.

Likewise, the peak at 144 ppm showed no change in intensity as it is the aromatic carbon with no bound protons. Furthermore, the peak between 60 and 80 ppm (sorbitol) completely dephased along with the broad aliphatic peak (45 ppm) as each carbon contains one or two bound protons.

3.3.2   Quantitative Aspects of Cross Polarization

As CP was used to acquire data, multiple parameters had to be measured and optimized before quantitative SSNMR data was acquired.

3.3.2.1   Cross Polarization Dynamics

The transfer of polarization from abundant spin nuclei (^{1}H) to dilute spin nuclei (^{13}C) is a non-instantaneous process which is highly dependent on the number of protons directly bound to the dilute spin nuclei (174, 177). Depending on the time allowed for the sample to cross polarize (contact time), certain nuclei may appear to have a greater integrated intensity than is actually present (185, 234). To account for this and choose an appropriate CT, a VCT experiment was performed. CP TOSS experiments were performed in series with the CT ranging from 0.5 ms to 10.0 ms.

The rise and decay in peak intensity is displayed graphically in Figure 3.4. The intensity of different peaks can change drastically, and at different rates as a function of CT. All functional groups in patiromer reached their maximum magnetization intensity within 2 ms. However, the aliphatic peak reached its maximum quicker than the carboxylate group. Using data points at long contact times, extrapolating back to zero yields the 'true' signal intensity (234). For the carboxylate, aromatics, quaternary, and aliphatic peaks, the signal area at zero CT was 2.245, 2.548, 2.585, and 2.419 times as intense as it was for a 3 ms CT, respectively. The total signal intensity of carbon (which includes the isotropic peak and all associated SSBs) was multiplied by its appropriate ratio which better approximates the peak area of each carbon if the CP process was instantaneous.
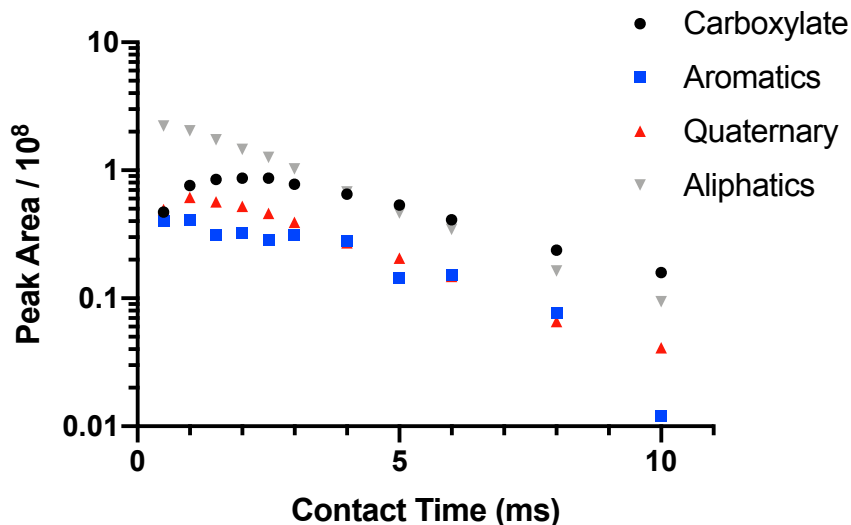
Figure 3.4. ^{13}C CP TOSS 4 kHz MAS variable contact time trends for different carbon atoms in Patiromer. The intensity scale is in arbitrary units.

3.3.2.2 Chemical Shift Anisotropy

While TOSS is useful for simplifying spectra and identifying isotropic peaks, some signal is typically lost when SSBs are suppressed (189). When integrating peaks for quantitative purposes, it is critical to include all signal, including that from SSBs. For this reason, a CPMAS spectra without TOSS was acquired to determine if significant signal intensity was contained in SSBs. As can be seen in Figure 3.5, compared to the CP TOSS spectrum, CP exhibits significant SSBs. The SSBs are particularly noticeable at 16, 207, 224, and 257 ppm. Failure to include all SSBs during peak integration would underestimate the number of carboxylate and aromatic groups present in each lot of patiromer.
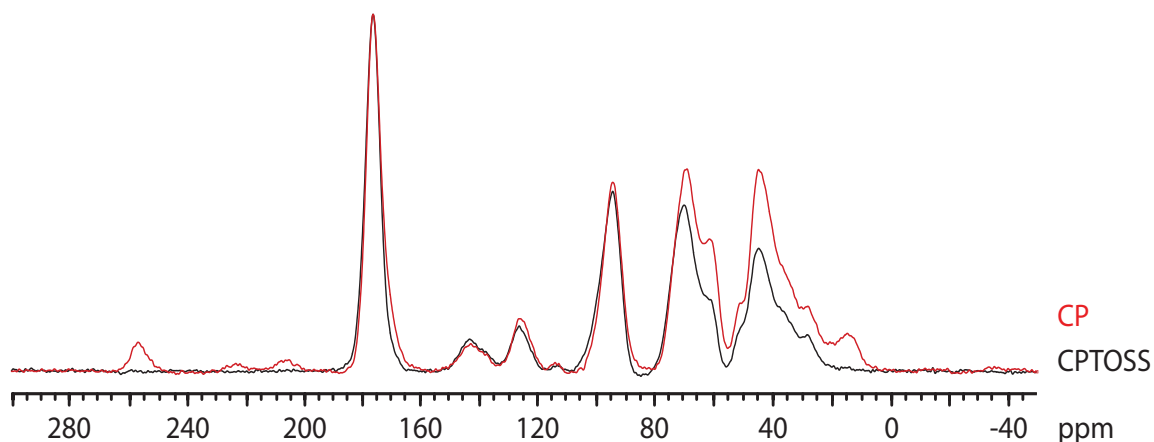
Figure 3.5. Overlaid ^{13}C CP and CP TOSS spectra at 6kHz MAS used to identify signal loss due to the use of TOSS in patiromer lot A.

Once it was identified that the patiromer spectrum contained sufficient SSBs, CP MAS spectra were acquired at varying spin speeds to determine the location and intensity of each SSB. SSBs are located on each side of the isotropic peak, and, as shown in Equation 3.3, separated by intervals directly proportional to the MAS frequency (239).

$$\text{SSB Spacing} = \frac{\text{MAS Frequency (Hz)}}{\text{Spectrometer Frequency (MHz)}} \tag{3.3}$$

As spin speed is increased, SSBs spread out and reduce in intensity relative to the isotropic peak. At speeds (frequencies) greater than the chemical shift anisotropy, SSBs are fully eliminated and all intensity is contained in the isotropic peak.

Spinning at 4 kHz, the SSBs were located approximately 53.5 ppm apart. Figure 3.6 shows that 4 kHz CP exhibits significant SSBs which overlap with other peaks. As the TOSS pulse sequence is known to reduce the absolute intensity of the isotropic peak, the contribution of the SSB relative to the peaks it overlaps with is unknown without further investigation. Spinning at 3 kHz makes SSBs more prominent yet increases the amount of

overlap in the spectral range of interest. Spinning at 6 kHz, separates carboxylate and aromatic SSBs while causing the carboxylate and quaternary SSBs to overlap.
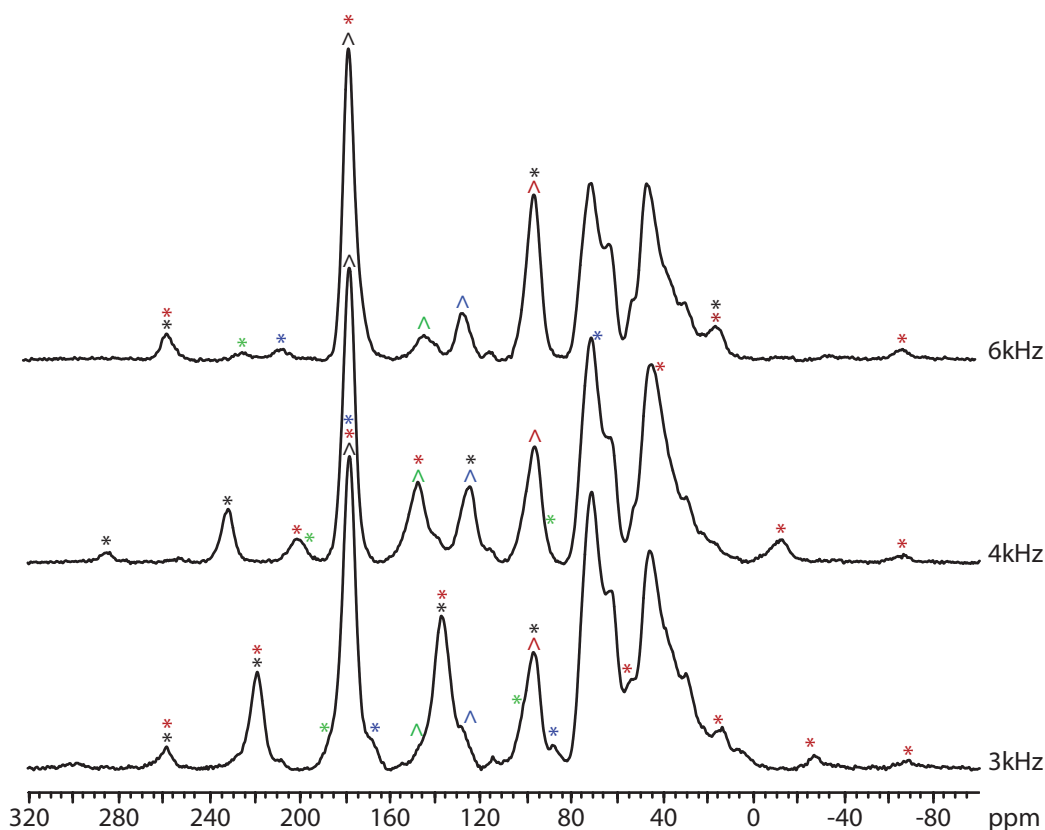
Figure 3.6. Stacked patiromer ^{13}C CP spectra acquired at varying MAS speeds used to identify the location and change in intensity of spinning sidebands. Black, green, blue, and red symbols above peaks correspond to the peaks for carboxylate, aromatic (without bound protons), aromatic, (with bound protons), and aliphatic carbons, respectively. ^ indicates the peak is the isotropic peak while * indicates a spinning sideband.

Typically, quantitative SSNMR spectra should be acquired at the fastest spin speed possible to minimize chemical shift anisotropy. However, in the current experimental set up, the 7.5 mm rotor was only able to spin to a maximum of 6.5 kHz. In order to spin faster, a switch to a 4 mm rotor was made with spin speed capabilities up to 12.5 kHz. While

spinning at 12.5 kHz eliminated all overlapping SSBs, the sensitivity was also largely reduced (data not shown). The gain in spin speed is offset by the decrease in sensitivity due to a reduced sample volume (350 mg vs. 50 mg). Within a reasonable timescale, this results in a signal-to-noise ratio inadequate for quantitative data acquisition. For this reason, the decision was made to use a 7.5 mm rotor spinning at 6 kHz for all quantitative calculations. It should be noted that in cases where potent or expensive APIs may limit the amount of drug available, the longer acquisition time may be necessary to obtain adequate quantitative data using this method.

Despite the carboxylate and quaternary SSBs overlapping at 6 kHz MAS, this spin speed was chosen for analysis as it provides good separation of other SSBs. The chemical shift of all isotropic peaks, along with any SSBs are listed in Table 3.2. Additionally, as the carboxylate and quaternary carbons only appear in the m-block of patiromer, this was not a major issue for quantitative purposes. As seen in Figure 3.6, the carboxylate and aromatic carbons express only first-order SSBs (one on each side) while the quaternary carbon also contains second-order SSBs, each of which is integrated and added to its respective isotropic peak intensity.

Table 3.2. Isotropic chemical shifts and associated spinning sidebands at 6kHz MAS.

Peak	Isotropic Chemical Shift (ppm)	Downfield 1st-Order SSB (ppm)	Upfield 1st-Order SSB (ppm)	Downfield 2nd-Order SSB (ppm)	Upfield 2nd-Order SSB (ppm)
Carboxylate	177	257	97	N/A	N/A
Aromatic (no ^{1}H)	144	224	64	None	None
Aromatic (w/ [1]H)	127	207	47	None	None
Quaternary	96	176	16	256	-64

3.3.2.3 Molecular Mobility

Certain functional groups inherently possess greater molecular mobility than others. As CP efficiency is inversely related to mobility, different functional groups may polarize to varying degrees if their molecular mobility is different (177, 240). Therefore, a patiromer (lot A) sample was cooled to -20°C using liquid nitrogen-cooled air while spinning at 4 kHz in the NMR spectrometer. This ensured that signal intensity was not lost due to mobility-induced variations in CP efficiency.

Figure 3.7 overlays patiromer spectra at two different temperatures. The spectral shape of each resonance is roughly the same, indicating that there are no major differences between the room temperature and cooled samples. When the low-temperature spectrum is normalized to the 20°C sorbitol resonance, the intensities of the carboxylate, aromatic, and quaternary carbons all increase slightly while the aliphatic intensity is approximately the same. This may indicate that the carboxylate, aromatic, and quaternary carbons possess greater mobility than the aliphatic carbons at higher temperatures. It should be noted that the TOSS parameters were not fully optimized at 20°C (evidenced by the partially folded SSB at ~230 ppm). Properly optimized TOSS parameters completely eliminate SSBs and

fold their intensity back into the centerband. In this case of suboptimal TOSS parameters, the SSBs of the carboxylate, aromatics, and/ or quaternary peaks may exist underneath other peaks and contribute to their reduced intensity at 20°C. Therefore, it may be safely assumed that mobility is not an issue when quantifying patiromer.
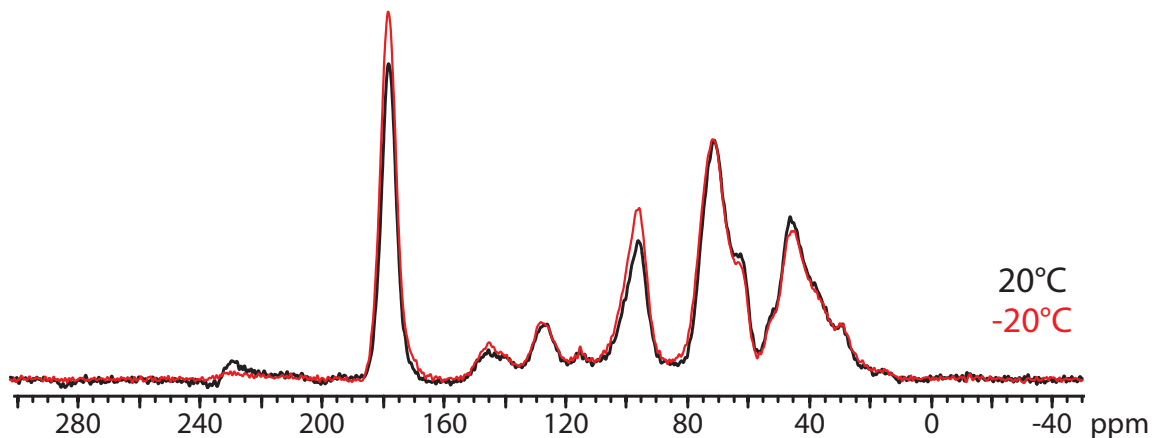
Figure 3.7. Overlaid $_{13}$C 4 kHz MAS CP TOSS spectra of Patiromer lot A acquired at different temperatures. Peak intensities were normalized to the sorbitol peak.

3.3.2.4 ^{1}H T_1 & $T_{1\rho}$ Relaxation Times

Both the ^{1}H T_1 and $T_{1\rho}$ values were calculated for different carbon atoms as part of accounting for CP dynamics. The proton spin-lattice relaxation time (^{1}H T_1) for each lot of patiromer was determined using a saturation-recovery pulse sequence. The $T_{1\rho}$ for each patiromer lot was calculated either by fitting Equation 3.2 to the results of the VCT experiment or by varying the spin-lock duration following a 90° pulse ($T_{1\rho}$ experiment) (181, 241). Table 3.3 shows the T_1 and $T_{1\rho}$ for each patiromer lot as well as for each isotropic peak in the spectrum. Aromatic $T_{1\rho}$ values (127 and 144 ppm) were not

determined as the signal-to-noise was too low in the chemical shift range to acquire accurate values.

Table 3.3. Isotropic peak ^1H T_1 and $T_{1\rho}$ values for each patiromer lot.

Lot	Dose (g)	Exp. Date		177ppm	144ppm	127ppm	95ppm	71ppm	44ppm
A	8.4	2021	T_1	1.76 ± 0.05	1.60 ± 0.09	1.41 ± 0.09	1.71 ± 0.04	1.75 ± 0.05	1.81 ± 0.10
			$T_{1\rho}$	3.01 ± 0.19			3.13 ± 0.22	3.26 ± 0.07	3.33 ± 0.15
B	16.8	2021	T_1	1.80 ± 0.04	1.48 ± 0.16	1.43 ± 0.08	1.72 ± 0.02	1.74 ± 0.03	1.75 ± 0.03
			$T_{1\rho}$	3.11 ± 0.26			3.07 ± 0.26	3.18 ± 0.15	3.01 ± 0.17
C	25.2	2020	T_1	2.18 ± 0.06	1.68 ± 0.19	1.83 ± 0.11	2.07 ± 0.06	2.16 ± 0.06	2.23 ± 0.11
			$T_{1\rho}$	3.09 ± 0.14			3.58 ± 0.37	3.21 ± 0.16	3.86 ± 0.21
D	8.4	2017	T_1	1.55 ± 0.03	1.32 ± 0.09	1.24 ± 0.09	1.42 ± 0.02	1.42 ± 0.02	1.45 ± 0.02
			$T_{1\rho}$	2.98 ± 0.30			3.69 ± 0.44	3.06 ± 0.11	3.40 ± 0.29
E	8.4	2018	T_1	1.84 ± 0.06	1.56 ± 0.15	1.53 ± 0.09	1.70 ± 0.05	1.77 ± 0.07	1.79 ± 0.09
			$T_{1\rho}$	3.36 ± 0.21			3.37 ± 0.36	3.13 ± 0.06	3.71 ± 0.19
F	16.8	2018	T_1	1.63 ± 0.03	1.32 ± 0.12	1.31 ± 0.07	1.53 ± 0.03	1.58 ± 0.02	1.56 ± 0.03
			$T_{1\rho}$	3.23 ± 0.13			3.26 ± 0.57	3.15 ± 0.17	3.45 ± 0.26
G	25.2	2017	T_1	1.61 ± 0.03	1.40 ± 0.10	1.35 ± 0.09	1.51 ± 0.02	1.52 ± 0.02	1.52 ± 0.03
			$T_{1\rho}$	3.30 ± 0.21			3.26 ± 0.49	3.05 ± 0.09	3.70 ± 0.23

The ^1H T_1 provides a measurement of the time it takes for magnetization to return to equilibrium in the sample. Other pharmaceutical systems have observed variations in T_1 linked to differences in formulation/ processing, which, in turn, has also been related to the physical stability of samples and their predicted dissolution profiles (221, 242).

In general, all peaks have similar T_1 values, indicating a homogeneous sample. However, both aromatic peaks have significantly shorter T_1 values compared to the carboxylate peak. Shorter aromatic T_1 values may simply be a result of inherently lower mobility in aromatic crosslinkers relative to other functional groups.

T_1 values were compared on a lot-to-lot basis, particularly looking at whether any changes in sample mobility were observed for different dosage strengths and/ or the expiration dates. When the dosage strength was investigated, the average T_1 value for each peak was compared across 8.4 g, 16.8 g, and 25.2 g samples. No differences were found at any peak as a function of dosage strength. However, the T_1 of each peak within a single dosage strength was not always the same. For 8.4 g (A, D, and E) and 16.8 g (B and F) lots, the carboxylate showed a significantly longer T_1 than the aromatic at 127 ppm. Similarly, in 16.8 g lots, the carboxylate had a significantly longer T_1 than both aromatic peaks while sorbitol and the aliphatic groups also had longer T_1 values than aromatic groups. No differences were observed within the 25.2 g lots (C and G).

When patiromer lots were grouped based on expiration date, there were no significant differences found for any peak, nor for any expiration year. It is interesting to note that the sorbitol T_1 decreases from 1.88 ± 0.24 s to 1.57 ± 0.15 s (mean $\pm$ SD, n = 3 and 4, respectfully) in expired samples. Concurrently, the carboxylate T_1 also decreases from 1.91 ± 0.23 s to 1.66 ± 0.13 s. If the sorbitol counterion, which is included in the last step of the API manufacturing to help stabilize the carboxylate portion of the m-block (202), begins to degrade or dissociate, it is possible that the carboxylate would exhibit enhanced mobility as evidenced through a reduced T_1.

Similar to T_1 values, $T_{1\rho}$ values were also compared based on dosage strength and expiration date. The aliphatic $T_{1\rho}$ was found to be significantly longer in 25.2 g samples than in 16.8 g samples. Additionally, the same aliphatic value was greater than any other peak in the 25.2 g lots. When the expiration date was compared, the $T_{1\rho}$ of sorbitol was significantly shorter in expired samples relative to samples which had not yet expired. In

both expired and non-expired, the sorbitol $T_{1\rho}$ was different than the carboxylate. Interestingly, in expired samples, the $T_{1\rho}$ of sorbitol was less than the carboxylate while in non-expired samples, the sorbitol $T_{1\rho}$ was greater than the carboxylate value. It is important to note that in both T_1 and $T_{1\rho}$, the small sample size can make it difficult to attribute differences in relaxation values solely to the dosage strength or expiration rather than lot-to-lot variation. Nonetheless, differences are observed in some samples.

3.3.3 Evaluation and Quantitation of Block Copolymer Species Present in Patiromer

All relevant peaks were integrated using TNMR 'Integrals.' This included downfield carboxylate (257 ppm) and aromatic (215 ppm) SSBs as well as the upfield first order quaternary/ second order carboxylate (15 ppm) and second order quaternary (-68 ppm) SSBs. Each peak was integrated with zero slope and zero offset. Second order downfield carboxylate (337 ppm) and aromatic (295 ppm) SSBs, as well as the second order upfield aromatic (-25 ppm) SSBs were not integrated as their signal-to-noise ratio was too low to be used in quantitative calculations. Each integrated peak area was normalized to the carboxylate peak (area = 1.0000).

To account for CP dynamics, the integrated peak areas of each functional group were extrapolated back to a CT of zero. Using data points at sufficiently long contact times such that the signal was only decaying, an exponential line was fit and extrapolated back to zero. The ratio of the line's y-intercept (CT = 0 ms) intensity and 3 ms CT intensity were used to scale the area of each functional group's peaks. The ratio of each functional group was also applied to its SSBs.

Each peak in Figure 3.8 was given a letter label. Table 3.4 lists each peak along with its associated carbon atom and integrated intensity while Table 3.5 lists integrated values used for quantifying each monomer block in patiromer. There are three types of carbon in the m-block contributing to the signal, corresponding to the carboxylate, fluorine-attached carbon (quaternary), and methylene (CH_2) carbon. The carboxylate and quaternary carbons were relatively well resolved compared to signals from the other blocks although at 6 kHz MAS, their SSBs overlapped with each other. However, the methylene carbon overlapped with multiple carbons from the n- and p-blocks. Therefore, to determine the amount of m-block carbons, the sum of all peaks associated with the carboxylate carbon and quaternary carbon were taken. This includes peaks A, C, F, A, and I. Peak H (15 ppm) is not counted towards the carboxylate and quaternary intensity as it is likely composed of two peaks including the carboxylate/ quaternary SSB and a portion of aliphatic peak G. Instead, peak A (257 ppm) is counted twice as it is assumed that it is of approximately the same intensity as the SSB component in peak H). The total m-block intensity (assigned peak J) is then divided by 2 to yield the average m-block signal (peak K).
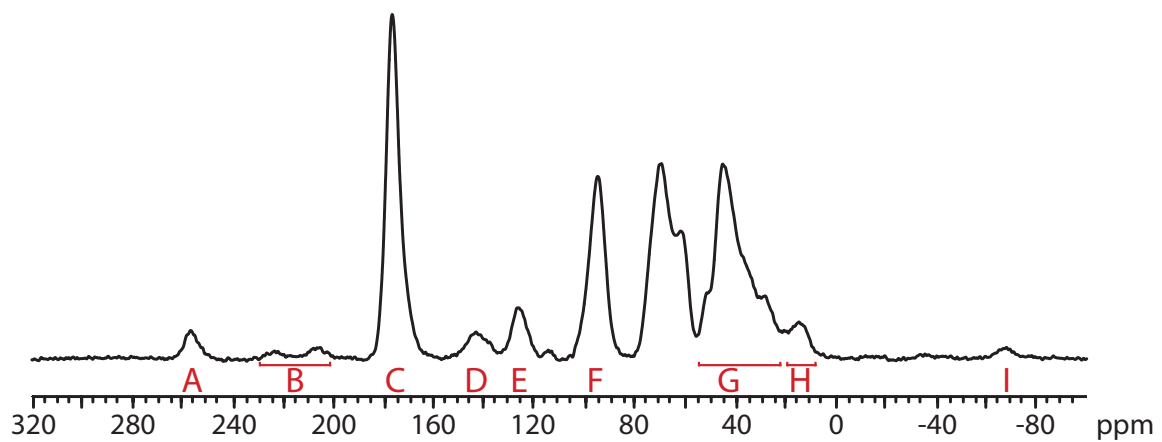
Figure 3.8. Patiromer lot A ^{13}C 6 kHz MAS CP spectrum with peaks labeled for use during the quantitation procedure.

Table 3.4. Peak identification information and integrated values used for monomer block quantitation of patiromer lot A.

Label	Peak	Chemical Shift (ppm)	Area at 3 ms CT	Area at Zero-CT	Label	Signal	Area at 3 ms CT	Area at Zero-CT
A	Downfield Carboxylate SSB	257	0.0851	0.1910	J	Total m-block	1.8220	4.3120
B	Downfield Aromatic SSB	215	0.0714	0.1819	K	Average m-block	0.9110	2.1560
C	Carboxylate	177	1.0000	2.2450	L	n- & p-block	0.3874	1.0165
D	Aromatic (no protons)	144	0.1198	0.3053	M	Average n-block	0.0718	0.1829
E	Aromatic (with protons)	127	0.1682	0.4286	N	Total n-block Backbone	0.2872	0.7318
F	Quaternary	96	0.6091	1.5745	O	Total p-block	0.1002	0.2847
G	Aliphatic	45	1.2911	3.1232	P	Average p-block	0.0125	0.0356
H	Upfield Aliphatic/ Carboxylate SSB	16	0.1341	0.3466	Q	Total m-, n-, & p-block	0.9953	2.3745
I	2nd Order Upfield Quaternary SSB	-68	0.0427	0.1104				

Next, the average signal from the n-block is determined. Peak G (45 ppm) contains the aliphatic signal for all of patiromer. Subtracting peak A from peak H eliminates the SSB signal from peak H and yields only the additional aliphatic signal contained between 15 and 20 ppm. This was added to the peak G aliphatic signal. There is also a portion of the upfield aromatic SSB that falls underneath the aliphatic peak G. This was accounted for by assuming that the downfield aromatic SSB was of equal intensity as the upfield SSB. The aromatic signal is found in two peaks, at 127 (peak E) and 144 ppm (peak D), presumably due to aromatic carbons with and without attached protons, respectively. Spinning at 6 kHz, only the SSB associated with peak E would be found underneath the aliphatic peak. Therefore, the area of peak E relative to peak D is scaled to the upfield aromatic SSB intensity and subtracted from peak G. Lastly, the average m-block signal (peak K) is subtracted from the aliphatic intensity. In total, the n- and p-block aliphatic signal is equal to $G+(H-A)-K-((E/(D+E)*B)$. This is designated as peak L.

The aromatic signal consists of the two aromatic peaks (D and E), the downfield aromatic SSB (B), and the upfield SSB (assumed to be of equal intensity as peak B). To find the average aromatic signal in the n-block, the sum of B, D, E, and B is divided by six to account for the 6 aromatic carbon nuclei present in the benzene ring. The resulting value is assigned as peak M.

In addition to the six aromatic carbons, the n-block also contains four backbone aliphatic carbons. Therefore, peak M is multiplied by four to determine the aliphatic signal in the n-block (peak N). Subtracting the n-block aliphatic signal (N) from the total aliphatic signal (L) yields the total aliphatic signal of the p-block (peak O). Peak O is divided by

eight to account for the 8 aliphatic carbons in the p-block. This yields the average p-block aliphatic signal and is designated as P.

The last step in the quantitation procedure involves dividing the average signal from each patiromer block by the sum total of the carboxylate (K), aromatic (M), and aliphatic (P) signals. The total signal from the analyzed patiromer is designated as Q (K+M+P). Therefore, the relative amounts of carboxylate, aromatic, and aliphatic blocks present are found by K/Q, M/Q, and P/Q, respectively.

3.3.3.1 Example Quantitation Calculations for Lot A

As described above, all peaks were integrated and normalized to the carboxylate peak. Table 3.4 contains all peak labels and the normalized signal intensity values for lot A. Using the signal ratios from CT extrapolated to zero (Figure 3.4), the carboxylate peak and its SSBs were multiplied by 2.245, the aromatic peaks and its SSBs were multiplied by 2.548, and the quaternary peak and its SSBs by 2.585. Similarly, the aliphatic peak was multiplied by 2.419. Therefore, when corrected for CT, the m-, n-, and p-blocks had average signals of 2.1560, 0.1829, and 0.0356, respectively.

Taking the ratio of each block's signal to the total signal gives the relative amount of each species present. Patiromer lot A was found to contain 90.8% m-block, 7.7% n-block, and 1.5% p-block. This compares well with the manufacturer-reported values of 91% m-block and a combined total of 9% n- and p-block (208). In addition to confirming the previously reported amount of m-block (the potassium-binding polymer block) present, this also provides the relative amounts of the n- and p-blocks (crosslinkers) which was not previously reported.

3.3.3.2 Theoretical Quantitative Values

Patiromer patent literature suggests that based on the specific polymerization procedure used, various amounts of the crosslinker components divinylbenzene and 1,7-octadiene (starting monomer components of the n- and p-blocks, respectively) could be used in the polymerization of patiromer (223, 243, 244). Depending on the results of the polymerization process, different amounts of the n- and p-blocks would be expected to be found in the final product. If the polymerization was 100% efficient, all divinylbenzene and 1,7-octadiene would incorporate into patiromer and the n- and p-blocks would show signal intensities corresponding to the amount of each monomer present in the polymerization reagents. If the polymerization is not completely efficient or favors the incorporation of one molecule relative to the other, the n- and p-block intensities will vary in the final product.

Ideally, standards of known n- and p-block contents would be synthesized and analyzed, however, this is not possible. In the absence of patiromer standards, calculations were used to verify the relative quantitative values obtained are in line with results for a theoretical patiromer standard of similar crosslinker composition. Table 3.5 shows the theoretical normalized signal intensities that would be expected for patiromer formulated with a constant amount of m-block (91%) and varying amounts of n- and p-blocks (9% total).

Table 3.5. Theoretical signal intensities for patiromer (at 91% m-block and 1x Signal at 0.91) with varying n- and p-block compositions.

n (%)	Signal (x4)	p (%)	Signal (x8)	Total (n & p) Signal
0	0.00	9	0.72	0.72
1	0.04	8	0.64	0.68
2	0.08	7	0.56	0.64
3	0.12	6	0.48	0.60
4	0.16	5	0.40	0.56
5	0.20	4	0.32	0.52
6	0.24	3	0.24	0.48
7	0.28	2	0.16	0.44
8	0.32	1	0.08	0.40
9	0.36	0	0.00	0.36

If patiromer contained equal amounts of n- and p-blocks (4.5% each), their total signal would be approximately 0.18 and 0.36, respectively. Conversely, a sample with 9% n-block and no p-block would show an n-block signal of 0.36. As is seen in Table 3.4, the observed total n-block signal is 0.2872 (peak N) and total p-block signal is 0.1002 (peak O). This corresponds to theoretical values of 7-8% n-block and 1-2% p-block, which agrees well with the reported values in all analyzed patiromer lots. The theoretical exercise above aids in validating the method proposed herein. Furthermore, as different patiromer lots are presumed to contain identical monomer compositions, analyzing multiple lots of should yield similar quantitative results and further validate the proposed method.

3.3.4　Lot-to-lot Variation in Patiromer Samples

In order to validate the new SSNMR methodology on multiple lots, six additional patiromer lots were run under identical SSNMR parameters (6 kHz CP MAS, 10 s PD, 3 ms CT, 64 kHz ^{1}H-decoupling, 4096 scans, and 512 acquisition points). To look at any differences that may exist between lots, the stacked spectra of each lot are shown in Figure 3.9.
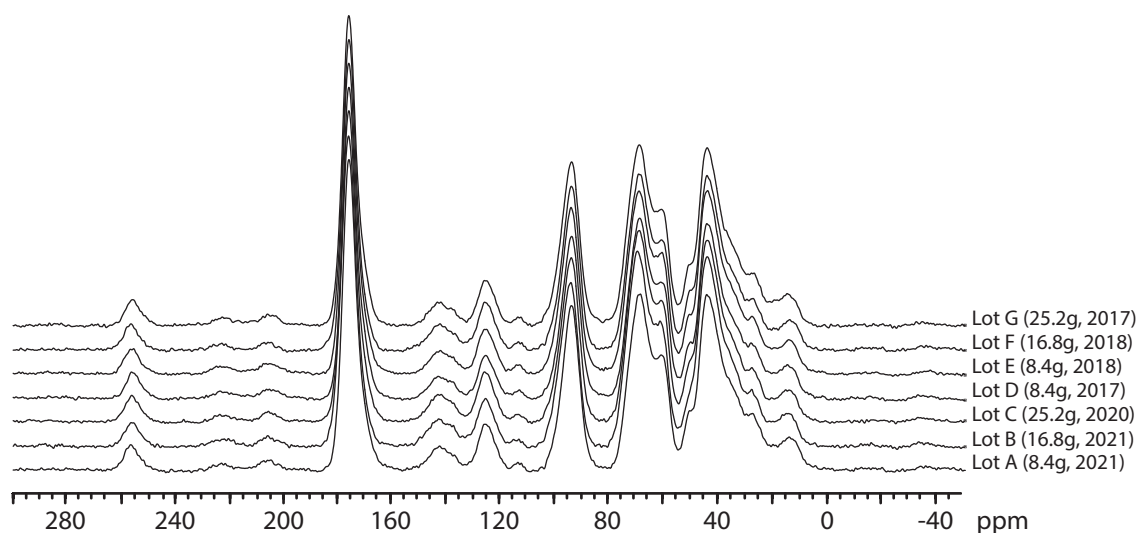
Figure 3.9. Stacked ^{13}C 6 kHz MAS spectra for all patiromer lots. Lot, dosage strength, and expiration date are listed next to each spectrum. Peak intensities are normalized to the carbonyl in lot A.

The stacked spectra show that each lot has the same peaks at the same chemical shift values. As expected, each lot shows a single carboxylate peak (177 ppm), two aromatic peaks (144 and 127 ppm), one quaternary peak (96 ppm), a broad aliphatic peak (45 ppm), and the appropriate SSBs. Each lot also shows a sorbitol counterion peak between 60 and 80 ppm. The intensity of each isotropic peak and SSBs are approximately the same. In

order to look more closely at the subtle differences between lots, the normalized spectra of different lots were overlaid (Figures 3.10A and 3.10B).
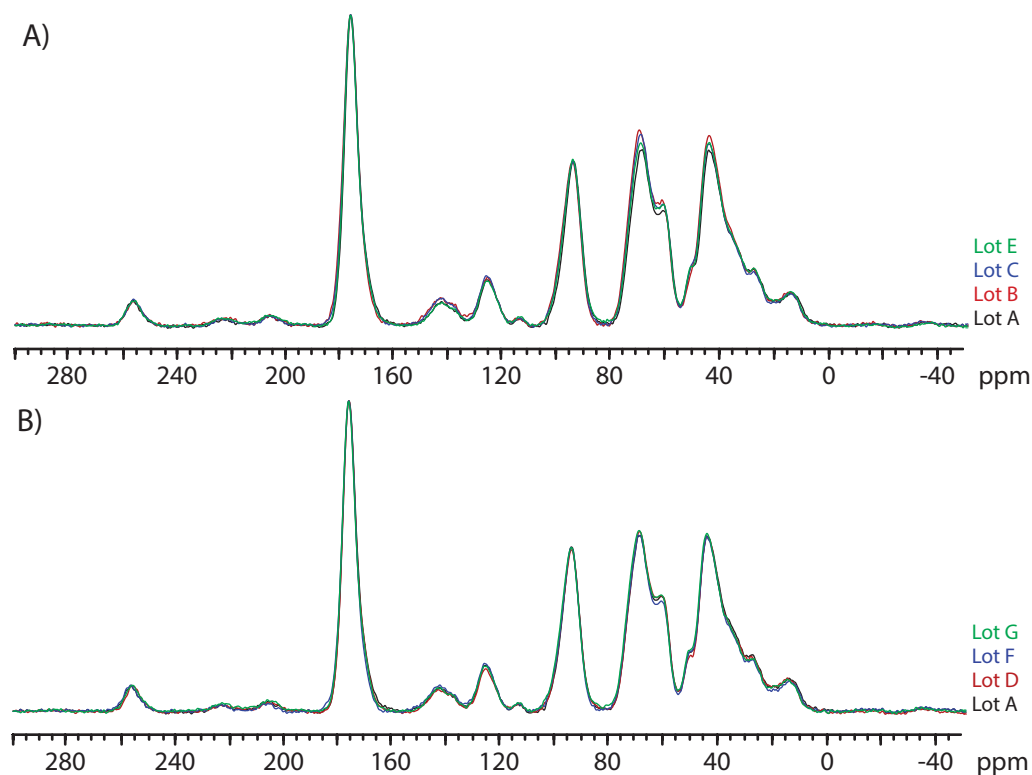
Figure 3.10. Overlay of ^{13}C 6 kHz MAS CP spectra for patiromer lots. (A) Lots A, B, C, and E. (B) Lots A, D, F, and G. All peaks in the figure were normalized to the carbonyl intensity of lot A.

The overlaid spectra help to confirm the results of the quantitation procedure that all patiromer lots contain approximately the same relative amounts of each block copolymer (Table 3.6). The average was 90.9 ± 0.4% m-block, 7.6 ± 0.3% n-block, and 1.5 ± 0.4% p-block (mean ± SD, n = 7). Similar to the results of lot A, this compares remarkably well with reported values of m-blocks while adding the additional information of the relative amounts of n- and p-blocks. This is especially important from a quality

control standpoint in that the final product contains a consistent amount of the physiologically active polymer (m-block) and each crosslinker (n- and p-blocks) as the total (9.1%) and relative (7.6% and 1.5% n- and p-block, respectively) crosslinker content controls the degree of swelling when exposed to water or gastrointestinal fluid (223).

Table 3.6. Relative amounts of each block copolymer in different patiromer lots.

Lot	Dose	Expiration	m-block (%)	n-block (%)	p-block (%)
A	8.4	2021	90.8	7.7	1.5
B	16.8	2021	90.2	7.9	1.9
C	25.2	2020	90.9	7.7	1.4
D	8.4	2017	91.2	7.2	1.7
E	8.4	2018	90.4	7.7	1.9
F	16.8	2018	91.4	7.4	1.2
G	25.2	2017	91.2	8.0	0.9
Average			90.9 ± 0.4	7.6 ± 0.3	1.5 ± 0.4

As the m-block contains both the carboxylate and quaternary groups, the intensity of the quaternary peak in all lots is also approximately identical. Similarly, the aromatic peaks at 144 and 127 ppm only show slight variations which are mostly reflected in the quantified n-block values in Table 3.6. The largest differences between spectra occur in the aliphatic block, particularly in Figure 3.10A. Of the non-expired samples (A, B, and C), lot B shows the highest intensity aliphatic peak and highest p-block value in Table 3.6 (1.9%) while lot A shows the least intense peak and only 1.5% p-block. Of the expired lots in Figure 3.10B, most variation is found near 30 and 50 ppm. This is reflected in variable p-block values for expired lots in Table 3.6. It should be noted that, as described in the

quantitation procedure, the p-block is determined by the difference between the combined aliphatic signal in the n- and p-blocks and the aliphatic signal contained only in the n-block. This inherently results in the p-block values having the most uncertainty as any errors in measuring/ calculating the m- and n-blocks is also contained in the p-block calculation.

The quantitative differences discussed above could be a result of testing different dosage strengths and/ or samples of varying expiration dates. Tables 3.7 and 3.8 look at quantitative differences in composition of patiromer as a function of the dosage strength and expiration date, respectively. It should be noted that with a small sample size, it is difficult to analyze the effect of dosage strength independent from the lot as each patiromer lot is only produced at a single strength. Furthermore, each sample was analyzed at a single time point rather than continuously analyzed over the course of its shelf-life and beyond which complicates whether spectral differences result from lot variation or expiration. Nonetheless, while there are slight differences in the average relative amounts of each copolymer present in various dosage strengths and lots with different expiration years, these differences are not significant.

Table 3.7. Average relative amounts of each block copolymer in different strength lots.

Dose (g)	m-block (%)	n-block (%)	p-block (%)
8.4 (n=3)	90.8 ± 0.4	7.5 ± 0.3	1.7 ± 0.2
16.8 (n=2)	90.8 ± 0.8	7.6 ± 0.4	1.6 ± 0.5
25.2 (n=2)	91.1 ± 0.2	7.8 ± 0.2	1.2 ± 0.4

Table 3.8. Average relative amounts of each block copolymer in different expiration date lots.

Expiration	m-block (%)	n-block (%)	p-block (%)
2017 (n=2)	91.2 ± 0.0	7.6 ± 0.6	1.3 ± 0.6
2018 (n=2)	90.9 ± 0.7	7.6 ± 0.2	1.5 ± 0.5
2020 (n=1)	90.9 ± 0.0	7.7 ± 0.0	1.4 ± 0.0
2021 (n=2)	90.5 ± 0.4	7.8 ± 0.1	1.7 ± 0.3

Additionally, the spectral differences between each lot could also be caused by a variety of other phenomena. Variations in temperature would likely have the most profound impact on signal intensities due to increased mobility at higher temperatures. However, extensive care was taken to ensure the temperature of the spectrometer was consistent between runs. Each sample was given adequate time to equilibrate to 20°C prior to spectral acquisition. In addition, a spectrum acquired at -20°C was found to not significantly effect quantitative procedure. Instrumental variations (variable MAS rate, the magic angle not being precisely set, different CP parameters, etc.) could also have an effect on differences seen between spectra. The spectrometer was calibrated prior to each sample change to ensure experimental conditions were consistent between each lot. Therefore, the variations observed are likely within the uncertainty of measurement.

3.4 Conclusion

Polymers with multivalent structures and high binding capacities are becoming more prevalent as polymeric APIs, particularly as sequestering agents. However,

polymeric drugs, particularly insoluble formulations, do not fall into traditional small molecule or biologic drug categories which have well-established analytical techniques. Therefore, there is a significant need to develop new analytical methods for the quantitative characterization and analysis of insoluble polymeric drug products. Patiromer (Veltassa®) is one such drug product containing three monomer units and calcium-sorbitol counterion. Controlling the relative amounts of each type of monomer incorporated in patiromer is critical for maintaining the quality standard and therapeutic effect. A novel SSNMR method was developed and validated for quantifying the relative amounts of each monomer present in different patiromer lots.

Various ^{13}C-SSNMR techniques were used to account for CP dynamics and ensure that quantitative data was acquired. From this, a quantitation procedure was developed by integrating the peaks of all functional groups and their associated SSBs. The signal attributed to each polymer block was normalized for the number of carbon nuclei present and compared to the total signal to yield quantitative values.

The average patiromer sample analyzed contained $90.9 \pm 0.4\%$, $7.6 \pm 0.3\%$, and $1.5 \pm 0.4\%$ m-, n-, and p-block, respectively. The results agree very well with values reported in the package insert while providing previously unpublished data in the relative amounts of n- and p-block rather than the total between the two monomers. To validate the method, theoretical calculations were performed, and the results compared to seven different patiromer lots, including three dosage strengths and four expired samples. Little to no differences existed between different dosage strengths or expiration date and the calculations agreed well with experimental results. Only slight lot-to-lot variations existed

between the relative amounts of each block copolymer present in each lot, likely caused by the inherent uncertainty of measurement.

Overall, SSNMR was found to yield good quality quantitative data which agrees will with literature values. If all aspects of CP dynamics are accounted for, SSNMR and the quantitative method reported herein can be used to accurately quantify intact patiromer. Adaptation of this method can be used to establish API sameness during generic drug development, or as a tool for the advanced characterization and analysis of other complex polymeric drug products. While this method works best for non-material-limited samples, it may also be applied using much smaller amounts of drug, albeit with the cost of longer experimental times.

CHAPTER 4: COMPARISON OF DIFFERENTIAL SCANNING CALORIMETRY, POWDER X-RAY DIFFRACTION, AND SOLID-STATE NUCLEAR MAGNETIC RESONANCE SPECTROSCOPY FOR MEASURING CRYSTALLINITY IN AMORPHOUS SOLID DISPERSIONS – APPLICATION TO DRUG-IN-POLYMER SOLUBILITY

4.1   Introduction

The majority of drug candidates under development are poorly water soluble (3, 4). Amorphous formulations are seen as a viable approach for improving the solubility of many biopharmaceutical classification system (BCS) class II and IV drugs (2). Amorphous solid dispersions (ASDs) are formed through the intimate mixing of drug and polymer to help to improve the physical stability of amorphous drugs while also maintaining improved solubility relative to the crystalline state. Still, the number of ASDs on the market is limited, likely due to the amorphous drug's potential for devitrification which can also impact bioavailability (245, 246).

The amorphous state is inherently higher in energy than the crystalline state. Because of this, amorphous drugs are often limited by their physical instability (i.e., tendency to recrystallize) (66). Characterization and quantification of the amorphous and potential crystalline phases is a necessary part of amorphous pharmaceutical development. The difference in energetics between the crystalline and amorphous forms

---

leads to vast differences in the physicochemical properties, stability, and in vivo performance of the two phases.

Most ASD formulations begin with a crystalline drug which is transformed to the amorphous state through varying process unit operations. Crystals may remain as residual crystals from unoptimized processing conditions or form during ASD storage and can affect the stability of different formulations (247). An adequate knowledge of the processing parameters is required to keep crystallinity below levels that are detrimental to product performance.

Moseson and Taylor demonstrate how the hot melt extrusion (HME) operating space impacts initial levels of crystallinity as well as the analytical methods available to quantify them (248). Crystals present in the initial formulation may also induce secondary nucleation and additional crystal growth. Haser et al. showed that ASDs produced by spray drying and HME had varying levels of initial crystallinity which also directly affected the extent of subsequent crystallization during storage (249).

Increasing levels of crystallinity negatively impact ASD in vitro dissolution rate, absorption, and bioavailability (250). Commercially available tacrolimus formulations showed varying crystallization kinetics which directly impacted their dissolution performance (251). Tacrolimus tablets increasingly failed USP dissolution tests I and II with increasing levels of crystallinity (250). However, the absolute amount of crystallinity in different dispersions does not necessarily indicate the effect on product performance. The same study by Haser et al. went on to suggest that spray dried dispersions containing higher levels of crystallinity may still perform better than HME during dissolution (249). Que et al. demonstrated that the impact on dissolution performance for equivalent amounts

of crystallinity is largely dependent on the crystal morphology (252). Purohit et al. found that endogenously formed crystals had less of an impact on dissolution than physical mixtures created to simulate residual crystallinity (253). Both studies underscore the importance of crystal properties on dissolution and the need to both characterize and quantify crystals present to determine their impacts on drug delivery. Furthermore, it has been shown that while increasing crystallinity leads to increasingly poor in vitro dissolution and absorption, it has varying effects in vivo. In fact, celecoxib-polyvinylpyrrolidone ASDs with up to 20% crystallinity were nearly bioequivalent to crystalline-free ASDs when dosed in rats (254).

Multiple techniques currently exist for characterizing and quantifying crystallinity. Differential scanning calorimetry (DSC), powder X-ray diffraction (PXRD), solid-state NMR (SSNMR), Raman spectroscopy, dynamic vapor sorption, solution calorimetry, isothermal microcalorimetry, dynamic mechanical analysis, Fourier-transform infrared spectroscopy, near-infrared spectroscopy, thermally stimulated current spectroscopy, and inverse gas phase chromatography have all quantified crystallinity at low levels in pharmaceutical systems (255). In particular, DSC, PXRD, SSNMR, and Raman are often applied to multi-component systems with PXRD and SSNMR being better suited to detect and quantify crystallinity in drug formulations relative to DSC (133, 185, 255).

DSC, PXRD, and SSNMR quantify the amount of crystalline and amorphous material using different properties associated with the material. For example, DSC measures changes in heat flow upon heating the material. Crystalline and amorphous phases react differently to changes in temperature where the magnitude of heat flow associated with various thermal events is directly related to the amount of a specific phase

present. The glass transition temperature (T_g) is related to the amount of an amorphous phase present and is usually an easily accessible parameter used to determine crystallinity. Even within DSC, variables other than T_g may be used to quantify crystallinity. The heat of fusion (ΔH_{fus}) or heat of dissolution (ΔH_{diss}) correspond to the crystalline phase rather than T_g, which corresponds to the amorphous phase (256, 257). Any crystalline drug present after annealing will dissolve back into the polymer upon reheating the ASD through the drug's melting point. Comparing ΔH_{diss} to ΔH_{fus} should, in theory, also yield drug crystallinity in the sample. However, using DSC for crystallinity measurements can be time-consuming and is reliant on the sensitivity of the calorimeter for detecting and quantifying crystals in a polymer matrix.

PXRD detects molecular order by differences in a materials interaction with X-ray radiation and is a powerful technique for detecting and quantifying crystals (133). Constructive interference occurs when X-rays diffracting off crystalline phases satisfy Bragg's law at a given incidence angle and is observed as sharp diffraction peaks. Amorphous regions of short-range molecular order do not satisfy Bragg's law and result in featureless 'halo' diffraction patterns. The diffraction intensity of the crystalline and amorphous phases is directly proportional to their respective fractions in the sample (258). The magnitude of diffraction can be measured either as peak intensity or integrated peak area and can be compared for a single peak, multiple peaks, or the entire diffraction range (whole powder pattern). Peak intensity or integrated peak areas are commonly used for the quantitation of single- or multi-component mixtures however whole pattern techniques may also be used to minimize the effects of preferred orientation which is common in small molecule pharmaceutical crystals (259).

SSNMR utilizes the signals from nuclei in the crystalline and amorphous phases and is an inherently quantitative technique because the response function of the signals from nuclei are the same regardless of phase. In other words, the integrated crystalline and amorphous peak areas of ^{13}C SSNMR spectra acquired with direct polarization are directly proportional to the amount of crystalline and amorphous content in the system, respectively. However, direct polarization pulse delays rely on ^{13}C T_1 relaxation times which are extremely long and typically hinder its use for quantitation. Cross polarization (CP) may also be used quantitatively provided that relaxation rates, CP dynamics, and the Hartmann-Hahn conditions are accounted for during data acquisition (189). Aside from integration, chemometric and relaxation-based methods can also be used to quantify mixtures, including crystalline versus amorphous (260). For example, the difference in ^{1}H T_1 relaxation times between crystalline and amorphous phases has been used for quantifying crystallinity. Direct exponential curve resolution algorithm (DECRA) is a chemometric method which quickly resolves mixtures into the weighted fractions of their pure components (261). Quantitative signal-filtering methods have also been proposed to isolate the crystalline signal in samples with overlapping resonances where deconvolution is difficult (262).

Another benefit to determining crystallinity is the measurement of drug-in-polymer solubility. Up to this point however, DSC has been almost exclusively used for these solubility measurements. Solubility measurement using DSC is a time-consuming procedure, is limited to certain systems which can accurately measure/ detect T_g or melting, and often requires additional heating of the sample, all of which can limit its applicability.

Development of a robust quantitative crystallinity method using analytical methods more sensitive than DSC may also be applied to improve drug-polymer solubility measurements.

Despite the importance of crystallinity in ASDs, little has been done outside of DSC to investigate the limitations of its measurement and application to drug-in-polymer solubility. There is a clear need to investigate different analytical techniques for their ability to quantify crystallinity as well as how external factors affect its measurement. Therefore, this chapter was designed to evaluate the ability of DSC, PXRD, and SSNMR to quantifying crystallinity in a single ASD system crystallized under different conditions. Specifically, the effects of drug loading, temperature, and annealing conditions on the quality of crystals formed were investigated as it pertains to the ability of a given analytical method to quantify crystallinity.

Nifedipine (NIF) and polyvinylpyrrolidone (PVP) K12 were chosen as a model drug-polymer system to compare techniques for quantifying ASD crystallinity. NIF is a poorly soluble drug which crystallizes relatively quickly and has been studied extensively for solubility-enhancing techniques. PVP is commonly used in polymeric ASDs due to its high aqueous solubility and crystallization inhibition properties. Together, NIF and PVP have shown to form miscible dispersions ideal for studying ASD physical stability (85). NIF-PVP presents a nearly ideal system to study recrystallization as it exhibits fast crystallization kinetics, displays a single, well-resolved T_g, and crystallizes into a single polymorph.

In this chapter, ASD crystallinity was quantified and compared using five different methods across three analytical techniques including DSC (T_g and ΔH_{diss}), PXRD (full powder pattern integration), and SSNMR (peak deconvolution and T_1 relaxation). The

results were then used to determine drug-in-polymer solubility. Initially amorphous ASDs of varying drug loadings were partially crystallized using in-situ (DSC) and ex-situ (oven) annealing methods. We report that in-situ and ex-situ annealing methods yielded equal amounts of crystallinity given sufficient annealing times. Despite its widespread use in the literature, both DSC techniques (T_g or ΔH_{diss}) struggled to accurately quantify crystallinity for ASDs containing high initial drug loadings. PXRD and SSNMR provided consistently accurate quantitative results even at high drug loadings. The SSNMR relaxation time method found that changes in the crystalline material (shown as changes in ^{1}H T_1) as a function of annealing temperature must be accounted for to accurately quantify crystallinity and helps to explain the shortcomings of enthalpy-based DSC quantitation methods. The results of the comparative crystallinity study may be directly applied for drug-in-polymer solubility measurements. This is the first report of SSNMR and PXRD being used for determining drug-in-polymer solubility. They have the potential to greatly expand the number of systems by which drug and polymer solubility can be measured. The advantages and limitations of each proposed technique are discussed, and it is found that SSNMR and PXRD each provide valuable information to better inform formulation development which would otherwise be missed using DSC. In situations where the DSC recrystallization method fails, PXRD or SSNMR techniques are proposed to enhance the characterization of ASDs and expand the options of formulations scientists for designing stable ASDs.

4.2 Materials and Methods

4.2.1 Materials

Nifedipine (lot YT4QE-BP) was purchased from TCI Americas (Portland, OR) and was used as received. Polyvinylpyrrolidone K12 (lot 0001970609) was kindly donated from Ashland Global (Covington, KY) and dried $\geq$ 18 hours under vacuum at 75°C prior to use. Figure 4.1 shows the chemical structures of NIF and PVP.

Nifedipine (NIF)   **Polyvinylpyrrolidone (PVP)**
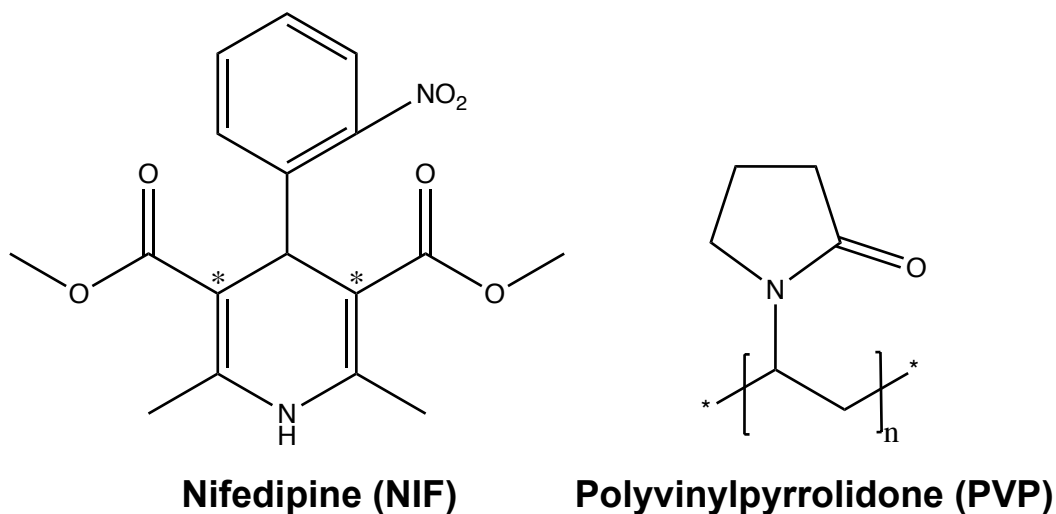
Figure 4.1. Chemical structures of nifedipine and polyvinylpyrrolidone. (* indicates the carbon atoms used for SSNMR quantitation).

4.2.2 Preparation of Amorphous Solid Dispersions

A melt-quench procedure was used to create ASDs of varying NIF contents. 70-30, 80-20, and 90-10 (% w/w) physical mixtures of nifedipine and dried PVP K12 were cryomilled at 10 Hz using a SPEX 6875 cryogenic grinder (SPEX SamplePrep LLC, Metuchen, NJ). A 5 min precool was following by 10 cycles of 2 min grinding and 2 min cooling at -196°C. The powdered sample was melted at 180°C for 5 min, quench-cooled in liquid nitrogen, then lightly ground using a mortar and pestle. The resulting ASD was dried for a minimum of 18 hr under vacuum at 25°C. Each ASD was annealed at elevated

temperatures in an oven or in the DSC to approach equilibrium through NIF crystallization. Table 4.1 summarizes each method used for quantifying crystallinity in ASDs and its corresponding abbreviation.

Table 4.1. Crystallinity quantitation methods.

Method Abbreviation	Annealing Mechanism	Analytical Technique	Description/ Variables Measured
OvTg	Oven	DSC	T_g (Gordon-Taylor equation)
OvHd	Oven	DSC	Heat of dissolution
DSCTg	DSC	DSC	T_g (Gordon-Taylor equation)
DSCHd	DSC	DSC	Heat of dissolution
PXRD	Oven	PXRD	Full powder pattern integration
NMRDec	Oven	SSNMR	Peak deconvolution
NMRT1	Oven	SSNMR	Biexponential T_1 measurement

4.2.3 Oven Annealing of Samples – Methods OvTg and OvHd

To ensure sample handling/ preparation was consistent between analytical methods, all samples were annealed together for a given annealing temperature (T_a). Powdered ASD samples were spread thinly over a flat aluminum weigh boat and placed into a dry oven between 130 and 160°C for at least 2 hours (methods OvTg and OvHd). Samples were

removed, lightly ground with mortar and pestle and stored over desiccant at -23°C until analysis by DSC, PXRD, or SSNMR.

4.2.4   Differential Scanning Calorimetry – Methods DSCTg and DSCHd

The T_g and ΔH_{diss} (methods DSCTg and DSCHd, respectively) of all samples were determined using a Discovery DSC 2500 (TA Instruments, New Castle, DE). (All DSC performed herein used modulation and will be referred to simply as DSC). The system was nitrogen purged at 50 mL/min and equipped with a RCS90 refrigerated cooling system. The DSC was calibrated for temperature and heat capacity using indium and sapphire standards, respectively. 3-4 mg of sample was loaded into a Tzero aluminum pan with a hermetic pinhole lid. Freshly prepared samples underwent a heat-cool-heat cycle in which they were heated at 5°C/min with modulation (+/- 0.7°C every 40 s) from 20°C to the T_a (130-160°C) and held for at least 2 hr. The sample was then cooled at 30°C/min to 0°C, held for 5 min, and reheated to 185°C at 5°C/min. Samples previously annealed in the oven were only scanned from 20°C to 185°C using the same heating rate and modulation (methods OvTg and OvHd).

A step-change in the baseline of the reversing heat flow signal indicated the glass transition. Reported T_g values correspond to the midpoint of the T_g. Methods OvTg and DSCTg used the measured T_g and the GT equation (76) to determine the weight fraction of amorphous NIF remaining in the ASD (X_{NIF}) (Equation 4.1).

$$X_{NIF} = \frac{K\left(T_{g,PVP} - T_g(X_{NIF})\right)}{K\left(T_{g,PVP} - T_g(X_{NIF})\right) - T_{g,NIF} + T_g(X_{NIF})} \tag{4.1}$$

$T_g(X_{NIF})$ is the glass transition temperature of an ASD at a given NIF-loading. $T_{g,PVP}$ and $T_{g,NIF}$ are the glass transition temperatures of pure PVP and pure NIF, respectively. K is the ratio of change in heat capacity for PVP and NIF at their respective T_g's.

Equation 4.2 compares the amount of amorphous NIF that remains after annealing (X_{NIF}) to the initial amorphous NIF-loading ($X_{NIF}^{initial}$) to determine the NIF crystallinity (X_C).

$$X_C = 1 - \frac{X_{NIF}\left(1-X_{NIF}^{initial}\right)}{X_{NIF}^{initial}(1-X_{NIF})} \tag{4.2}$$

Upon further heating, the reversing and non-reversing heat flow signals were used for ΔH_{diss} measurements. The endothermic reversing heat flow signal was integrated from approximately 125°C to 175°C while a running integral was performed on the non-reversing heat flow signal from just after T_g to slightly above the melting/ dissolution event. Subtraction of the non-reversing integral from the reversing integral corrects for any additional crystallization occurring upon heating to yield the pure NIF heat of fusion (ΔH_{fus}) or NIF-PVP ASD heat of dissolution (ΔH_{diss}). Using Equation 4.3, methods OvHd and DSCHd take the ratio of ΔH_{diss} to ΔH_{fus} to determine NIF crystallinity (X_C).

$$X_C = \frac{\Delta H_{diss}}{\Delta H_{fus}} \tag{4.3}$$

From Equation 4.3, the fraction of amorphous NIF remaining in the ASD can also be determined where $X_{NIF}^{initial}$ and X_{PVP} are the initial fractions of amorphous NIF and PVP in the ASD, respectively (Equation 4.4).

$$X_{NIF} = \frac{X_{NIF}^{initial}(1-X_C)}{X_{NIF}^{initial}(1-X_C)+X_{PVP}} \tag{4.4}$$

4.2.5   Powder X-ray Diffraction – Method PXRD

Powder X-ray diffraction patterns were obtained using a Rigaku SmartLab diffractometer (Rigaku Americas, The Woodlands, TX). 135-140 mg of oven-annealed sample was placed on a glass sample holder and scanned from 5-50°C 2θ at 2°/min and

0.02° step size. The diffractometer was operated at 40kV and 44mA in Bragg-Brentano mode with a Cu-Kα radiation source and d/tex ultra detector. As the samples investigated using PXRD were sensitive to preferred orientation, the entire 2θ range was used for the quantitative analysis to help minimize this effect. Instrumental background intensity was subtracted from the observed diffraction intensity. The remaining amorphous area (A_{halo}) was subtracted from the corrected intensity to yield only sharp peaks (total crystalline area, A_{peaks}). ASD crystallinity was determined by dividing A_{peaks} by the total diffraction intensity. Equation 4.5 corrects for the initial fraction of amorphous NIF in the ASD ($X_{NIF}^{initial}$) to yield the drug crystallinity.

$$X_C = \frac{A_{peaks}}{X_{NIF}^{initial}(A_{peaks}+A_{halo})} \tag{4.5}$$

Likewise, the weight fraction of amorphous NIF remaining in the ASD after annealing (X_{NIF}) was solved via Equation 4.6.

$$X_{NIF} = \frac{X_{NIF}^{initial}-X_C}{1-X_C} \tag{4.6}$$

4.2.6   Solid-state Nuclear Magnetic Resonance Spectroscopy – Methods NMRT1 and NMRDec

Method 4 used ^{13}C solid-state NMR experiments performed either on a Bruker Avance 400 (Bruker Corporation, Billerica, MA) or Tecmag Redstone HF3 2RX (Tecmag Inc., Houston, TX) spectrometer operating at a ^{1}H resonance frequency of 399.66 MHz or 300.05 MHz, respectively. The same oven-annealed sample used in methods OvTg, OvHd, and PXRD were used for SSNMR analysis. The Bruker spectrometer used approximately 200 mg of powdered sample packed into a 6 mm zirconia rotor with Teflon of Kel-f

endcaps while the Tecmag used 300 mg packed into a 7.5 mm rotor. Each spectrum was acquired using cross polarization (CP) (174), total sideband suppression (TOSS) (171), magic angle spinning (MAS) (169) at 4 kHz, SPINAL64 decoupling (237) with an approximately 62.5 kHz (Bruker) or 61 kHz (Tecmag) ^{1}H decoupling field and 1.5 ms contact time (CT). The methyl peak of an external standard, 3-methylglutaric acid, was referenced to 18.84 ppm to optimize spectrometer properties (238).

Deconvolution of CP TOSS spectra was performed for 80-20 ASDs (method NMRDec). Each CP TOSS spectra was acquired on the Tecmag spectrometer with 4096 acquisition points and a PD approximately 5 times the crystalline T_1 (*vide infra*) for at least 24 hours. This ranged from 616 scans at a 140 s PD to 1024 scans at an 86s PD. Overlapping crystalline and amorphous peaks were deconvoluted using MestReNova version 14.2 (Mestrelab Research S.L., Santiago de Compostela, Spain). Amorphous and crystalline line shapes (isotropic chemical shift, width at half-max, and Lorentzian/ Gaussian ratio) were determined from the unannealed ASD and annealed T_1 experiment with 128 ms $T_{1\rho}$ filter, respectively. Deconvolution parameters were kept approximately constant when fitting at all T_as to avoid biasing results.

Method NMRT1 used relaxation experiments performed on the Bruker spectrometer at 20°C in a 6 mm Phoenix HX probe (Phoenix NMR, Loveland, CO) for 80-20 and 90-10 ASDs. The proton spin-lattice relaxation time (^{1}H T_1) was determined using a saturation-recovery experiment through ^{13}C observation. 160 scans, each with 3996 acquisition points were acquired for a list of 21 different pulse delays (PD). The integrated area (M) of the NIF doublet peak at 102.6 ppm was fit to the biexponential recovery

equation to determine the T_1 of the crystalline ($T_{1,C}$) and amorphous NIF ($T_{1,A}$) (Equation 4.7).

$$M = M_{0,C}\left(1 - e^{-\frac{\tau}{T_{1,C}}}\right) + M_{0,A}\left(1 - e^{-\frac{\tau}{T_{1,A}}}\right) \tag{4.7}$$

$M_{0,C}$ and $M_{0,A}$ are the preexponential coefficients of crystalline and amorphous NIF, respectively and can be used to approximate the amount of each phase present. The fraction of crystalline NIF present in the ASD after annealing is shown in Equation 4.8.

$$X_C = \frac{M_{0,C}}{M_{0,C} + M_{0,A}} \tag{4.8}$$

Similarly, Equation 4.8 can also be used to calculate the weight fraction of amorphous NIF remaining in the ASD. A variable CT experiment was also performed and the ratio between signal intensity at 1.5 ms CT and the extrapolated intensity at 0 ms CT taken to correct for differences in CP dynamics between the crystalline and amorphous NIF.

4.2.7 Polarized Light Microscopy

Crystals formed during the annealing process were visualized using an Axio Imager.A2m polarized light microscope (Carl Zeiss Microscopy, LLC, White Plains, NY) equipped with a LTS 420 hotstage (Linkam Scientific Instruments, Ltd., Surrey, UK). Powdered ASD was melted on a microscope slide, then quench-cooled by placing on a precooled stainless-steel block. The microscope slide was heated on the hotstage and held at T_a for a minimum of four hours. Images were captured using a Zeiss AxioCam MRc digital camera.

4.2.8 Drug-in-Polymer Solubility Measurements

The crystalline solubility of NIF in PVP K12 was determined using X_{NIF} values obtained through annealing at high temperatures for a minimum of 2 hours. This assumes that annealing allowed sufficient time for crystallization to occur and the system reached equilibrium. While most samples reached equilibrium in 2 hours, lower T_as, particularly for 70-30 ASDs, required upwards of 24 hours of annealing to reach equilibrium crystallinity. The amorphous weight fraction was converted into the amorphous volume fraction (υ_{NIF}) and used in the Flory-Huggins solubility equation (Equation 4.9):

$$\frac{\Delta H_{fus}}{R}\left(\frac{1}{T_m} - \frac{1}{T}\right) = ln(\upsilon_{NIF}) + \left(1 - \frac{1}{\lambda}\right)(1 - \upsilon_{NIF}) + \chi(1 - \upsilon_{NIF})^2 \qquad (4.9)$$

where ΔH_{fus} and T_m are the pure NIF heat of fusion at its melting point, respectively. R is the ideal gas constant and T is the annealing temperature. λ is the molar volume ratio and χ is the drug-polymer interaction parameter, an indication of the miscibility of drug and polymer upon mixing χ is optimized by linear regression to extrapolate from high temperatures to the glassy state (65).

4.3 Results

4.3.1 Creating Supersaturated Amorphous Solid Dispersions

Supersaturated ASDs were created by mixing NIF and PVP K12 at concentrations of 70-30, 80-20, and 90-10 % (w/w). After mixing and cryogrinding, samples were heated above the melting point of NIF in a teflon beaker in an oil bath then quench-cooled before lightly grinding with mortar and pestle. Freshly prepared NIF-PVP ASDs were analyzed for initial crystallinity using PXRD. The PXRD diffraction patterns for NIF, PVP, and each ASD are shown in Figure 4.2. Crystalline NIF shows well defined Bragg peaks

corresponding to the α-NIF polymorph (263). The α-NIF pattern lacks any amorphous halo nor any unexpected diffraction peaks indicating a fully crystalline starting material containing no other NIF polymorphs. PVP and all NIF-PVP ASDs studied lack any Bragg peaks indicating the cryomill/ melt-quench procedure was successful in producing X-ray amorphous ASDs.
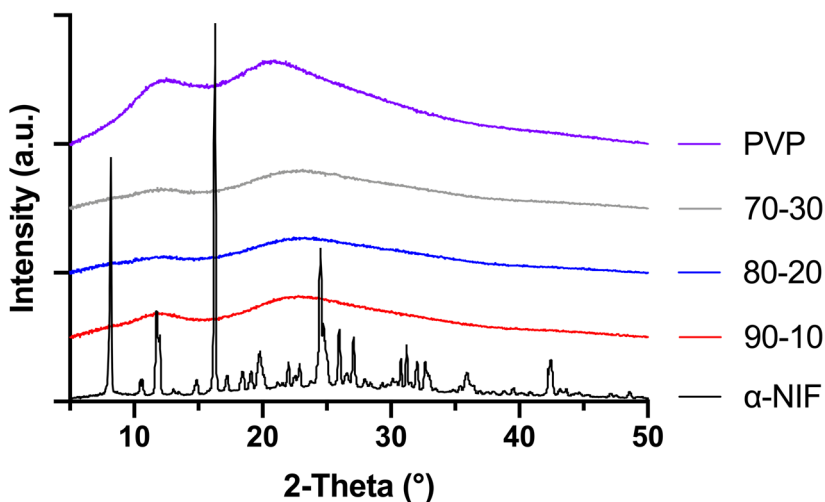
Figure 4.2. Sample and reference PXRD diffractograms for the initial analysis of NIF-PVP ASDs.

The ASDs were also analyzed by DSC to confirm the absence of crystallinity and determine the T_g at each NIF concentration. The lack of a dissolution endotherm in the Figure 4.3 thermograms suggests the ASDs do not have any crystallinity. They also exhibit a single T_g intermediate to the T_g of pure components suggesting miscibility over an approximately 30 nm domain size (264, 265). Increasing amounts of polymer raised the T_g from 50.5°C at 10% PVP to 68.2°C at 30% PVP, consistent with values predicted by the GT equation. This indicates the GT equation predicts the T_g of NIF-PVP ASDs very well across a wide compositional range and are consistent with previously reported results from our laboratory (Figure 4.4) (85).

The initial ASDs were also analyzed by ^{13}C SSNMR for signs of residual crystallinity and a more sensitive measure of miscibility to ensure completely amorphous systems were created. Spectra for all initial ASDs contained spectral features which were consistent with a fully amorphous ASD (85). The ^{1}H T_1 of NIF and PVP were equal in all initial ASDs indicating PVP initially stabilized amorphous NIF by homogeneous molecular mixing on a length scale of ≤ 40 nm, also consistent with our previous results (85).

4.3.2 Annealing-induced Crystallinity

Samples were heated either in a DSC cell or in an oven to temperatures between the ASD T_g (50.5 – 68.2°C) and T_m of NIF (173°C) and held isothermally for 2 – 24 hours to allow the supersaturated NIF to crystallize. Annealing at temperatures significantly above T_g (130 – 160°C) provided NIF with the molecular mobility required for rapid crystallization. No chemical degradation was observed in the annealed samples, consistent with the results of Aso et al. and Sun et al. (66, 156).

4.3.3 Analytical Methods for Quantifying Crystallinity

Three different analytical techniques and five different methods were used to quantify the resulting crystallinity of samples annealed between 130°C and 160°C. DSC either applied the GT equation by measuring T_g or integrated the dissolution endotherm to determine ΔH_{diss}. PXRD used a full powder pattern integration and background subtraction. SSNMR quantified crystallinity using either a two-component saturation recovery (T_1) experiment or deconvolution of overlapping crystalline and amorphous peaks. Each method was first compared for its ability to quantify crystallinity across a range of temperatures. Methods which provided comparable crystallinity values were then applied to predict drug-in-polymer solubility.

4.3.3.1 Differential Scanning Calorimetry

Figure 4.3 shows the final heating scan of DSC-annealed NIF-PVP ASDs at different annealing temperatures, and Table 4.2 lists the T_g and ΔH_{diss} values for each dispersion. Crystallinity was measured in all samples using the reversing and non-reversing heat flow signals shown in Figure 4.3A. T_g is measured as the midpoint of the step change in the baseline of the reversing heat flow while ΔH_{diss} is measured from the reversing and non-reversing signals. A running integral is applied to the non-reversing heat flow from just above T_g to above the offset of the dissolution endotherm to account for any crystallization occurring upon heating. The non-reversing integral is subtracted from any reversing dissolution endotherm which may be present to yield the heat of dissolution attributed only to crystals formed during annealing. For simplicity, Figures 4.3B, C, and D show only the total heat flow (sum of reversing and non-reversing) thermograms during the final heating scan to show both the glass transition and dissolution endotherm. T_gs depicted in the total heat flow in Figures 4.3B, C, and D are slightly higher than the T_g used in GT calculations, a result of enthalpic recovery upon heating through the T_g (Figure 4.3A).
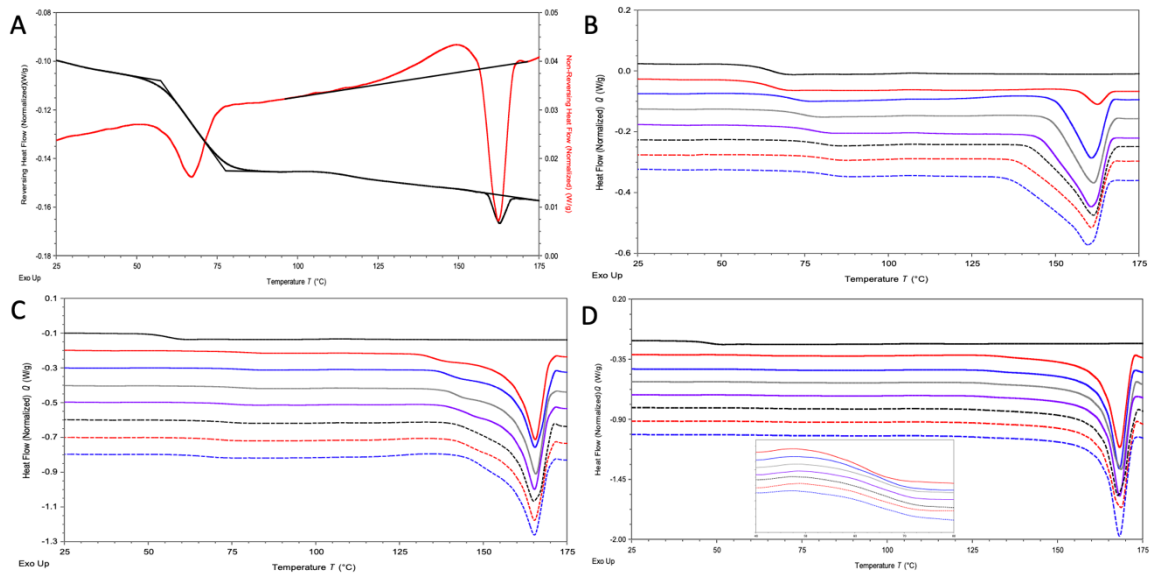
Figure 4.3. Thermograms of NIF-PVP ASDs annealed for 2 hours in the DSC. (A) Example reversing and non-reversing heat flow trace from an 80-20 ASD used to calculate crystallinity. (Reversing heat flow shown in black, non-reversing heat flow shown in red.) (B – D) Heating scan measuring total heat flow of NIF-PVP ASDs as a function of T_a for different drug loadings. (B) 70-30, (C) 80-20, and (D) 90-10 (smaller window shown to easily view T_g). *From top to bottom*: unannealed, 160°C, 155°C, 150°C, 145°C, 140°C, 135°C, and 130°C.
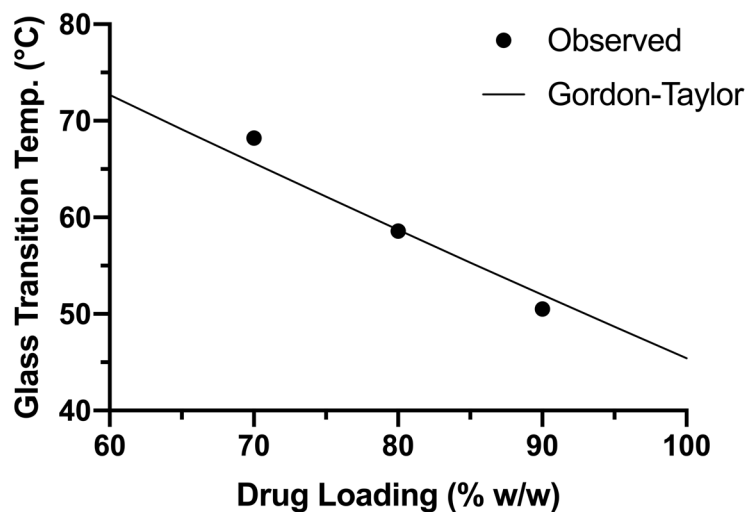
Figure 4.4. Experimentally observed and glass transition temperatures predicted by the Gordon-Taylor equation for NIF-PVP K12 ASDs at varying drug loadings.

Table 4.2. T_g and ΔH_{diss} values for DSC-annealed NIF-PVP ASDs.

T_a (°C)	70-30		80-20		90-10	
	T_g (°C)	ΔH_{diss} (J/g)	T_g (°C)	ΔH_{diss} (J/g)	T_g (°C)	ΔH_{diss} (J/g)
130	85.2	39.35	83.9	60.67	70.3	79.60
135	84.4	37.39	82.5	58.19	69.6	77.86
140	82.8	35.24	80.9	56.45	70.3	77.35
145	80.7	31.23	79.3	55.16	70.2	77.44
150	77.5	25.77	77.0	53.06	69.7	78.39
155	74.5	19.19	74.9	49.54	68.8	76.99
160	68.3	2.07	71.0	43.95	65.9	76.56

The T_g was measured and used with the GT equation to determine the weight fraction of amorphous NIF present in the resulting ASD (methods OvTg and DSCTg). The T_g of ASDs generally decreased with either increasing annealing temperature (T_a) or annealing times. The T_g of an annealed ASD at a given T_a should be the same regardless of the initial drug loading because any excess NIF above the supersaturation limit should crystallize out leaving a saturated ASD of NIF-PVP. As T_a decreases, NIF becomes less soluble in PVP and T_g will increase at lower annealing temperatures. However, these equilibrium conditions may not be reached at short annealing times or if the NIF concentration does not exceed the supersaturation level. The T_g of 90-10 ASDs were particularly difficult to measure due to a broad glass transition as well as a small change in heat capacity because of the low mass of amorphous drug/polymer remaining after annealing. The T_g of 90-10 ASDs appeared approximately constant (~69°C) from $T_a = 130$ – 155°C before decreasing at 160°C. The T_g of 70-30 and 80-20 ASDs decreased slightly up to $T_a = 150$°C then decreased more significantly above 150°C. At $T_a = 160$°C, the T_g of the annealed 70-30 ASD is equal to the unannealed 70-30 ASD indicating no crystallization has occurred due to either significant melting point depression or insufficient supersaturation in 70-30 NIF-PVP mixtures at 160°C. Crystallization was observed at 160°C for the 80-20 and 90-10 dispersions (*vide infra*).

Figures 4.3B, C, and D also measure ΔH_{diss} as crystallized NIF redissolves into PVP at high temperatures. The intensity of the dissolution endotherm decreases as T_a increases across all drug loadings while the integrated ΔH_{diss} increases with drug loading. The endotherm value decreases slowly up to $T_a = 150$°C for 70-30 and 80-20 ASDs before rapidly decreasing. At $T_a = 160$°C for the 70-30 ASD, only a small endotherm is observed

and is attributed only to the non-isothermal crystallization of NIF upon reheating. Again, similar to the T_g, the dissolution endotherm of 90-10 ASDs remains approximately constant up to 155°C before finally decreasing.

Melting point depression (MPD) is observed as the onset and end point of dissolution are decreased relative to the melting point of pure NIF (173°C). Although particularly noticeable for 70-30, this is observed in ASDs of all drug loadings tested indicating miscibility between NIF and PVP K12 (65). The absence of crystallization at 160°C for the 70-30 ASD is explained by MPD, a minimal dissolution endotherm, and no change in T_g relative to the unannealed ASD. The additional NIF present in 80-20 and 90-10 dispersions is enough to cause measurable crystallization in ASDs at 160°C despite the decreased thermodynamic driving force for crystallization at temperatures approaching the NIF melting point.

Lastly, it was also observed that the dissolution endotherm was asymmetric, and a shoulder was present near the onset of dissolution, especially visible for 70-30 and 80-20 ASDs. The width of the dissolution endotherm showed opposite trends for the 70-30 and 80-20 ASDs with the peak narrowing and slightly broadening as T_a increased, respectively. 90-10 ASDs exhibit a small shoulder and constant peak width across all T_a. The likely cause is the presence of a metastable polymorph (β-NIF) which has been observed in NIF-PVP ASDs previously (266, 267). However, PXRD data confirmed that only the stable α-NIF polymorph was formed during annealing (*vide infra*) indicating β-NIF would have formed during the final heating scan.

4.3.3.1.1 Oven-Annealed versus DSC-Annealed Dispersions

The T_g of DSC-annealed samples was greater than the T_g of oven-annealed samples at short annealing times, particularly at lower T_as and drug loadings. However, this effect was minimized at longer annealing times as samples annealed via DSC were observed to have approximately the same T_g and ΔH_{diss} as those annealed in an oven (Figure 4.5 and Table 4.3). In turn, this resulted in almost identical levels of crystallinity regardless of the annealing method at long annealing times (see Figure 4.10). It should be noted that the DSC-annealed and oven-annealed thermograms (Figures 4.3 and 4.5, respectively) are shown after annealing for 2 hours. Crystallization kinetics in the oven are slower and results in incomplete crystallization. Upon reheating, some amorphous NIF recrystallizes as evidenced by the small exotherm in some samples.
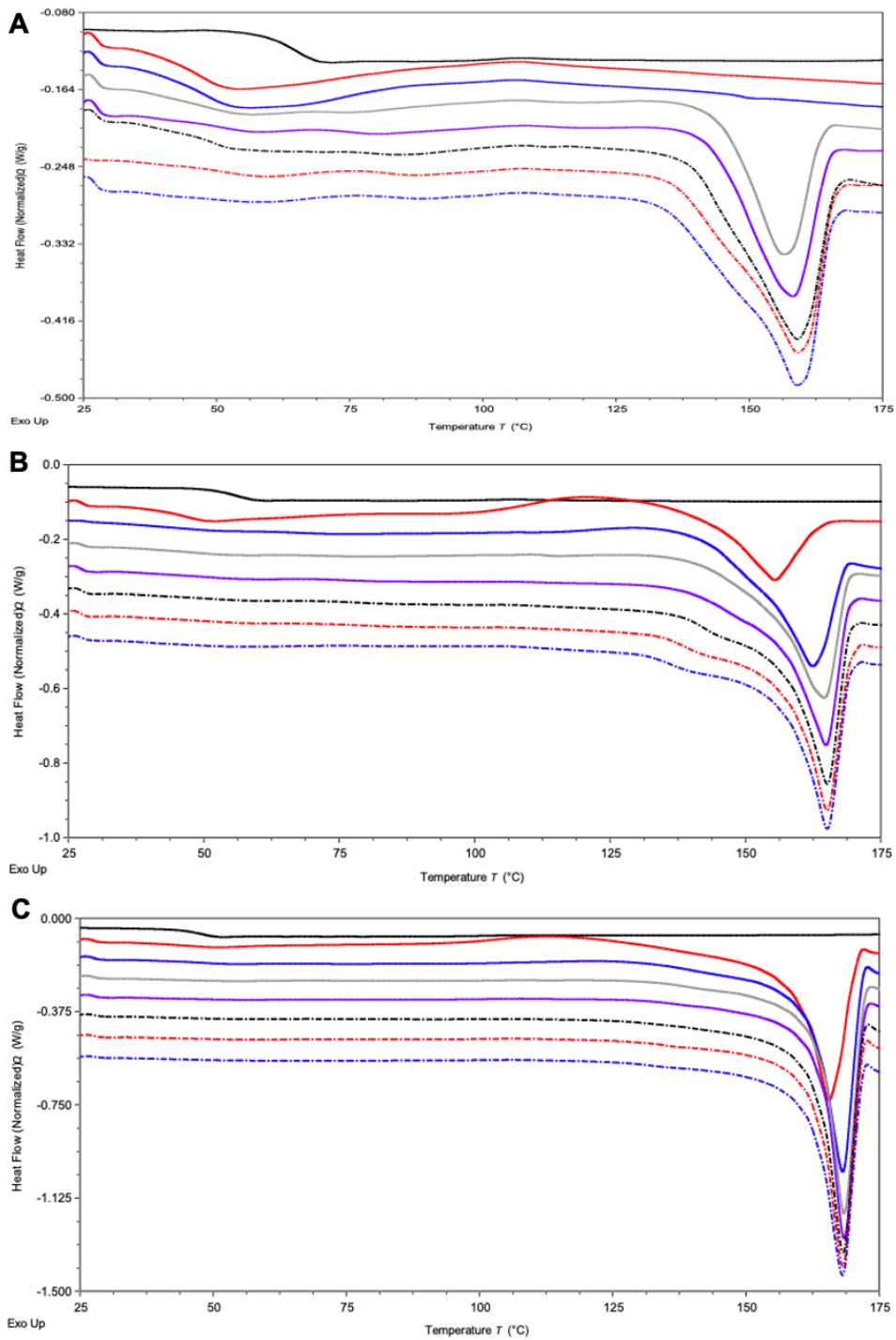
Figure 4.5. Thermograms of NIF-PVP ASDs annealed for 2 hours in an oven. (A) 70-30, (B) 80-20, and (C) 90-10. *From top to bottom*: unannealed, 160°C, 155°C, 150°C, 145°C, 140°C, 135°C, and 130°C.

Table 4.3. T_g and ΔH_{diss} values for oven-annealed NIF-PVP ASDs.

T_a (°C)	70-30		80-20		90-10	
	T_g (°C)	ΔH_{diss} (J/g)	T_g (°C)	ΔH_{diss} (J/g)	T_g (°C)	ΔH_{diss} (J/g)
130	85.2	37.58	82.2	55.92	68.5	76.21
135	83.9	37.01	82.0	56.28	69.6	76.69
140	80.8	32.17	81.1	54.37	69.5	76.74
145	79.0	29.37	78.6	51.47	69.5	75.54
150	75.9	25.30	76.8	49.59	69.7	74.18
155	73.4	19.63	73.8	44.42	64.3	70.84
160	65.3	1.20	68.1	38.60	59.4	69.23

4.3.3.2 Powder X-ray Diffraction

PXRD diffractograms for each ASD as a function of T_a are shown in Figure 4.6. The amount of crystallinity was quantified using the entire powder diffraction pattern to minimize the error due to preferred orientation. The relative intensity of the diffraction peaks and amorphous background remain approximately the same in 70-30 ASDs from 130°C to 150°C indicating the crystallinity does not change significantly over that temperature range. The crystalline peaks disappear above 150°C corresponding to an absence of crystallinity. While similar trends are observed for 80-20 and 90-10 NIF-PVP ASDs, small crystalline peaks remain at 160°C as small amounts of crystalline NIF are present. The peak positions were compared to reference standards and indicated that NIF crystallized to the stable α-polymorph at all drug loadings and T_as (263). While it is possible that polymorphic form changes during the course of annealing, the diffraction patterns shown indicate only the α-polymorph is present in the equilibrated ASDs.
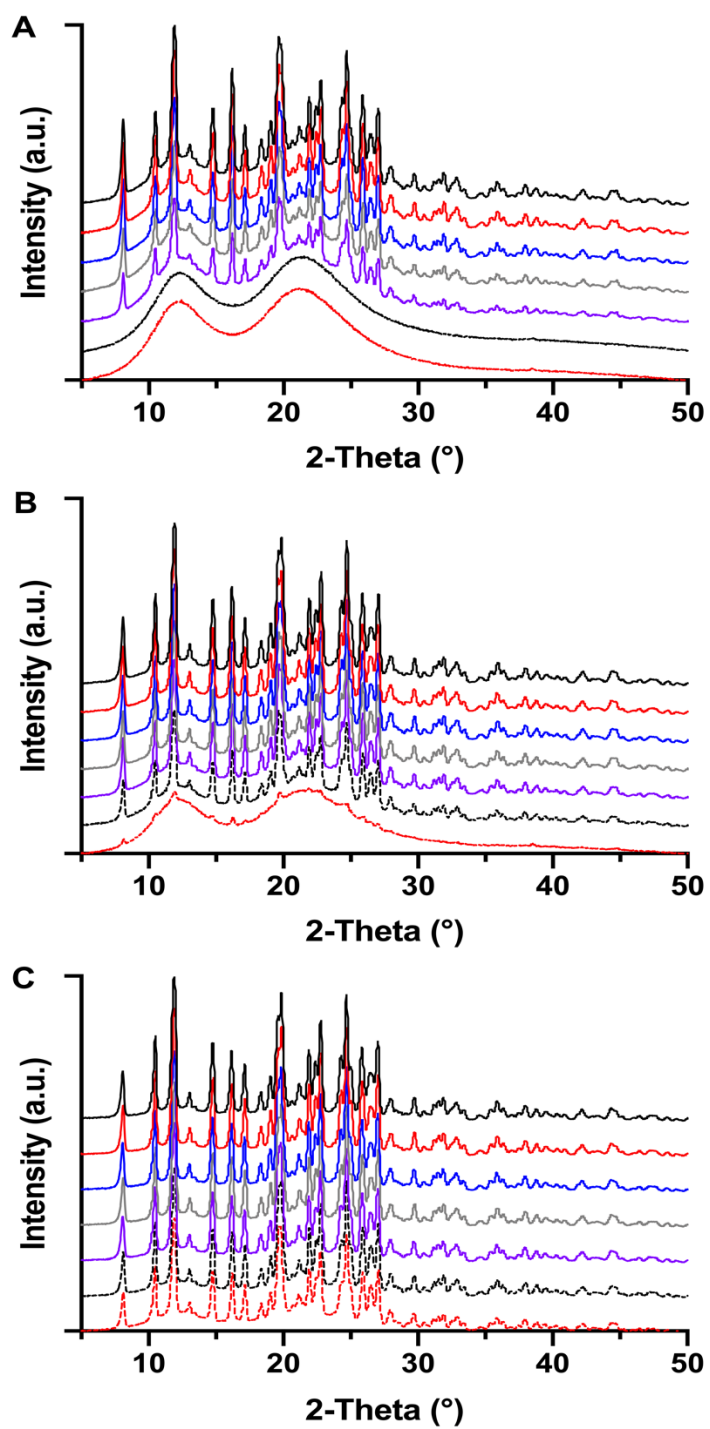
Figure 4.6. PXRD patterns for (A) 70-30, (B) 80-20, and (C) 90-10 NIF-PVP ASDs after annealing. *From top to bottom* T_a = 130°C, 135°C, 140°C, 145°C, 150°C, 155°C, 160°C. Instrumental background has been subtracted.

4.3.3.3   Solid-state NMR

Two different approaches were used to quantify the equilibrium crystallinity using SSNMR. First, overlapping NIF peaks were deconvoluted into their underlying crystalline and amorphous peaks to provide a direct measure of crystallinity. Second, the difference in crystalline and amorphous T_1 relaxation times provided an indirect measure of the relative proportions of each phase present in the equilibrated sample. The two SSNMR methods will be described first in this section, followed by experimental results for crystallinity in the following section.

Figure 4.7 shows SSNMR spectra of NIF, PVP, and ASDs made from NIF and PVP. Figure 4.7A shows CP TOSS spectra of PVP, α-NIF, and an initial 80-20 NIF-PVP K12 ASD. Figure 4.7B shows CP TOSS spectra acquired at room temperature for samples annealed at each T_a.
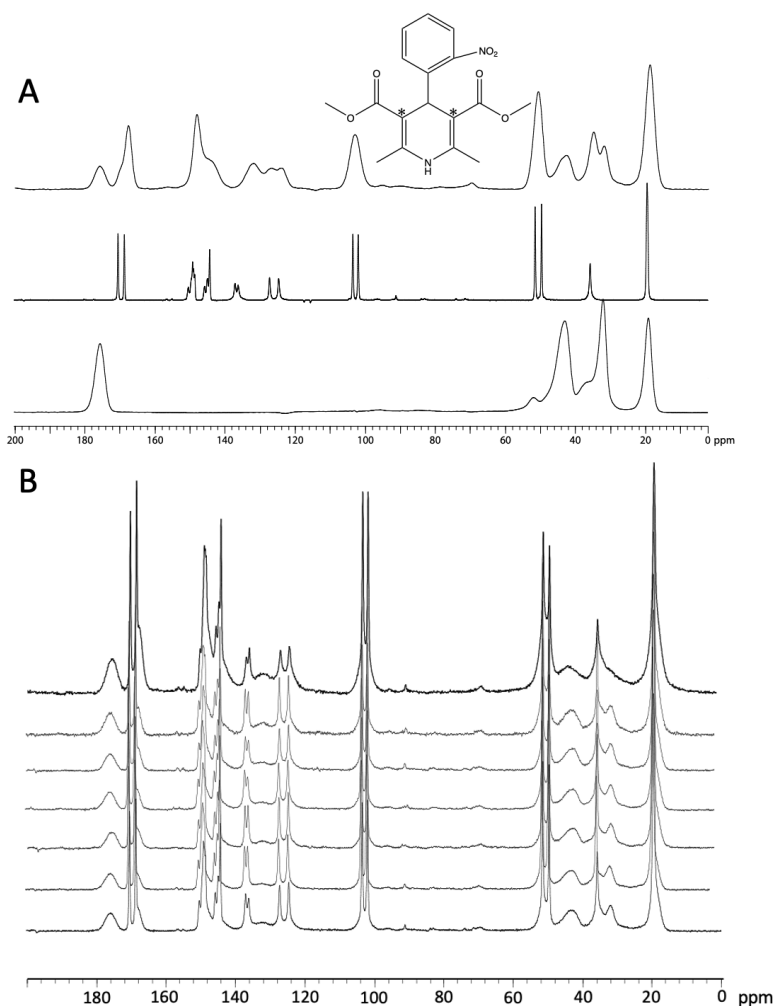
Figure 4.7. ^{13}C SSNMR CP TOSS spectra at 4 kHz MAS spectra. (A) *From top to bottom*: Unannealed 80-20 NIF-PVP K12 ASD, α-NIF, and PVP K12. The structure of NIF is shown in the inlay where the asterisks represent the carbon atoms used for quantitation. (B) 80-20 NIF-PVP ASDs annealed at varying temperatures (*From top to bottom*: T_a = 160°C, 155°C, 150°C, 145°C, 140°C, 135°C, and 130°C).

The crystalline α-NIF spectrum shows a single sharp peak for each unique ^{13}C nuclei present in the sample indicating there is one molecule in an asymmetric crystalline unit (263, 268). Peak assignments were made previously (269). The alpha carbons of NIF ester groups (denoted by * in Figure 4.1) were chosen for quantitation as they are

completely resolved from PVP or other NIF resonances in ASD spectra. They appear as two sharp peaks at 101.9 and 103.4 ppm or as a single broad peak at 103.2 ppm in the α-crystalline and amorphous states, respectively. Samples annealed between 130°C and 160°C show a combination of broad amorphous peaks and sharp crystalline peaks indicating a significant fraction of the sample crystallized during annealing.

CP TOSS spectra were acquired for 80-20 ASDs as a direct measurement of NIF crystallinity at each T_a (method NMRDec). The doublet at 102.6 ppm was deconvoluted into two sharp crystalline peaks and an underlying broad amorphous peak. To avoid biasing results, the line shapes of the two crystalline peaks and broad amorphous peak were determined from a CP TOSS $T_{1\rho}$-filter experiment and the unannealed 80-20 ASD CP TOSS spectrum, respectively. The line shapes and isotropic chemical shifts were held approximately constant for the deconvolution at each T_a. The spectral deconvolution at each annealing temperature is shown in Figure 4.8.
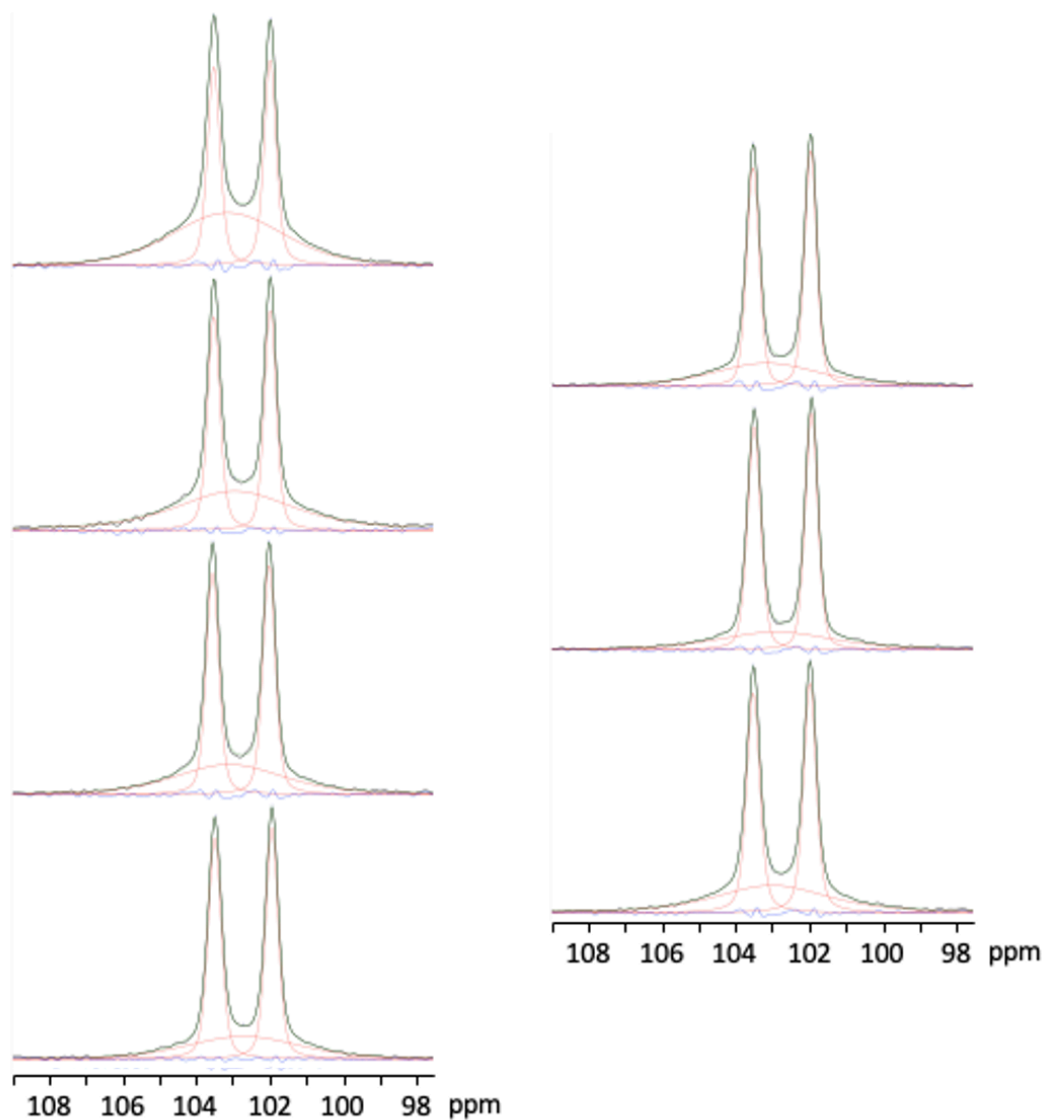
Figure 4.8. Deconvolution of CP TOSS ^{13}C SSNMR spectrum of 80-20 NIF-PVP ASDs annealed at different temperatures. *From top to bottom*: T$_a$ = 160, 155, 150, 145 (on left), 140, 135, and 130°C (on right). The experimental spectrum is shown in black, the fitted peaks representing the crystalline and amorphous NIF are shown in red, the sum of the fitted peaks are shown in green, and the residual difference between experimental and fitted peaks is in blue.

After the relative amounts of crystalline and amorphous NIF were determined using deconvolution, CP dynamics, TOSS signal loss, and differences in the T1 of each component were accounted for to ensure the results were quantitative. Each is briefly discussed; however, the interested reader is referred to the literature for excellent examples of ensuring quantitative CP data is acquired (185, 189). A variable CT experiment revealed the CP dynamics were not equal between crystalline and amorphous NIF. The crystalline ^1H $T_{1\rho}$ decreased significantly with annealing temperatures while the amorphous ^1H $T_{1\rho}$ increased slightly. The T_{CH} of both components was approximately constant with T_a. This results in crystallinity being underestimated across all temperatures, especially at lower T_as. The ratio between the observed signal at 1.5 ms CT and the predicted signal at 0 ms CT served as a correction factor for variable CP dynamics between the crystalline and amorphous NIF. For example, correction factors of 1.25 and 1.03 were applied to the crystalline and amorphous NIF, respectively, at 130°C. Other correction factors can be found in Table 4.4. Conversely, no correction was made for TOSS as the centerband signal lost to the spinning sidebands of the crystalline and amorphous NIF phases was expected to be approximately equal (*vide infra*). The pulse delay (PD) used to acquire each CP TOSS spectra in Figure 4.7B was also considered to account for the differences in relaxation rate between crystalline and amorphous NIF and ensure quantitative data was collected. A PD of nearly 5-times the crystalline NIF T_1 was chosen to avoid saturating the crystalline NIF signal. Although the effect was minimal, the observed integrated peak area (A_{obs}) of each phase was corrected to the predicted integrated area after full relaxation (A_∞) using Equation 4.10:

$$A_\infty = \frac{A_{obs}}{1 - e^{-\frac{\tau}{T_{1,i}}}} \qquad (4.10)$$

where τ is the pulse delay and $T_{1,i}$ is the ^{1}H T_1 of either the crystalline or amorphous phase.

Table 4.4. Variable contact time correction factors for crystalline and amorphous NIF in 80-20 NIF-PVP ASDs based on the amount of signal observed at 1.5 ms relative to instantaneous CP dynamics.

	Crystalline NIF		Amorphous NIF	
T_a (°C)	% Signal	Correction Factor	% Signal	Correction Factor
130	80	1.25	96.9	1.03
135	80.3	1.25	94.9	1.05
140	90.6	1.24	92.9	1.08
145	80.9	1.24	90.8	1.10
150	81.2	1.23	88.8	1.13
155	81.5	1.23	86.8	1.15
160	81.8	1.22	84.7	1.18

In the second method, saturation-recovery ^{1}H T_1 experiments were used to indirectly determine crystallinity by fitting a biexponential relaxation curve corresponding to the crystalline and amorphous NIF relaxation times (NMRT1 method). The detailed explanation for how the biexponential curves and relaxation times were measured can be found in the Methods section. The saturation recovery curves for the NIF peak at 103.2 ppm acquired under standard and $T_{1\rho}$-filtering conditions are shown in Figure 4.9.
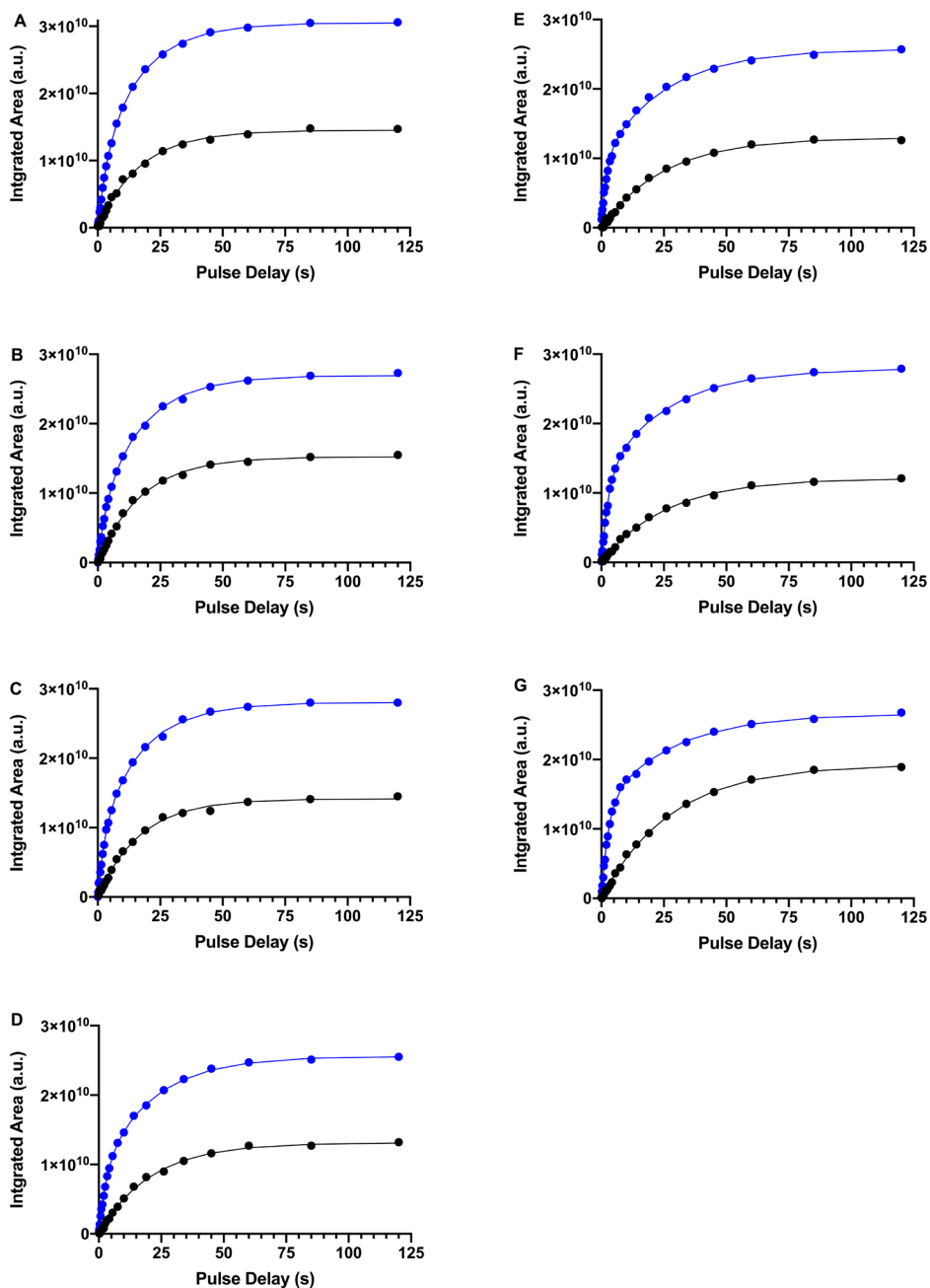
Figure 4.9. One- and two-component ^1H T_1 fits of 80-20 NIF-PVP K12 ASDs acquired with (black) and without (blue) a 128 ms $T_{1\rho}$-filter at different annealing temperatures: (A) 130°C, (B) 135°C, (C) 140°C, (D) 145°C, (E) 150°C, (F) 155°C, and (G) 160°C. Magnetization intensity shown is for the NIF peak at 102 ppm. Experimental data is shown as circles, predicted ^1H T_1 relaxation is shown as solid lines.

The standard T_1 experiment corresponds to the crystalline and amorphous components while the $T_{1\rho}$-filter shows only the crystalline NIF. The $T_{1\rho}$-filtering results were used to determine the crystalline T_1 ($T_{1,C}$). Integrated peak area data from a standard saturation-recovery experiment was fit to Equation 4.7 to determine the amorphous T_1 ($T_{1,A}$) and preexponential factors ($M_{0,C}$ and $M_{0,A}$), corresponding to the relative fractions of crystalline and amorphous NIF. $M_{0,C}$ and $M_{0,A}$ were then used to calculate crystallinity via Equation 4.8. This process was repeated for all T_a with results shown in Figure 4.12.

The ^1H T_1 values for crystalline and amorphous NIF, as well as PVP, are found in Table 4.5 and Figure 4.10. Figure 4.10A demonstrates how α-NIF T_1 changes after cryomilling while Figures 4.10B and C plot the T_1 relaxation time of each phase as a function of annealing temperature.

Table 4.5. ^1H T_1 values for crystalline and amorphous NIF and PVP.

	80-20 T_1 (s)			90-10 T_1 (s)		
T_a (°C)	PVP	Amorphous	Crystal	PVP	Amorphous	Crystal
130	2.95	3.90	16.65	2.17	2.17	20.88
135	3.20	3.52	17.28	3.71	3.76	21.73
140	2.27	2.85	16.95	3.79	4.31	23.33
145	2.50	3.04	20.57	4.26	3.32	25.67
150	2.32	1.94	24.97	4.74	3.93	27.28
155	2.89	2.89	26.11	2.72	3.19	28.51
160	3.05	2.80	28.07	5.84	3.58	29.80
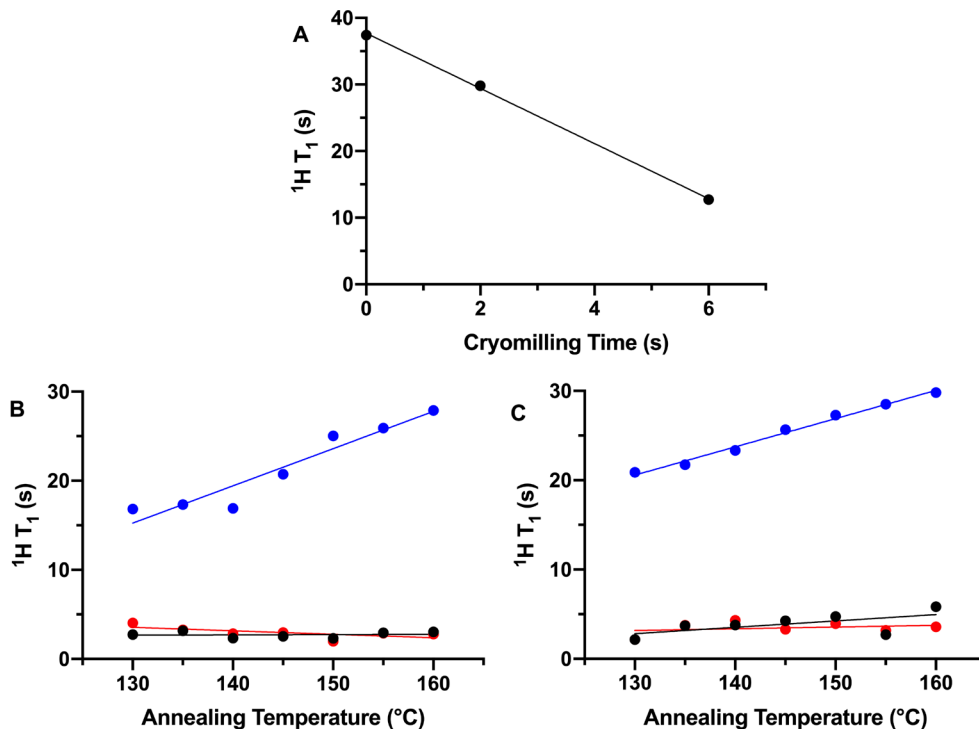
Figure 4.10. (A) ^{1}H T_1 of α-NIF cryomilled for varying times representing changes in crystal quality. (B and C) ^{1}H T_1 measured at various annealing temperatures for all components is shown for (B) 80-20, and (C) 90-10 NIF-PVP ASDs and cryomilled NIF. In (B) and (C) PVP is represented by black symbols, amorphous NIF is red, and crystalline NIF is blue. The crystalline NIF T_1 was determined using a modified saturation-recovery ^{1}H T_1 pulse sequence with a 128 ms $T_{1\rho}$-filter.

Amorphous NIF and PVP share a common ^{1}H T_1 value which is constant with increasing T_a. This indicates the resulting ASD remains intimately mixed on an approximately 40 nm domain size (85). The ^{1}H T_1 of crystalline NIF is different from pure α-NIF and increases with T_a, nearly doubling over the 30°C annealing range. This is likely due to the combined effect of a reduced crystallite size and greater crystalline defects at lower temperatures. The differences in crystalline T_1 are visually explained by the

polarized light microscopy (PLM) images in Figure 4.11 which show NIF crystals grown at different annealing temperatures.
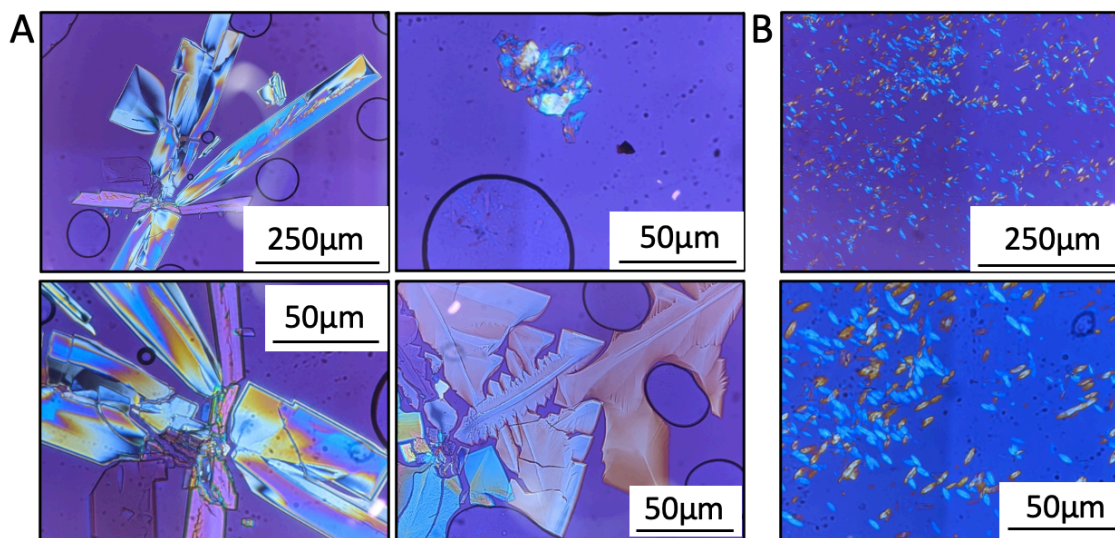
Figure 4.11. Polarized light microscopy images of NIF crystals formed during 80-20 NIF-PVP ASD annealing at (A) 130°C, or (B) 160°C.

An increase in crystalline T_1 with T_a is explained by a corresponding increase in crystal quality despite a decrease in NIF crystallite size (see Figures 4.10B and 4.11). Crystals grown at lower T_a show a wide crystallite size distribution and contain a high degree of crystal defects including fractures and rough edges. Crystal growth is highly irregular and occurs mainly in clusters (Figure 4.11A). It also appears that a small amount of β-NIF, whose T_1 is nearly 20 s shorter than α-NIF, may form at lower T_a and was not detected by DSC or PXRD (Figure 4.11A bottom right panel) (85). Crystals formed at 160°C are much more uniform in size, smaller, appear to be of higher quality, and are homogeneously dispersed throughout the entire sample (Figure 4.11B). The causes and implications of changing crystalline T_1 times are examined further in section 4.4.2.2.

4.3.4　Crystallinity Method Comparison

Figure 4.12 compares the drug crystallinity in 70-30, 80-20, and 90-10 NIF-PVP ASDs calculated using DSC (heat of dissolution and GT equation), PXRD, and SSNMR (T_1 and deconvolution). As the polymer content increases, the amount of drug required to saturate the polymer also increases, thereby decreasing the amount of crystalline drug after annealing. At higher annealing temperatures, NIF is more soluble in PVP, also resulting in lower crystallinity. Methods OvHd and DSCHd consistently yielded $10 - 35\%$ less crystallinity than T_g-based methods across all drug loadings regardless of whether samples were annealed in-situ (DSC) or ex-situ (oven). This difference was amplified at lower drug loadings. Likewise, methods OvTg, DSCTg, and PXRD all show almost identical levels of crystallinity across all annealing temperatures for 70-30 and 80-20 ASDs indicating a similar ability of DSC (GT equation) and PXRD to quantify crystallinity in NIF-PVP ASDs of moderate drug loadings. Crystallinity measured using methods NMRT1 and NMRDec agreed well with one another and provided slightly lower levels of crystallinity in 80-20 ASDs compared to T_g- and PXRD-methods. Likewise, method NMRT1 agreed very well with PXRD results in 90-10 ASDs.
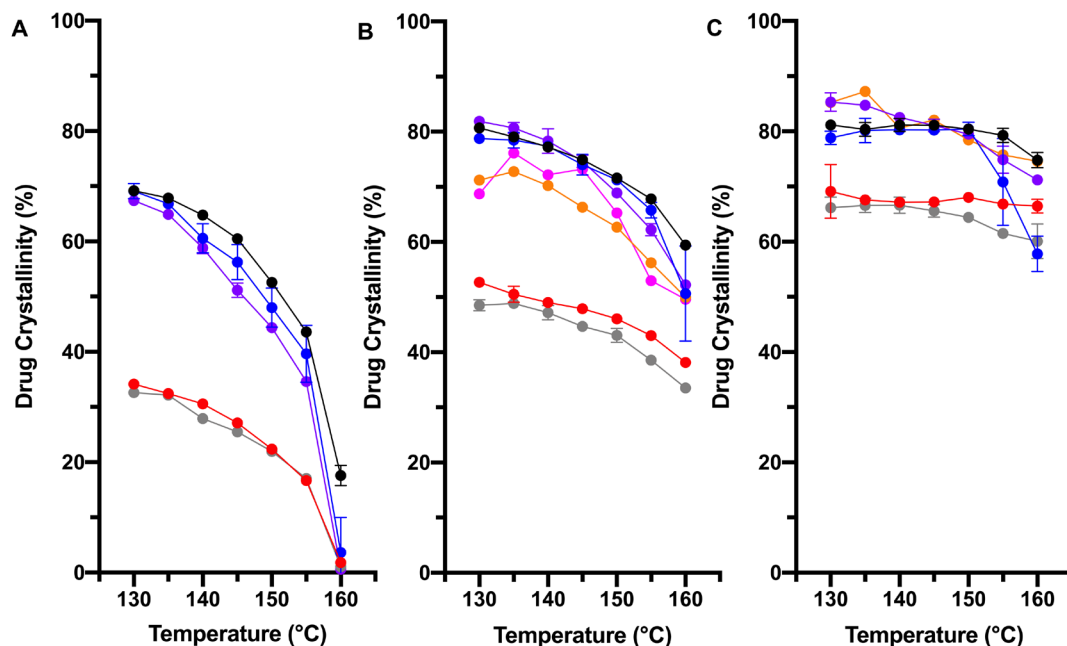
Figure 4.12. NIF crystallinity in (A) 70-30, (B) 80-20, and (C) 90-10 NIF-PVP K12 ASDs measured using different methods. The color of the data points indicates the method used: black (DSC GT), red (DSC ΔH_{diss}), blue (oven GT), gray (oven ΔH_{diss}), purple (PXRD), orange (SSNMR T_1), and pink (SSNMR deconvolution).

90-10 ASDs appeared mostly crystalline after annealing and crystallinity was constant with Ta when analyzed by the GT equation (methods OvTg and DSCTg). The accuracy of the measurements was suspect because the T_g values were poorly resolved. Similar trends were again observed measuring ΔH_{diss}. Methods OvHd and DSCHd measured 15% lower crystallinity than that predicted by methods OvTg and DSCTg. Methods PXRD and NMRT1 were the only methods to observe a continual decline in crystallinity with increasing T_a for 90-10 ASDs.

Crystallinity measured by PXRD agreed well with results of the GT equation and SSNMR (Figure 4.12) for lower drug loadings. At high drug loadings, PXRD crystallinity

decreases more with T_a than methods OvTg or DSCTg and predicts greater crystallinity at lower T_as and less crystallinity at higher T_as in agreement with SSNMR. PXRD relies mostly on the crystalline component for quantitation which is much more prevalent and easily measured compared to methods OvTg and DSCTg which rely on the small amorphous fraction remaining after annealing to quantify crystallinity.

Lastly, two SSNMR techniques (NMRT1 and NMRDec) were used to quantify crystallinity and agree very well with one another. Each exhibited similar trends compared to methods OvTg, DSCTg, and PXRD although the measured crystallinity was 5-10% lower for 80-20 ASDs. Interestingly, both NMRT1 and NMRDec measured lower crystallinity at 130°C relative to 135°C, disagreeing with DSC and PXRD techniques and suggests equilibrium crystallinity was not achieved during the annealing time.

4.3.5 Solubility Method Comparison

The solubility plot in Figure 4.13 displays the amorphous weight fraction of NIF remaining in the ASD at a given temperature. Predicted solubility at 25°C, 100° C, and T_g using each analytical method is shown in Table 4.6. Figure 4.13 shows that methods OvTg, DSCTg, PXRD, NMRT1, and NMRDec yield comparable levels of crystallinity. Therefore, each method was expected to predict similar solubility. Conversely, methods DSCTg and DSCHd yielded significantly lower levels of crystallinity so it follows that the predicted solubility would be significantly higher.
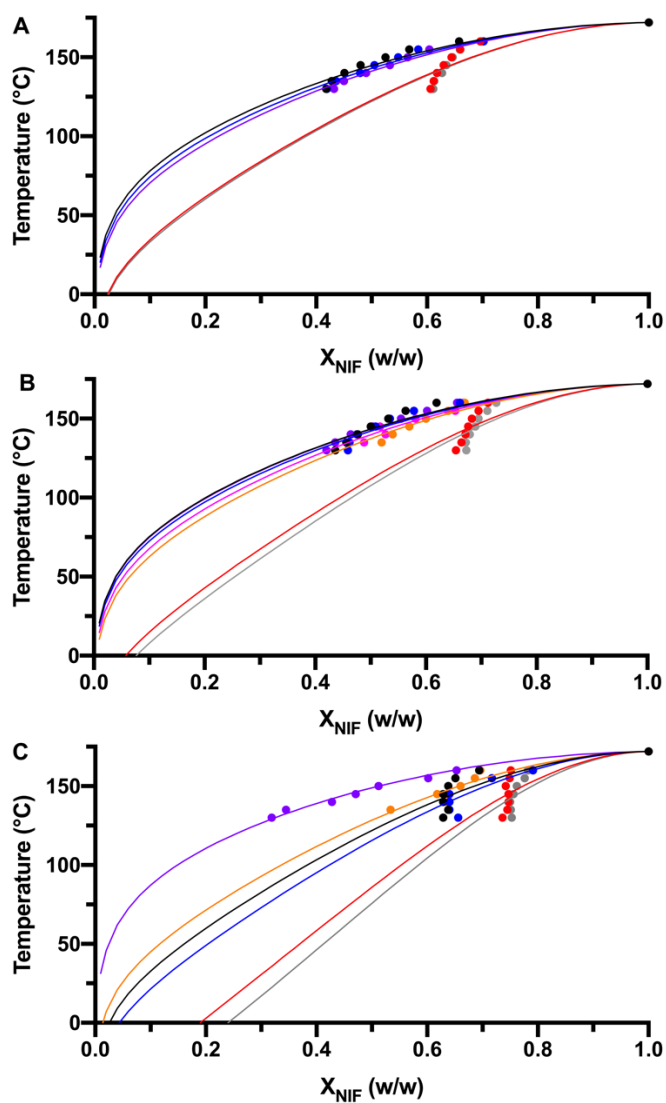
Figure 4.13. The equilibrium weight fraction of amorphous nifedipine at different temperatures determined using different analytical methods. Experimental data (filled circles) fitted to the Flory-Huggins equation is represented by the solid lines and used to predict solubility at low temperatures. (A) 70-30, (B) 80-20, and (C) 90-10 NIF-PVP K12 ASDs. The color of the data points indicates the method used: black (DSC GT), red (DSC ΔH_{diss}), blue (oven GT), gray (oven ΔH_{diss}), purple (PXRD), orange (SSNMR T_1), and pink (SSNMR deconvolution).

Table 4.6. Predicted solubility of NIF-in-PVP at 25°C, T_g, and 100°C using different analytical methods.

Method	Temp. (°C)	Oven GT	Oven ΔH_{diss}	DSC GT	DSC ΔH_{diss}	PXRD	SSNMR
	25	1.3	$(7.6)^c$	1.1	$(7.2)^c$	1.5	
70-30	T_g=68.2	8.2	$(23.3)^c$	7.1	$(22.8)^c$	9.3	--
	100	20.6	$(38.2)^c$	$(18.9)^c$	$(37.7)^c$	22.4	
	25	1.4	$(15.6)^c$	1.2	$(13.4)^c$	1.3	2.2^a (2.4^b)
80-20	T_g=58.6	6.2	$(28.9)^c$	5.6	$(26.3)^c$	5.7	8.8^a (7.3^b)
	100	21.5	$(46.5)^c$	20.2	$(44.4)^c$	20.4	26.0^a (23.7^b)
	25	$(11.2)^c$	$(32.8)^c$	$(7.7)^c$	$(30.0)^c$	0.7	4.8
90-10	T_g=50.5	$(20.6)^c$	$(41.5)^c$	$(16.3)^c$	$(37.2)^c$	2.5	11.9
	100	$(42.3)^c$	$(58.4)^c$	$(38.3)^c$	$(55.3)^c$	14.9	33.6

[a]Calculated with method NMRDec. [b]Calculated with method NMRT1. [c]Data did not fit to the Flory-Huggins equation.

NIF solubility in PVP decreases with temperature from approximately 70% at 160°C to less than 2% at 25°C, agreeing well with the literature (66). Use of the GT or PXRD methods (OvTg, DSCTg, and PXRD) yields similar solubilities of approximately 1.3% at 25°C when measured with 70-30 or 80-20 ASDs. Likewise, both SSNMR methods NMRT1 and NMRDec predict similar, albeit slightly higher solubilities. The way in which the sample is annealed seems to have no impact on crystallinity and solubility for moderate drug loadings as the solubility of oven- (OvTg) and DSC-annealed (DSCTg) samples is nearly identical at all temperatures in 70-30 and 80-20 ASDs, respectively. However, DSC methods consistently overestimated solubility when high drug loadings were used while

PXRD is able to accurately detect and quantify the remaining amorphous NIF in ASDs with high drug loading resulting in a similar solubility measured even in 90-10 ASDs.

Crystallinity data was fit to the Flory-Huggins equation by linear regression while solving for the drug-polymer interaction parameter, χ. Table 4.7 lists the calculated χ for each method and drug loading.

Table 4.7. Experimental Flory-Huggins drug-polymer interaction parameter, χ, measured for each technique and drug loading.

| | DSC | | Oven | | | |
	DSC GT	ΔH_{diss}	Oven GT	ΔH_{diss}	PXRD	SSNMR
70-30	-1.5	(-3.9)[c]	-1.7	(-3.9)[c]	-1.9	N/A
80-20	-1.7	(-5.1)[c]	-1.8	(-5.6)[c]	-1.7	-2.4[a] (-2.0[b])
90-10	(-4.0)[c]	-(8.4)[c]	(-4.7)[c]	(-9.8)[c]	-1.1	-3.2

[a]Calculated with method NMRDec. [b]Calculated with method NMRT1. [c]Data did not fit to the Flory-Huggins equation.

For 70-30 and 80-20 ASDs, the Flory-Huggins equation fit the solubility data predicted by methods OvTg, DSCTg, PXRD, NMRT1, and NMRDec very well. Each had comparable χ values similar to those reported in the literature and indicated similar drug-polymer miscibility regardless of the method used (66, 157). The Flory-Huggins equation was a very poor fit to solubility predicted by ΔH_{diss} regardless of the annealing method (OvHd or DSCHd). This is a result of ΔH_{diss} being a poor parameter for calculating crystallinity. Consequently, methods OvHd and DSCHd inaccurately predicted solubilities between 5 and 12 times greater than methods OvTg, DSCTg, and PXRD at 25°C.

4.4 Discussion

4.4.1 DSC Analysis

The T_g (via the Gordon-Taylor equation) and ΔH_{diss} were two DSC-based methods chosen to compare their ability to measure crystallinity and determine solubility. While other DSC methods exist for predicting solubility (66, 157), all DSC methods suffer from the same challenges including calorimeter sensitivity, long analysis times, and sample heating. However, the primary focus of this research was on quantifying crystallinity so the two methods in this study were chosen as they first calculate crystallinity as opposed to other DSC methods which focus solely on solubility.

4.4.1.1 T_g and Gordon-Taylor

Using T_g and Gordon-Taylor (GT) equation, methods OvTg and DSCTg easily measured crystallinity and compared well with most other methods in this study. However, their application is still limited in some cases; most notably at high drug loadings (90-10) which resulted in a T_g which was poorly resolved and difficult to measure. While the absolute value of T_g is independent of sample mass, the magnitude of heat capacity change at T_g (i.e., T_g resolution) is directly related to the amorphous mass present.

NIF-PVP shows an experimental adherence to T_g values predicted by the GT equation which is required for accurate quantitation. Typically, the GT equation fails when specific drug-polymer interactions exist (76), however, the formation of weak NIF-PVP hydrogen bonds energetically balance the breaking of NIF-NIF hydrogen bonds and no significant deviation in T_g is observed across all drug loadings (82, 85). Deviation from the GT equation would result in a systematic error between the measured and actual amorphous fraction but may be corrected through an empirical T_g vs. drug fraction relationship.

The usefulness of methods OvTg and DSCTg is also affected by a combination of glass forming ability, drug-polymer combination, and sensitivity of the calorimeter. Small differences in T_g between the drug and polymer result in changes too small to accurately measure as a function of amorphous content. Complex polymers with a poorly resolved T_g (e.g., HPMCAS) make measuring the pure or mixture T_g more difficult. Similarly, drugs with a poor glass forming ability may also lead phase separation and errors in T_g measurement (40). Faster DSC heating rates may be used to improve sensitivity and better detect weak glass transitions, but the corresponding loss of resolution may ultimately limit its applicability.

4.4.1.2 Heat of Dissolution

The attractiveness of methods OvHd and DSCHd stem from directly measuring the crystalline component rather than probing the amorphous phase and may be useful in situations where T_g is difficult to measure. In theory, any crystals present will melt upon heating through T_m and should be captured by the heat of fusion (ΔH_{fus}). However, in the presence of polymer, a more appropriate depiction is crystalline drug dissolving into an undersaturated dispersion which is measured by the heat of dissolution (ΔH_{diss}). The proposed methods OvHd and DSCHd require an accurate measure of ΔH_{fus} and ΔH_{diss} which may be difficult using DSC (270). Certain difficulties associated with enthalpy-based crystallinity measurements are well documented in the literature and include assumptions which must be satisfied (75). The methods assume: (1) that ΔH_{fus} represents a perfect crystal free of defects and remains constant regardless of crystal growth conditions, (2) the reference ΔH_{fus} value corresponds to the same polymorph as the crystals

being analyzed, and (3) that any amorphous drug already dissolved in the polymer does not contribute to the excess crystalline drug which dissolves into the polymer upon heating.

Crystallinity measured using ΔH_{diss} was consistently found to be significantly lower than crystallinity measured using T_g-based DSC techniques, PXRD, or SSNMR. Measuring ΔH_{diss} requires reheating the annealed sample through its T_m which introduces the possibility for changes to occur in the sample (crystallization, dissolution, polymorphic transitions, melting point depression (MPD), etc.) prior to melting which can convolute crystallinity and/ or solubility measurements. For instance, Ostwald's rule of stages states that certain systems may crystallize into a metastable polymorph prior to either melting and recrystallizing into the stable polymorph or a solid-state polymorphic transition (271). The metastable β- and γ-NIF polymorphs observed in other NIF-PVP systems were not observed in this work and are likely not the cause of low predicted crystallinity (266, 267). Even in non-ideal systems where polymorphic transitions are known, they are often difficult to detect, let alone obtain accurate values of ΔH_{fus} (75, 85, 263). Without knowledge of specific polymorphic transitions or a reliable deconvolution method, the ΔH_{diss} method may be limited to ASDs containing drugs with a single polymorph or sufficient polymer present to retard polymorphic transitions. Previous studies using enthalpy-based measurements have only employed standard DSC with fast heating rates in an attempt to kinetically suppress any additional crystallization or dissolution upon reheating (272-274). The results were heating rate dependent and consistently lower than identical studies using T_g-based or melting point depression methods. Methods OvHd and DSCHd used modulated DSC to eliminate the heating rate dependence and better

deconvolute any simultaneous thermal events upon heating yet still predicted significantly lower crystallinities than T_g-based methods.

Methods OvHd and DSCHd are further complicated by MPD which was observed at all drug loadings, particularly for 70-30 ASDs. NIF and PVP are miscible and mix during dissolution causing a reduction in the observed 'melting' temperature. As enthalpy is temperature dependent, the integrated area of the dissolution endotherm is therefore artificially lower than in reality (75). Therefore, it was not surprising that ΔH_{diss} underestimated crystallinity while overestimating solubility, particularly at lower drug loadings.

The results indicate that, although additional thermal events are suppressed, crystallinity is still poorly predicted and the first two method-specific assumptions mentioned above likely do not hold true. Therefore, the results indicate that ΔH_{fus} does not remain constant across the range of annealing temperatures used in this study. Drug crystallization at varying conditions will change the properties of the crystal especially when polymers are present (253). Imperfect NIF crystals formed in the presence of PVP require less energy to melt or dissolve. A less endothermic dissolution would underestimate crystallinity relative to the dissolution of perfect drug crystals and explain the deviations of methods OvHd and DSCHd. Still, the explanation proposed above is only speculative and cannot be easily explained by DSC without calibration standards. It would be beneficial from a formulation perspective to have a quantitative method which also can probe the quality of the crystals formed during annealing while avoiding potential heating induced changes encountered during DSC analysis (*vide infra*).

4.4.2   Alternative Analytical Methods

It is shown above that DSC is often adequate for quantifying crystallinity in ASDs. However, there are many caveats when calculating crystallinity using T_g or ΔH_{diss}. In particular, it was especially difficult to measure the thermal events of interest in ASDs with high initial drug loadings, ultimately restricting existing DSC methods to certain drug-polymer ratios. There are more sensitive analytical techniques which avoid many of the issues associated with using T_g or ΔH_{diss} for quantitation. Ideally, these methods would be robust enough to characterize any drug-polymer system, including ones with high drug loadings, slow crystallization kinetics, and poorly resolved thermal events. Since oven- and DSC-annealing yielded equivalent results, oven-annealed samples were also used for PXRD and SSNMR analysis to provide a direct comparison of the impact of the analytical method on solubility determinations. Hence, the crystallinity and solubility at a given temperature should be equivalent in each sample with differences only arising due to the analytical method.

4.4.2.1   PXRD

PXRD has been used extensively for the detection and quantitation of molecular order (i.e., crystallinity) in pharmaceutical systems (133). As the integrated intensity of a phase's diffraction peak can be directly related to the phase's concentration in the sample, PXRD is naturally suited for crystallinity and solubility measurements for ASD systems containing only drug and polymer (133, 275, 276). Similar to ΔH_{diss} methods, PXRD probes the crystalline component rather than the amorphous component (T_g in DSC) for quantitation. However, unlike DSC methods, PXRD does not require any additional sample heating and, because a full powder pattern integration was used, variations in crystal

quality, particle size, or preferred orientation have less of an effect on quantitation (133). Quantitation based on the prominent crystalline peaks rather than the small amorphous component is preferable and provides the option for faster solubility analysis for high drug loadings. Maximum drug loadings found in the literature typically range from 80 – 85% for the recrystallization method while much lower contents are often used for other solubility methods such as melting point depression (68, 277).

PXRD gives better crystallinity results and exhibited much better adherence to the Flory-Huggins equation compared to DSC-based methods even at 90% NIF. The predicted solubility at 90% drug loading compared very well to PXRD measurements in 70-30 and 80-20 ASDs, as well values reported in the literature. The unique diffraction pattern of distinct crystalline phases can be used to help clarify any thermal events, including crystallization or polymorphic transitions, that may have occurring during annealing that were obscured by reheating in the DSC to measure ΔH_{diss}. This includes the identification of various polymorphs and temperature regimes in which they may exist. MPD has also been observed in miscible drug-polymer systems and may hide the melting of a metastable polymorph and/ or recrystallization to another polymorph (65). PXRD analysis at ambient temperatures avoids the issues involved with sample reheating and provides a snapshot of the equilibrated system at an individual T_a.

4.4.2.2 SSNMR

SSNMR was also used as an alternate method for quantifying crystallinity as it is an inherently quantitative technique where the signal intensity is directly proportional the number of distinct nuclei present. In this case, this refers to the number of amorphous and crystalline NIF molecules. Spectra acquired using cross polarization (CP) and total

suppression of spinning sidebands (TOSS) were deconvoluted to directly measure the populations mentioned above however CP TOSS is often assumed to be non-quantitative (185). Quantitative phase data was acquired by deconvolution of CP TOSS spectra by properly characterizing and accounting for CP dynamics, chemical shift anisotropy (CSA) and signal saturation. Differences in CP dynamics were found to vary with T_a and were corrected using the results of a variable CT experiment. TOSS was used to simplify each spectrum as carbonyl and aromatic peaks exhibited spinning sidebands (SSBs). Without TOSS, there was no single spinning speed which isolated the aromatic (isotropic peak = 102 ppm) SSBs from other peaks. Thus, deconvolution of the isotropic peak into its crystalline and amorphous components may be erroneous if there are differences in the intensity of SSBs relative to the isotropic peak between crystalline and amorphous phases. Chemical shift anisotropy and the spinning SSB powder pattern is determined by the structure of a molecule and the resulting asymmetric three-dimensional distribution of electrons around a ^{13}C nucleus. In other words, the chemical structure, rather than the phase, of the molecule determines the proportion of signal intensity contained in the SSBs relative to the centerband. Shen et al. found that the SSB intensity ratio of crystalline to amorphous poly(3-hexylthiophene) was approximately the same as that in the isotropic peak (278). Similarly, crystalline and amorphous NIF exhibited almost identical SSB patterns in CP spectra acquired without TOSS (data not shown). Therefore, the proportion of signal lost to TOSS in each NIF phase was expected to be approximately equal.

Direct and indirect measurement of crystallinity with SSNMR was similar albeit slightly lower than GT and PXRD methods but estimated solubilities at 25°C were ≤1% higher. Like PXRD, SSNMR may also be applied to higher drug loadings as either the

crystalline or amorphous component (or both) component can be used for quantification. SSNMR can also be used for the simultaneous detection and quantification of polymorphic and amorphous phases with superior limits of detection (185).

Deconvolution has been used previously for crystalline/ amorphous quantitation. However, this was typically performed or verified using physical mixtures of crystalline and amorphous drug assuming that the crystalline T_1 in the mixture was constant and equal to the pure component T_1 in each system (185, 279). While beneficial from a quantitation viewpoint, this looks at the final product and provides no information as to how the system crystallizes. However, Figure 4.10A showed that T_1 varied with cryomilling time and reflects the fact that the ^1H T_1 of pharmaceuticals is sensitive to changes in crystal quality as well as polymorphic form, purity, particle size, and sample preparation (85, 187, 242). Therefore, any changes to the crystal would lead to error in quantitation. Thus, it would be beneficial from a formulation perspective to develop a quantitative method which can also probe differences in crystals formed.

Method NMTR1 was proposed based on the different T_1 relaxation behavior of crystalline and amorphous solids as a way to account for differences in crystal quality (187, 261). Although the peak at 102.6 ppm contains both crystalline and amorphous phases relaxed according to Equation 4.7, fitting the relaxation data was undesirable as it would require solving for four parameters simultaneously. Previous studies have assumed a constant crystalline T_1 to simplify the fitting procedure (279). The pure crystalline NIF ^1H T_1 was easy to measure but values ranging from 29.3 – 32.4 s have been reported in the literature (85, 269). However, since crystal quality is directly affected by crystallization conditions and the presence of polymers, it follows that processing parameters (i.e., drug

loading, annealing temperature, etc.) will also affect the quality of crystalline material formed (61, 253). Therefore, the pure α-NIF T_1 was not considered constant nor representative of crystals formed during the annealing study. A $T_{1\rho}$-filter was applied to a separate T_1 experiment to eliminate any signal from amorphous NIF and allow for an accurate in-situ measurement of the crystalline T_1.

Figures 4.10B and C showed that differences in T_1 exist between pure α-NIF and α-NIF crystallized in the presence of PVP. The crystalline T_1 increases with drug loading and T_a and is explained by crystallite size and quality. Namely, polymers used to inhibit crystallization (e.g., PVP) caused the formation of imperfect crystals with the degree of imperfections modulated by the crystal growth temperature (T_a). The T_1 of amorphous NIF and PVP remained approximately constant indicating the formation NIF crystals has no effect on the mobility of the remaining ASD and the NIF and PVP remain intimately mixed on an approximately 40 nm domain size (85). SSNMR can therefore be used to distinguish between residual crystals after processing and crystals formed in situ during storage. The differences in crystalline T_1 are visually explained by the polarized light microscopy (PLM) images in Figure 4.11 which show NIF crystals grown at different annealing temperatures.

The difference in crystal size and quality can be explained through the kinetics of crystallization and supersaturation. The Hoffman equation predicts the thermodynamic driving force for crystallization of NIF at 130°C is over three times greater than at 160°C (44). In reality, the difference in driving force is likely greater as the Hoffman equation does not consider the presence of polymer and the relative supersaturation at each temperature. The Flory-Huggins equation predicts nearly a two-fold increase in NIF

solubility from 130°C to 160°C. Specifically, the supersaturation ratio at 130°C is approximately 1.75-times that at 160°C and directly affects both crystal quality and growth rate (280). Equilibrium is reached rather quickly at 160°C while the lower supersaturation ratio at 160°C is more conducive to growing higher quality crystals. Conversely, the greater supersaturation ratio at 130°C results in the faster growth of larger crystals before equilibrium is reached. Additionally, samples at 130°C are also closer to the temperature regime of maximum nucleation rate which increases the likelihood for continuous nucleation during the crystallization process and a reduction in crystal quality (38).

Method NMRT1 is shown to be a useful approach to accurately quantify crystallinity even at high drug loadings while also providing a way to further characterize the entire system. Perhaps most importantly, the T_1 relaxation times determined using method NMRT1 shed light on the changing crystal properties and help to explain the failure of other methods in accurately predicting crystallinity. In particular, the heat of dissolution methods assumes that ΔH_{fus} is constant and representative of crystals formed at all conditions and does not account for imperfect crystals formed in the presence of PVP. In addition, crystal quality further changes as a function of T_a as indicated by a reduction in crystalline T_1. Reduced crystal quality and particle size reduces the effective ΔH_{fus} causing an underestimation of crystallinity and explain the large temperature- and composition-dependent changes in Figure 4.12. Crystalline quality (measured with ^1H T_1 values) increased with annealing temperature with the highest quality crystals most similar to pure α-NIF formed at high T_a. Further, the crystal quality is inversely related to the amount of polymer present (Figures 4.10B and C). As a result, the difference in crystallinity measured with methods OvHd/ DSCHd and other methods decreases with increasing drug loading

(Figure 4.12). Smaller T_1 values at low annealing temperatures indicate the lowest quality of crystals formed in this study whereas high annealing temperatures resulted in T_1 values closer to pure α-NIF. The magnitude of crystallinity deviation between ΔH_{diss}-based methods and other methods also decreases with temperature. Further, the amount of polymer present is inversely related to crystal quality. Crystals formed in the presence of 20% PVP (Figure 4.10B) have a lower T_1 at all annealing temperatures than crystals formed with only 10% PVP (Figure 4.10C). This difference is also reflected in Figure 4.12A, B, and C where the average crystallinity difference between methods OvHd or DSCHd and other methods decreases with increasing drug loading.

The changing crystalline T_1 for crystallization out of an ASD also has implications for quantification using peak deconvolution. Previous techniques including direct exponential curve resolution algorithm (DECRA) or similar reference methods often assume a constant T_1 which we can now assume is incorrect and leads to systematic errors for ASD analysis (260, 261). Similarly, the proposed $T_{1\rho}$-filter method improves upon existing methods to isolate the crystalline and amorphous T_1 times in solid dispersions by requiring minimal optimization and the ability to easily discriminate between physical mixtures and ASDs (262).

Information pertaining to the crystal quality would also be beneficial for troubleshooting or root cause analysis in situations in which the amorphous drug product fails quality testing. Using the ^{1}H T_1 relaxation time measurements provides additional information as to where in the production process the crystals formed. For instance, a short crystalline T_1 measured would suggest the crystals formed during a low-temperature stage of processing while a longer T_1 would indicate high-temperature crystallization.

4.4.3 Equilibrium Crystallinity and Drug-in-Polymer Solubility

The predicted NIF-PVP solubility using SSNMR, PXRD, and T_g-based methods is approximately 1.5% at 25°C and agrees relatively well with values reported in the literature (65, 66). The structurally similar drug, felodipine, has a predicted solubility between 5 and 8% in PVP at 25°C based on the method used regardless of polymer viscosity (68, 157). Other drugs, including indomethacin (IND), have much higher predicted solubilities of 30 – 40% at 20°C in various PVP grades (66, 74, 277). The solubility of some drugs, including NIF and IND may be improved by changes in the polymer, the magnitude of which is dependent on the drug. For instance, at 25°C, IND and NIF are essentially insoluble in PVA but switching to PVP K12 improves IND solubility to nearly 40% while NIF is only increased to 2% (66).

The low crystalline solubility of most drugs in polymers means that high polymer contents are required to thermodynamically stabilize a drug formulated in an ASD. This is undesirable as it would only be feasible for low dose formulations of a highly potent drug (65). Therefore, it seems that the potential of ASDs lies in the ability to kinetically stabilize the amorphous drug. Indeed, the predicted NIF-PVP solubility agrees well with the literature but was only ca. 1.5% at 25°C (65, 66). Still, the drug-polymer solubility is an important system property which, when correctly calculated, remains useful for the rational design of ASD formulations.

The correct measurement of drug-in-polymer solubility using ASD crystallinity requires that equilibrium is reached. While there is more than one way to reach equilibrium, the results of this study can be directly applied to the recrystallization method. The most difficult part of measuring a solid-state solubility is the attainment of equilibrium. A

decreasing chemical potential difference results in the considerable slowing of crystallization kinetics out of a supersaturated dispersion as equilibrium is approached. Although recrystallization is thought to be faster than dissolution/ mixing, it is likely that previous studies measuring drug-in-polymer solubility suffered from not truly reaching equilibrium as the extent of crystallization or mixing is limited by practical in-situ annealing times and DSC heating rates, respectively (65, 66, 69, 157, 277). Failure to reach equilibrium through the recrystallization method will overestimate solubility, possibly resulting in the formulation of an ASD falsely believed to be thermodynamically stable. In this study, variable annealing time experiments showed complete crystallization took up to 24 hours in some system indicating sufficiently long annealing times must be allowed for crystallization to conclude.

Achieving equilibrium is non-trivial as it is dependent on time, temperature, and drug loading. Almost all approaches to determine drug-in-polymer solubility to this point have used DSC for annealing and analysis which limited the time allowed to reach equilibrium to reasonable experimental times. Therefore, three options exist to improve the likelihood that equilibrium is achieved: raise the temperature, increase drug loading, or a non-time-constrained ex-situ annealing method (i.e., oven annealing).

4.4.3.1 In-situ DSC Annealing versus Ex-situ Oven Annealing

In order to achieve equilibrium at lower temperatures either the annealing time must increase, or the thermodynamic driving force must increase through a higher drug loading. There are practical limits on each of these approaches when recrystallizing out of a supersaturated ASD to approach equilibrium. At high temperatures and moderate drug loadings, crystallization occurs quickly, reaching equilibrium relatively fast. Increasing

viscosity reduces molecular mobility and slows crystallization kinetics at lower T_as despite an increasing thermodynamic driving force. The change in system dynamics with temperature limits crystallinity and solubility measurements to high temperatures which are then extrapolated to temperatures of interest.

Annealing would ideally be performed at the temperature of interest (storage or processing) or as low as possible to minimize the extrapolation of the Flory-Huggins equation. Shake-flask methods have been proposed at ambient temperatures however they are limited to polymers with low molecular weight liquid analogues and tend to overestimate solubility (68, 157, 158). In theory, the lower temperature limit, T_a^{limit}, is reached at $T_a = T_g$ but in practice is slightly higher due to slowing crystallization kinetics as T_g is approached with the exact difference in temperature between T_a and T_g being system dependent. At temperatures below T_g, the system is not in equilibrium and may lead to overestimated solubility using the Flory-Huggins equation. Nonetheless, the Flory-Huggins equation is a useful tool for extrapolation when comparing between analytical methods. Thus, it is of great interest to reduce T_a^{limit} through increased drug loadings or new anneal techniques.

The measured solubility is a thermodynamic property and should theoretically be constant regardless of the initial drug loading. Increasing the initial drug loading increases the supersaturation ratio which is directly related to the crystal growth rate. Therefore, changing the thermodynamic driving force (supersaturation ratio) at a constant temperature will only affect the rate at which equilibrium is achieved through faster crystal growth and possibly a decreased nucleation induction time (280).

Selecting an appropriate drug loading for determining solubility from crystallinity measurements is a balance between experimental time, stability, and analytical sensitivity. Low drug loadings are easily quantified by DSC but are sufficiently stabilized by the polymer and require long annealing times. Increasing the drug loading is usually preferred to increasing the annealing time as experimental throughput is improved for DSC-annealing methods. However, DSC struggles to accurately quantify crystallinity in high drug loadings while PXRD and SSNMR may not always be readily available. Hence, it may be preferred to use a lower drug loading that is more representative of the final formulation and more easily quantified by DSC despite the longer annealing times. It is therefore desirable to develop a method to allow sufficient annealing times when lower drug loadings are required.

Annealing in ovens (methods OvTg and OvHd) rather than DSC (methods DSCTg and DSCHd) was proposed as a way to overcome the annealing time limitations of DSC and better represents an annealing process encountered in the drug development process. Comparison of DSC- and oven-annealed samples confirmed that each technique showed equivalent levels of crystallinity across almost all drug loadings and temperatures (oven-annealed crystallinity was slightly lower at high T_as) regardless of whether T_g or ΔH_{diss} was used for quantitation. We believe this is the first instance of using ex-situ crystallization for measuring drug-polymer solubility. Provided that the drug remains chemically stable, this methodology can overcome the experimental time limitations which often restrict the use of recrystallization for solubility calculations to fast-crystallizing drugs and high drug loadings.

4.4.4 Summary of Methods

This research demonstrates that a while variety of analytical methods may be used to determine crystallinity in ASDs, there are caveats to each technique that must be accounted for in order to accurately measure crystallinity. Furthermore, crystallinity may be used to predict drug-in-polymer solubility provided that sufficient annealing time is allowed to reach equilibrium. Table 4.8 provides a summary of each method used and its potential limits to application for drug-polymer solubility measurements.

Table 4.8. Summary of each technique used for drug-in-polymer solubility measurements.

Method	Advantages	Disadvantages
Gordon-Taylor DSC	Relies only on amorphous content Small sample volume	Potentially difficult to measure T_g Assumes GT equation adherence
Heat of Dissolution DSC	Measurement at given temperature Small sample volume	Poor crystallinity prediction (insensitive to crystal quality and polymorphic changes)
PXRD	Potential to use higher drug loadings Sensitive to polymorphic changes and potentially crystal quality	Potentially large sample volume Requires background subtraction Preferred orientation May mistake nanocrystals for amorphous material
SSNMR	Enhanced sensitivity of crystalline and amorphous components Sensitive to polymorphs and crystal quality Potential to apply to formulated products Distinguishes between residual and induced crystals	Large sample volume Long analysis time

These results demonstrate not only the importance of a method which can accurately quantify the crystallinity of various drug-polymer combinations but also the difficulties facing the stable formulation of an ASD. The newly presented use of PXRD and SSNMR to measure drug-in-polymer solubility expands the ways in which a critical formulation parameter can be accessed from a previously DSC-dominated field. However, it is crucial to understand how the strengths and weaknesses of each method limit the applicability of each to certain situations. In situations where all analytical methods are available, concurrently using multiple methods allows for a range of crystallinity and solubility values to be determined including conservative and liberal estimates. PXRD or SSNMR may be preferred as they provide additional information including polymorphic forms and crystal quality which is missed using DSC. Similarly, if only DSC is available, analysis may be limited to moderate drug loadings and or systems with a single polymorph.

4.5   Conclusion

This work compared various analytical methods and techniques for quantifying endogenous crystallinity in an ASD. Annealing-induced crystallinity was analyzed using various DSC, PXRD, and SSNMR techniques. DSC measurements of the T_g (GT method) accurately quantified crystallinity while ΔH_{diss} was a poor measure of crystallinity. PXRD and two different SSNMR methods agreed well and also provided a good measure of crystallinity. The results of the crystallinity analysis at various temperatures were used to determine the solubility of NIF in PVP via extrapolation of the Flory-Huggins equation. At moderate drug loadings, the GT method, PXRD, and SSNMR all produced results in agreement with published literature values. While the GT or other DSC methods are the

industry standard, they are often limited by high drug loadings or to 'ideal' systems. PXRD and SSNMR can overcome these limitations and expand crystallinity and drug-polymer solubility measurements to high drug loadings and non-ideal systems including where T_g is poorly resolved, T_g is similar between drug and polymer, multiple polymorphs exist, and/ or slow crystallization kinetics. For the first time, it was shown that ex-situ annealing in ovens provided equivalent results to in-situ DSC annealing and provides a way to increase experimental throughput while ensuring equilibrium crystallinity was achieved. Additionally, PXRD and SSNMR enable the advanced in-situ characterization of the equilibrated system beyond what is possible with DSC. A new SSNMR T_1 relaxation time method showed that crystalline T_1 changes with annealing conditions and must be accounted for to obtain accurate quantitative data. In addition, SSNMR may be used to distinguish between residual crystals and crystals formed during storage. The PXRD or either SSNMR technique can help improve the reliability of measurements and expand the number of systems able to be analyzed for drug-polymer solubility.

CHAPTER 5: IMPACT OF STORAGE CONDITIONS ON THE PHYSICAL STABILITY OF AMORPHOUS SOLID DISPERSIONS CONTAINING TWO STRUCTURALLY SIMILAR DRUGS

5.1 Introduction

A significant number of drugs on the market and drug candidates in development suffer from poor solubility (281). An increasingly common formulation strategy to improve dissolution and apparent solubility is the amorphization of drugs. The improved solubility of the amorphous state is offset by its inherent physical instability and propensity to recrystallize. Homogeneous incorporation of the drug with a water-soluble polymer to create an amorphous solid dispersion (ASD) has been shown to result in improved solubility relative to the crystalline state while also improving stability relative to the purely amorphous drug.

The drug should remain in the amorphous state during manufacture, storage, and dissolution to maintain the solubility advantage relative to the crystalline form. For example, Hate et al. showed that residual crystallization in tacrolimus-HPMC leads to decreased solubility, absorption, and bioavailability with the effects exacerbated as crystallinity increases (247). Extensive research has been done to improve the understanding of how to stabilize ASDs against crystallization (282-286). This includes strategies for the selection of polymers, processing techniques, storage conditions, and their effect on product performance. Despite a general knowledge of amorphous stability, ASDs must still be analyzed over the course of a stability study to ensure crystallization is inhibited over the course of the shelf life.

There are three main ways by which a polymer typically acts to prevent or delay crystallization in ASDs depending on the drug-polymer combination and their relative concentrations: antiplasticization, specific interactions, and dilution/ physical barrier. First, antiplasticizing polymers raise the glass transition temperature (T_g) of the mixture relative to the pure drug while reducing drug's molecular mobility. Second, the polymer may also form specific interactions with the drug when certain functional groups are present on the drug and polymer. These bonds may form in the amorphous state and resist recrystallization. The strength and number of drug-polymer interactions are thought to correlate directly with the physical stability of the ASD (282, 287). Systems in which the drug-polymer interactions are energetically more favorable than crystalline drug-drug and polymer-polymer interactions are expected to have improved amorphous stability (58). Third, polymers present in high enough concentrations can dilute the drug molecules in the solid solution and/ or may act as a physical barrier between drug molecules thereby stabilizing the amorphous phase (89, 288). Understanding and applying the specific mechanisms by which a polymer stabilizes the amorphous API improves the likelihood that the ASD will remain stable over its shelf life.

The ability of ASDs to resist crystallization is a complex relationship involving storage temperature, drug loading, and other factors, such as humidity, which can impact molecular mobility. This complicates the ability to predict the shelf life of an amorphous formulation. Kinetic data observed in the supercooled liquid state can ideally be extrapolated to predict crystallization near and well below T_g. However, unlike chemical degradation, physical instability (i.e., crystallization) typically does not follow Arrhenius kinetics and cannot necessarily be extrapolated to relevant storage conditions. Molecular

mobility and various thermodynamic properties are dynamic and their temperature dependence can change dramatically as the ASD passes through the T_g, yet some molecular motions have been successfully linked to crystallization (20). Crystallization onset was coupled to molecular mobility above T_g to predict crystallization onset below T_g from relaxation measurements in amorphous sucrose and three poorly soluble drugs (114, 289). Later, these results were expanded to ASDs (290). Similarly, dynamic dielectric spectroscopy was used to predict stability in amorphous itraconazole and itraconazole-ASDs (287, 291). However, their predictions only were valid above the T_g. The molecular motions contributing to crystallization above T_g (α-relaxation) may not necessarily be the main contributors to crystallization below T_g (Johari-Goldstein β-relaxations). Conversely, Greco et al. did not measure molecular mobility yet were still successful in predicting crystallization onset below T_g over a year after thermal and gravimetric measurements above T_g (292). Therefore, the stability of amorphous systems must be observed both in the glassy and supercooled liquid states with particular attention paid near T_g where viscosity and heat capacity change drastically.

Predicting the rate of crystallization in some organic systems is further complicated by an acceleration in crystal growth kinetics near and just below T_g. Crystal growth rate in supercooled liquids is normally well predicted by diffusivity. However, certain molecules unexpectedly exhibit an increase in growth rate of up to four orders of magnitude near T_g relative to their diffusion-controlled crystal growth rate. This anomalous change in crystal growth kinetics is termed glass-crystal (GC) or diffusionless crystal growth. It was first observed in o-terphenyl and has since been studied extensively (51-53). The exact origin of this anomalous change in growth rate is still unknown although multiple theories have

been proposed including homogeneous-nucleation-based crystallization, tension-induced interfacial mobility, crystal growth by local mobility, and, recently, free surface accelerated crystal growth (52, 54, 55, 293). Diffusionless crystal growth has been observed in indomethacin and 99-1 (w/w) IND-polyvinylpyrrolidone ASDs and may help to explain experimental observations herein (294, 295). To the best of the authors' knowledge, GC growth has only been observed to affect crystal growth rate. However, its often difficult to separate the two steps of crystallization: nucleation and crystal growth (131). Presumably, the similar phenomenon (now termed 'diffusionless crystallization') could be observed for nucleation rate or crystallization onset times. Regardless, the existence of diffusionless crystallization underscores the need for sufficient characterization of ASD stability near T_g in addition to accelerated stability in the supercooled liquid state.

The purpose of this study was to compare the physical stability of indomethacin (IND)-polyvinylpyrrolidone (PVP) and indomethacin methyl ester (INDME)-PVP ASDs containing different ratios of drug and polymer that were stored both above and below T_g. IND is a poorly soluble nonsteroidal anti-inflammatory drug that has been used extensively as a model drug for ASD formulations. PVP is a commonly used polymer to help stabilize amorphous formulations through antiplasticization and the formation of drug-polymer hydrogen bonds (84, 284). INDME is a structural analogue of IND which lacks the ability to donate hydrogen bonds through the carboxylic acid and provides a unique opportunity to directly measure the impact of hydrogen bonding on physical stability while minimizing confounding structural effects. ASDs of varying drug-polymer ratios were prepared and stored at temperatures 7-40°C for INDME and 40-100°C for IND. It was found that the crystallization onset time of both IND and INDME is exponentially related to the polymer

content in the dispersion. INDME generally crystallized faster than IND at a constant drug loading above T_g but crystallization rates were much closer in the glassy state. IND crystallization occurs faster than expected near and below T_g while INDME onset times above T_g could be extrapolated below T_g. IND crystallization was governed by a combination of storage temperature and drug-polymer hydrogen bonding while INDME lacks strong hydrogen bonds with PVP and its crystallization is controlled only by antiplasticizing effects. IND was better stabilized by PVP above T_g while INDME was better stabilized near and below T_g. For the first time, diffusionless crystallization was observed in amorphous systems with formulation-relevant polymer contents. Changes in molecular mobility, similar hydrogen bonding configurations between the crystalline and amorphous state, and an increased thermodynamic driving force are found to contribute to diffusionless crystallization in IND-PVP ASDs.

5.2 Materials and Methods

5.2.1 Materials

The γ-polymorph of IND (lots YT4QE-OC and YT4QE-BP) was purchased from MilliporeSigma (St. Louis, MO) and used as received in all experiments. PVP K12 (lot 0001970609, MW = 4 – 6 kg/mol) was a generous gift from Ashland Inc. (Covington, KY). PVP was dried overnight in a vacuum oven at 75°C and stored over Drierite at all times to minimize absorbed moisture prior to use. Indomethacin methyl ester (INDME) was synthesized in a method similar to Yuan (154). 7.5 g of IND (lot YT4QE-BP), 150 mL high-purity methanol, 0.375 mL sulfuric acid, and ca. 2 g of molecular sieves (3Å, 4x8 mesh size) were refluxed at 70°C while stirring for 40 hours. The reaction product was

filtered and purified by recrystallization and repeated washing with methanol and milliQ water. INDME purity was confirmed through thin layer chromatography, powder X-ray diffraction (PXRD), differential scanning calorimetry (DSC), thermogravimetric analysis (TGA), and ^{1}H nuclear magnetic resonance (NMR) spectroscopy. The chemical structures of IND, INDME, and PVP are shown in Figure 5.1.

Indomethacin
(IND)

Indomethacin Methyl Ester
(INDME)

Polyvinylpyrrolidone
(PVP)
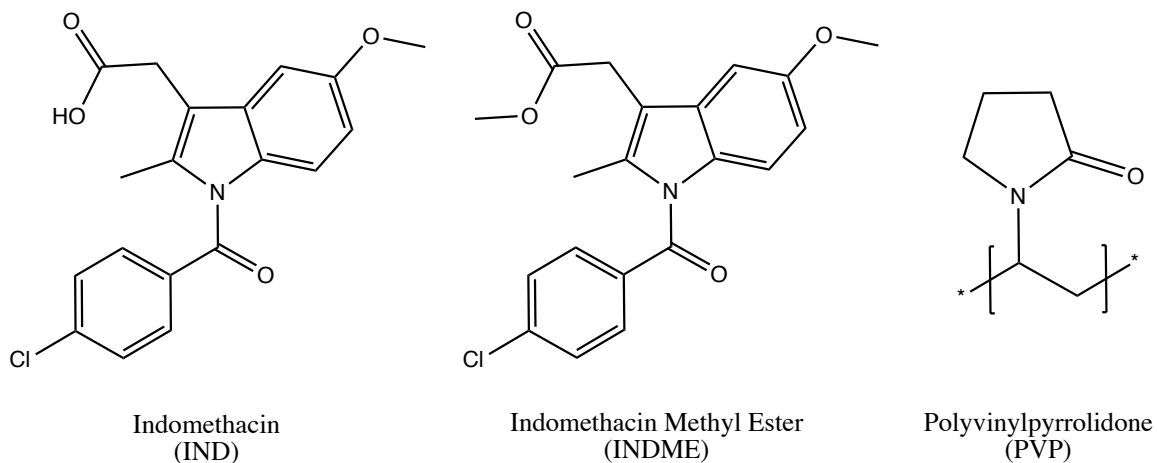
Figure 5.1. Chemical structures of indomethacin (IND), indomethacin methyl ester (INDME), and polyvinylpyrrolidone (PVP).

5.2.2 Preparation of Amorphous Solid Dispersions

ASDs of IND or INDME and PVP were prepared by a cryo-mill and melt-quench method. Physical mixtures were milled using a SPEX 6775 Cryogenic Grinder (Metuchen, NJ). A 2 minute precool was followed by 6 cycles of 2 minutes grinding and 2 minutes cool-down. IND or INDME samples were equilibrated to room temperature then melted in Teflon beakers at 190°C or 150°C, respectively, for 5 minutes. The molten sample was then placed directly into liquid nitrogen. The resulting glassy ASDs containing IND were lightly ground into a fine powder using a mortar and pestle. ASDs containing 80% (w/w) or more of INDME were not ground due to its low T_g and stickiness at room temperature.

Powdered samples were dried overnight at 25°C using a vacuum oven to remove any moisture absorbed during formulation.

5.2.3 Differential Scanning Calorimetry

DSC experiments were performed using a Discovery DSC 2500 (TA Instruments, New Castle, DE). They system was purged with 50 mL/min nitrogen gas and cooled with a RCS90 cooling accessory. Indium and sapphire were used to calibrate the DSC for temperature and heat capacity, respectively. Unless otherwise noted, 3 – 5mg of sample was placed in Tzero Hermetic Aluminum pans with a single pinhole.

5.2.3.1 Glass Transition Temperature Measurement

The T_g of dried ASDs and pure amorphous IND or INDME were determined using modulated DSC (+/- 0.7°C every 40 seconds). IND-PVP ASDs were first heated from 20°C to 200°C at a rate of 10°C/min, cooled to -10°C at -30°C/min, then reheated to 200°C at 5°C/min. INDME-PVP ASDs were heated from 20°C to 150°C at 10°C/min, cooled to -50°C at -30°C/min, then reheated to 150°C at 5°C/min.

The T_g was recorded as the midpoint of the glass transition event and used to assign storage temperatures such that the ASDs were stored both above and below the T_g. The dried ASDs were divided into scintillation vials and placed into desiccators filled with Drierite. Desiccators containing IND ASDs were placed into ovens at between 40°C and 100°C for at least 6 months. Desiccators holding INDME ASDs were stored at between 7°C and 40°C for a minimum of 2 months.

5.2.3.2 Crystallization Thermodynamics

The thermodynamic driving force for crystallization of pure drug above T_g was estimated using the Hoffman equation (Equation 5.1) (44).

$$\Delta G_C = \frac{\Delta H_{fus}(T_m - T)T}{T_m^2} \tag{5.1}$$

The change in free energy (ΔG_C) upon crystallization at a given temperature (T) is determined using pure drug melting temperature (T_m) and heat of fusion (ΔH_{fus}). T_m and ΔH_{fus} were determined using standard DSC at a 2°C/min heating rate. The Hoffman equation assumes that enthalpy is a linear function of temperature for both the supercooled liquid and crystal. This is not necessarily true, particularly near T_g (58). Therefore, configurational properties were also determined based on the difference in the amorphous ($C_{P,amorph}$) and crystalline ($C_{P,crystal}$) heat capacity. Equations 5.2 – 5.5 shows the configurational heat capacity ($C_{P,config}$), enthalpy (H_{config}), entropy (S_{config}), and free energy (G_{config}) (56).

$$C_{P,config} = C_{P,amorph} - C_{P,crystal} \tag{5.2}$$

$$H_{config} = \Delta H_{fus} - \int_T^{T_m} C_{P,config} dT \tag{5.3}$$

$$S_{config} = \Delta S_m - \int_T^{T_m} \frac{C_{P,config}}{T} dT \tag{5.4}$$

$$G_{config} = \Delta H_{config} - T\Delta S_{config} \tag{5.5}$$

Here, the entropy of fusion (ΔS_{fus}) equals $\Delta H_{fus}/T_m$. Configurational properties were determined using a modulated DSC heat-cool-heat procedure of 2°C/min heating, 30°C/min cooling, +/- 0.5°C every 60 seconds.

5.2.4 Powder X-ray Diffraction

Samples were analyzed via PXRD for crystallization. The samples were scanned initially (before storage at elevated temperatures) and then periodically for upwards of 9 months using either a Rigaku MiniFlex 600 PXRD or Rigaku SmartLab diffratometer (Rigaku Americas, The Woodlands, TX). Initial powder samples were used 'as is' in the

MiniFlex operating at 15mV and 40mA. Approximately 10 mg of aged sample was removed from the scintillation vial at each time point and scanned using the SmartLab (40mV and 44mA). Each sample was scanned from 5 – 50° 2θ at 2°/min, and 0.02° step size in Bragg-Brentano mode with a Cu-Kα radiation source. Diffraction peaks were indicative of sample crystallization. All INDME stability was acquired using the Smartlab diffractometer.

5.2.5 Fourier Transform Infrared Spectroscopy

The hydrogen bonding of samples was studied using Fourier Transform Infrared Spectroscopy (FTIR) with an Attenuated Total Reflectance (ATR) diamond crystal attached. A Nicolet iS50 FTIR (Thermo Fisher Scientific, Waltham, MA) or Bruker Vertex 70 FTIR spectrometer (Bruker Corporation, Billerica, MA) was used for the analysis. Powdered samples were placed on the diamond ATR crystal (single bounce, 42° angle of incidence). Each sample was scanned 64 times from 4000 to 400 cm^{-1} with 4 cm^{-1} resolution. Experiments were repeated in triplicate with the mean spectra reported. An ATR correction was applied to account for varying evanescent wave penetration as a function of wavelength and a rubber band baseline correction was also applied. The carbonyl peak intensity in each spectrum was normalized for comparison purposes.

5.3 Results

The purpose of this study was to investigate the effects of drug-polymer hydrogen bonding on the physical stability of ASDs by comparing the crystallization onset times of IND-PVP and INDME-PVP ASDs. ASDs were first prepared and characterized to ensure that they were fully amorphous and consistent with prior studies of the identical ASDs (84,

89, 154, 284). The ASDs were then stored around their glass transition temperature and monitored for signs of crystallization using PXRD.

5.3.1 Initial Amorphous Solid Dispersions

All IND-PVP ASDs were analyzed to confirm that their formulation resulted in the complete loss of crystallinity. All initial IND- and INDME-PVP ASDs were X-ray amorphous as evidenced by the presence of broad amorphous halos and the lack of sharp peaks in the PXRD diffractograms (Figure 5.2).
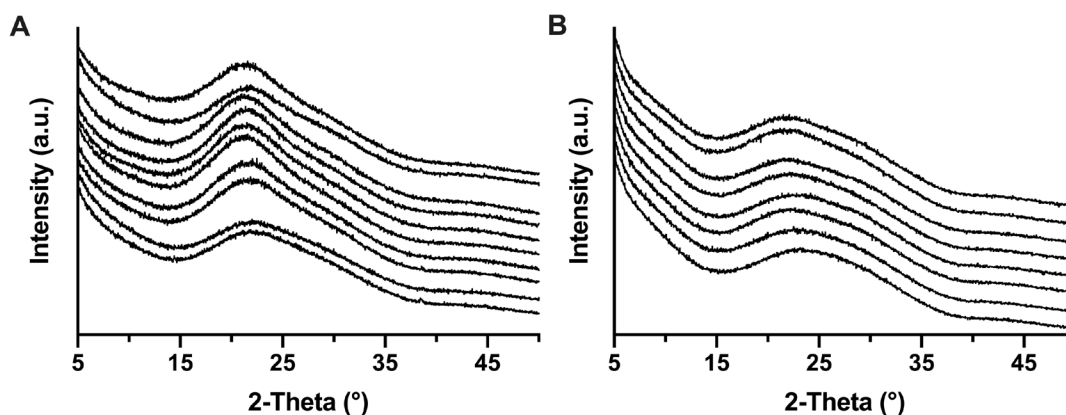
Figure 5.2. Initial powder diffraction patterns for (A) IND-PVP and (B) INDME-PVP ASDs. Drug loading increases from 65% (top) to 100% (bottom).

Each initial sample was also analyzed using modulated DSC with a heat-cool-heat cycle. The first heating cycle showed a single T_g, along with the absence of a melting endotherm, indicating the melt-quench procedure created fully amorphous ASDs. Heating to 200°C erased any thermal history attributed to the formulation process. The second heating cycle T_g corresponds to the 'ideal' ASD and was used to assign storage temperatures. Increasing drug content results in a linear decrease in the observed T_g from the second heating scan (Figure 5.3).
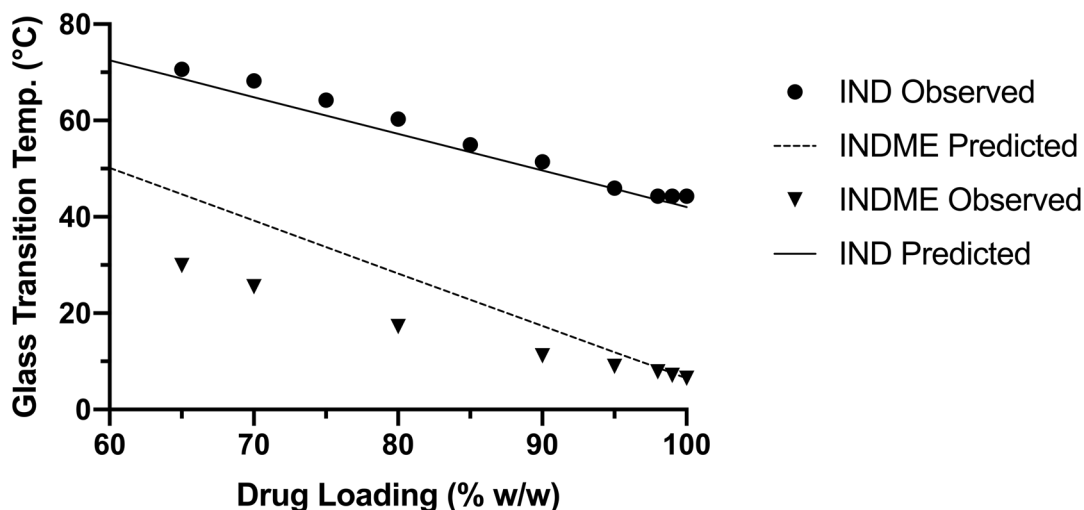
Figure 5.3. Observed and predicted (Gordon-Taylor equation) glass transition temperatures for IND- and INDME-PVP ASDs. T_g values shown correspond to the second heating cycle.

The T_g of IND dispersions decreases from 70.6°C in 65-35 ASDs to 44.2°C in pure IND and is well predicted by the Gordon-Taylor equation. The T_g of INDME dispersions decreases from 29.9°C to 6.5°C between 65% and 100% INDME and shows a large negative deviation from the Gordon-Taylor equation. Deviations from the Gordon-Taylor equation have previously been related to the presence of specific drug-polymer interactions such as hydrogen bonds. However, specific interactions do not always result in deviations nor does adherence to the Gordon-Taylor equation necessarily indicate the absence of specific interactions (58, 75, 256, 296). Previous studies show extensive drug-polymer hydrogen bonds are present in IND-PVP ASDs yet its T_g is well predicted by the Gordon-Taylor equation as IND-IND bonds are approximately the same strength as IND-PVP bonds formed (84, 89, 126, 284). The presence and degree of specific drug-polymer

interactions in INDME-PVP is not as well understood currently and may contribute to the significant deviation from the Gordon-Taylor equation.

ATR-FTIR spectra were acquired for pure crystalline and amorphous drugs, polymer, and initial ASDs to probe any specific interactions that may exist (Figure 5.4). As mentioned above, extensive drug-polymer hydrogen bonding exists in IND-PVP ASDs and the hydrogen bonding states associated with the carbonyl stretch of IND-containing systems have been assigned previously (Figure 5.4A) (67, 84). Briefly, IND (carboxylic acid)-PVP (amide) hydrogen bonds in ASDs replace the IND carboxylic acid dimers found in γ-IND (89).
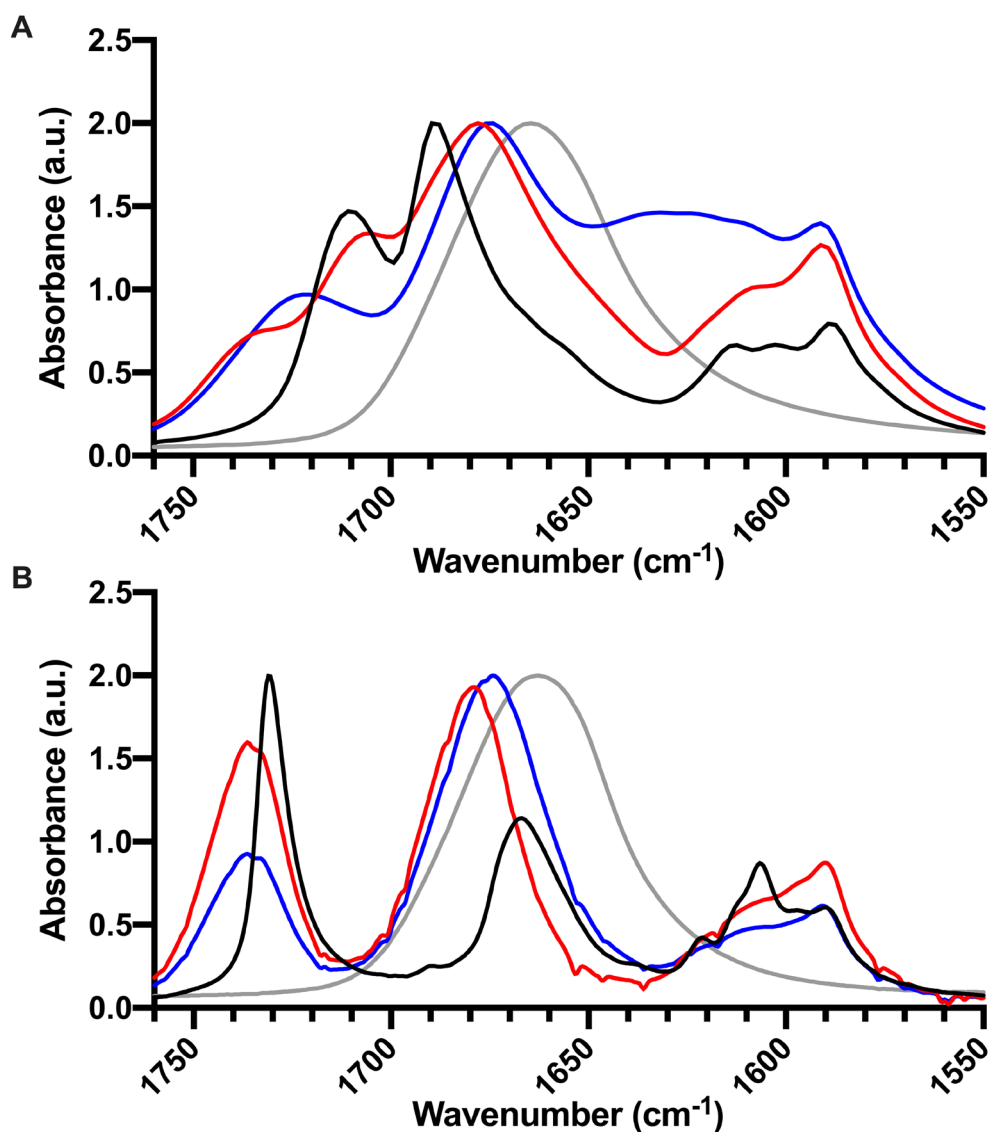
Figure 5.4. The carbonyl region of ATR-FTIR spectra of initial (unaged) materials for (A) IND and (B) INDME. Crystalline drug (black), amorphous drug (red), 80-20 ASD (blue), and PVP K12 (gray).

Analogous FTIR peak assignments can be made in INDME systems based on its similar chemical structure to IND (Figure 5.4B). Despite having no strong hydrogen bond donor groups, weak CH-O intermolecular hydrogen bonds between the amide oxygen and

aromatic protons, as well as a Cl-O halogen bond with the carboxylic acid, are reported in crystalline INDME (297). Presumably some degree of these weak interactions also exists in amorphous INDME. No direct evidence of INDME-PVP specific interactions were found, however weak intermolecular INDME interactions causing subtle spectral changes are not easily detected using FTIR and may help to explain the deviation of INDME-PVP ASDs from T_g predicted by the Gordon-Taylor equation.

IND-PVP and, to some extent, INDME-PVP ASDs have been studied previously using solid-state nuclear magnetic resonance (SSNMR) spectroscopy. SSNMR confirmed the presence of IND-PVP hydrogen bonds previously detected using DSC and FTIR and was also used to quantify the relative populations of intermolecular hydrogen bonded species as a function of drug loading (84, 89, 284). INDME showed no obvious signs of hydrogen bonding with PVP via SSNMR although it has been studied in less detail than IND (154). Additional SSNMR analysis may help to explain its large T_g deviations from the Gordon-Taylor equation.

5.3.2 Stability Study

The effects of drug loading, storage temperature, and drug-polymer hydrogen bonding on the physical stability of ASDs were investigated by comparing the crystallization tendencies of IND and INDME as well as their dispersions with PVP. ASDs were stored under identical conditions relative to their glass transition temperature to isolate the effects of hydrogen bonding on crystallization onset time in two structurally similar compounds.

5.3.2.1 Storage Conditions

Samples were stored between $T/T_g = 0.89$ and $T/T_g = 1.17$ to directly compare IND and INDME crystallization. Normalizing storage temperature to T_g allowed for the direct comparison of compounds with widely varying T_g values (Figure 5.3). The effects of water were minimized by storage over desiccant prior to testing for crystallization. Certain samples were stored for longer periods of time to confirm whether crystallization trends in the supercooled liquid continue at lower temperatures and/ or drug loadings.

Samples were assayed using PXRD at various time points starting at 30 minutes for the highest drug-loadings or temperatures. Most samples were analyzed after one day and then twice a week for two months after which the samples were analyzed weekly. After six months, extended stability samples were scanned monthly.

IND diffraction patterns showed peaks consistent with γ-IND (298). No other peaks were present indicating all IND-PVP ASDs crystallized as the stable γ-IND polymorph, regardless of drug loading or storage temperature. Similarly, there is only one reported INDME polymorph. All INDME diffraction peaks are consistent with the only reported INDME crystal structure (297). This indicates consistency in crystallization of INDME across the design space.

5.3.2.2 Crystallization Onset Time

The crystallization onset time (t_c) is defined as the earliest time at which crystals are detectable and was determined when peaks emerged in PXRD patterns. Figure 5.5 shows the onset of crystallization for ASDs stored at varying drug loadings and temperatures.
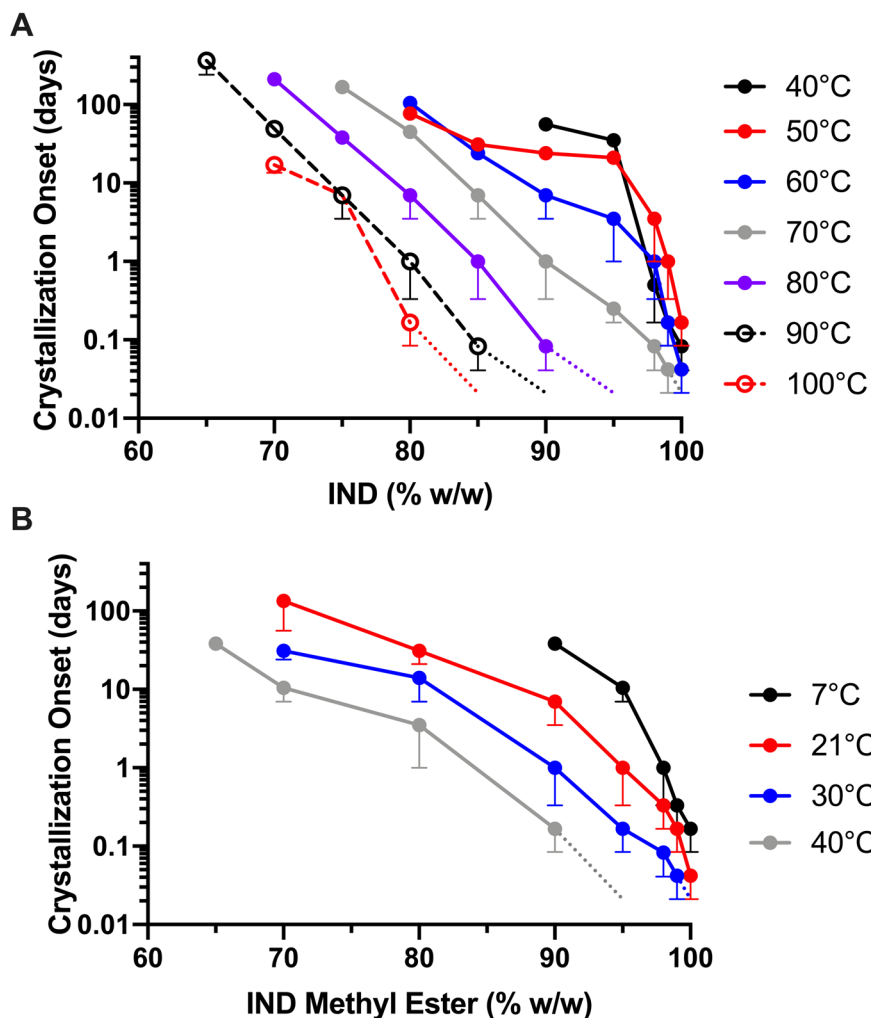
Figure 5.5. Crystallization onset time detected by PXRD as a function of drug loading at constant temperature for (A) IND-PVP and (B) INDME-PVP ASDs. Error bars correspond to the difference between the last measurement and observed crystallization onset time. The dotted lines at high temperatures and drug loadings indicate that crystallization was observed at the earliest observation point (30 minutes).

The time for crystallization onset to occur decreased exponentially with drug loading and storage temperature for both IND and INDME. Pure drugs crystallized in less than a day at all storage temperatures. In fact, IND and INDME crystallized in less than 30

minutes when stored in the supercooled liquid state above 70°C and 30°C, respectively. A linear relationship was observed for the plot of log(t_c) versus IND content for ASDs stored where all drug-polymer concentrations studied were in the supercooled liquid state ($\geq$ 70°C). A similar linear relationship was observed for the plot of log(t_c) versus drug INDME content for ASDs stored where all drug-polymer concentrations studied were in the supercooled liquid state ($\geq$ 35°C). The slope of IND-PVP ASDs in Figure 5.5 was generally greater than INDME-PVP ASDs indicating that PVP addition provided a greater stabilizing effect against IND crystallization than INDME crystallization in most cases.

At lower temperatures ($\leq$ 60°C) approaching T_g, IND crystallization is no longer predicted by trends observed at higher temperatures (see Figure 5.6). The rate of IND crystallization changes as a function of drug loading with crystallization occurring faster than expected at low drug loadings based on trends at high drug loadings. The unexpected change in t_c is highlighted by samples having longer crystallization onset times at higher temperatures which is the opposite of the observed trend above T_g. For example, 80-20 IND-PVP ASDs (T_g = 60.3°C) crystallized in 105 days at 60°C while the same dispersion at 50°C (T_g – 10°C) crystallized in only 77 days. The changes in crystallization kinetics are investigated further, including a discussion of their potential causes and implications.

5.3.2.3 Crystallization Near the Glass Transition Temperature

Figure 5.6 shows the crystallization onset time as a function of the scaled inverse temperature, T_g/T. This accounts for the differences in T_g between IND- and INDME-ASDs and allows for the direct comparison of molecular mobility in each system relative to its T_g rather than storage temperature.
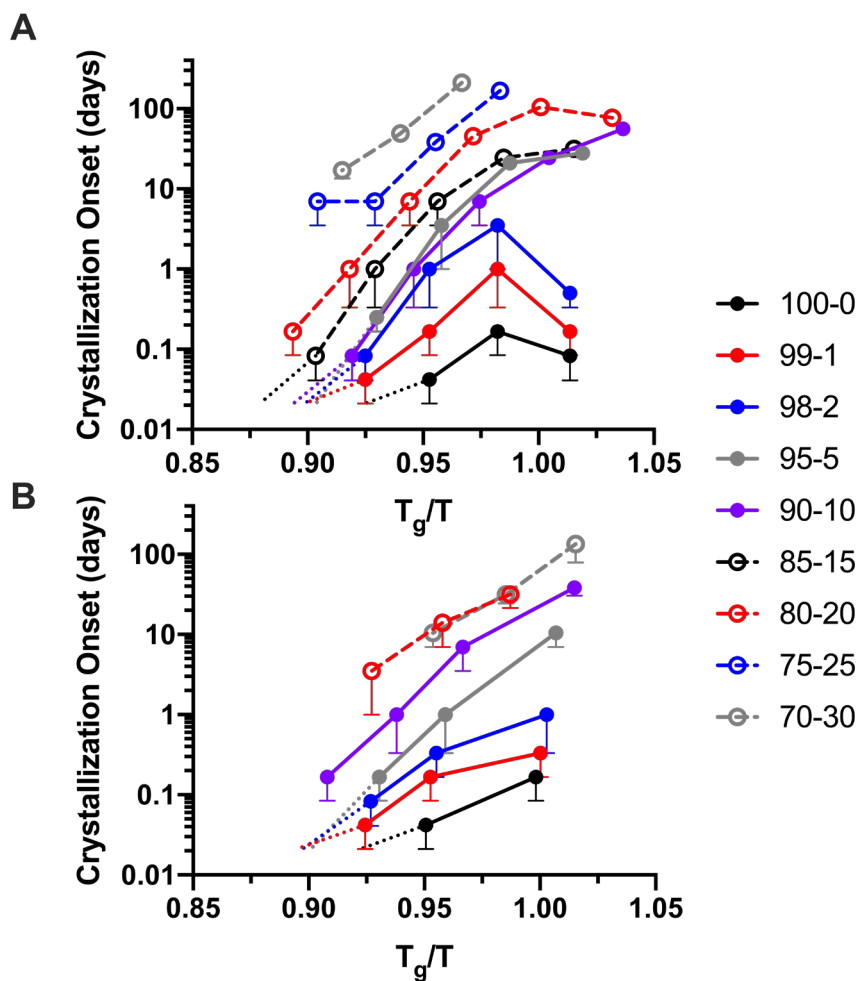
Figure 5.6. Crystallization onset time as a function of the inverse temperature relative to T_g for (A) IND-PVP and (B) INDME-PVP ASDs. Error bars correspond to the difference between the last measurement and the observed crystallization onset time. The dotted lines at high temperatures and drug loadings indicate that crystallization was observed at the earliest observation point (30 minutes).

IND t_c exponentially increases with decreasing temperature in the supercooled liquid state but a negative deviation (beginning at approximately $T_g/T = 0.97$) from the exponential trend is observed near T_g indicating crystallization occurs faster than expected in the glassy state. The magnitude of the deviation is directly dependent on drug loading

and allows Figure 5.6A to be further divided into three regions based on drug loading (region I > 95% IND, 95% ≥ region II ≥ 80%, region III < 80%). In region I, t_c decreases near and slightly below T_g for 100-0, 99-1, and 98-2 IND-PVP ASDs. Region II still sees a non-Arrhenius change in t_c with temperature around T_g although the changes are less drastic than in region I. Furthermore, significant overlap exists in this region across multiple drug loadings as drug-polymer hydrogen bonding becomes increasingly important for stabilizing the system. No IND crystallization was observed below T_g in region III. This was consistent with trends observed in the supercooled liquid state when extrapolated into the glassy state. This suggests that any crystallization observed below T_g during an extended stability study can be predicted by observed t_c above T_g and any deviations would be expected to be minimal. For all concentrations of INDME, the $\log(t_c)$ of INDME (Figure 5.6B) follows a linear relationship with T_g/T from the supercooled liquid into the glassy state.

Figure 5.7 is similar to Figure 5.6 but shows the relationship between the natural logarithm of the inverse t_c and the scaled inverse temperature, T_g/T, at constant drug loadings. The inverse of the crystallization onset time can be interpreted approximately as the rate of crystallization (299, 300). Further, the isothermal crystallization activation energy can be determined from the slope of the lines for $T_g/T < 0.97$.
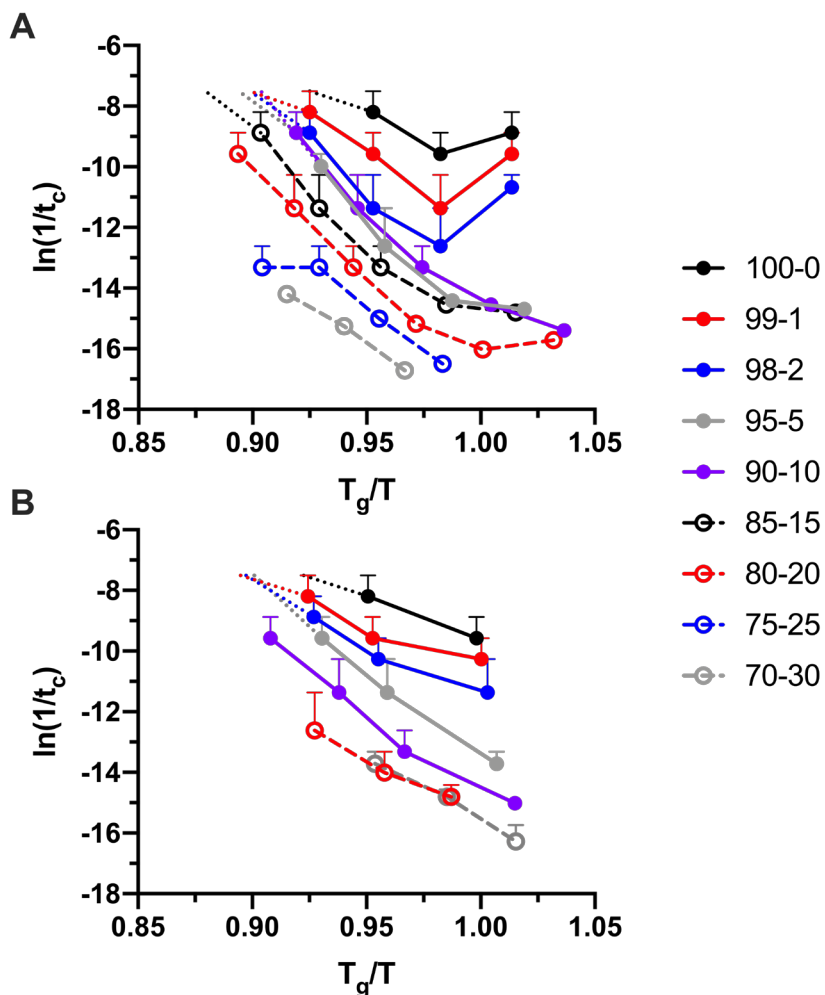
Figure 5.7. The rate of crystallization as a function of scaled inverse temperature for (A) IND-PVP and (B) INDME-PVP ASDs. Error bars correspond to the difference between the last measurement and the observed crystallization onset time. The dotted lines at high temperatures and drug loadings indicate that crystallization was observed at the earliest observation point (30 minutes).

Figure 5.7 shows the crystallization kinetics in the supercooled liquid ($T_g/T < 1$) and glassy states ($T_g/T > 1$). The rates of pure drug crystallization of IND and INDME are approximately the same above T_g and only varies near T_g for IND. The rate of crystallization increases with increasing drug loading in both IND and INDME ASDs

although this difference decreases at lower drug loadings (Figure 5.7A and B). In general, the rate of crystallization decreases with temperature for IND and IND-PVP ASDs. However, the same deviation seen in Figure 5.6A is also observed near T_g for IND systems. Figure 5.7A can similarly be divided into the same three regions based on IND content. The slope of the lines indicates the activation energy required for isothermal crystallization of either IND or INDME in the presence of absence of PVP. The change in slope as T_g is approached in Figure 5.7A may indicate a change in the rate-limiting step of crystallization (54).

Figure 5.8 plots the activation energy of isothermal crystallization onset (ΔE_a) above T_g as a function of drug loading (measured from the slopes in Figures 5.7A and B) for IND and INDME ASDs. Figure 5.8 also overlays the different forms of amorphous IND that exist as a function of drug loading based on a previous study by Yuan et al. which used solid-state NMR to quantify the different hydrogen bonding motifs that exist between IND and PVP (89). It should be noted that Yuan et al. acquired the quantitative speciation data at 20°C (well below T_g) and may not accurately reflect the species present at the temperature range used to determine ΔE_a (above T_g). For comparison purposes, the data points from Figure 11A in Yuan et al. (89) and this study are displayed in the same chart.
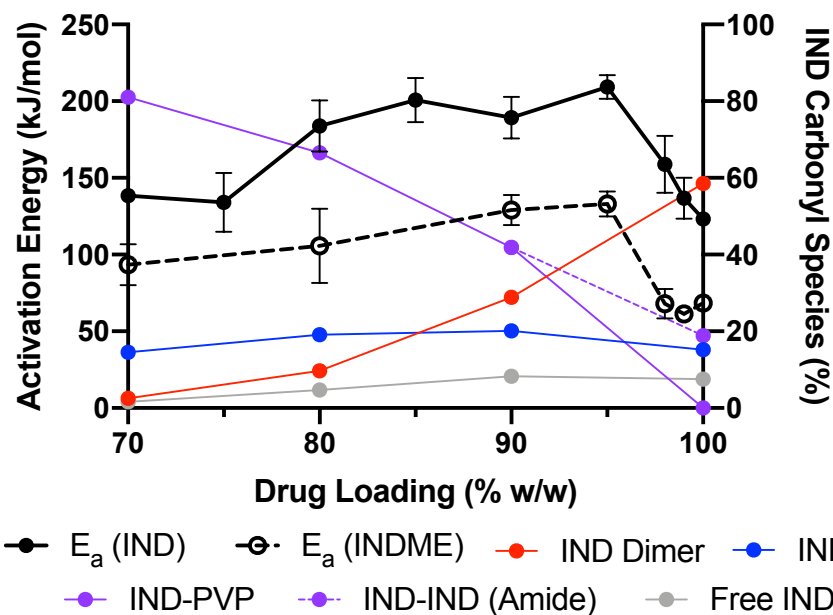
Figure 5.8. Crystallization activation energy for IND and INDME in the presence of varying amounts of PVP. The relative populations of IND species (determined by Yuan et al. using SSNMR (89)) are also shown. Crystallization observed at the earliest time point (30 minutes) was not included in activation energy calculations. Error bars correspond to the difference between the activation energy determined used either the last measurement prior to crystallization and the observed crystallization onset time.

ΔE_a generally increases with increasing drug loading over the concentration range investigated, reaching a maximum between 85% and 95% drug loading before decreasing sharply towards pure drug. The ΔE_a of IND crystallization is 1.5- to 2.3-times greater than INDME across all drug loadings. This corresponds to an average ΔE_a of 67 kJ/mol which is well within the range of reported hydrogen bond strengths (83). ATR-FTIR provided no evidence of INDME-PVP hydrogen bonding. However, extensive hydrogen bonding exists in IND-PVP ASDs which was highlighted previously by Yuan et al. and is applied here to provide insights into the physical stability of ASDs (89). It also appears that changing E_a

also corresponds to changes in hydrogen bonded species. While the specific changes in hydrogen bonded species shown in Figure 5.8 were determined below T_g, speciation still likely changes with drug loading above T_g although the dimer is expected to dominate at higher temperatures (89). At 70% IND, virtually all IND-IND dimers and free IND have been eliminated. Interestingly, this drug loading also corresponds to the point at which accelerating crystallization was no longer observed. Quantitative analysis via SSNMR is currently underway to investigate the changes in hydrogen bonding above T_g. The implications for changing hydrogen bond speciation and activation energy will be discussed further in section 5.4.2.2.

5.3.2.4   Differences in IND and INDME Crystallization

Various molecular, physicochemical, and thermodynamic properties were explored to explain the difference between IND and INDME crystallization kinetics near the glass transition, particularly the unexplained increase in IND crystallization rate. First, DSC measured enthalpic recovery to probe molecular mobility just below T_g. Data was fit to the Kohlrausch-Williams-Watts equation however, at 40°C (IND) and 2.7°C (INDME), molecular mobility was still too high to measure meaningful structural relaxation times (110).

Next, the thermodynamic driving force for crystallization (i.e., the difference in Gibbs free energy between the crystalline and amorphous state) was investigated. As outlined in section 5.2.3.2, the Hoffman equation (Equation 5.1) used physical properties of the pure drug to predict free energy differences (44). Figure 5.9A shows the free energy change upon crystallization for IND and INDME in the supercooled liquid state. Similarly, the configurational heat capacity was calculated from the difference in the amorphous heat

capacities of both drugs and used to calculate configurational properties (Equations 5.2 – 5.5). Figure 5.9B shows the configurational enthalpy (H_{config}), entropy (S_{config}), and free energy (G_{config}) as a reduced temperature, $(T - T_g)/(T_m - T_g)$.
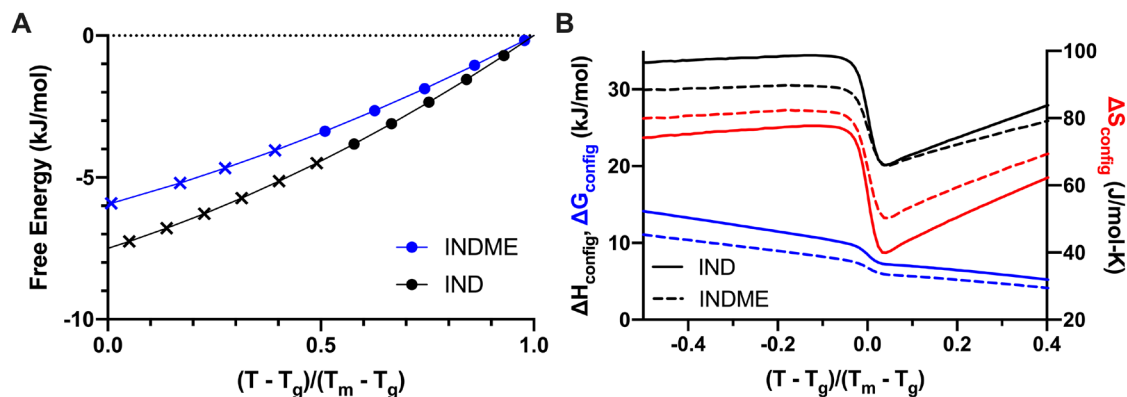
Figure 5.9. (A) Thermodynamic driving force for crystallization as a function of reduced temperature as predicted by the Hoffman equation. (B) Configurational thermodynamic properties as a function of reduced temperature. Configurational enthalpy is shown in black; configuration entropy is in red; and configurational free energy is in blue.

Both the Hoffman equation (Figure 5.9A) and the configurational properties (Figure 5.9B) predict the free energy change upon crystallization to be greater for IND at all temperatures between T_g and T_m relative to INDME. While the absolute value of free energy change was greater by configurational properties, the relative difference in free energy change is the same. IND crystallization at T_g results in a 26.1% or 25.5% greater free energy change (compared to INDME) when predicted by the Hoffman equation or ΔG_{config}, respectively. It is also noted from Figure 5.9B that H_{config} of IND and INDME is nearly the same close to T_g while there is a greater relative difference in S_{config}. Therefore, S_{config} is the main contributor to the difference in G_{config} between IND and INDME. While it is interesting that the thermodynamic analysis above provides some evidence as to why

IND may have a greater tendency to crystallize near T_g, it must be noted that both the Hoffman equation and configurational properties apply only to the pure drugs and may not necessarily be applicable in their respective ASDs.

Other properties, including glass forming ability (GFA), fragility, strength, non-isothermal E_a, and glass transition E_a, were measured and recorded in Table 5.1 to better understand the differences in crystallization between IND and INDME. Baird et al. previously described how to measure GFA, fragility parameter, strength parameter, and the glass transition activation energy (40). The details of isothermal and nonisothermal crystallization activation energy are found in references (131, 299, 301).

Table 5.1. Comparison of physicochemical properties between indomethacin and indomethacin methyl ester.

	IND	INDME
Molecular Weight (g/mol)	357.79	371.82
Crystal Density (g/cm^3)	1.37[a]	1.404[b]
Amorphous Density (g/cm^3)	1.34	1.34[c]
T_g (°C)	44.3	6.5
T_m (°C)	160.0	91.9
T_K (°C)	9	-65
$\Delta G_{config}(T_g)$ (kJ/mol)	-7.5	-5.9
ΔH_{fus} (kJ/mol)	38.6	33.2
ΔS_{fus} (J/molK)	89.6	90.9
Glass Forming Ability	Class 3	Class 3
Fragility Parameter, m	58.25[d]	66
Strength Parameter, D	14.25[d]	12
Isothermal Cryst. E_a (kJ/mol)	123.2	68.5
Nonisothermal Cryst. E_a (kJ/mol)	N/A	135.9
Glass Transition E_a (kJ/mol)	356.25	351
Hydrogen Bond Donors/ Acceptors	1/5	0/6

[a]Reference (302). [b]Reference (297). [c]Assuming amorphous density is 5% less than crystalline density. [d]Reference (40).

INDME is a slightly larger molecule that forms crystals 2.5% more dense than IND. The estimated amorphous density of INDME is equal to that of IND. The thermodynamics of crystallization are approximately equal between the two compounds with the heat of fusion in IND being slightly higher than INDME. Both were class 3 (good) glass formers based on Baird's GFA classification system which also implies they will form stable ASDs (40, 116). Similarly, both were moderately fragile liquids based on both their fragility and strength parameters although INDME was slightly more fragile by both measures. As shown in Figure 5.8, the isothermal crystallization activation energy is greater in IND than INDME. The non-isothermal crystallization activation energy of INDME was approximately twice that of its isothermal activation energy while no IND crystallization was observed upon heating even at rates as slow as 0.5°C/min. Lastly, the glass transition activation energy was approximately equal between IND and INDME although greater values for IND have been reported in the literature (303).

5.4 Discussion

IND has been extensively studied in the literature, particularly as it pertains to ASD formulations. Its structural analogue, INDME, has not been studied in nearly as much detail and provides the opportunity to directly compare the effects of hydrogen bonding on crystallization while minimizing differences in structure. The causes for markedly different crystallization behavior around T_g are explored and the implications for formulating ASDs are discussed.

5.4.1 ASD Stability

IND and INDME display similar trends in crystallization above T_g however their behavior becomes markedly different near and below T_g. Crystallization at a given temperature, both nucleation and crystal growth, is a balance between thermodynamic driving force and kinetic factors such as molecular mobility (46). Molecular mobility encompasses the translational, rotational, and vibrational movement of molecules required to locate other molecules and nucleate or integrate on to a growing crystal surface. While all molecular mobility decreases with temperature, translational mobility is significantly reduced below T_g relative to the supercooled liquid state. Conversely, the difference in free energy between the amorphous and crystalline state represents the thermodynamic driving force for crystallization and increases continuously below T_m. The crystallization rates of both compounds shown in Figure 5.7 are directly compared in Figure 5.10. To make it easier to read the plots, they are divided into high (Figure 5.10A) and low (Figure 5.10B) drug loadings.
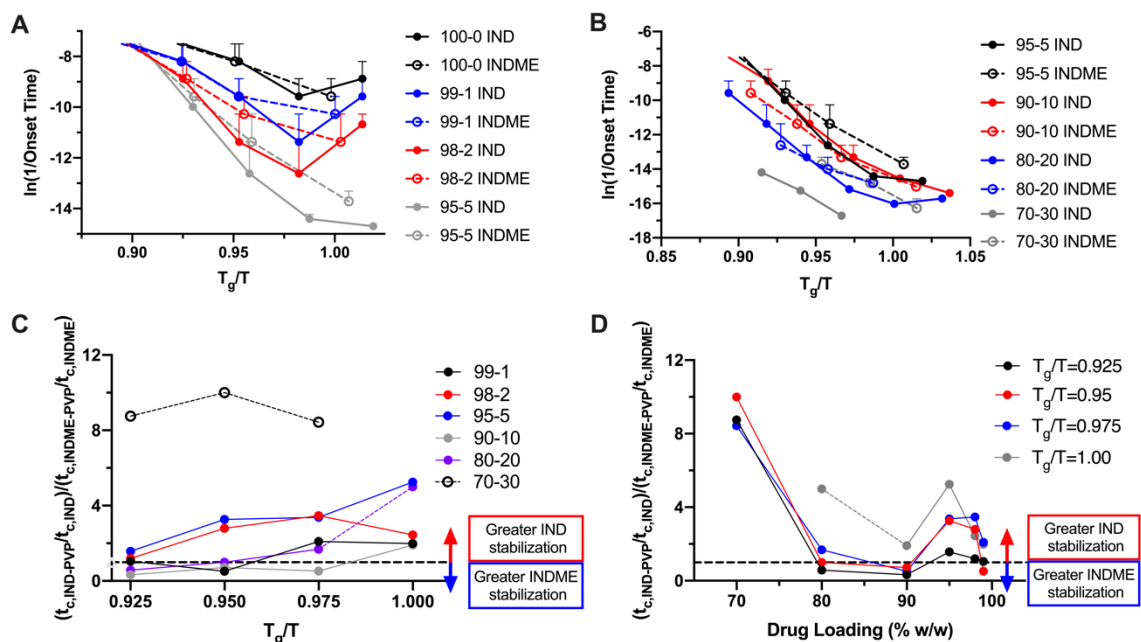
Figure 5.10. Comparison of the rates of crystallization between IND- and INDME-PVP ASDs as a function of scaled inverse temperature for (A) 95 – 100% (w/w) drug loading and (B) 70 – 95% (w/w) drug loading. The ability of PVP to suppress IND crystallization onset in ASDs relative to pure IND compared to the ability of PVP to suppress INDME crystallization in ASDs relative to pure INDME is shown in (C) at constant drug loadings and in (D) at constant temperatures.

The rate of crystallization, $\ln(1/t_c)$, is approximately equal between IND and INDME systems at temperatures far above T_g where molecular mobility is high. The rates diverge as T_g is approached with INDME crystallizing faster than IND due to reduced mobility and the increasing importance of IND-PVP hydrogen bonding (Fsigure 5.10A). The temperature relative to T_g at which the rates diverge generally increases as drug loading decreases. For example, 100-0 and 99-1 ASDs diverge at $T_g/T = 0.95$ while 98-2 and 95-5 diverge at $T_g/T = 0.925$ and 0.90, respectively. However, the difference in IND and INDME crystallization rates is relatively small for most lower drug loadings (Figure 5.10B). This

indicates that the degree to which IND is better stabilized by PVP increases towards T_g. Additional PVP reduces the crystallization rate of IND at T_g while INDME crystallization rate is approximately equal at T_g regardless of PVP content. Once in the glassy state, the non-Arrhenius behavior of high drug loading IND-PVP ASDs causes faster crystallization than INDME systems. While INDME-PVP ASDs generally crystallize faster than IND-PVP ASDs of equivalent drug loadings above the T_g and IND-PVP ASDs crystallize faster slightly below T_g, no conclusions can be made about the difference in crystallization rates deeper into the glassy state as crystallization was not observed below $T_g/T > 1.03$.

The ability of PVP to stabilize amorphous drug in an ASD relative to pure drug is compared between IND and INDME in Figures 5.10C and D. The relative stability of IND or INDME in the presence of PVP is a complex relationship that is dependent on both temperature and drug loading. At high drug loadings, PVP generally stabilizes IND better than INDME although the effect is temperature dependent. Specifically, all IND ASDs were better stabilized by PVP at T_g while the difference in relative stabilization diminishes at higher temperatures. It is important to note here the difference in crystallization rates near T_g. On an absolute scale, INDME-PVP ASDs crystallize faster than IND-PVP ASDs slightly above and at T_g. However, despite the acceleration in IND crystallization near T_g, IND-PVP ASDs are better stabilized *relative to 100% IND* when compared to the relative stability of INDME-PVP ASDs and 100% INDME.

Figure 5.10D shows that PVP better stabilizes INDME relative to IND at high temperatures where intermolecular hydrogen bond strengths are weaker. It also shows the drug loading at which hydrogen bonding becomes the primary stabilizing mechanism at different temperatures. Near T_g, drug-polymer hydrogen bonding becomes more important

for stabilizing the amorphous drug as the molecules possess less translational mobility. As polymer content increases, the degree to which lowering the storage temperature improves stability also generally increases. The data points at 70-30 clearly show how the ability to form extensive intermolecular hydrogen bonds improves stability at different temperatures.

The importance of drug-polymer hydrogen bonds in stabilizing an amorphous drug generally increases near T_g (aside from 90-10, *vide infra*). A reduction in drug loading near T_g is more effective in stabilizing a drug when hydrogen bonds are present whereas the effect is more similar regardless of whether hydrogen bonds exist or not at higher temperatures. For example, if drug loading decreases from 90% to 80% at $T_g/T=1$, an IND-PVP ASD sees a disproportional increase in stability compared to the same INDME-PVP ASD. The same change in drug loading at $T_g/T=0.925$ does little to affect the relative stability between the two ASDs where INDME is still better stabilized than IND.

As shown in Figure 5.10D, in the drug loading range around 90%, IND and INDME seem to have comparable normalized crystallization onset times whereas both above and below this range, the normalized crystallization onset time for INDME is faster than IND. While the exact reason is unclear, Yuan et al. showed that there are multiple different species present (IND-IND carboxylic acid dimer, chain, free, IND carboxylic acid-PVP amide/ IND carboxylic acid-IND amide) and that these species interconvert around T_g at this concentration (vide infra) (89).

The effects of phase separation must also be considered. The lack of extensive drug-polymer hydrogen bonding in INDME-PVP ASDs likely causes phase separation in those ASDs. In fact, phase separation was previously observed in 90-10 INDME-PVP ASDs but not in 70-30 ASDs (154). Samples in this study were prepared in a similar fashion so phase

separation likely begins somewhere between 70% and 90% INDME and is at least present for all drug loadings of 90% INDME or more. The stabilizing effect of PVP is diminished in domains containing disproportionately high drug levels and leads to the faster crystallization of INDME at most temperatures above T_g.

5.4.1.1 Thermodynamics

Typical thermodynamic values do not explain the difference in crystallization tendency between IND and INDME. The heat of fusion (ΔH_{fus}) is related to the energy required to break the crystalline lattice is slightly greater for IND and agrees very well with the enthalpy of IND dimerization reported by Yuan et al. (89). Similarly, the entropy of fusion (ΔS_{fus}) is related to the difference in molecular ordering between the crystal and liquid and is similar between the two compounds. Since ΔH_{fus} and ΔS_{fus} were approximately equal between IND and INDME, the difference in their thermodynamic stability lies in the heat capacity difference at T_g. This is reflected through their configurational properties.

Configurational free energy and the Hoffman equation show that IND crystallization is more favorable than INDME at all temperatures relative to T_g. Therefore, IND would be expected to crystallize faster than INDME. This was generally not the case as INDME crystallized faster than IND in most cases, particularly in the supercooled liquid state where extensive hydrogen bonding exists between IND and PVP. Slight differences are observed between the thermodynamic properties of IND and INDME (Figure 5.9B and Table 5.1) which may contribute to the differences in crystallization. The slight differences in ΔH_{fus} are reflected in the Hoffman equation while there is minimal difference in H_{config} near T_g.

The large difference in S_{config} between IND and INDME is the main reason for differences in thermodynamic driving force. S_{config} represents the difference between the number of molecular configurations that exist in the amorphous state and the well-defined configuration of a crystalline phase (56, 57). Therefore, less constricted molecules which are able to exist in a number of configurations in the supercooled liquid state typically have greater S_{config} values and are less likely to be in a preferrable orientation for crystallization (57). The effect of hydrogen bonding on configurational entropy has not been directly studied. Presumably, the lack of intermolecular hydrogen bonding or specific interactions will increase the number of possible amorphous orientations and increase S_{config}. We assume that the strongly hydrogen bonded network in amorphous IND decreases the number of possible configurations relative to INDME which contains no or weak interactions thus explaining the larger S_{config} for INDME. Further, the presence of polymer will likely hinder crystallization through stabilizing drug-polymer interactions or dilution effects (57). As Zhou et al. point out, the polymer may increase the effective configurational entropy by keeping the drug in a configuration very different from the crystalline phase (57).

5.4.1.2 Kinetics

Locking the drug into configurations unfavorable for crystallization can alternatively be viewed similarly to reducing the molecular mobility of the drug. Polymers typically used in ASDs have a T_g significantly higher than the T_g of the drug and act as antiplasticizers by increasing the T_g of the mixture. Increasing amounts of PVP increased the T_g of IND and INDME ASDs. Drugs stored at an equivalent temperature relative to T_g can be approximated as having the same level of molecular mobility (57). However, IND

and INDME exhibited different crystallization behavior with INDME often crystallizing prior to IND relative to T_g. Clearly, antiplasticization alone cannot explain the difference in crystallization behavior. Extensive IND-PVP hydrogen bonding helps stabilize the amorphous state relative to INDME-PVP ASDs (84). Figure 5.10 demonstrates the impact of additional stabilization by hydrogen bonding where increasing PVP content decreases the crystallization rate at T_g due to hydrogen bonding between the IND carboxylic acid and PVP amide. Conversely, the lack of specific INDME-PVP interactions results in crystallization being governed by temperature relative to T_g. Increasing the PVP content from 10 – 30% has nearly no effect on the INDME crystallization rate near T_g whereas increasing PVP content from 10 – 30% dramatically changed the IND crystallization rate near T_g.

Molecular mobility is highly temperature dependent and is difficult to compare between molecular systems for a single temperature unless done relative to the glass transition where molecular mobility is approximately the same (structural relaxation, $\tau \sim$ 100 s) (57). Measuring structural relaxation times at $T_g/T = 1.014$ (40°C and 2.7°C for IND and INDME, respectively) yielded inconclusive results as mobility was still relatively high so close to T_g.

Fragility relates the relative change in local structure or mobility with decreasing temperature near T_g (304). Both the strength (D) and fragility parameters (m) classified IND and INDME as moderately fragile although IND could be considered slightly more fragile than INDME. Being more fragile than INDME, IND was expected to display a larger glass transition activation energy (ΔE_{Tg}), or, the energy required for structural relaxation to occur (305). A small difference was observed but it is unlikely that such a

small increase in activation energy for IND relative to INDME can account for the drastic changes in crystallization.

The strength parameter, D, represents the rate at which an ideal glass loses molecular mobility with decreasing temperature. Compounds with higher D values lose molecular mobility slowly and results in higher mobility for a longer amount of time (57). Zhou et al. demonstrated that this is also true after aging and, therefore, also applies to real structurally relaxed glasses (57). Whereas IND had a greater D value than INDME, it was expected to have a greater likelihood of crystallization at a specific T_g/T. In addition, the INDME was farther from its Kauzmann or "zero mobility" temperature (T_K) relative to IND when stored at its T_g. Both D and T_g/T_K suggest that IND possessed greater molecular mobility near and below T_g relative to INDME. However, it is unclear whether these small differences can explain the large difference in crystallization behavior. The implications of differences in other properties measured for IND and INDME are discussed further in section 5.4.2.2.

5.4.1.3 Drug-in-Polymer Solubility

Crystallization in an ASD is also dependent on the concentration of drug dispersed within the polymer matrix relative to its crystalline solubility. Aside from highly potent APIs, most pharmaceutically relevant drug loadings will be supersaturated and thermodynamically unstable. Therefore, most drug products must be kinetically stabilized through storage below T_g to help delay crystallization. Figure 5.11 shows the IND-PVP solubility phase diagram overlaid with the results of IND crystallization as well as a similar plot for INDME-PVP.
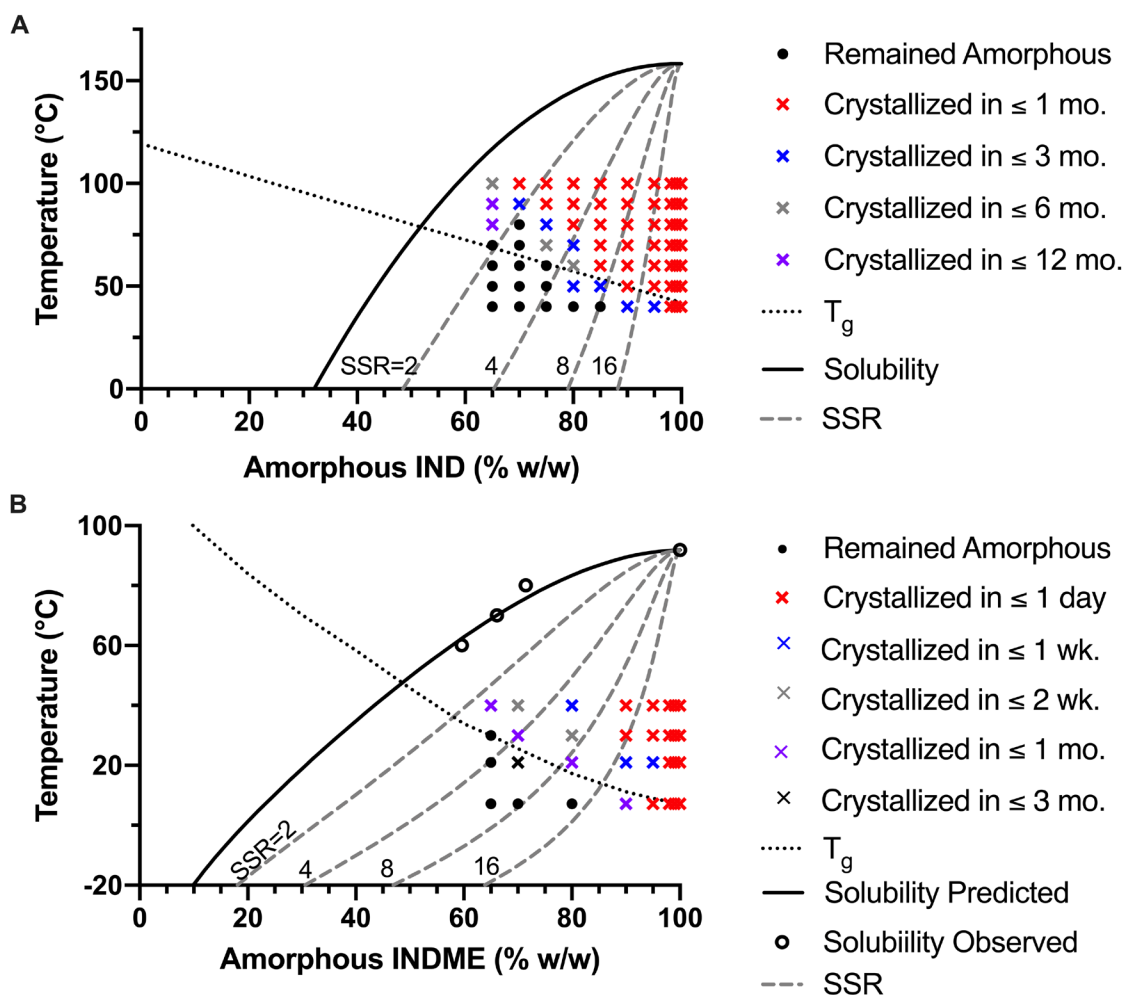
Figure 5.11. Solubility phase diagram overlaid with the experimental design space for (A) IND-PVP ASDs and the time at which crystallization was observed. The IND solubility line was constructed based on reference (46). (SSR = Supersaturation ratio.) (B) Experimental design space for INDME-PVP ASDs and the time at which crystallization was observed. The initial data points used to construct the INDME solubility and SSR curves are shown only as an estimate.

Figure 5.11A displays the effects of thermodynamics, kinetics, and solubility on crystallization onset time. All samples were supersaturated with respect to IND-PVP solubility and therefore were thermodynamically unstable. Approximately one quarter of

samples were kinetically stabilized by storage below T_g however not all glassy samples remained amorphous. In fact, some 100-0, 99-1, and 98-2 IND-PVP ASDs stored below T_g crystallized in less than a month highlighting that drug loading dominates the crystallization process at those conditions.

Indomethacin crystallization appears to follow an approximately sigmoidal pattern as a function of time with respect to temperature and drug loading. At high IND loadings or a combination of high temperatures and IND loadings, IND crystallizes fastest, but lower IND contents at high temperature, IND crystallizes more slowly. However, both IND-PVP solubility and T_g must also be considered to better describe IND crystallization. As the supersaturation level increases, crystallization not only occurs above T_g (70% drug loading, SSR ~ 2), but also below T_g (90% drug loading, SSR > 10). The difference in solubility along the T_g line alone greatly increases the thermodynamic driving force for crystallization. In addition, T_g seems to become more important in inhibiting crystallization at lower drug loadings due to reduced levels of supersaturation. For example, 99-1 IND-PVP crystallized at 40°C ($T_g/T = 1.01$, SSR = 142) in less than a day while 75-25 IND-PVP at 60°C ($T_g/T = 1.01$, SSR = 3.5) remained amorphous for over nine months. Still, solubility alone does not fully explain why some IND samples crystallize faster below T_g than above T_g as large differences in stability still exist near even in the glassy state. For instance, 75-25 IND-PVP ASDs at 50°C did not crystallize in over 9 months while 80-20 IND-PVP ASDs at the same temperature crystallized within three months. This indicates that T_g may not necessarily be the best indicator to use for predicting stability.

In contrast to IND, Figure 5.11B shows INDME follows an approximately linear crystallization pattern with respect to time and drug loading. A combination of high storage

temperature and drug loading results in the fastest crystallization. Research to more accurately determine the INDME-PVP solubility is currently underway. The estimated solubility of INDME in PVP is shown but is only an approximation due to extremely slow crystal growth kinetics preventing crystallization from reaching equilibrium over reasonable experimental timescales.

As expected, INDME is less soluble in PVP than IND at all temperatures (e.g., 30% versus 40% w/w at 25°C). The lack of hydrogen bonding between INDME and PVP was expected to decrease solubility and stability. However, INDME's increased stability relative to IND near T_g may indicate a non-obvious decoupling between supersaturation and stability in the absence of hydrogen bonding. Indeed, similar results have been found in the literature. Fenofibrate has very low solubility in copovidone, neither of which have hydrogen bond donating groups, yet fenofibrate-copovidone ASDs exhibit exceptional kinetic stability, remaining amorphous over 15 years at ambient conditions (306)

5.4.2   Diffusionless Crystallization

The rate of crystallization was expected to decrease continuously through the glass transition as a reduction in molecular mobility creates conditions less favorable for nucleation and crystal growth. Crystallization rates of INDME-containing systems exhibited Arrhenius behavior but IND and IND-PVP ASDs of high drug loadings were markedly non-Arrhenius to the point that crystallization was observed to occur faster than expected near and slightly below T_g. Despite slowing kinetics near T_g, certain organic systems have shown an acceleration in crystal growth rate near and slightly below T_g. Up to this point, this has only been observed in 12 organic molecular liquids or ASDs with 1 – 2% polymers present (50, 54, 55, 150, 267, 307, 308). This acceleration in crystal growth

rate has been attributed to a switch from diffusion-controlled to diffusionless/ glass-crystal (GC) crystal growth. Here, the rate of nucleation and/ or crystal growth is no longer limited by IND diffusivity (i.e., the rate at which amorphous IND molecules migrate to the nucleus or crystal surface). Many theories have been previously proposed to account for this anomalous behavior whereby the crystal growth rate increases up to 4 orders of magnitude near the T_g compared to the expected behavior extrapolated from above the T_g (52, 54, 55, 293, 309, 310). Briefly, homogeneous nucleation-based crystallization assumes that diffusionless crystal growth occurs by the coalescence of homogeneous crystal nuclei onto an existing crystal surface at a rate determined by β-relaxation (52). Alternatively, a tension-induced interfacial mobility process proposes that the density difference between phases at the glass-crystal interface creates tension which provides free volume for molecules near the growing crystal front to have enhanced molecular mobility needed for rapid crystal growth (293, 310, 311). The tension-induced model was further refined to be a surfaced-facilitated transformation in which it is proposed that the interfacial tension is continually relieved through the creation of voids or fractures (55). The creation of new surfaces allows for surface crystal growth which is much faster than bulk crystal growth including bulk diffusionless IND crystal growth (312). It was also proposed that the molecular motions responsible for diffusionless crystal growth are native to the local glassy state rather than α-relaxation or bulk-liquid diffusion (54). Rotational and vibrational motions effectively allow for the growth of certain crystal structures due to a favorable orientation in the liquid state near the crystal interface rather than relatively larger rearrangements such as diffusion.

5.4.2.1 Structural Considerations

Larger molecules with a greater number of rotatable bonds are typically better glass formers due to the specific conformations required for crystallization (40). Interestingly, IND is the largest molecule for which diffusionless crystal growth has been observed (308). In addition, it is observed to occur at the greatest degree of supercooling and proceed at the slowest rate indicating that sufficient molecular mobility must exist relatively far into the glassy state.

Diffusionless crystal growth has been shown to occur more often in molecules with more isotropic crystal structures (54). This was rationalized by the nearest neighbors being at approximately the same distance (i.e., similar to the liquid state) and suggests diffusionless crystal growth is more likely if molecular packing is sufficiently similar between the liquid state and the crystalline state (313). Indeed, the structure of γ-IND is isotropic and similar to the short-range ordering in the amorphous state where carboxylic acid dimers dominate (89, 314, 315). While only γ-IND was observed in this study, diffusionless crystal growth was observed previously in γ-IND and α-IND (48).

5.4.2.2 Activation Energy and Hydrogen Bonding Speciation

Activation energy is expected to increase with additional PVP present as the polymer can inhibit nucleation and crystal growth. Only the crystallization onset time was monitored in this study, so the question remains as to whether the observed activation energy represents that of nucleation or crystal growth. Woldt determined the activation energies of nucleation and crystal growth based on differences in the isothermal and non-isothermal crystallization activation energies (316). Non-isothermal crystallization (even when heating amorphous IND at rates as slow as 0.5°C/min) was not observed in IND or

IND-PVP implying that the activation energy was much greater than the isothermal activation energy observed from crystallization onset times. Conversely, INDME isothermal and non-isothermal activation energies were approximately equal. This suggests a difference in nucleation mechanism between the two compounds and may be related to the slow initial growth of nuclei to an observable size (131, 317). Further, the measured activation energy in this study for 90-10 IND-PVP was almost identical to the viscous flow activation energy (i.e., crystal growth) of a 90-10 IND-PVP ASD by Tian et al. (318). Therefore, it is likely that the measured activation energies in this study are reflective of the initial growth process (from nucleation to a crystal of an observable size) in IND and INDME where a larger energy barrier must be overcome for the initial growth of γ-IND crystals. While informative, this still does not explain the acceleration in IND crystallization near T_g, so it is likely that the nucleation process is largely involved in the diffusionless crystallization phenomenon.

Figure 5.8 showed that the measured activation energies overlaid with hydrogen bonding arrangements in amorphous IND change as a function of PVP content (89). The introduction of PVP inhibits nucleation and crystal growth through the formation of drug-polymer hydrogen bonds and reduces the molecular mobility of IND. The isothermal IND crystallization activation energy increases as a result. The activation energy of INDME also follows a similar trend with increasing PVP content despite the lack of any significant hydrogen bonding. However, as previously mentioned, the T_g of INDME-PVP ASDs significantly deviates from the predictions of the Gordon-Taylor equation which likely indicates the presence of some drug-polymer interactions or lack of drug-drug interactions. This is likely a halogen interaction and would not be as energetically favorable as IND-

PVP hydrogen bonding. Therefore, the magnitude of the difference in activation energy measured corresponds to the energy required to break IND-IND or IND-PVP hydrogen bonds prior to recrystallization and agrees well with hydrogen bonding energy values reported in the literature (83). Conversely, the greater thermodynamic driving force for γ-IND crystallization is due to the formation of hydrogen bonds in IND-IND cyclic carboxylic acid dimers. The enthalpy and entropy of fusion measured in this study are almost exactly equal and opposite of the standard enthalpy and entropy of dimerization reported by Yuan et al (89). Therefore, the energies measured in this study directly reflect the effects of hydrogen bonding. Drug-polymer hydrogen bonds in ASDs increase the activation energy of isothermal crystallization but do not seem to impact how activation energy changes with increasing polymer content.

The hydrogen bond speciation of IND as a function of PVP concentration shown in Figure 5.8 is determined by thermodynamics for a specific temperature. The speciation data in Figure 5.8 was acquired at 20°C which is significantly below IND's T_g and the range of IND storage conditions. The relative proportions of hydrogen bonded species will likely be skewed towards more IND-IND dimers in the supercooled liquid state.

The presence of drug-polymer hydrogen bonding (rather than the relative proportion of each species) seems to affect the isothermal activation energy. Despite similar changes in isothermal activation energy as a function of PVP content, similar hydrogen bonded species are not expected to exist in INDME due to replacing the carboxylic acid of IND with an ester. Any hydrogen bonded or intermolecular species existing in INDME are likely much different than those of IND. Rather, it is the changes in molecular mobility accompanying the addition of PVP which is expected to impact the

236

activation energy. In the case of IND near the T_g, similar hydrogen bonded species in the amorphous and crystalline states are proposed to contribute to diffusionless crystallization.

The IND acid-PVP amide hydrogen bonds stabilize amorphous IND as they replace the IND-IND carboxylic acid dimers and also reduce the translational mobility of the dimers remaining. Cyclic IND dimers exist in both amorphous and crystalline γ-IND and may presumably act as nucleation sites when mobility is reduced in the presence of PVP or at temperatures near T_g. The maximum in activation energy is likely explained as a balance between reducing concentrations of IND dimers and a reduction in molecular mobility which can allow for diffusion away from the crystal nucleus. Even at reduced diffusional mobilities, dimers may still possess rotational and vibrational modes of motion required to incorporate onto a growing crystalline nucleus. Eventually nearly all IND dimers have been replaced by IND-PVP hydrogen bonds such that a critical nucleus is less likely to form, and crystallization becomes more difficult as hydrogen bonds must be broken prior to crystallization. This occurs at 30% PVP which is also the concentration below which no diffusionless crystallization was observed. This agrees well with the observation that diffusionless crystal growth occurs in molecules with similar liquid and crystalline structures.

The contribution of hydrogen bonding can be further explored by considering its temperature dependence. Increased thermal energy weakens hydrogen bonds at high temperatures so the fraction of dimers in the amorphous state is expected to increase at lower temperatures (89). Yuan et al. showed this was the case where, below T_g, the fraction of dimers increases dramatically with decreasing temperature compared to the slope above T_g (89). They attribute the deviation from the supercooled liquid trend occurring below T_g

to the increased free energy of the non-equilibrium glass. The increased number of dimers in the glassy state serves as the building blocks for crystallization to γ-IND and likely contribute to increased accelerated crystallization onset near and slightly below T_g.

For the above arguments to hold, the molecular mobility of IND near T_g must be considered in greater detail. Two-dimensional (2D) exchange solid-state NMR spectroscopy (SSNMR) was previously used to investigate the local mobility of pure amorphous IND and IND-PVP ASDs (154). Cross peaks near and slightly below the T_g in samples indicated IND systems have sufficient translational mobility required for exchange to occur during the experimental mixing time. In particular, cross peaks in pure amorphous IND at 50°C ($T_g = 46$°C) indicated amorphous IND was able to continually break cyclic dimer (dimer) hydrogen bonds and form carboxylic acid-amide (complex) hydrogen bonds (and vice versa) as the T_g is approached (154). Furthermore, cross peaks were observed in 90-10 IND-PVP ASDs ($T_g = 53$°C) at 50°C. At 60°C the same cross peaks were observed with greater intensity indicating dimers and complexes continually break and form near T_g in the presence of PVP. Comparable results were obtained at 60°C and 70°C for 80-20 IND-PVP ASDs ($T_g = 64$°C). Remarkably similar results were obtained in this study for crystallization onset where t_c deviated from the expected exponential relationship for a given drug loading near the T_g for some samples (Figure 5.6A). No deviations from the t_c trends in 70-30 ASDs indicated the diffusionless crystallization mode was not active. Similarly, no cross peaks were observed at 70°C or 80°C for 70-30 IND-PVP ASDs ($T_g = 73$°C) (154). 30% PVP disrupts and replaces nearly all dimers with IND (carboxylic acid)-PVP (amide) hydrogen bonds (89). This confirms that the diffusionless crystal growth and crystallization mode accessed near the T_g in certain systems is influenced by the local

mobility and the ability to break and form hydrogen bonds. Cross peaks in other polymeric systems have also been associated with other modes of molecular mobility including β-relaxation (319). This is particularly relevant in the glassy state where diffusional α-relaxations slow dramatically and may explain why diffusionless crystal growth and its enhanced crystal growth rate is observed in some amorphous drugs where sufficient translational or other molecular mobility exists near the T_g. It may also help to explain why this phenomenon had previously not been observed above 2% polymer content. In the presence of polymer, crystal growth rate not only depends on the movement of drug molecules to the crystal interface (drug diffusivity, D_{drug}) but is also dependent on the diffusivity of the polymer ($D_{polymer}$) away from the growing crystal interface. $D_{polymer}$ decreases faster than D_{drug} with decreasing temperatures such that the system again becomes diffusion controlled and diffusionless crystal growth ceases (267). At higher polymer concentrations, the polymer suppresses the nucleation and/ or crystal growth rate such that diffusionless crystallization is not observed on experimental timescales typically used with microscopy. Therefore, crystallization onset must be observed over long periods of time rather than measuring crystal growth rate to observe diffusionless crystallization as it manifests as a decrease in t_c from expected trends above T_g.

Ultimately, it is proposed that a combination of factors explain the difference in IND and INDME crystallization and the observation of diffusionless crystallization in IND. Most importantly, the presence of dimers in the amorphous and crystalline state serves as nucleation sites. Hydrogen bond formation drives the greater thermodynamic driving force for crystallization to γ-IND despite a greater activation energy barrier. These observations highlight the importance of β-relaxations to diffusionless crystallization and agree most

closely with the explanations of Musumeci et al. (52, 308). Specifically, diffusionless crystallization in a solid-state process which is disrupted by greater levels of translational mobility above T_g and inhibition of β-relaxations deeper into the glassy state. At higher temperatures, molecules may diffuse away from the crystal interface prior to incorporation whereas structural reorientation required is too great at temperatures far below T_g or significant polymer contents to occur solely through local mobility (308). Other strongly hydrogen bonded systems, especially those with similar speciation in the crystalline and amorphous phases, are likely to exhibit the same phenomenon despite it being difficult to observe under typical stability conditions.

5.4.3 Formulation Implications

Amorphous drug products should always be stored below T_g to minimize the likelihood of crystallization. Storage of amorphous drugs or ASDs more than 50°C below the T_g is generally agreed to prevent crystallization on pharmaceutically relevant timescales (284, 320). Despite an extremely high thermodynamic driving force for crystallization, storage that far in the glassy state effectively eliminates the translational molecular motions typically associated with crystallization. However, some molecules, including indomethacin, still possess sufficient molecular mobility in the form of β-relaxations to induce nucleation and crystal growth (79, 283). Besides, storage at such low temperatures may not always be feasible for low-T_g drugs or due to a lack of cold chain. Therefore, the storage of amorphous formulations near T_g is not uncommon.

An acceleration in drug crystallization onset time near T_g for an ASD with pharmaceutically relevant concentrations of polymer present has been shown for the first time. Crystallization presumably adversely affects bioavailability and/ or indicates a failed

240

stability study and is observed orders of magnitude faster than expected just below T_g. This clearly shows that IND stability in the supercooled liquid state cannot be extrapolated into the glassy state. The changes in crystallization trends can occur over small temperature ranges and may be missed or insufficiently characterized with standard stability studies. Future stability studies should be designed to account for the possibility of these drastic changes near T_g by storing additional samples near T_g.

While IND and 11 other molecules have exhibited diffusionless crystal growth, to the best of our knowledge, only IND has also shown the acceleration in crystallization onset. From a stability perspective, the diffusionless crystallization observed is more detrimental to the physical stability of an ASD assuming that the presence of crystallization adversely affects bioavailability. However, similarities are likely to exist between the two phenomena and diffusionless crystallization may also be present in the other molecules. Pure amorphous drug candidates which exhibit diffusionless crystal growth may therefore indicate that stability studies of the corresponding ASD should be designed with special attention paid to crystallization kinetics near T_g.

5.5 Conclusions

Indomethacin is more mobile than indomethacin methyl ester, has a greater thermodynamic driving force for crystallization, and a greater crystallization activation energy for all drug loadings and storage temperatures but is better stabilized by PVP above T_g due to extensive hydrogen bonding in both the crystalline and amorphous state. Amorphous solid dispersions of IND and INDME, which lacks hydrogen bond donors, show markedly different crystallization tendencies. Crystallization onset above T_g in both

drugs follows an exponential dependence on drug loading. While this trend can predict INDME crystallization in the glassy state, IND-PVP ASDs crystallize faster than expected near and below T_g. This was attributed to diffusionless crystallization and, to the best of the authors knowledge, was the first time this was observed in ASDs with pharmaceutically relevant polymer contents.

The occurrence of diffusionless crystallization was further investigated and found to be driven by hydrogen bonding and molecular mobility. IND-IND hydrogen bonded dimers exist in both the amorphous state and γ-IND. Decreasing mobility near T_g and in the presence of PVP restrict IND dimer mobility which eventually serve as nuclei for accelerated crystallization. At 30% PVP, IND dimers are nearly absent and corresponds to the point at which diffusionless crystallization is no longer observed.

While the results here help to explain the occurrence of diffusionless crystallization in indomethacin, other systems exhibiting diffusionless crystal growth have not been studied as extensively. Additional comprehensive stability studies would be useful in identifying whether the same phenomenon can be observed in the crystallization onset times of other systems. Similarly, additional studies on other compounds are needed to determine whether the changes in hydrogen bonding and activation energy observed here are also found in other fast crystallizing systems. To this end, a data mining or extended stability study of all GC compounds may be fruitful.

CHAPTER 6: SUMMARY AND FUTURE DIRECTIONS

6.1   Summary

Amorphous solid dispersions (ASDs) have become a leading formulation approach to improve the bioavailability of many poorly soluble drugs. Their emergence in the pharmaceutical industry has been driven by drug discovery and combinatorial chemistry techniques that produce highly target-specific but poorly water-soluble drug candidates. These poorly soluble drug candidates now comprise a significant fraction of pipeline molecules and marketed products. However, the main drawback hindering the widespread commercialization of ASDs is their inherently poor physical stability and propensity to crystallize. Crystallization can occur during formulation, storage, or during dissolution if the amorphous drug is not adequately stabilized within the polymer matrix. While crystallization is generally detrimental to dissolution rate and solubility, the degree to which bioavailability is affected depends on the amount and quality of the crystals formed.

Polymers used in ASDs usually stabilize the amorphous API in at least one of three ways: (1) through specific drug-polymer interactions including hydrogen bonding, (2) through a reduction in the molecular mobility of the API molecules (i.e., antiplasticization), and (3) by diluting the concentration of drug molecules or acting as a physical barrier to nucleation and crystallization. Among others, the mechanism(s) by which a polymer stabilizes an amorphous drug is dependent on the drug-polymer combination, drug concentration, preparation technique, and other environmental factors such as storage temperature and relative humidity. General guidelines exist for improving the long-term physical stability of an amorphous formulation including storage at temperatures as far below T_g as possible, drug loadings below the drug-polymer solubility, and minimizing

exposure to elevated relative humidity. However, each of the suggestions mentioned above are not always feasible and each ASD must be adequately characterized to ensure stability over the shelf life of the drug product.

Advanced analytical methods are needed to sufficiently characterize amorphous formulations both from a research and regulatory standpoint. A molecular-level understanding drug-polymer interactions is often needed to help rationally formulate ASDs which remain stable over their shelf life and remain bioequivalent to their unaged drug product. This means that the analytical method used should be able to identify, qualitatively analyze, and quantify aspects of the formulation that are critical to its stability and performance. This information may also be applied to better predict the stability of ASDs and/ or compare generic and innovator products during generic drug development. To this end, solid-state nuclear magnetic resonance (SSNMR) spectroscopy has been used extensively to investigate pharmaceutical solids and better understand their interactions in the amorphous state on a molecular level. This dissertation focused on using SSNMR, as well as other analytical techniques, to better characterize the structure and composition of amorphous formulations, their physical stability, and their broad applications to drug development.

In addition to small molecules, larger molecules including some polymers have also been used as active pharmaceutical ingredients. Recently, advances in polymerization chemistry and the desire to minimize adverse side effects associated with poor ligand-receptor specificity has led to the development of more polymeric APIs. The increased complexity of polymeric APIs compared to small molecules leads to their classification as non-biological complex drugs (NBCDs). NBCDs are more difficult to structurally

characterize which leads to difficulties demonstrating API sameness during generic drug development. Chapter 3 focused on developing a SSNMR method for the quantitation of the three block copolymer units present in patiromer (Veltassa®). Poor aqueous solubility prevented quantitative analysis with typical solution-based techniques. A new peak integration method which accounted for cross polarization dynamics and spinning sidebands was successful in quantifying the carboxylate (m-block), aromatic (n-block), and aliphatic (p-block) blocks in patiromer. It was found that the average lot of patiromer contained 90.9 ± 0.4%, 7.6 ± 0.3%, and 1.5 ± 0.4% m-, n-, and p-blocks, respectively. These values agreed well with reported values on the package insert (m = 91%, n+p = 9%) and also provided the specific proportions of n- and p-blocks present. The FDA is actively pursuing the quantitation method in Chapter 3 for the development of a generic form of patiromer.

More often, however, characterization of amorphous pharmaceuticals is applied to amorphous solid dispersions. Various methods exist to detect and, in some cases, quantify crystallinity in ASDs. Chapter 4 compares DSC, PXRD, and SSNMR for their ability to quantify crystallinity in nifedipine-PVP ASDs which were annealed in-situ in the DSC or ex-situ in an oven. Equivalent levels of crystallinity were observed in DSC- or oven-annealed samples. Using the resulting T_g from DSC measurements is commonly used to quantify crystallinity and typically yields accurate data but is limited at high drug loadings. The DSC heat of dissolution method was found to grossly underestimate crystallinity due to changing crystal quality at different annealing temperatures. Conversely, PXRD and SSNMR were both found to provide accurate measurements of crystallinity in ASDs with both SSNMR methods (peak deconvolution and two-component ^1H T_1 relaxation time

measurements) yielding similar results. Since PXRD and SSNMR each provided accurate measures of crystallinity, they were also applied, for the first time, to measure drug-in-polymer solubility and are particularly useful for systems that are difficult to measure with DSC.

While Chapter 4 focuses mostly on characterizing the thermodynamic stability of ASDs, Chapter 5 investigates the difference in crystallization kinetics of two structurally similar drugs, indomethacin (IND) and indomethacin methyl ester (INDME), dispersed in PVP solid dispersions. The lack of hydrogen bonding in INDME compared to IND resulted in markedly different crystallization onset times in their respective ASDs. IND was better stabilized by PVP above T_g but showed an unexpected acceleration in crystallization rate near and slightly below T_g. This was attributed to diffusionless crystal growth and found to be the first occurrence of the phenomena at pharmaceutically relevant polymer concentrations. Drug-polymer hydrogen bonds are typically assumed to improve amorphous stability but are likely a contributor to the instability of IND near its T_g. The results of Chapter 5 highlight the need to extensive stability studies in ASDs, especially near the glass transition temperature.

Most of the work performed in this dissertation was done in the absence (or minimal) moisture. However, solvents and other sources of moisture are commonly encountered during formulation, manufacturing, and storage of amorphous pharmaceuticals. For example, multiple solvents are often used to dissolve a drug and polymer during spray drying which must then be sufficiently removed during the drying process. Additionally, formulated drug products encounter moisture during storage at or exposure to ambient relative humidity. Appendix A began to investigate the effects

246

atmospheric moisture and mixed spray drying solvents have on the physical properties (glass transition temperature and diffusivity) of pharmaceutical polymers using dynamic vapor sorption. Both polymers, PVPVA and HPMCAS, were significantly plasticized by water and acetone although the degree to which T_g was reduced was independent of the identity of the solvent. Rather, the total mass of solvent absorbed was found to control the plasticization indicating that most of the absorbed mass was loosely bound or does not interact with the polymer. The rate of solvent diffusion out of the polymer during drying was dependent on the polymer-solvent combination as well as the difference in initial and final solvent activities. The results of Appendix A may be useful in helping to model the spray drying process.

6.2   Future Directions

Chapters 3, 4, 5, and Appendix A investigated a wide variety of issues and developed methods to better characterize amorphous pharmaceutics. However, the due to the immense complexity of amorphous solids, not all aspects of physical stability were explored. This left many questions unanswered and led to the development of new questions along the way. In particular, it would be useful, and necessary, to further validate some of the proposed methods through the investigation of other amorphous systems. For example, SSNMR and PXRD should be compared with DSC crystallinity results in other drug-polymer systems with known drug-polymer solubilities prior to their application to systems which are difficult or impossible to measure with DSC. This may include ASDs with cellulose-based polymers (e.g., HPMCAS) or drugs crystallizing to multiple polymorphs. Furthermore, the SSNMR T_1 relaxation time quantitation method from

Chapter 4 holds great potential for differentiating between residual and process-induced crystallinity.

It is also desirable to quantify how hydrogen bonding affects ASD stability through drug-in-polymer solubility measurements. Even though the methods to quantify crystallinity in Chapter 4 greatly expand the number of systems in which drug-polymer solubility can be determined, further method development is needed to determine solubility in systems with extremely slow crystal growth kinetics. For example, while IND-PVP solubility is easy to measure, the T_g of annealed INDME-PVP ASDs was poorly resolved and crystallinity did not appear to reach equilibrium even after five days. Although the PXRD and SSNMR method demonstrated in Chapter 4 can quantify crystallinity using measures other than T_g, they both require large amounts of sample and do not address the fact that the time required to reach equilibrium is the rate-limiting step. Development of new methods to rapidly attain equilibrium or reduce the sample volume required would be especially useful, particularly for material-limited samples such as in the early stages of drug development.

Diffusionless crystallization is a particularly interesting research area due to the extremely low number of molecules in which it has been observed. A better understanding of the causes of this mode of crystallization may be improved through a data mining approach to see whether common trends can be identified across systems in which diffusion crystal growth is active. A further investigation into the effects of hydrogen bonding on crystallization near T_g and diffusionless crystallization is also warranted. In particular, combining the stability study from Chapter 5 with the work of Yuan et al. (89) to quantify hydrogen bonded species that exist in other ASDs would shed light as to how hydrogen

bonds change and confer stability at different storage conditions. This may be used to more definitively connect the changes in hydrogen bonding to diffusionless crystallization. In addition, it would be especially interesting to use SSNMR to quantitatively monitor any changes in hydrogen bonding that may occur as a function of preparation method or during structural relaxation.

Lastly, Karl Fischer titration, solution-state NMR, and solid-state NMR were all unsuccessful in quantifying the relative amounts of water and acetone present in dual solvent systems. Accurate quantitation of all spray drying solvents is necessary to develop a reliable model of particle drying or attributing changes in T_g to relative sorbate content. Additional analytical methods should be explored to develop a quantitative method. Headspace gas chromatography has been successful for the quantitation of six volatile organic impurities in an API and may also be useful in polymers or ASDs (321). Similarly, tandem techniques including TGA-FTIR or TGA-mass spectrometry may provide viable options for solvent quantitation once it desorbs during heating. A natural next step would be the investigation of additional polymers and/ or different solvent mixtures to see the observed trends in plasticization are solvent-dependent or occur in all systems. Finally, absorption and desorption experiments should be repeated on ASDs which better represent a spray dried dispersion.

APPENDIX A: INVESTIGATING CO-SORPTION BEHAVIOR OF WATER AND ACETONE IN PHARMACEUTICALLY RELEVANT POLYMERS: ISOTHERMS, DIFFUSIVITY, AND PLASTICIZATION

A.1   Introduction

Water is typically assumed to be detrimental to the chemical and physical stability of amorphous pharmaceuticals yet an amorphous drug product may be exposed to water and/ or other solvents along the pharmaceutical supply chain such as during formulation, manufacturing, or storage (322, 323). Spray drying is a commonly used unit operation for the formulation of poorly soluble drugs as the drug can be made amorphous to improve its aqueous solubility. However, this comes with the risk of recrystallization as the amorphous drug is inherently unstable. Often, the drug is formulated with a polymer with the goal of creating an amorphous solid dispersion (i.e., spray dried dispersion (SSD)) which maintains a greater aqueous solubility relative to the crystalline drug but is more stable than pure amorphous drug (33).

Spray drying first involves selecting a suitable solvent or co-solvent mixture to dissolve the API and excipients. Droplets containing API and excipient are then formed as the solution is sprayed into a low humidity chamber at elevated temperatures. As a spray-dried droplet undergoes the particle formation process, moisture conditions change rapidly while the particle temperature converges to the dryer's outlet temperature (324).

To maintain the solubility advantage of the amorphous phase, the drug must remain fully amorphous during all stages of manufacturing (e.g., spray drying) and during storage. However, the physical stability and other physicochemical properties of a spray dried amorphous drug product are affected by residual water or other residual solvents after

drying. Water and other small molecular liquids are strong plasticizers and increase the molecular mobility of the system. This is observed as a reduction in the glass transition temperature (T_g) with increasing solvent content (325). The increased molecular mobility at lower T_gs is related to amorphous instability and crystallization (5).

Elevated solvent contents are typically a result of absorption or residual solvent remaining after the spray drying process. In spray dried dispersions (SSDs) or amorphous solid dispersions (ASDs), significant water absorption by exposure to elevated relative humidity can cause phase separation and/ or crystallization (67). During spray drying, the solvent content and the T_g of the drying droplet continually change during the particle formation process. It is nearly impossible to remove all solvent during the primary drying stage and the rate is in part determined by the diffusivity of each spray drying solvent out of the drying droplet (326). Acceptable final solvent contents are determined by desired product properties and solvent-specific ICH Q3C guidelines (327). Insufficient evaporation during primary drying can result in the presence of residual solvents in a SSD with similar effects on stability to those seen from absorption. In fact, as little as 1% residual water was shown to create drug rich regions in itraconazole-HPMC SSDs (328). Residual solvents can further spur crystallization or chemical degradation reactions including hydrolysis (323). Other moisture-induced changes may include opacification and hydrate or solvate formation (323, 329).

The rise in the number of poorly soluble drug candidates and the resulting research interest in amorphous formulations has led to many amorphous products produced via spray drying. Therefore, the spray drying process and the resulting products must be adequately characterized to ensure consistent product performance and solid-state stability.

From a process development standpoint, understanding material properties during the drying process (i.e., relevant solvent content, T_g, diffusivity, etc.) would be useful in developing a model of the process or a design space. Similarly, a better understanding of the kinetics of solvent uptake in ASDs and their effects on physicochemical properties would be useful for designing systems more resistant to moisture-induced instabilities. Polymers typically make up the largest fraction of an ASD and are more hygroscopic than the API component (67). Therefore, by first studying the effects of mixed solvents on only a polymer (in the absence of drug), it provides a simplified system where the component most affected by exposure to moisture can be investigated without any complicating effects of a drug.

In this chapter, the moisture uptake, drying, and diffusivity behavior in the presence of two processing solvents is shown for two polymers commonly used in ASDs manufactured by spray drying. HF-grade hydroxypropylmethylcellulose acetate succinate (HPMCAS−HF) and polyvinylpyrrolidone-co-vinyl acetate (PVPVA) (Figure A.1) are equilibrated with water and acetone vapors to simulate the spray drying process and a simplified SSD. Solvent absorption and desorption were analyzed using dynamic vapor sorption isotherms and diffusivity analysis. Thermal analysis was performed to investigate the plasticizing effects of co-sorption solvent systems of water and acetone using differential scanning calorimetry. Various analytical techniques were used during initial attempts to quantify the relative amount of each sorbed solvent. We report that both PVPVA and HPMCAS are significantly plasticized by water and acetone although the magnitude of T_g reduction is dependent on the total solvent uptake rather than the identity of the solvent. The diffusivity and plasticizing ability of a solvent depends on the polymer

and its density. Initial diffusivity out of HPMCAS during desorption is independent of the difference in solvent activity (thermodynamic driving force) but the relative diffusivity of acetone compared to water increases with solvent activity in PVPVA. Attempts to quantify the relative proportions of water and acetone absorbed into each polymer using Karl Fischer titration, solution-state nuclear magnetic resonance (NMR) spectroscopy, or solid-state NMR were unsuccessful.
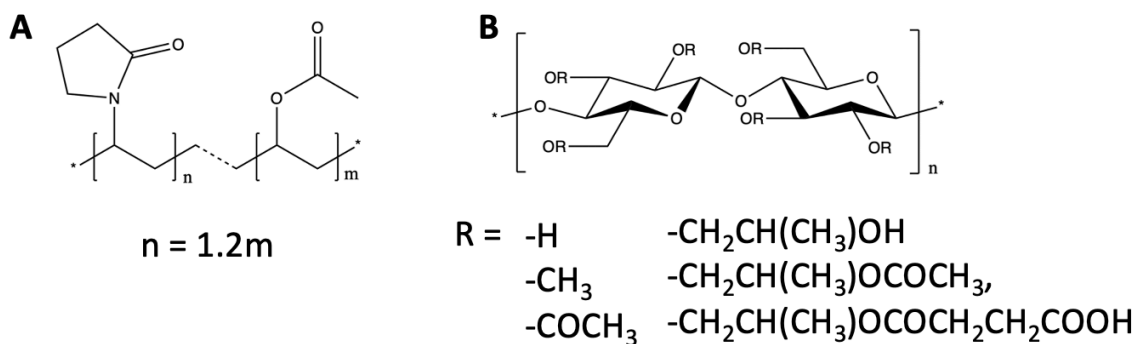
Figure A.1. Chemical structures of polyvinylpyrrolidone-co-vinyl acetate (PVPVA) and hydroxypropylmethylcellulose acetate succinate (HPMCAS).

A.2   Materials and Methods

HPMCAS-HF (lot 9023040) was purchased from Shin-Etsu (Tokyo, Japan) and PVPVA (lot MKCL5134) was purchased from Sigma (St. Louis, MO). Each polymer was dried at least 18 hours at 25°C under vacuum and stored in desiccators over Drierite (0% RH) prior to use. HPLC-grade acetone was purchased from VWR International (Radnor, PA) and Milli-Q water was obtained in house via a Millipore Milli-Pak 40 Q-Pod (Burlington, MA).

A.2.1 Dynamic Vapor Sorption

All isotherms were generated on a dynamic vapor sorption (DVS) Resolution (Surface Measurement Systems, Allentown, PA). Unless otherwise noted, all samples were packed into a T-zero aluminum differential scanning calorimetry (DSC) pan using $20 – 25$ mg of polymer such that the surface was approximately planar. Extreme care was taken such that no polymer was present on the lip, side, or bottom of the pan. The sample and pan were then placed on a sample holder and suspended from a hang-down wire in the sample compartment at 25°C. Total dry nitrogen gas flow rates of 200 sccm were used for all experiments (200 sccm through the water or acetone compartments for single solvent measurements, and a combination totaling 200 sccm through the water and acetone compartments for dual solvent measurements). Unless otherwise noted, the first stage of all DVS experiments began with a 5 hour drying period at 0% RH.

A.2.1.1 Isotherm Generation

Samples were exposed to step changes in relative humidity or partial pressure from $0 – 90\%$ and back to 0% in 10% increments. The sample was exposed to a given solvent activity until its change in mass with respect to time (DMDT) was less than 0.002%/min for 10 minutes at which point the sample was assumed to be in equilibrium.

A.2.1.2 Diffusivity

Diffusion coefficients were measured using the same DVS Resolution system as mentioned previously. Polymer samples were packed into T-Zero DSC pans at a known thickness. The flat surface of the polymer was approximated as a thin film for one-sided diffusion. Some samples were prepared by melt casting to minimize the void fraction present in the polymer. Packed DSC pans were melted on a hot plate (approximately 5

minutes at 180°C) then transferred to the DVS. The melt cast film was dried at 25°C and 0% RH for 2 hours and the initial mass and film thickness were then recorded.

The packed or melt cast films were then exposed to various relative humidities or partial pressures for diffusivity measurements. Each sample was stepped from 0% RH to 10% RH to 0% RH to 20% RH and so on up to 50% RH before returning to 0% RH. The same sample was used for all diffusivity measurements unless hysteresis was observed at 0% RH. The rate of uptake was measured in each step and fitted to the following equation (A.1) where M_t is the amount adsorbed at time, t; M_∞ is the amount adsorbed at thermodynamic equilibrium; l is the film thickness; and D is the diffusion constant.

$$\frac{M_t}{M_\infty} = \frac{4}{l}\sqrt{\frac{Dt}{\pi}} \tag{A.1}$$

The equation is applied over the range $M_t/M_\infty < 0.4$ and D is calculated as the initial diffusivity for each RH step change.

A.2.2 Differential Scanning Calorimetry

Uptake at a given relative humidity, partial pressure, or combination of two solvents was accomplished by exposing dry samples to the desired % RH or % P/Po via a single step and allowed to equilibrate for 18 hours. Equilibrated samples were then removed from the DVS Resolution and immediately sealed using a Tzero hermetic lid then transferred to a Q2000 DSC (TA Instruments, New Castle, DE) for scanning to determine the T_g. Standard (non-modulated) DSC with no pinhole was used to better capture the sample's environment from the DVS. Samples were equilibrated at 20°C before heating at 10°C/min to 150°C. Samples were held at 150°C for 5 minutes before cooling at 1°C/min to 0°C. The samples remained at 0°C for 5 minutes before reheating at 10°C/min back to 150°C. The cooling scan was performed at a sufficiently slow rate to allow all desorbed solvent to

reabsorb into the polymer and effectively erase its thermal history. The final heating scan is performed quickly enough to capture the T_g of the plasticized system such that the heating rate is greater than the rate of desorption. Reported T_g values were determined from the midpoint of the glass transition step-change in the resulting heat flow curves.

Theoretical T_g values were calculated via the Gordon-Taylor and Fox equations, as shown by Equation A.2 and A.3, respectively.

$$T_{g,mix} = \frac{X_1 T_{g,1} + K X_2 T_{g,2}}{X_1 + K X_2} \tag{A.2}$$

$$\frac{1}{T_{g,mix}} = \frac{X_1}{T_{g,1}} + \frac{X_2}{T_{g,2}} \tag{A.3}$$

$T_{g,1}$ and $T_{g,2}$ are the glass transition temperature of polymer and sorbate, respectively. X_1 and X_2 are the weight fractions of polymer and sorbate, respectively, and K is the fitting constant.

A.2.3 Sorbate Quantitation

The total amount of sorbate in each equilibrated polymer sample was determined as the change in mass from DVS measurements in single solvent experiments. However, the relative amounts of each sorbate present were not easily measured so various analytical techniques were used in an attempt to quantify absorbed water and acetone in dual sorption experiments.

A.2.3.1 Solid-state Nuclear Magnetic Resonance Spectroscopy

^{1}H and ^{13}C solid-state nuclear magnetic resonance (SSNMR) spectroscopy with magic angle spinning (MAS) was acquired on a Bruker NEO Spectrometer (Bruker, Billerica, MA) operating at a ^{1}H resonant frequency of 399.49 MHz and ^{13}C frequency of 100.46 MHz. Approximately 50mg of powdered polymer samples (equilibrated using DVS

procedure described above) were quickly packed into 4mm zirconia rotors and sealed with teflon end caps. A Revolution NMR HX probe (Revolution NMR, Fort Collins, CO) spun the sample at the magic angle at speeds of 10 – 13 kHz while at 18.5°C. ^{13}C spectra were acquired with a 1.5 ms contact time for cross polarization (CP), approximately 50 ms acquisition time, and sample-dependent pulse delay. ^{1}H/^{13}C 1D and 2D SSNMR spectra were acquired using a 2.5 μs ^{1}H-90° pulse and 100 kHz ^{1}H decoupling with SPINAL64. A dried polymer sample was used as a standard. Samples equilibrated in the presence of only water or acetone were also used as a reference to identify the location of sorbate peaks. Ideally, the relative amounts of water and acetone present in dual-solvent samples can be determined by integration of the respective water and acetone peaks in the ^{1}H-SSNMR spectra.

A.2.3.2 Solution-state Nuclear Magnetic Resonance Spectroscopy

^{1}H NMR were performed on a Bruker DRX500-2 spectrometer with a 499.87 MHz ^{1}H resonance frequency. 64 scans with a 1 s pulse delay, each containing 16384 acquisition points, were collected for each sample. Dried or equilibrated polymer samples were dissolved in d_4-methanol to form 10 mg/mL solutions. Additional dried polymer solutions were spiked with varying amounts of water or acetone for comparison with the equilibrated samples.

A.2.3.3 Karl Fischer Titration

Equilibrated samples were analyzed for water content using Karl Fischer titration (KFT). A C20S coulometric KF titrator (Mettler Toledo, Columbus, OH) was used to dissolve 2 – 10 mg of polymer in Karl Fischer reagent. Residual water content was determined from the KFT analysis of samples dried under vacuum and then in the DVS at

0% RH for 5 hours. The acetone content in equilibrated samples was calculated as the difference between the total uptake in the DVS and the water content measured by KFT after correcting for residual water.

A.3   Results

A.3.1   Isotherm Analysis

Water and acetone sorption and desorption isotherms were obtained for dried polymer systems. The single component isotherms are shown in Figure A.2. Sorption and desorption isotherms for both polymers were acquired for up to 90% RH or P/P_o prior to T_g analysis in the DSC.
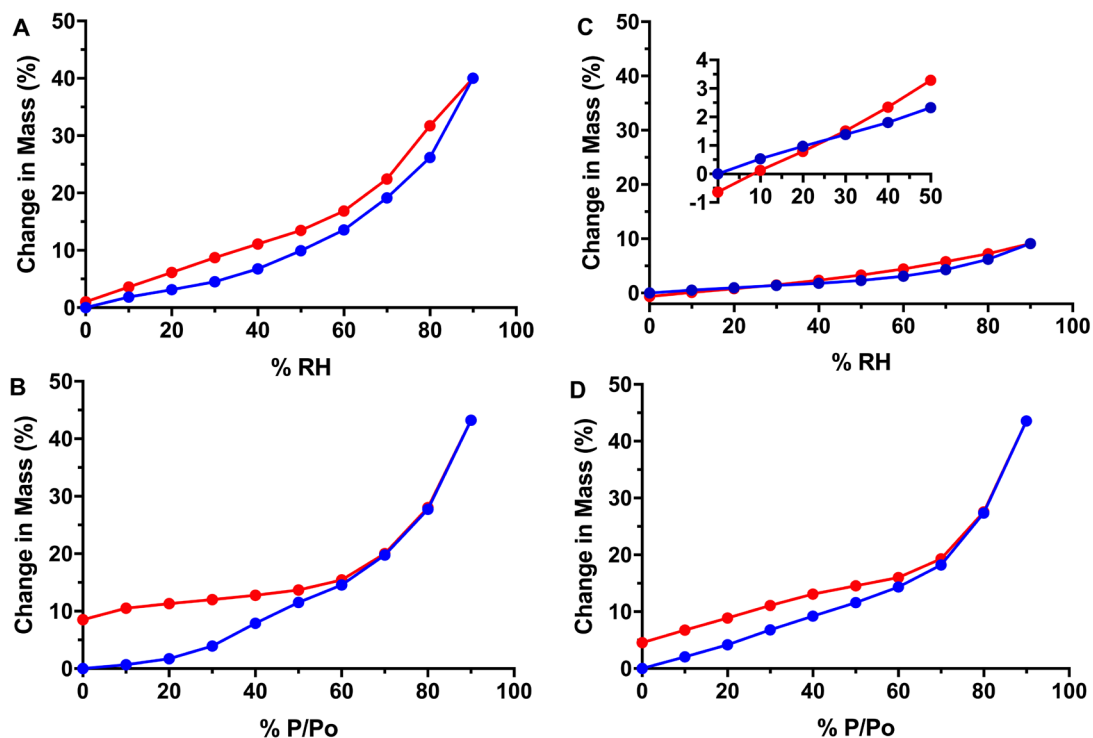
Figure A.2. Full cycle isotherms for dried PVPVA or HPMCAS-HF exposed to water or acetone at 25°C. (A) PVPVA-water, (B) PVPVA-acetone, (C) HPMCAS-water, and (D)

HPMCAS-acetone. Blue = uptake; red = desorption. The insert in (C) shows the negative hysteresis at low % RH.

The isotherm shapes for water uptake are similar between PVPVA and HPMCAS although PVPVA absorbs approximately four-times as much water as HPMCAS at 90% RH. Each appears to contain a small amount of type II isotherm at low partial pressures then follows a reversible type III isotherm and are similar to PVPVA and HPMCAS reported in the literature at 25°C (330). Desorption also follows similar trends in each polymer as positive hysteresis is observed. The difference arises below 30% RH where HPMCAS loses residual water which was tightly bound prior to absorption. Acetone sorption in PVPVA and HPMCAS is approximately linear up to 30% and 70% P/P_o, respectively, at which point rapid solvent uptake is observed. In this case, total acetone uptake at 90% P/P_o is approximately equal between the polymers. No hysteresis is initially observed for acetone systems upon desorption. However, below 70% and 80% respectively, PVPVA and HPMCAS exhibit positive hysteresis which remains even at dry conditions. PVPVA contains ca. 8% acetone after drying while HPMCAS contains ca. 4% acetone.

A.3.2 Plasticization

The glass transition temperature is a critical parameter which can indicate the stability of amorphous systems and is very sensitive to absorbed species. Therefore, the T_g of HPMCAS and PVPVA equilibrated in the presence of water, acetone, or both was measured to determine how the presence of moisture affects T_g. Figure A.3 plots the changes in adsorbent uptake and glass transition temperature as a function of partial pressure in pure solvent systems.
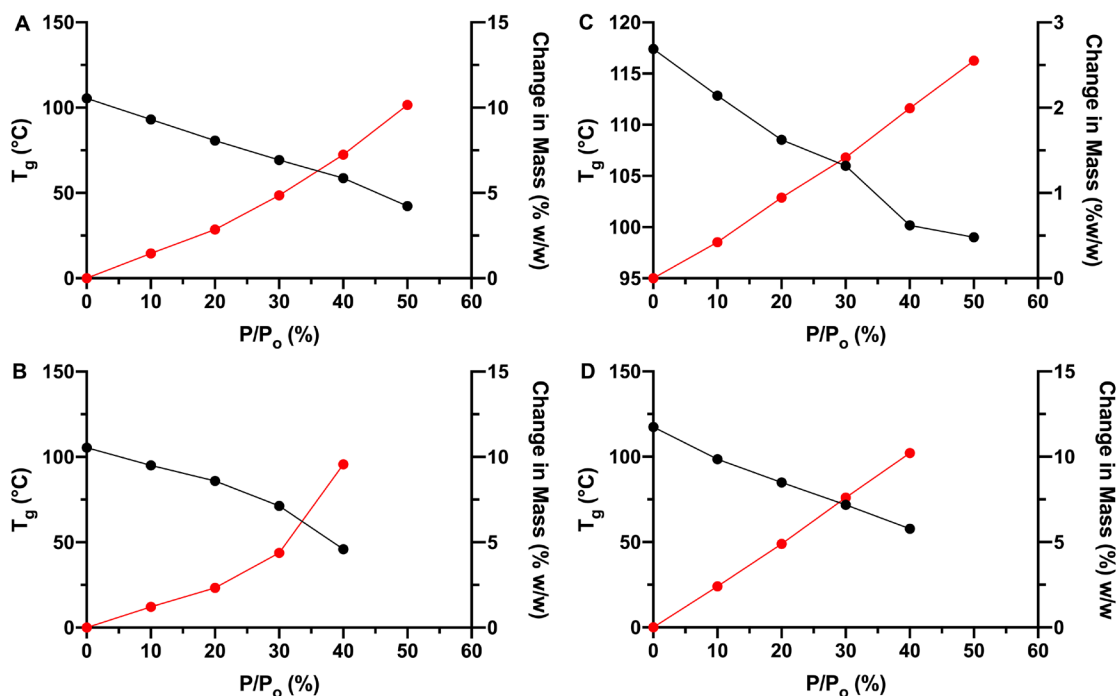
Figure A.3. Change in mass and glass transition temperature as a function of solvent activity. (A) PVPVA-water, (B) PVPVA-acetone, (C) HPMCAS-water, and (D) HPMCAS-acetone. Note the difference in the scale of the dm axis for (C).

Exposure to increasing activities of solvent causes an increase in sorbate uptake equal to that seen in Figure A.2. Similarly, the increasing solvent content causes an approximately linear decrease T_g in all systems studied. Water and acetone both have an extremely low T_g (-136°C and ca. -176°C, respectively) and are much smaller molecules relative to polymers (331). Therefore, both solvents act as plasticizers, with increasing amounts absorbed into the polymer causing an approximately linear decrease in T_g and increasing the molecular mobility of the polymer.

The change in mass due to solvent uptake and the corresponding change in T_g varies between each polymer-solvent system. For example, when held constant at 40% RH or

P/P$_o$, 7.2% water reduces the T$_g$ of PVPVA from 105°C to 59°C while 2% water reduces

the T$_g$ of HPMCAS from 117°C to 100°C. Similarly, approximately 10% acetone uptake

decreases the T$_g$ of both polymers by 60°. Similar results were observed in the literature

for spray dried HPMCAS systems (125).

Figure A.4 shows the T$_g$ as a function of water content predicted by the Gordon-

Taylor and Fox equations.
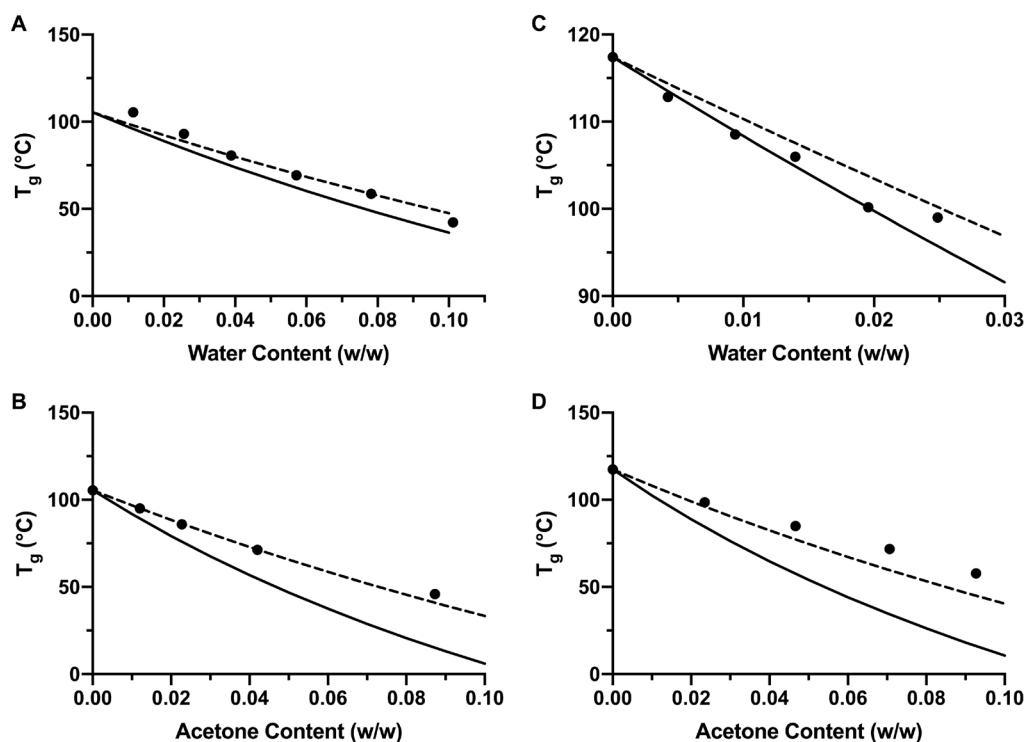
Figure A.4. Observed and predicted glass transition temperature as a function of solvent

content for (A) PVPVA-water, (B) PVPVA-acetone, (C) HPMCAS-water, and (D)

HPMCAS-acetone. Observed (black circles), the Gordon-Taylor equation (solid line), and

the Fox equation (dashed line).

Figure A.4 shows that the ad-/absorbed solvent plasticizes the polymer and reduces

the glass transition temperature. As mentioned in Figure A.3, the degree to which T$_g$ is

reduced varies between different polymer-solvent systems. Figure A.4 also shows the predicted T_g when calculated with either the Gordon-Taylor or Fox equation. Most systems are relatively well predicted by the Fox equation although less so for HPMCAS (Figure A.4C and A.4D). Interestingly, the Gordon-Taylor equation underestimates the T_g in all systems except for HPMCAS-water which is the only system which is overestimated by the Fox equation.

Differences between the observed and predicted T_g values can potentially indicate some degree of interactions between the polymer and solvent. The Gordon-Taylor equation is based on volume additivity and assumes that the mixture components are non-interacting (76). A positive deviation from predicted values can indicate the presence of polymer-solvent interactions which are energetically more favorable than the sum of any polymer-polymer or solvent-solvent interactions that may exist. Both PVPVA and HPMCAS form hydrogen bonds with absorbed water molecules but only PVPVA has measured T_g values greater than Gordon-Taylor predictions (332, 333). The T_g of HPMCAS was difficult to measure due to its extensive sidechain substitution. In theory, each sidechain inherently has varying levels of molecular mobility due to the different functional groups present which are then further affected to varying degrees by the presence of moisture. Therefore, individual sidechain mobility will contribute in varying amounts to the structural changes near T_g. Nonetheless, the T_g of HPMCAS equilibrated at elevated relative humidities is well predicted by the Gordon-Taylor equation. Acetone and PVPVA each lack hydrogen bond donor groups and are well predicted by the Fox equation but still show positive deviations from the Gordon-Taylor equation. Conversely, T_g is underestimated by the

Gordon-Taylor equation for HPMCAS-acetone systems possibly due to the interaction of acetone with the hydroxyl and/ or carboxylic acid side chains of HPMCAS.

The relative plasticizing effects of water and acetone were also compared based on Figure A.4. The slope of T_g versus solvent content indicates the magnitude to which a given amount of solvent plasticizes the polymer. Acetone reduces the glass transition temperature of both PVPVA and HPMCAS by approximately 6.5°C (6.8% and 6.3%, respectively) for every one percent of solvent absorbed. Water varies in the extent to which the polymer is plasticized. In good agreement with values reported in the literature, the T_g of PVPVA is reduced by 6.8°C for every one percent water uptake (332). An equivalent water uptake of 1% plasticizes HPMCAS to a greater extent as T_g is reduced by 7.5°C.

To this point, only single-solvent systems have been considered. However, mixed solvent systems are often used during spray drying to solubilize all solid components. Therefore, the combined plasticizing effect of water and acetone was also investigated to better represent a real spray drying solution. Figure A.5 shows the reduction in T_g when PVPVA and HPMCAS are exposed to mixed solvent systems with constant partial pressures of acetone.
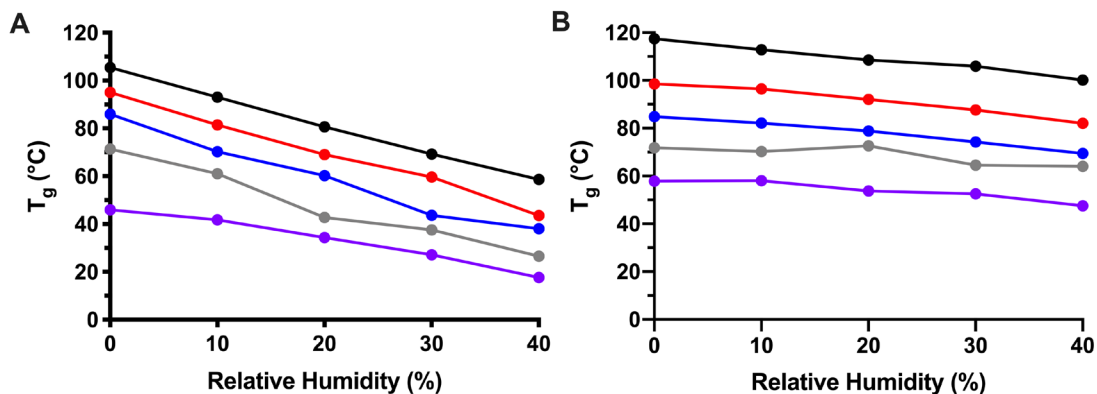
Figure A.5. Glass transition temperature as a function of relative humidity with a constant background partial pressure of acetone for (A) PVPVA and (B) HPMCAS-HF. (Background acetone partial pressure: black = 0%, red = 10%, blue = 20%, gray = 30%, purple = 40%.)

The black line (0% P/P_o acetone) shows the same reduction in T_g with relative humidity as that shown in Figure A.3A and A.3B. The greater water absorption at an equivalent relative humidity in PVPVA compared to HPMCAS is also evident in Figure A.5 based the slopes of the lines. This difference has implications relating to spray dried product stability. Exposure of a PVPVA-containing product to a particular relative humidity is more susceptible to moisture uptake relative to a HPMCAS-containing product at the same humidity. The introduction of a background partial pressure of acetone causes a roughly linear reduction in T_g for a constant relative humidity. For example, for every 10% P/P_o, the T_g of PVPVA or HPMCAS is reduced by approximately 10°C or 14°C, respectively.

The effect of total solvent content on the glass transition temperature is shown in Figure A.6.
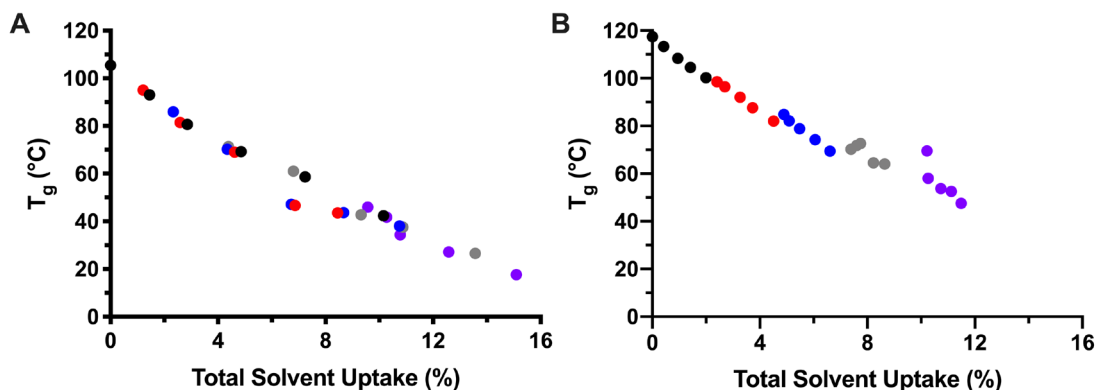
Figure A.6. Glass transition temperature as a function of total solvent uptake for single and mixed solvent systems. (A) PVPVA. (B) HPMCAS-HF. (Acetone partial pressure: black = 0%, red = 10%, blue = 20%, gray = 30%, purple = 40%.)

The glass transition temperature of both PVPVA (Figure A.6A) and HPMCAS (Figure A.6B) decreases linearly with the total solvent content regardless of the solvent combination used to equilibrate the polymer. Presumably, the linear change in T_g is independent of the relative amounts of each solvent present (see section A.4.4). The difference in overlap in partial pressure data is also observed in Figure A.6. PVPVA shows significant overlap between samples equilibrated with varying background partial pressures of acetone while HPMCAS shows a continual reduction in T_g with increasing acetone background. The difference is due to the relative uptake of each solvent. PVPVA absorbed comparable amounts of water and acetone at all solvent activities while HPMCAS absorbed significantly more water relative to acetone. Any water uptake in HPMCAS, even at 40% RH, was overcome by acetone absorption, even at as little as 10% P/P_o. This is further illustrated by the difference in the slopes of Figure A.5A and A.5B.

A.3.3 Sorbate Quantitation

The DVS used in this study provided the total mass change during sorption but did not quantify the relative amounts of sorbate present in dual sorption experiments. Various analytical methods were used in an attempt to quantify each sorbate present in an equilibrated sample however none were successful. The results are included here for informational purposes only.

First, Karl Fischer titration (KFT) was used to measure the water content. In theory, the difference between the total uptake (measured using DVS) and water content (from KFT) should yield the mass of acetone in the sample. The entire equilibrated sample was placed in the electrolysis cell. Dry samples were first analyzed by KFT to determine the initial residual water content. The average PVPVA residual water content (0.181%) was used to correct for residual water in other equilibrated samples.

Preliminary samples equilibrated only in the presence of water (up to 90% RH) were used to compare measured water content using the DVS or KFT. Samples equilibrated at low relative humidity showed equivalent water contents when analyzed by either DVS or KFT. However, PVPVA samples equilibrated above 60% or 70% RH changed from a loose dry powder into a sticky gel due to absorbing enough water to plasticize the system into the supercooled liquid state. The sample did not fully dissolve into the Karl Fischer solution. Water content measured with KFT plateaued above 60% RH and became significantly less than values measured with DVS.

Nonetheless, PVPVA test samples equilibrated in the presence of water and acetone at 10% RH and 10% P/P_o or 30%/30% were first analyzed. The relative amounts of water and acetone absorbed in each sample are shown in Table A.1.

Table A.1. Relative uptake of water and acetone in PVPVA dual solvent experiments as measured by Karl Fischer titration.

	Total Mass Uptake (%)	Water (%)	Acetone (%)
10% RH, 10% P/P$_o$	3.028	77.05	22.95
30% RH, 30% P/P$_o$	11.037	22.41	77.59

The relative uptake of water and acetone varies as a function of total solvent activity in equilibrated PVPVA samples. At low solvent activities (10%/10%), nearly three-times as much water is absorbed compared to acetone. This is not surprising considering that 2.5-times as much water absorbed at 10% RH compared to 10% P/P$_o$ acetone in single solvent experiments. It is interesting to note that a greater total solvent uptake is observed in the dual solvent experiment compared to adding together the single component data. One may hypothesize that the presence of acetone causes extra swelling of the polymer to allow additional water uptake. Indeed, this was seen previously during water and acetone absorption into polyvinyl alcohol (334).

At higher total solvent activities (30%/30%), acetone appears to absorb to a greater extent than water. This would indicate that acetone out-competes water at higher solvent activities. However, this is unlikely as the relative affinity of either sorbate should not significantly change with uptake. A more likely explanation is the incomplete dissolution of the equilibrated PVPVA in the Karl Fischer solution. The 30%/30% PVPVA sample changed into a viscous gel similar to the water-equilibrated samples above 60% RH. Presumably, a significant amount of water (and acetone) remained in the undissolved

PVPVA which was unaccounted for by the KFT calculation and led to the underestimation of water/ overestimation of acetone. As many samples exhibited a similar change in morphology at high solvent activities, Karl Fischer titration was not seen as a viable quantitative technique at least within the scope of this experiment.

Solution-state nuclear magnetic resonance (NMR) spectroscopy was explored as an alternative quantitative analytical technique. Deuterated methanol (CD_3OD) was found to adequately solubilize both PVPVA and HPMCAS. Dried polymer samples spiked with the equivalent of 1% solvent uptake were analyzed using ^1H NMR (Figure A.7).
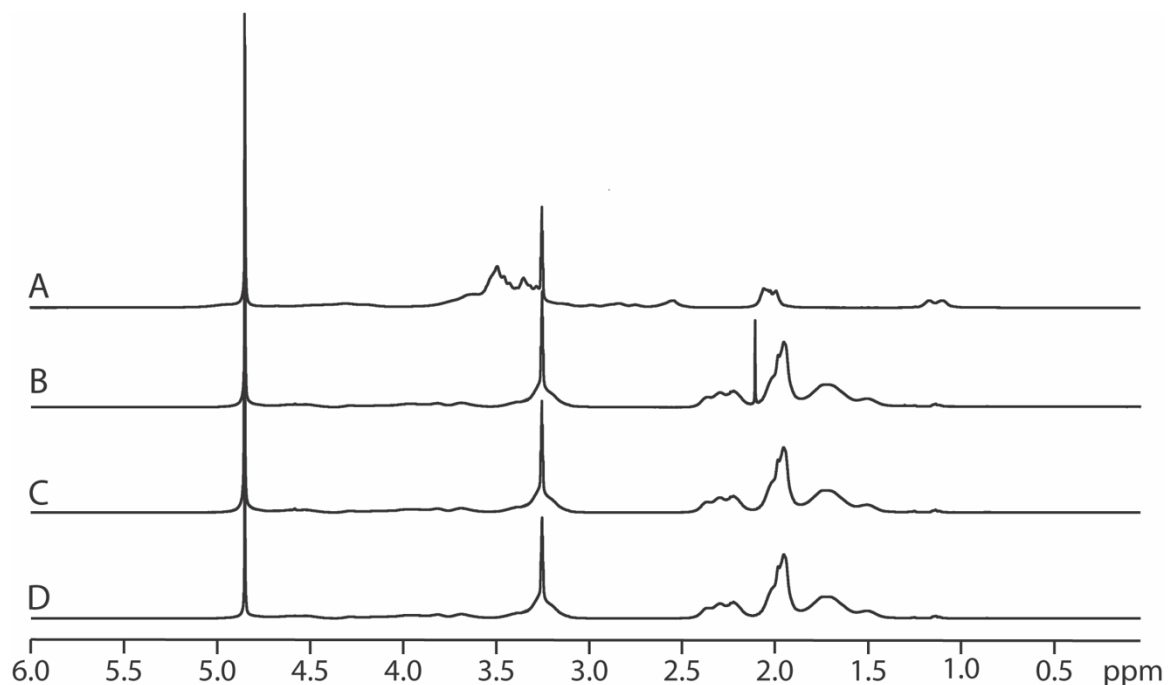
Figure A.7. Initial 1H NMR spectra for quantitative analysis. All samples were dissolved at 10-15 mg/ml in methanol-d4. (A) Dried HPMCAS-HF, (B) PVPVA with 10% acetone, (C) PVPVA with 10% water, and (D) dried PVPVA. (Percentage refers to uptake in the polymer prior to dissolving in the NMR solvent.

The water peak (4.9 ppm) was well resolved although significant amounts of residual water were also present and must be corrected for. The acetone peak (2.15 ppm) did overlap slightly with peaks in both polymer spectra which makes deconvolution and accurate quantitation more difficult. At the time of writing, NMR is still being explored as a quantitative analytical technique. For the purposes of this experiment, the biggest challenge facing its implementation is finding a suitable NMR solvent (solubilizes all components and has a well-resolved residual solvent peak). Furthermore, the solvent selected will be system dependent as the polymer (and drug, for SSDs) and each solvent will all have different chemical shifts.

Lastly, solid-state NMR (SSNMR) was used for quantifying water and acetone as well as to provide additional molecular-level information into the state of the sorbate in the polymer. One-dimensional and two-dimensional ^{1}H and ^{13}C spectra were acquired for each polymer before and after exposure to solvents. Figures A.8 and A.9 show ^{1}H and ^{13}C SSNMR spectra for PVPVA, respectively. ^{1}H and ^{13}C spectra are shown for HPMCAS in Figures A.10 and A.11, respectively.
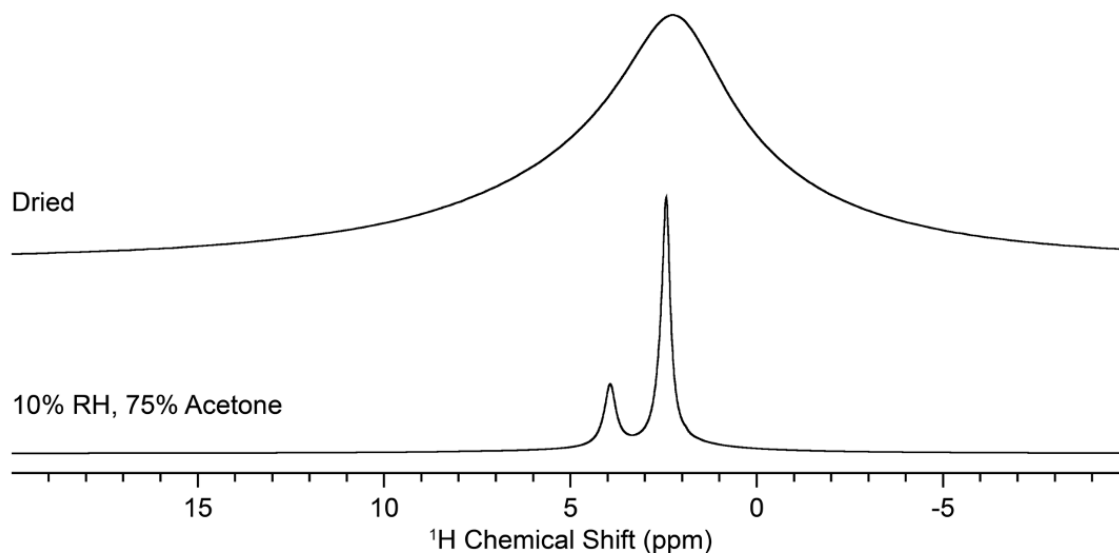
Figure A.8. ^{1}H SSNMR spectra of PVPVA after drying or exposure to mixed solvents.
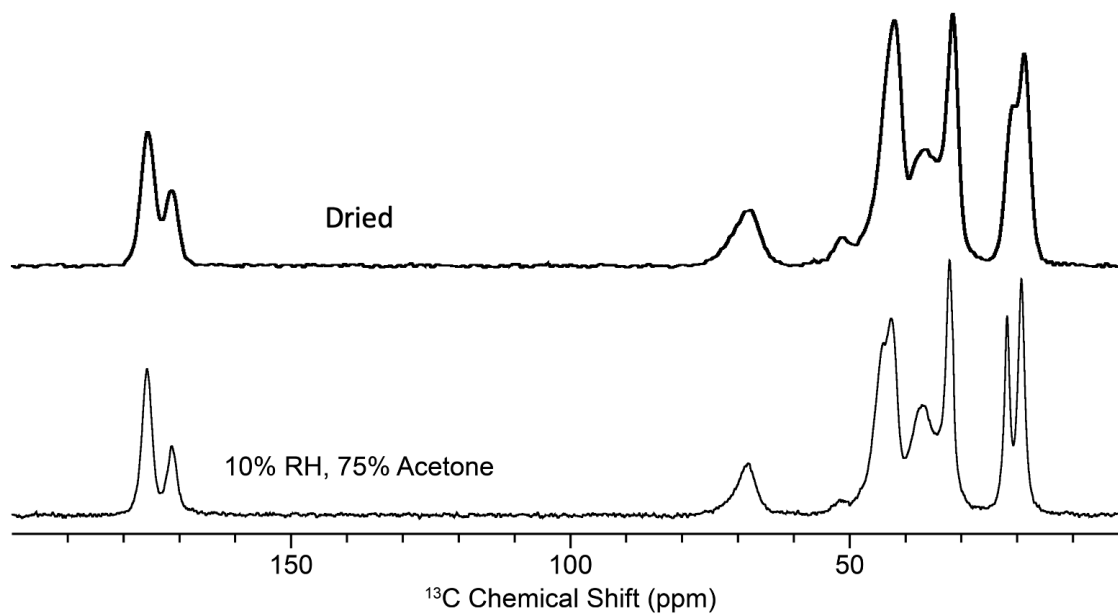
Figure A.9. ^{13}C SSNMR spectra of PVPVA after drying or exposure to mixed solvents.
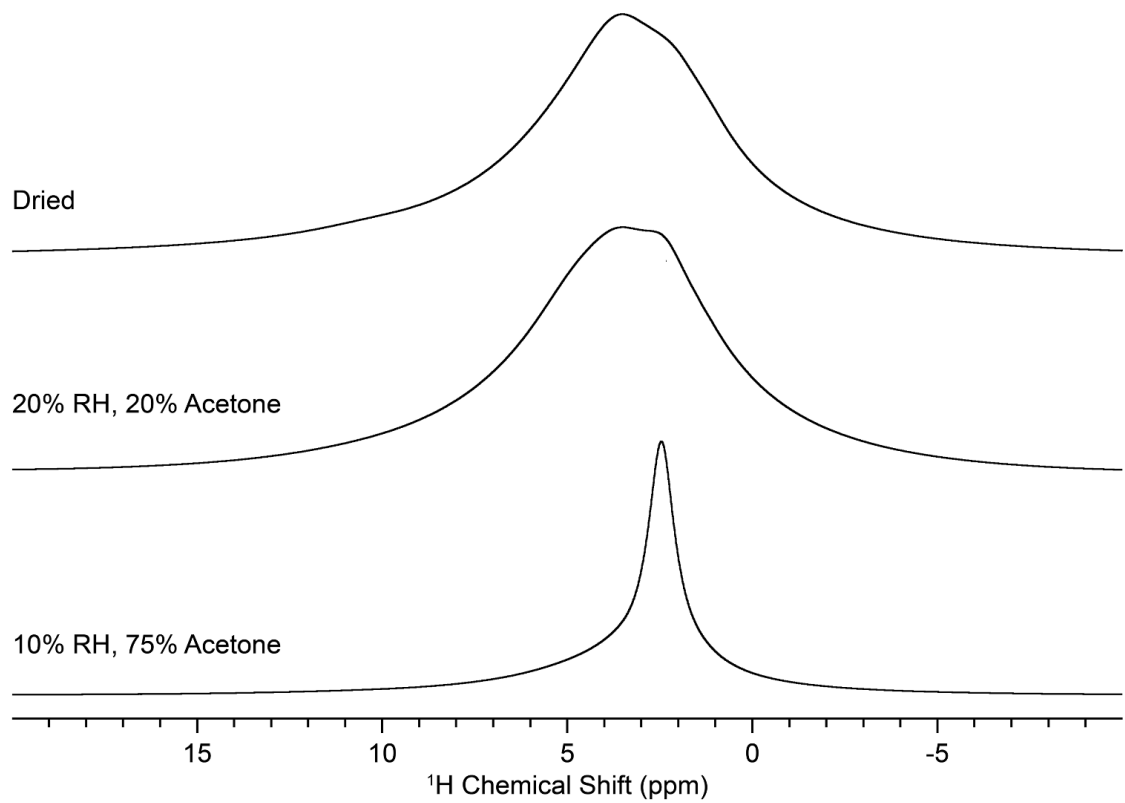
Figure A.10. ^{1}H SSNMR spectra of HPMCAS-HF after drying or exposure to mixed solvents.
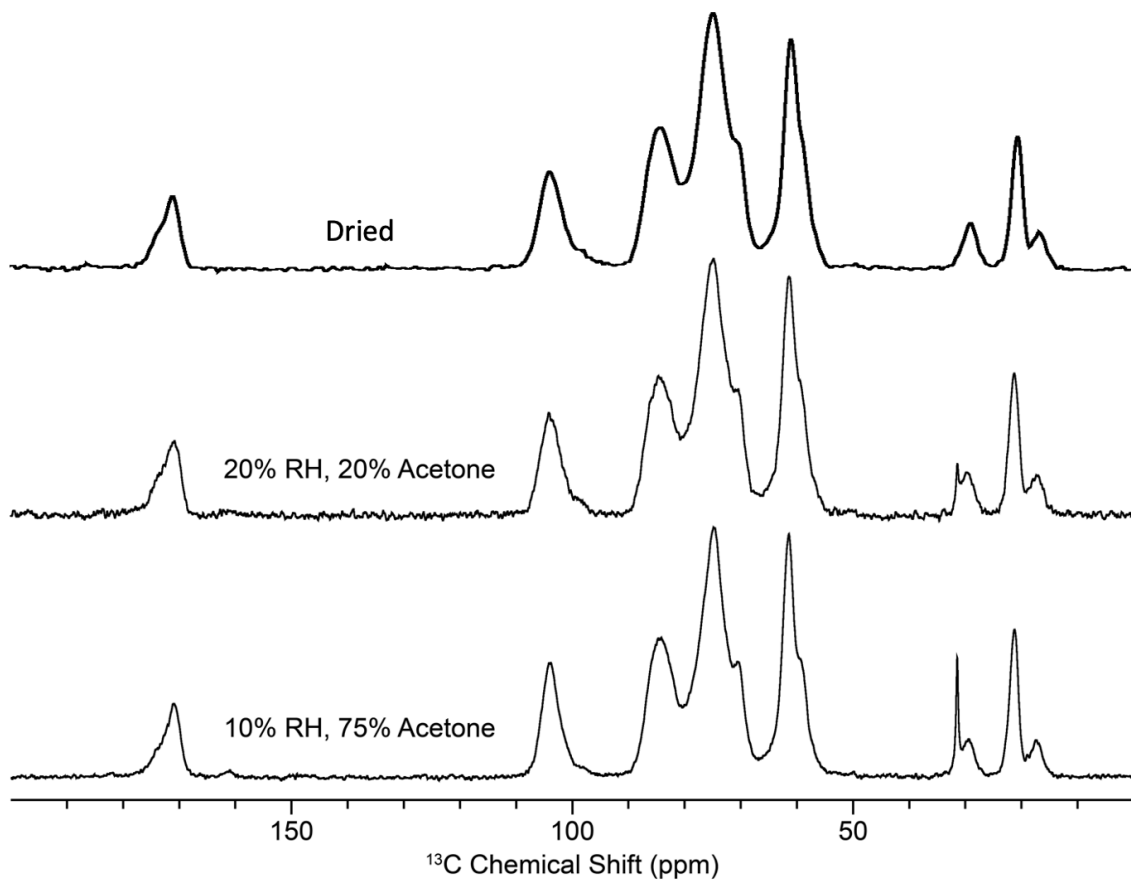
Figure A.11. ^{13}C SSNMR spectra of HPMCAS-HF after drying or exposure to mixed solvents.

^{1}H SSNMR peaks in both dried polymers are very broad due to ^{1}H-^{1}H homonuclear dipolar coupling. Peak shape changed with solvent absorption. PVPVA exposed to 10% RH and 75% P/P_o acetone developed two peaks. The smaller peak at 4 ppm is attributed to water while the larger peak at 2.5 ppm is attributed to greater acetone uptake. The underlying PVPVA peak is still very broad and difficult to deconvolute. Similar results are found for HPMCAS however the water peak at 4 ppm does not appear indicating either that water is highly mobile or that very little was absorbed into the polymer. In addition, there are many hydroxyl groups in HPMCAS sidechains which would have similar chemical shifts to water. ^{13}C SSNMR showed a sharp peak at 32 ppm in HPMCAS

attributed to acetone. A similar peak was also found in PVPVA although a resonance also appears at the same chemical shift in the dry polymer. Water was not detected using ^{13}C SSNMR.

To improve the resolution of the ^{1}H spectra, DUMBO (decoupling using mind-boggling optimization) was applied to reduce ^{1}H-^{1}H coupling and achieve more solution-like spectra. Figures A.12, A.13 and A.14 show the 2D spectra of various equilibrated polymers using DUMBO. The abscissa shows the original ^{1}H spectra while the ordinate shows the results of enhanced decoupling.
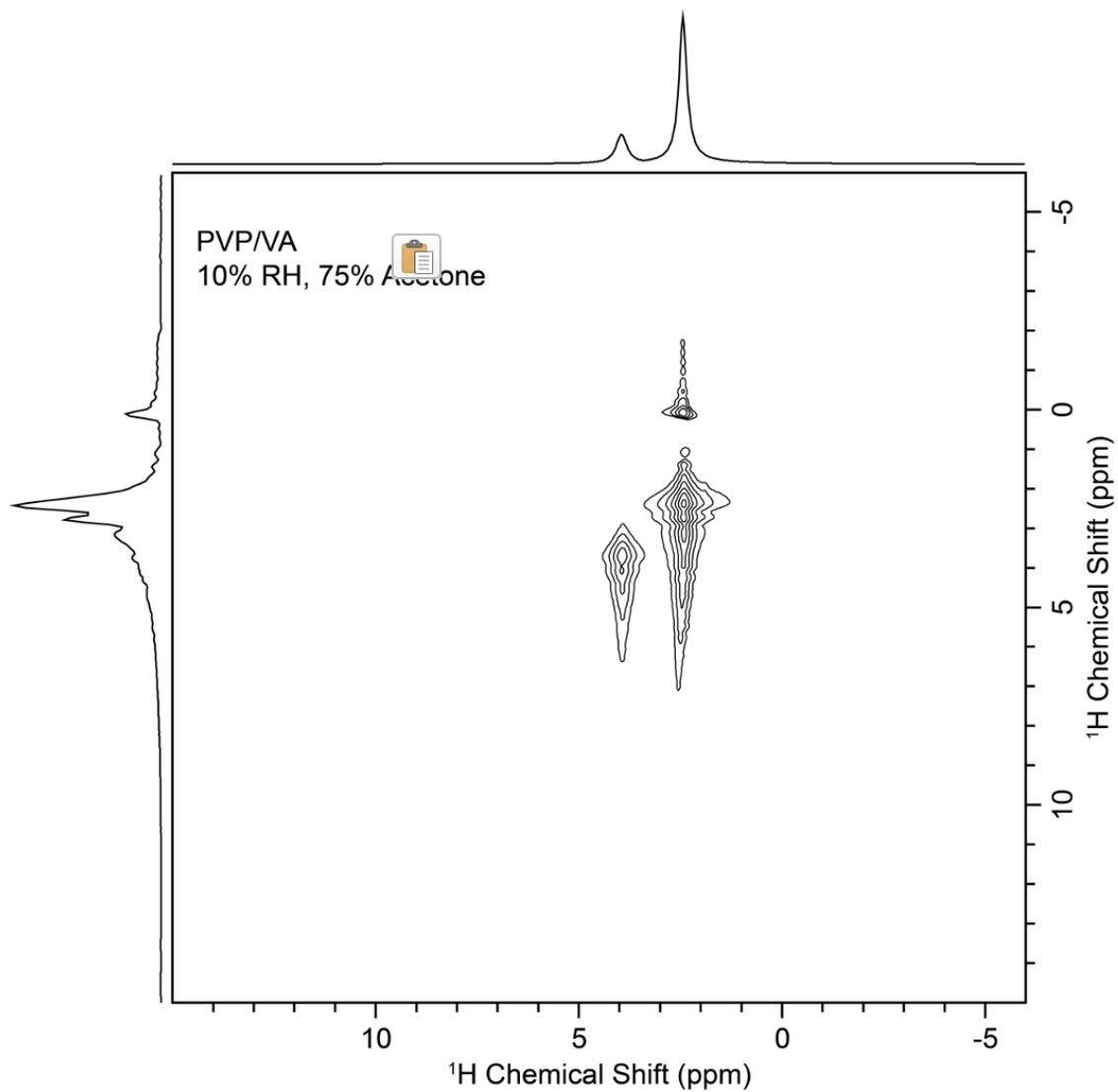
Figure A.12. [1]H-^{1}H homonuclear 2D spectrum of PVPVA equilibrated at 10% RH and 75% P/P$_o$ acetone acquired using DUMBO.
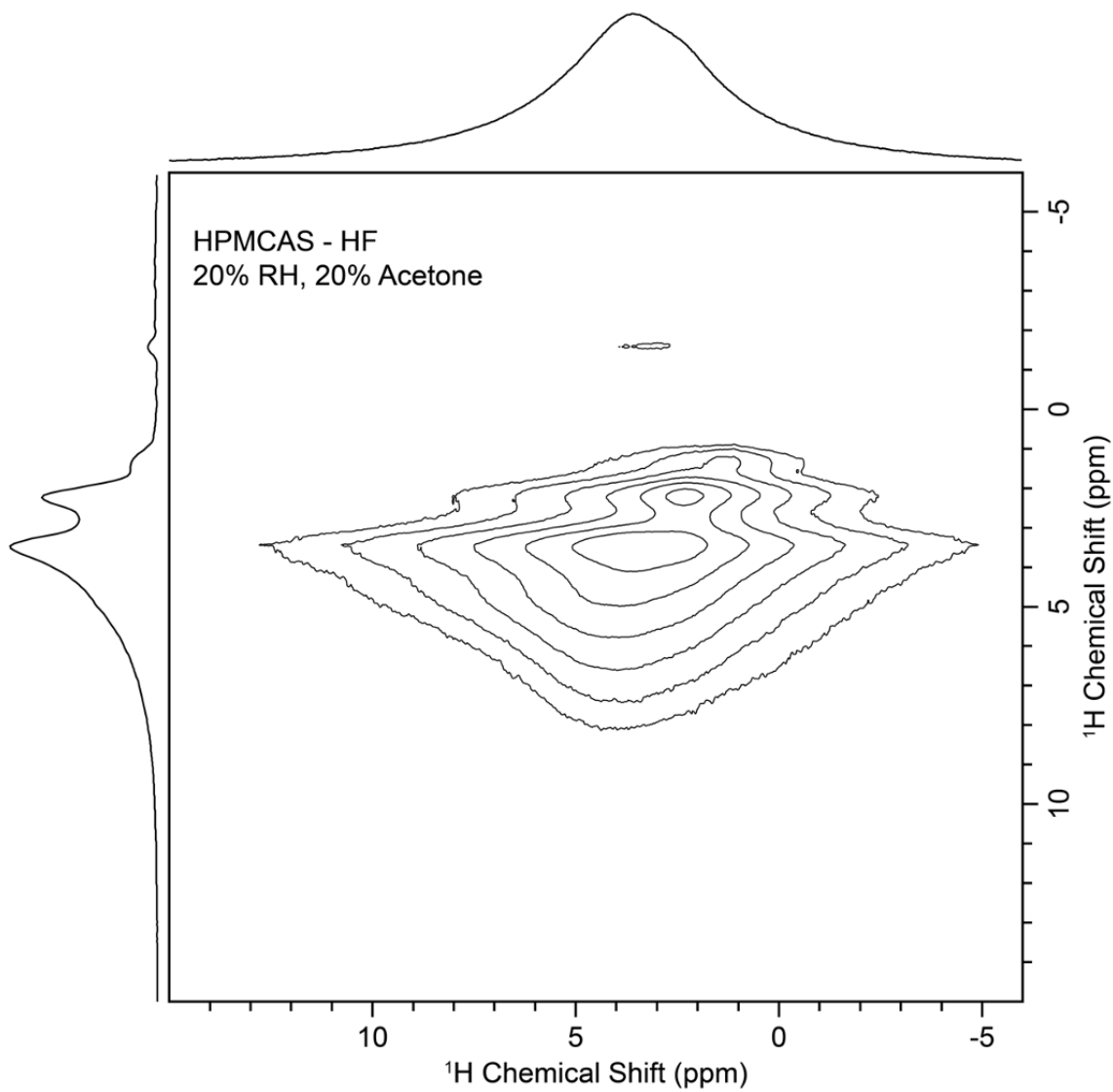
Figure A.13. ^{1}H-^{1}H homonuclear 2D spectrum of HPMCAS-HF equilibrated at 20% RH and 20% P/P$_o$ acetone acquired using DUMBO.
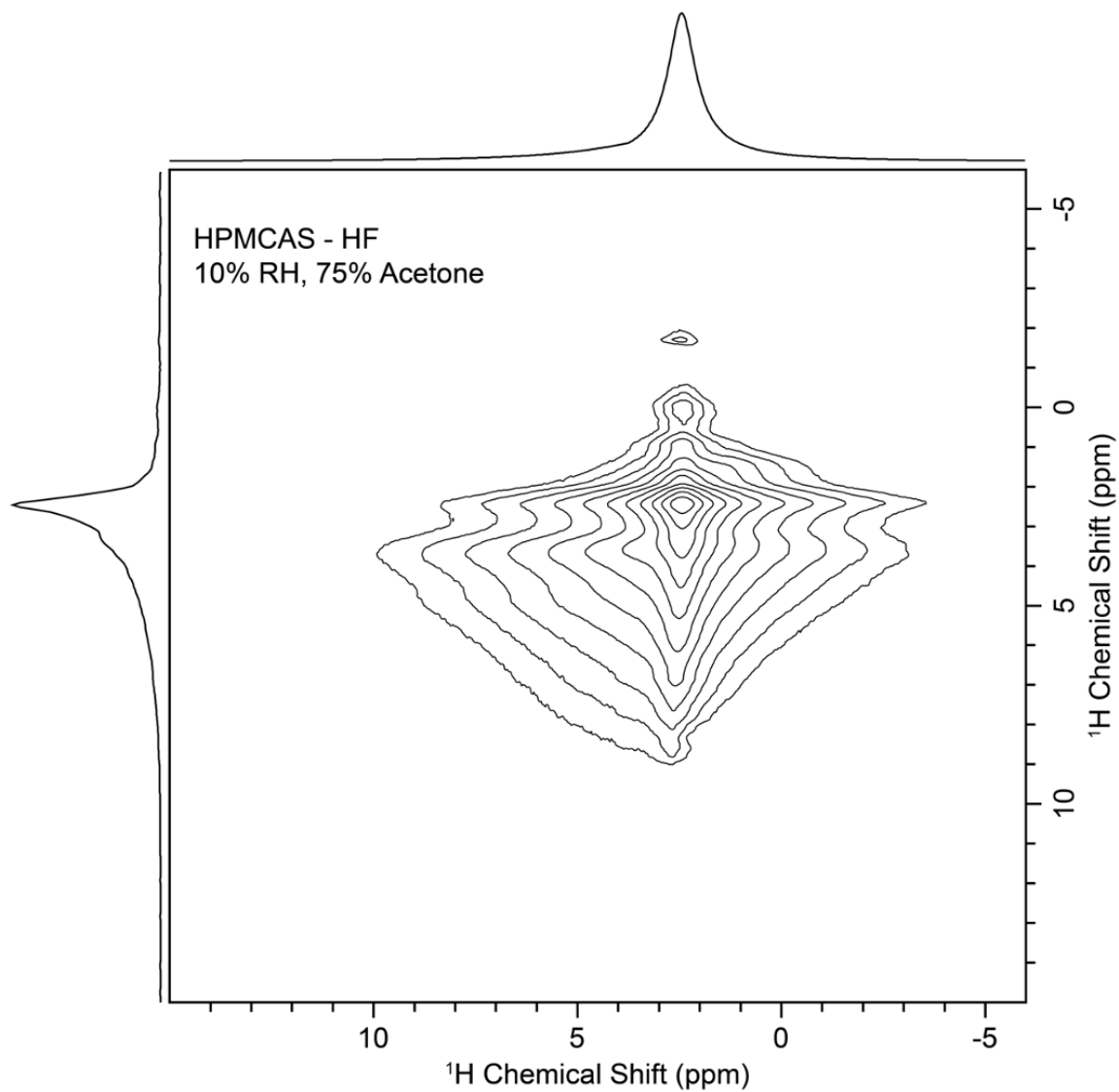
Figure A.14. ^{1}H-^{1}H homonuclear 2D spectrum of HPMCAS-HF equilibrated at 10% RH and 75% P/P$_{o}$ acetone acquired using DUMBO.

The resolution of the ^{1}H DUMBO spectra is improved but the ^{1}H peaks are still too broad for quantitative purposes. At this point, further experiments are needed to identify the peaks present, including the creation of a calibration curve at a series of relative humidities and partial pressures. Faster MAS speeds would also help to reduce linewidths and improve resolution.

A.3.4 Diffusivity

The initial rate at which solvents moved into or out of the polymers were measured as diffusion coefficients or diffusivity. Respectively, Figures A.15 and A.16 plot the diffusivity of water vapor into and out of PVPVA or HPMCAS at varying relative humidities. Samples of varying density or morphology (packed versus melt cast) were analyzed to represent changes in particle density that occur throughout the spray drying process or variations in the particle morphology of the final product (326). All absorption diffusion experiments started at 0% RH or P/P_o and all desorption diffusion experiments ended at 0%. For absorption experiments, the x-axis represents the size of the step change or the final activity that the sample was equilibrated. For desorption experiments, the x-axis represents the activity the sample was initially equilibrated at prior to a step change to 0% RH or P/P_o.
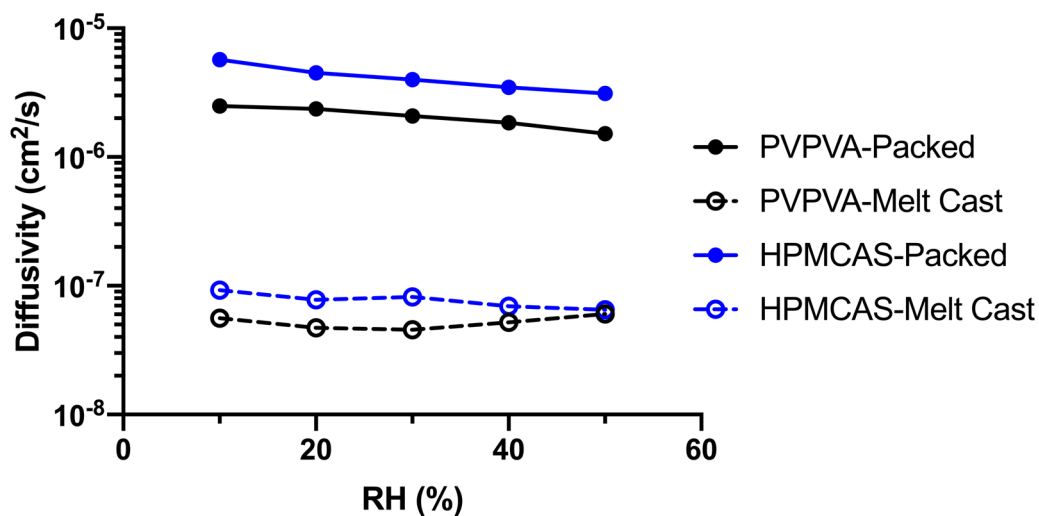
Figure A.15. Initial diffusivity during absorption of water into a polymer at varying activities and different morphologies.
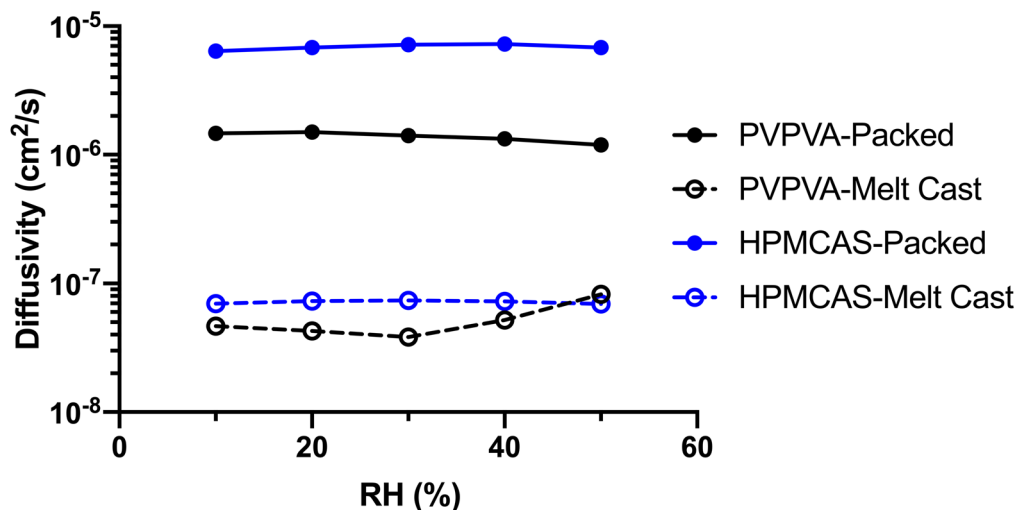
Figure A.16. Desorption diffusivity of water out of PVPVA or HPMCAS with varying particle morphologies.

Diffusivity of water into HPMCAS occurs at twice the rate of water into PVPVA and is constant across the relative humidity range observed. Melt quenched samples contain less void space and are denser than the packed samples. The diffusivity of water in both polymers decreases by nearly two orders of magnitude in the in melt-quenched samples relative to the packed samples. The difference in diffusivity between PVPVA and HPMCAS decreases as relative humidity increases. The initial diffusivity of water uptake at 50% RH in each polymer is approximately the same.

Water diffusivity during desorption out of the polymer shows similar results to absorption. Diffusion out of HPMCAS is greater than PVPVA diffusivity for packed and melt-quenched samples. Again, this difference is approximately constant in packed samples but decreases at high relative humidity in melt-quenched samples.

Under normal circumstances, samples will only be dissolved in acetone and no acetone vapor will be absorbed in a spray dried product. Therefore, the diffusivity of

acetone during desorption was also investigated to better understand the difference between water and organic solvent removal during spray drying. Figure A.17 shows the desorption diffusivity of water or acetone in either polymer as well as the acetone/ water relative diffusivity.
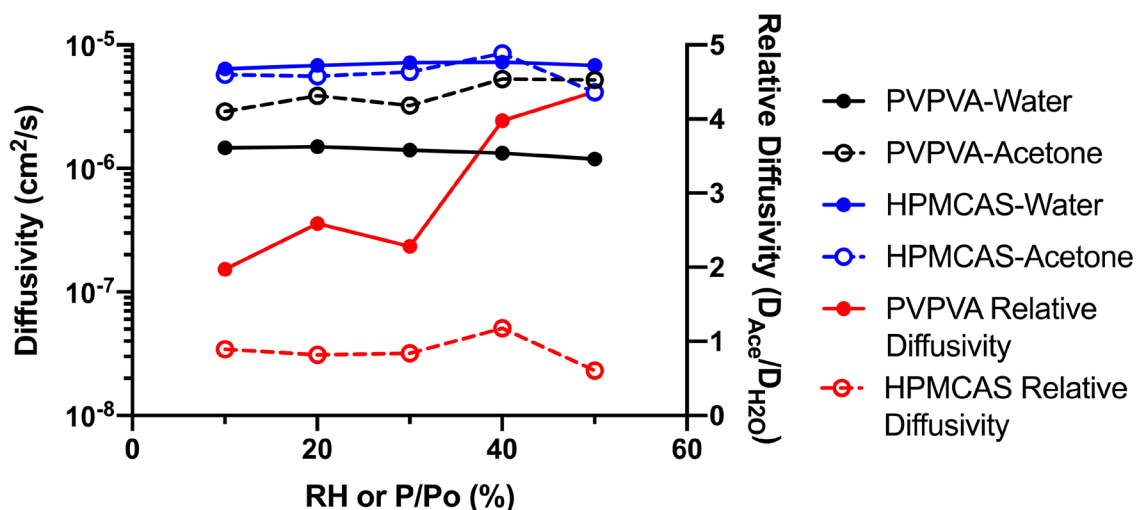
Figure A.17. Desorption diffusivity of solvent in polymer at varying activities. The relative diffusivity of acetone compared to water in each polymer is also shown.

The diffusivity of acetone is greater than the diffusivity of water out of PVPVA while the two solvents diffuse out of HPMCAS at approximately the same rate. The water desorption diffusivity shown in Figure A.17 is the same as in Figure A.16. Water and acetone diffusion out of HPMCAS appears to be independent of the change in activity (i.e., desorption driving force). On the other hand, acetone diffusion out of PVPVA increases with increasing driving force while water diffusion remains approximately constant. Therefore, the relative rate of diffusivity ($D_{acetone}/D_{water}$) decreases with decreasing solvent activity. Practically, this means that, while acetone is removed from PVPVA at a greater rate during the entire drying process, its rate of removal will slow as the particle dries. The

majority of acetone is removed rapidly, creating a drying particle with increased water content relative to the initial feed solution concentration.

A.4   Discussion

Water or various organic solvents may be found in a drug substance or drug product as a result of processing/ manufacturing or exposure to environmental humidity. In each case, the presence of solvent may have unintended consequences relating to the stability of a pharmaceutical formulation. Dynamic vapor sorption is an important analytical technique as it can investigate how materials both respond to exposure to elevated levels of water or organic solvents as well as how solvents are removed during drying. The latter of which allows DVS to be used as an approximation of solvent removal during spray drying.

A.4.1   Water and Acetone Uptake

Water uptake is of particular interest since nearly all pharmaceutical systems are exposed to environmental humidity. The greatest benefit to acetone absorption is the creation of systems with acetone contents representing various timepoints in the spray drying process. Type III isotherms indicate that water is adsorbed in a multilayer fashion. However, the small amount of type II isotherm at low partial pressures may suggest that water forms or begins to form an incomplete monolayer in each polymer prior to multiple adsorbate layers forming (335). The increase from linear acetone uptake above a polymer-specific solvent activity may indicate a shift to multilayer absorption at higher partial pressures. Since water and acetone are two commonly used spray drying solvents, their dual solvent absorption experiments allow the creation of systems with mixed solvent contents and material properties similar to various time points during spray drying.

A.4.2 Drying and Desorption

PVPVA and HPMCAS retain a greater moisture content after drying than their initial moisture content prior to ad-/ absorption and may be problematic from a product drying/ residual solvent standpoint (see section A.4.3.2). A positive hysteresis loop (Figures A.2A, A.2B, and A.2D) indicates that pores exist in the polymer adsorbents and absorption into the interior of the dried polymer is likely regardless of the adsorbent and adsorbate present. Incomplete drying or exposure to elevated humidity during either production or storage may result in elevated solvent content despite a return to the previous equilibrium conditions. Negative hysteresis at low relative humidity (e.g., water desorption from HPMCAS) can indicate that a phase change has occurred and water which was initially tightly bound is now free to leave during drying. In either case, hysteresis may affect product properties, as the solvent content after spray drying may not necessarily match the solvent content after exposure to elevated humidity conditions. This further complicates the adequate characterization of amorphous products produced by unit operations utilizing solvents including spray drying. Therefore, the spray drying process must be well characterized to control drug product uniformity especially as the presence of residual solvents must be controlled from both a regulatory and product stability standpoint (327).

A.4.3 Application to Amorphous Product Stability

The stability of a spray dried product is dependent on a variety of factors including the kinetics of solvent uptake or desorption, as well as plasticization from increased solvent content. Therefore, the stability must be considered both during and after drying where the SSD may be exposed to environmental stresses. For the purposes of this chapter, the

discussion focus will be limited to the movement of moisture into/ out of polymeric systems and their effect on the glass transition temperature.

A.4.3.1 Stability During Spray Drying

Desorption studies are most applicable to approximate the solvent removal process during spray drying. The rate of solvent removal was found to be dependent on the solvent-polymer combination, and, for acetone out of PVPVA, also dependent on the difference between the initial and final solvent content. In spray dried systems, the rate of solvent removal has been shown previously to affect the final particle morphology and dissolution performance (336, 337). In addition to the drying rate, the solubility, feed solution concentration, and inlet/ outlet temperatures also affect the morphology of the spray dried product (326). Therefore, a thorough investigation of desorption during dynamic vapor sorption may be used to gain insights into the spray drying process and how diffusivity and T_g can affect stability during and after drying.

Most drugs manufactured by spray drying are poorly water soluble. For a multicomponent system, such as an amorphous solid dispersion, an organic solvent or mixed solvent system is often needed to fully solubilize the drug and polymer. These solvents are then rapidly removed during the primary drying to form an intimately mixed drug-polymer amorphous solid dispersion. However, variable solvent removal rates have also been shown to affect the product homogeneity in ASDs produced from a single solvent (338). One could hypothesize then, that the disproportionate removal of the organic solvent and water observed for PVPVA (Figure A.17), especially early in the drying process, may cause changes to the physicochemical properties of the final SSD. In the least, spray dried

systems with relatively slow water diffusivity may result in a product with high residual water content.

Changes in the mixed solvent composition relative to the feed solution composition can also affect the miscibility and/ or solubility of the dissolved solids. The solvent(s) comprising a feed solution should maximize solute-solvent interactions and fully solubilize solid components. In the case of a polymer, a good solvent would result in polymer swelling which helps stabilize an amorphous drug in a SSD (339). Therefore, a change in solvent composition during drying can affect solvent quality which may be detrimental to final SSD product quality and performance (337, 339). Furthermore, rapid changes to the solvent composition and solids concentration can potentially cause the system to pass through phase envelopes leading to phase separation and/ or crystallization (326, 340). Since the organic solvent is added mainly to solubilize the drug, its removal prior to/ at a faster rate than water may be particularly problematic concerning moisture-induced phase separation and crystallization.

The changing solvent content during spray drying also affects the physical properties of the drying droplet including the glass transition temperature. Therefore, the T_g may also be used to understand changes occurring within a drying droplet during spray drying. Typical spray drying solvents, including water and acetone, plasticize the system and their presence can significantly affect the physical stability of a SSD. Changes in T_g indicate changes to the relative mobility of the system and can provide information regarding the likelihood of phase separation or crystallization occurring as the particle dries.

From a mobility standpoint, the initial stages of primary drying represent the greatest chance for crystallization as the solvent content is highest and the drug/ polymer is significantly plasticized. The polymer is likely in the supercooled liquid state as the T_g may be reduced below the drying temperature. However, the concentration of the dissolved solids is also low during the early stages of primary drying and less likely to crystallize. The concentration of dissolved solids increases and eventually can become supersaturated with the removal of solvent through additional drying. This increases the likelihood for crystallization despite an increase in T_g. This is especially concerning given that the relative rates of solvent removal may vary due to differences in water and acetone diffusivity. For example, acetone desorption diffuses out of PVPVA faster than water which creates an excess of water remaining in the droplet at the later stages of drying. Again, since most drugs being spray dried are poorly water soluble, the increase in relative water content will further increase the supersaturation in the remaining mixed solvent and may complicate their formulation as an ASD using spray drying. Therefore, the relative rates of solvent diffusion out of a drying droplet must be considered during spray drying if they are significantly different.

It cannot be overlooked that the diffusivity values measured in this study were for single component systems. While the diffusivities measured in this study agree well with values reported in the literature, it is possible that the presence of one solvent changes the diffusivity of the other (326). For example, increasing proportions of acetone in polyvinyl alcohol decreases the diffusivity of water (334). Again, this underscores the need for a quantitative method so that the diffusivity of each solvent in the presence of another can be more accurately measured to account for cosolvent effects.

A.4.3.2 Residual Solvent & Stability During Storage

Spray drying conditions and the resulting material properties (e.g., particle size, morphology, and residual solvent content) ultimately affect the downstream processability, physical stability, and shelf life of the spray dried material (326, 340-342). The amount of residual solvent should be minimized as they can catalyze both physical and chemical degradation reactions. Chemically, residual water can often cause hydrolysis in a sample whereas physically, residual solvents can cause polymorphic transformations, aggregation, or crystallization, etc. (343). As far as amorphous stability is concerned, solvents with a large plasticizing ability, especially those which are difficult to remove during primary or secondary drying, are of the greatest concern to product stability.

In addition to the physical stability implications resulting from residual solvent content, toxicity resulting from residual solvents must also be considered. Therefore, the concentration of residual solvent must be controlled to limit unintended side effects to the patient. The allowable solvent concentration is specific to each individual solvent and is explicitly outlined by the International Conference of Harmonization's Q3C guidelines (327).

While the residual solvent content after spray drying affects physical stability, the impact of the storage conditions on stability must also be considered. Exposure to elevated temperature or humidity conditions will affect the water content of the spray dried material. The temperature, pressure, and solvent activity determine the equilibrium sorbate content of a polymer-solvent combination, but the diffusivity affects the rate at which the solvent moves into or out of the polymer to reach equilibrium. Nearly all excipients, drug substances, and formulated drug products will all uptake some amount of water when

exposed to environmental relative humidity either through adsorption to the surface and/or absorption and diffusion into the bulk. The rate of absorption is strongly material dependent. In the case of polymeric excipients, differences in water absorption diffusivity may be partially explained by each polymer's affinity for water. The greater number of hydrophilic groups in HPMCAS would explain the greater initial diffusivity of water compared to PVPVA. However, PVPVA is more hygroscopic and forms a greater number of strong hydrogen bonds between its carbonyl groups and water compared to weaker hydrogen bond formation in HPMCAS which results in its increased equilibrium water content (344, 345). When considering the shelf life of a SSD, the use of polymeric excipients which absorb large amounts of water should be balanced against the polymer's ability to stabilize the drug against crystallization in the presence of moisture and other product properties such as viscosity. For example, the additional stability imparted by the hygroscopic polymer PVP in ASDs was shown to outweigh the instability of increased moisture uptake (67, 130). However, this cannot be assumed for all drug-polymer combinations and should be investigated for each ASD.

The water absorbed into an amorphous solid will plasticize the material (observed as a reduction in T_g) and may increase the likelihood of crystallization. Polymers which absorb greater amounts of water or are plasticized to a greater extent by a constant amount of water may be at greater risk of moisture-induced instability. For a given water content, HPMCAS is slightly more plasticized by water (7.5°C/%) than PVPVA (6.8°C/%). Despite the difference, the relative effect of plasticization on stability in these two polymers exposed to environmental humidity conditions is expected to be minimal, especially as PVPVA absorbs much more water than HPMCAS across all humidities tested. PVPVA is

more hygroscopic than HPMCAS although its diffusivity is lower which means that, despite its greater water uptake, it will absorb environmental water slower over the range of relative humidity conditions studied. Practically, this means that the greater rate of absorption in HPMCAS may pose a greater stability risk to HPMCAS-containing SSDs when exposed for a short period of time. However, exposure of PVPVA-containing SSDs to elevated humidities for longer amounts of time may be at a greater risk of phase separation or crystallization. Further studies are required to investigate how the stabilizing ability of the polymer changes in the presence of moisture to determine the true risk of moisture-induced instability in ASDs.

A.4.4   Effects Dual Solvent Sorption on the Glass Transition Temperature

The effect of absorbed water on the glass transition temperature has been extensively studied and well characterized in the literature (126, 325, 346, 347). However, spray drying often exposes drugs and/ or polymers to multiple solvents, each of which can plasticize the system, yet the effect of multiple solvents on T_g has not been studied in much detail. DVS in tandem with DSC allowed for the determination of T_g across a variety of mixed solvent partial pressures.

Increasing amounts of a single solvent absorbed into each polymer caused a linear decrease in T_g where the magnitude of the reduction in T_g was dependent on polymer-solvent combination (see Figure A.6). Previous studies indicated the extent to which T_g changes at a constant solvent content may be related to differences in solvent-polymer interaction (332). Therefore, it is particularly surprising that the T_g values measured after equilibration in the presence of two solvents all condense to a master curve in each system regardless of the combination of solvents. In other words, T_g is dependent on the total

solvent uptake rather than the identity of the solvent for the two polymer-water-acetone systems studied. This suggests that the solvent molecules are non-interacting or weakly bound to the polymers such that the change in T_g is dependent on the T_g of the solvent. However, this does not appear to be the case. The T_g of water and acetone are significantly different (-136°C versus -176°C, respectively) and they have been shown previously to have varying extents and strengths of hydrogen bonding with each polymer (331-333).

This finding also has implications relating to developing a model for the spray drying process. Since the T_g seems to depend on the total solvent content rather than the relative amounts of each solvent, only the total moisture content is needed to determine the extent of plasticization at any point in the drying process. This value is easily accessible, especially towards the later stages of drying. Nonetheless, to truly model the drying droplet, the relative amounts of each solvent are needed and underscores the need for the development of an analytical technique to do so. Section A.4.5 discusses the need and challenges of quantitation in greater detail.

A.4.5   Relative Solvent Quantitation

Quantifying the relative amount of each absorbed solvent proved to be difficult even when using a variety of analytical techniques including DSC, DVS, KFT, SSNMR and solution-state NMR. However, it is necessary to be able to quantify each solvent to develop a model to better predict the changes in solvent content during spray drying. It was shown in sections A.3.2 and A.4.4 that the change in T_g with solvent content depends on the total solvent content rather than the relative amounts of water and acetone. This would make predicting T_g much easier however, this cannot be assumed to be true for all systems without the further analysis of additional polymer-mixed solvent systems. In addition, the

results of single isotherm experiments for water and acetone cannot necessarily be assumed to be additive. For example, even for single solvents, Crowley and Zografi showed that water absorption was not additive in ASDs based on drug and polymer single component isotherms (348). The differences were attributed to differences in the amount of available hydrogen bonding sites between the pure components and water versus the ASD and water. Similarly, differences in each solvent's affinity for a polymer are reflected through differences in their individual isotherms. This explains why total solvent uptake in dual solvent isotherms does not equal the sum of individual water and acetone uptake experiments. This is all relevant information which must be considered when developing a predictive model.

While the analytical techniques discussed in this chapter were unsuccessful in quantifying the relative amounts of water and acetone, there is a clear need for further research. Tandem or chromatographic techniques such as thermogravimetric analysis-mass spectrometry (TGA-MS) or headspace gas chromatography (HSGC), respectively, are likely next steps to attempt quantification. Indeed, HSGC has recently been used to quantify up to six volatile organic compounds in an API (321). A similar approach may also be useful for polymers or ASDs with the ultimate goal of combining known solvent contents, glass transition temperatures, and diffusivity values to characterize the spray drying process.

A.5   Conclusion

Appendix A investigated the absorption and desorption of water and acetone in PVPVA and HPMCAS and their effects on the glass transition temperature and diffusivity.

Sorption experiments were performed using dynamic vapor sorption while the extent of plasticization caused by the presence of solvents was determined using differential scanning calorimetry. PVPVA and HPMCAS, both commonly used during spray drying, behaved very differently when exposed to water and/ or acetone. Water absorption was used to approximate the effects environmental humidity during storage. Similarly, exposure of polymers to varying combinations of partial pressures of water and acetone was used to approximate the spray drying process where a drying particle has varying solvent contents at different points in the drying process.

Despite their different glass transition temperature's, a given amount of water and acetone plasticize each polymer to a similar extent. In addition, the reduction in T_g was dependent on the total amount of absorbed solvent content rather than the identity of the solvent. This is particularly surprising based on the differences in solvent T_g, molecular size, and hydrogen bonding ability. This implies that the sorbed solvent is loosely bound with the polymer and was confirmed using solid-state NMR. Although the solution- and solid-state NMR techniques used in Appendix A were unsuccessful in quantifying the relative amounts of solvent in a polymer, it was shown that the total solvent uptake may be useful in predicting plasticization (i.e., T_g) in the equilibrated polymer.

REFERENCES

1.   Zhong H, Chan G, Hu Y, Hu H, Ouyang D. A Comprehensive Map of FDA-Approved Pharmaceutical Products. Pharmaceutics. 2018;10(4):263.

2.   Amidon GL, Lennernas H, Shah VP, Crison JR. A theoretical basis for a biopharmaceutic drug classification: the correlation of in vitro drug product dissolution and in vivo bioavailability. Pharm Res. 1995;12(3):413-20.

3.   Di L, Kerns EH, Carter GT. Drug-like property concepts in pharmaceutical design. Curr Pharm Des. 2009;15(19):2184-94.

4.   Di L, Fish PV, Mano T. Bridging solubility between drug discovery and development. Drug Discov Today. 2012;17(9-10):486-95.

5.   Williams HD, Trevaskis NL, Charman SA, Shanker RM, Charman WN, Pouton CW, et al. Strategies to address low drug solubility in discovery and development. Pharmacol Rev. 2013;65(1):315-499.

6.   Kawabata Y, Wada K, Nakatani M, Yamada S, Onoue S. Formulation design for poorly water-soluble drugs based on biopharmaceutics classification system: basic approaches and practical applications. Int J Pharm. 2011;420(1):1-10.

7.   Lobenberg R, Amidon GL. Modern bioavailability, bioequivalence and biopharmaceutics classification system. New scientific approaches to international regulatory standards. Eur J Pharm Biopharm. 2000;50(1):3-12.

8.   Bragg WH, Bragg WL. The structure of the diamond. Proceedings of the Royal Society of London Series A, Containing Papers of a Mathematical and Physical Character. 1913;89(610):277-91.

9.   Hull AW. A new method of X-ray crystal analysis. Physical Review. 1917;10(6):661.

10.   McCrone WC. Polymorphism. Physics and chemistry of the organic solid state. 1965;2:725-67.

11.   Levesque A, Maris T, Wuest JD. ROY Reclaims Its Crown: New Ways To Increase Polymorphic Diversity. J Am Chem Soc. 2020;142(27):11873-83.

12.   Kersten K, Kaur R, Matzger A. Survey and analysis of crystal polymorphism in organic structures. IUCrJ. 2018;5(2):124-9.

13.   Byrn SR, Pfeiffer RR, Stowell JG. Solid-State Chemistry of Drugs. 2nd ed. West Lafayette, IN: SSCI; 1999.

14.   Haleblian J, McCrone W. Pharmaceutical applications of polymorphism. J Pharm Sci. 1969;58(8):911-29.

15.   Chemburkar SR, Bauer J, Deming K, Spiwek H, Patel K, Morris J, et al. Dealing with the Impact of Ritonavir Polymorphs on the Late Stages of Bulk Drug Process Development. Organic Process Research & Development. 2000;4(5):413-7.

16.   Burger A, Ramberger R. On the polymorphism of pharmaceuticals and other molecular crystals. I. Mikrochimica Acta. 1979;72(3-4):259-71.

17.   Yu L. Amorphous pharmaceutical solids: preparation, characterization and stabilization. Advanced Drug Delivery Reviews. 2001;48(1):27-42.

18.   Donth E. The glass transition: relaxation dynamics in liquids and disordered materials: Springer Science & Business Media; 2013.

19.   Kawakami K, Pikal MJ. Calorimetric investigation of the structural relaxation of amorphous materials: evaluating validity of the methodologies. J Pharm Sci. 2005;94(5):948-65.

20.   Hancock BC, Zografi G. Characteristics and significance of the amorphous state in pharmaceutical systems. J Pharm Sci. 1997;86(1):1-12.

21.   Kauzmann W. The Nature of the Glassy State and the Behavior of Liquids at Low Temperatures. Chemical Reviews. 1948;43(2):219-56.

22.   Vyazovkin S, Dranca I. Physical stability and relaxation of amorphous indomethacin. J Phys Chem B. 2005;109(39):18637-44.

23.   Grzybowska K, Paluch M, Grzybowski A, Wojnarowska Z, Hawelek L, Kolodziejczyk K, et al. Molecular dynamics and physical stability of amorphous anti-inflammatory drug: celecoxib. The Journal of Physical Chemistry B. 2010;114(40):12792-801.

24.   Johari GP, Goldstein M. Viscous liquids and the glass transition. II. Secondary relaxations in glasses of rigid molecules. The Journal of chemical physics. 1970;53(6):2372-88.

25.   Byrn SR, Zografi G, Chen S. Solid state properties of pharmaceutical materials: Wiley Online Library; 2017.

26.   Ngai K, Paluch M. Classification of secondary relaxation in glass-formers based on dynamic properties. The Journal of chemical physics. 2004;120(2):857-73.

27.   Paul IC, Curtin DY. Thermally induced organic reactions in the solid state. Accounts of Chemical Research. 1973;6(7):217-25.

28.   Yoshioka S, Stella VJ. Stability of drugs and dosage forms: Springer Science & Business Media; 2000.

29.   Byrn SR, Xu W, Newman AW. Chemical reactivity in solid-state pharmaceuticals: formulation implications. Adv Drug Deliv Rev. 2001;48(1):115-36.

30.   Xu W. Investigation of solid-state stability of selected bioactive compounds: Purdue University; 1997.

31.   Khawam A, Flanagan DR. Basics and applications of solid-state kinetics: a pharmaceutical perspective. J Pharm Sci. 2006;95(3):472-98.

32.   Khawam A, Flanagan DR. Solid-state kinetic models: basics and mathematical fundamentals. J Phys Chem B. 2006;110(35):17315-28.

33.   Harmon P, Li L, Marsac P, McKelvey C, Variankaval N, Xu W. Amorphous solid dispersions: analytical challenges and opportunities. AAPS Newsmagazine. 2009;12:14-20.

34.   Saleki-Gerhardt A, Zografi G. Non-isothermal and isothermal crystallization of sucrose from the amorphous state. Pharm Res. 1994;11(8):1166-73.

35.   Andronis V, Zografi G. Crystal nucleation and growth of indomethacin polymorphs from the amorphous state. Journal of Non-Crystalline Solids. 2000;271(3):236-48.

36.   Descamps M, Dudognon E. Crystallization from the amorphous state: nucleation-growth decoupling, polymorphism interplay, and the role of interfaces. J Pharm Sci. 2014;103(9):2615-28.

37.   Mullin JW. Crystallization: Elsevier; 2001.

38.   Gutzow I, Avramov I, Kästner K. Glass formation and crystallization. Journal of Non-Crystalline Solids. 1990;123(1-3):97-113.

39.   Trasi NS, Taylor LS. Nucleation and crystal growth of amorphous nilutamide–unusual low temperature behavior. CrystEngComm. 2014;16(31):7186-95.

40.   Baird JA, Van Eerdenbrugh B, Taylor LS. A classification system to assess the crystallization tendency of organic molecules from undercooled melts. J Pharm Sci. 2010;99(9):3787-806.

41.   Myerson A. Handbook of industrial crystallization: Butterworth-Heinemann; 2002.

42.   Volmer M. Kinetik der phasenbildung. 1939.

43.   Nielsen AE. Kinetics of precipitation. New York: Macmillan; 1964. x, 153 p. p.

44.   Hoffman JD. Thermodynamic driving force in nucleation and growth processes. The Journal of Chemical Physics. 1958;29(5):1192-3.

45.   Tammann GHJA. The States of Aggregation: The Changes in the State of Matter in Their Dependence Upon Pressure and Temperature: van Nostrand; 1925.

46.   Turnbull D, Fisher JC. Rate of Nucleation in Condensed Systems. Journal of Chemical Physics. 1949;17(1):71-3.

47.   Wu T, Yu L. Surface crystallization of indomethacin below T-g. Pharmaceutical Research. 2006;23(10):2350-5.

48.   Wu T, Yu L. Origin of enhanced crystal growth kinetics near T-g probed with indomethacin polymorphs. Journal of Physical Chemistry B. 2006;110(32):15694-9.

49.   Powell CT, Cai T, Hasebe M, Gunn EM, Gao P, Zhang G, et al. Low-Concentration Polymers Inhibit and Accelerate Crystal Growth in Organic Glasses in Correlation with Segmental Mobility. Journal of Physical Chemistry B. 2013;117(35):10334-41.

50.   Xi H, Sun Y, Yu L. Diffusion-controlled and diffusionless crystal growth in liquid o-terphenyl near its glass transition temperature. J Chem Phys. 2009;130(9):094508.

51.   Greet RJ, Turnbull D. GLASS TRANSITION IN O-TERPHENYL. Journal of Chemical Physics. 1967;46(4):1243-&.

52.   Hikima T, Adachi Y, Hanaya M, Oguni M. DETERMINATION OF POTENTIALLY HOMOGENEOUS-NUCLEATION-BASED CRYSTALLIZATION IN O-TERPHERNYL AND AN INTERPRETATION OF THE NUCLEATION-ENHANCEMENT MECHANISM. Physical Review B. 1995;52(6):3900-8.

53.   Hatase M, Hanaya M, Oguni M. Studies of homogeneous-nucleation-based crystal growth: significant role of phenyl ring in the structure formation. Journal of Non-Crystalline Solids. 2004;333(2):129-36.

54.   Sun Y, Xi HM, Chen S, Ediger MD, Yu L. Crystallization near glass transition: Transition from diffusion-controlled to diffusionless crystal growth studied with seven polymorphs. Journal of Physical Chemistry B. 2008;112(18):5594-601.

55.   Powell CT, Xi H, Sun Y, Gunn E, Chen Y, Ediger MD, et al. Fast Crystal Growth in o-Terphenyl Glasses: A Possible Role for Fracture and Surface Mobility. J Phys Chem B. 2015;119(31):10124-30.

56.   Zhou DL, Zhang GGZ, Law D, Grant DJW, Schmitt EA. Physical stability of amorphous pharmaceuticals: Importance of configurational thermodynamic quantities and molecular mobility. Journal of Pharmaceutical Sciences. 2002;91(8):1863-72.

57.   Zhou D, Schmitt EA, Law D, Brackemeyer PJ, Zhang GGZ. Assessing Physical Stability Risk Using the Amorphous Classification System (ACS) Based on Simple Thermal Analysis. Mol Pharm. 2019;16(6):2742-54.

58.   Marsac PJ, Konno H, Taylor LS. A comparison of the physical stability of amorphous felodipine and nifedipine systems. Pharm Res. 2006;23(10):2306-16.

59.   Brough C, Williams RO. Amorphous solid dispersions and nano-crystal technologies for poorly water-soluble drug delivery. International Journal of Pharmaceutics. 2013;453(1):157-66.

60.   Pandi P, Bulusu R, Kommineni N, Khan W, Singh M. Amorphous solid dispersions: An update for preparation, characterization, mechanism on bioavailability, stability, regulatory considerations and marketed products. International Journal of Pharmaceutics. 2020;586:119560.

61.   Konno H, Taylor LS. Influence of Different Polymers on the Crystallization Tendency of Molecularly Dispersed Amorphous Felodipine. Journal of Pharmaceutical Sciences. 2006;95(12):2692-705.

62.   Flory PJ. Principles of polymer chemistry: Cornell University Press; 1953.

63.   Lin D, Huang Y. A thermal analysis method to predict the complete phase diagram of drug-polymer solid dispersions. Int J Pharm. 2010;399(1-2):109-15.

64.   Greenhalgh DJ, Williams AC, Timmins P, York P. Solubility parameters as predictors of miscibility in solid dispersions. Journal of Pharmaceutical Sciences. 1999;88(11):1182-90.

65.   Marsac PJ, Shamblin SL, Taylor LS. Theoretical and practical approaches for prediction of drug-polymer miscibility and solubility. Pharm Res. 2006;23(10):2417-26.

66.   Sun Y, Tao J, Zhang GG, Yu L. Solubilities of crystalline drugs in polymers: an improved analytical method and comparison of solubilities of indomethacin and nifedipine in PVP, PVP/VA, and PVAc. J Pharm Sci. 2010;99(9):4023-31.

67.   Rumondor AC, Marsac PJ, Stanford LA, Taylor LS. Phase behavior of poly(vinylpyrrolidone) containing amorphous solid dispersions in the presence of moisture. Mol Pharm. 2009;6(5):1492-505.

68.   Knopp MM, Tajber L, Tian Y, Olesen NE, Jones DS, Kozyra A, et al. Comparative Study of Different Methods for the Prediction of Drug-Polymer Solubility. Mol Pharm. 2015;12(9):3408-19.

69.   Tao J, Sun Y, Zhang GG, Yu L. Solubility of small-molecule crystals in polymers: D-mannitol in PVP, indomethacin in PVP/VA, and nifedipine in PVP/VA. Pharm Res. 2009;26(4):855-64.

70.   Mistry P, Mohapatra S, Gopinath T, Vogt FG, Suryanarayanan R. Role of the Strength of Drug-Polymer Interactions on the Molecular Mobility and Crystallization Inhibition in Ketoconazole Solid Dispersions. Mol Pharm. 2015;12(9):3339-50.

71.   Anderson BD. Predicting Solubility/Miscibility in Amorphous Dispersions: It Is Time to Move Beyond Regular Solution Theories. J Pharm Sci. 2018;107(1):24-33.

72.   Kyeremateng SO, Pudlas M, Woehrle GH. A fast and reliable empirical approach for estimating solubility of crystalline drugs in polymers for hot melt extrusion formulations. J Pharm Sci. 2014;103(9):2847-58.

73.   Gross J, Sadowski G. Perturbed-chain SAFT: An equation of state based on a perturbation theory for chain molecules. Industrial & engineering chemistry research. 2001;40(4):1244-60.

74.   Knopp MM, Olesen NE, Holm P, Langguth P, Holm R, Rades T. Influence of Polymer Molecular Weight on Drug-Polymer Solubility: A Comparison between Experimentally Determined Solubility in PVP and Prediction Derived from Solubility in Monomer. J Pharm Sci. 2015;104(9):2905-12.

75.   Baird JA, Taylor LS. Evaluation of amorphous solid dispersion properties using thermal analysis techniques. Adv Drug Deliv Rev. 2012;64(5):396-421.
76.   Gordon M, Taylor JS. Ideal copolymers and the second-order transitions in synthetic rubbers. I. Non-crystalline copolymers. J Appl Chem. 1952;2(9):493 - 500.
77.   Couchman PR, Karasz FE. A Classical Thermodynamic Discussion of the Effect of Composition on Glass-Transition Temperatures. Macromolecules. 1978;11(1):117-9.
78.   Simha R, Boyer R. On a general relation involving the glass temperature and coefficients of expansion of polymers. The Journal of Chemical Physics. 1962;37(5):1003-7.
79.   Vyazovkin S, Dranca I. Effect of physical aging on nucleation of amorphous indomethacin. Journal of Physical Chemistry B. 2007;111(25):7283-7.
80.   Kothari K, Ragoonanan V, Suryanarayanan R. The Role of Polymer Concentration on the Molecular Mobility and Physical Stability of Nifedipine Solid Dispersions. Molecular Pharmaceutics. 2015;12(5):1477-84.
81.   Matsumoto T, Zografi G. Physical properties of solid molecular dispersions of indomethacin with poly(vinylpyrrolidone) and poly(vinylpyrrolidone-co-vinyl-acetate) in relation to indomethacin crystallization. Pharm Res. 1999;16(11):1722-8.
82.   Kothari K, Ragoonanan V, Suryanarayanan R. The role of drug-polymer hydrogen bonding interactions on the molecular mobility and physical stability of nifedipine solid dispersions. Mol Pharm. 2015;12(1):162-70.
83.   Yang Z, Han CD. Rheology of Miscible Polymer Blends with Hydrogen Bonding. Macromolecules. 2008;41(6):2104-18.
84.   Taylor LS, Zografi G. Spectroscopic characterization of interactions between PVP and indomethacin in amorphous molecular dispersions. Pharm Res. 1997;14(12):1691-8.
85.   Yuan XD, Sperger D, Munson EJ. Investigating Miscibility and Molecular Mobility of Nifedipine-PVP Amorphous Solid Dispersions Using Solid-State NMR Spectroscopy. Molecular Pharmaceutics. 2014;11(1):329-37.
86.   Dougherty RC. Temperature and pressure dependence of hydrogen bond strength: A perturbation molecular orbital approach. The Journal of chemical physics. 1998;109(17):7372-8.
87.   Andronis V, Yoshioka M, Zografi G. Effects of sorbed water on the crystallization of indomethacin from the amorphous state. J Pharm Sci. 1997;86(3):346-51.
88.   Shamblin SL, Zografi G. The effects of absorbed water on the properties of amorphous mixtures containing sucrose. Pharmaceutical Research. 1999;16(7):1119-24.
89.   Yuan XD, Xiang TX, Anderson BD, Munson EJ. Hydrogen Bonding Interactions in Amorphous Indomethacin and Its Amorphous Solid Dispersions with Poly(vinylpyrrolidone) and Poly(vinylpyrrolidone-co-vinyl acetate) Studied Using C-13 Solid-State NMR. Molecular Pharmaceutics. 2015;12(12):4518-28.
90.   Baghel S, Cathcart H, O'Reilly NJ. Polymeric Amorphous Solid Dispersions: A Review of Amorphization, Crystallization, Stabilization, Solid-State Characterization, and Aqueous Solubilization of Biopharmaceutical Classification System Class II Drugs. J Pharm Sci. 2016;105(9):2527-44.
91.   Sekiguchi K, Obi N. Studies on Absorption of Eutectic Mixture. I. A Comparison of the Behavior of Eutectic Mixture of Sulfathiazole and that of Ordinary Sulfathiazole in Man. Chemical and Pharmaceutical Bulletin. 1961;9(11):866-72.

92. Munjal M, Elsohly MA, Repka MA. Polymeric systems for amorphous Delta9-tetrahydrocannabinol produced by a hot-melt method. Part II: Effect of oxidation mechanisms and chemical interactions on stability. J Pharm Sci. 2006;95(11):2473-85.

93. Ghebremeskel AN, Vemavarapu C, Lodaya M. Use of surfactants as plasticizers in preparing solid dispersions of poorly soluble API: stability testing of selected solid dispersions. Pharm Res. 2006;23(8):1928-36.

94. Narayan Sahoo R, De A, Kataria V, Mallick S. Solvent-free Hot Melt Extrusion Technique in Improving Mesalamine Release for Better Management of Inflammatory Bowel Disease. Indian Journal of Pharmaceutical Education and Research. 2019;53(4s):s554-s62.

95. Repka MA, Bandari S, Kallakunta VR, Vo AQ, McFall H, Pimparade MB, et al. Melt extrusion with poorly soluble drugs - An integrated review. Int J Pharm. 2018;535(1-2):68-85.

96. Patil H, Tiwari RV, Repka MA. Hot-Melt Extrusion: from Theory to Application in Pharmaceutical Formulation. AAPS PharmSciTech. 2016;17(1):20-42.

97. Vo CL-N, Park C, Lee B-J. Current trends and future perspectives of solid dispersions containing poorly water-soluble drugs. European Journal of Pharmaceutics and Biopharmaceutics. 2013;85(3):799-813.

98. Janssens S, Van Den Mooter G. Review: physical chemistry of solid dispersions. Journal of Pharmacy and Pharmacology. 2009;61(12):1571-86.

99. Paudel A, Worku ZA, Meeus J, Guns S, Van den Mooter G. Manufacturing of solid dispersions of poorly water soluble drugs by spray drying: formulation and process considerations. Int J Pharm. 2013;453(1):253-84.

100. Singh A, Van den Mooter G. Spray drying formulation of amorphous solid dispersions. Adv Drug Deliv Rev. 2016;100:27-50.

101. Parikh DM. Handbook of pharmaceutical granulation technology: CRC Press; 2016.

102. Sosnik A, Seremeta KP. Advantages and challenges of the spray-drying technology for the production of pure drug particles and drug-loaded polymeric carriers. Advances in Colloid and Interface Science. 2015;223:40-54.

103. Mahlin D, Ponnambalam S, Hockerfelt MH, Bergstrom CA. Toward in silico prediction of glass-forming ability from molecular structure alone: a screening tool in early drug development. Mol Pharm. 2011;8(2):498-506.

104. Baird JA, Santiago-Quinonez D, Rinaldi C, Taylor LS. Role of viscosity in influencing the glass-forming ability of organic molecules from the undercooled melt state. Pharm Res. 2012;29(1):271-84.

105. Dong Z, Chatterji A, Sandhu H, Choi DS, Chokshi H, Shah N. Evaluation of solid state properties of solid dispersions prepared by hot-melt extrusion and solvent co-precipitation. Int J Pharm. 2008;355(1-2):141-9.

106. Knopp MM, Lobmann K, Elder DP, Rades T, Holm R. Recent advances and potential applications of modulated differential scanning calorimetry (mDSC) in drug development. Eur J Pharm Sci. 2016;87:164-73.

107. Richardson MJ, Savill NG. Derivation of accurate glass transition temperatures by differential scanning calorimetry. Polymer. 1975;16(10):753 - 7.

108.   Williams ML, Landel RF, Ferry JD. The Temperature Dependence of Relaxation Mechanisms in Amorphous Polymers and Other Glass-forming Liquids. Journal of the American Chemical Society. 1955;77(14):3701-7.

109.   Adam G, Gibbs JH. On the Temperature Dependence of Cooperative Relaxation Properties in Glass-Forming Liquids. The Journal of Chemical Physics. 1965;43(1):139-46.

110.   Williams G, Watts DC. Non-symmetrical dielectric relaxation behaviour arising from a simple empirical decay function. Transactions of the Faraday Society. 1970;66:80.

111.   Hodge IM. Effects of annealing and prior history on enthalpy relaxation in glassy polymers. 6. Adam-Gibbs formulation of nonlinearity. Macromolecules. 1987;20(11):2897-908.

112.   Böhmer R, Ngai KL, Angell CA, Plazek DJ. Nonexponential relaxations in strong and fragile glass formers. The Journal of Chemical Physics. 1993;99(5):4201-9.

113.   Shamblin SL, Zografi G. Enthalpy relaxation in binary amorphous mixtures containing sucrose. Pharm Res. 1998;15(12):1828-34.

114.   Bhugra C, Shmeis R, Krill SL, Pikal MJ. Prediction of onset of crystallization from experimental relaxation times. II. Comparison between predicted and experimental onset times. Journal of Pharmaceutical Sciences. 2008;97(1):455-72.

115.   Graeser KA, Patterson JE, Zeitler JA, Gordon KC, Rades T. Correlating thermodynamic and kinetic parameters with amorphous stability. Eur J Pharm Sci. 2009;37(3-4):492-8.

116.   Blaabjerg LI, Bulduk B, Lindenberg E, Löbmann K, Rades T, Grohganz H. Influence of Glass Forming Ability on the Physical Stability of Supersaturated Amorphous Solid Dispersions. Journal of Pharmaceutical Sciences. 2019;108(8):2561-9.

117.   Wendlandt WW. Thermal methods of analysis1974.

118.   Bhujbal SV, Pathak V, Zemlyanov DY, Taylor LS, Zhou QT. Physical Stability and Dissolution of Lumefantrine Amorphous Solid Dispersions Produced by Spray Anti-Solvent Precipitation. Journal of Pharmaceutical Sciences. 2021;110(6):2423-31.

119.   Calahan JL, Paul S, Yanez EG, Deneve D, Sun CC, Munson EJ. The impact of solid-state form, water content and surface area of magnesium stearate on lubrication efficiency, tabletability, and dissolution. Pharmaceutical Development and Technology. 2021;26(2):150-6.

120.   Ben Osman Y, Liavitskaya T, Vyazovkin S. Polyvinylpyrrolidone affects thermal stability of drugs in solid dispersions. Int J Pharm. 2018;551(1-2):111-20.

121.   Rodriguez C, Bugay DE. Characterization of Pharmaceutical Solvates by Combined Thermogravimetric and Infrared Analysis. Journal of Pharmaceutical Sciences. 1997;86(2):263-6.

122.   Newman A, Zografi G. An Examination of Water Vapor Sorption by Multicomponent Crystalline and Amorphous Solids and Its Effects on Their Solid-State Properties. J Pharm Sci. 2019;108(3):1061-80.

123.   Mauer LJ, Taylor LS. Deliquescence of pharmaceutical systems. Pharm Dev Technol. 2010;15(6):582-94.

124.   Newman AW, Reutzel-Edens SM, Zografi G. Characterization of the "hygroscopic" properties of active pharmaceutical ingredients. J Pharm Sci. 2008;97(3):1047-59.

125.   Friesen DT, Shanker R, Crew M, Smithey DT, Curatolo WJ, Nightingale JA. Hydroxypropyl methylcellulose acetate succinate-based spray-dried dispersions: an overview. Mol Pharm. 2008;5(6):1003-19.

126.   Hancock BC, Zografi G. The relationship between the glass transition temperature and the water content of amorphous pharmaceutical solids. Pharm Res. 1994;11(4):471-7.

127.   Saleki-Gerhardt A, Ahlneck C, Zografi G. Assessment of disorder in crystalline solids. International Journal of Pharmaceutics. 1994;101(3):237-47.

128.   Sheokand S, Modi SR, Bansal AK. Dynamic vapor sorption as a tool for characterization and quantification of amorphous content in predominantly crystalline materials. J Pharm Sci. 2014;103(11):3364-76.

129.   Mackin L, Zanon R, Park JM, Foster K, Opalenik H, Demonte M. Quantification of low levels (<10%) of amorphous content in micronised active batches using dynamic vapour sorption and isothermal microcalorimetry. Int J Pharm. 2002;231(2):227-36.

130.   Marsac PJ, Konno H, Rumondor AC, Taylor LS. Recrystallization of nifedipine and felodipine from amorphous molecular level solid dispersions containing poly(vinylpyrrolidone) and sorbed water. Pharm Res. 2008;25(3):647-56.

131.   Schmitt EA, Law D, Zhang GG. Nucleation and crystallization kinetics of hydrated amorphous lactose above the glass transition temperature. J Pharm Sci. 1999;88(3):291-6.

132.   Yang J, Grey K, Doney J. An improved kinetics approach to describe the physical stability of amorphous solid dispersions. International Journal of Pharmaceutics. 2010;384(1-2):24-31.

133.   Shah B, Kakumanu VK, Bansal AK. Analytical techniques for quantification of amorphous/crystalline phases in pharmaceutical solids. Journal of Pharmaceutical Sciences. 2006;95(8):1641-65.

134.   Vogt FG. Solid-State Characterization of Amorphous Dispersions. Pharmaceutical Sciences Encyclopedia: Drug Discovery, Development, and Manufacturing. 2010:1-62.

135.   Desai SR, Dharwadkar SR. Study of process induced polymorphic transformations in fluconazole drug. microscopy (SEM). 2009;7:9.

136.   Luebbert C, Sadowski G. In-situ determination of crystallization kinetics in ASDs via water sorption experiments. European Journal of Pharmaceutics and Biopharmaceutics. 2018;127:183-93.

137.   Byard SJ, Jackson SL, Smail A, Bauer M, Apperley DC. Studies on the crystallinity of a pharmaceutical development drug substance. J Pharm Sci. 2005;94(6):1321-35.

138.   Liu X, Feng X, Williams RO, Zhang F. Characterization of amorphous solid dispersions. Journal of Pharmaceutical Investigation. 2018;48(1):19-41.

139.   Young CA, Goodwin AL. Applications of pair distribution function methods to contemporary problems in materials chemistry. Journal of Materials Chemistry. 2011;21(18):6464.

140.   Newman JA, Schmitt PD, Toth SJ, Deng F, Zhang S, Simpson GJ. Parts per Million Powder X-ray Diffraction. Anal Chem. 2015;87(21):10950-5.

141.   Nollenberger K, Gryczke A, Meier C, Dressman J, Schmidt MU, Brühne S. Pair distribution function X-ray analysis explains dissolution characteristics of felodipine melt extrusion products. Journal of Pharmaceutical Sciences. 2009;98(4):1476-86.

142.   Alm E, Bro R, Engelsen SB, Karlberg B, Torgrip RJO. Vibrational overtone combination spectroscopy (VOCSY)—a new way of using IR and NIR data. Analytical and Bioanalytical Chemistry. 2007;388(1):179-88.

143.   Jamrogiewicz M. Application of the near-infrared spectroscopy in the pharmaceutical technology. J Pharm Biomed Anal. 2012;66:1-10.

144.   Mantsch HH, Naumann D. Terahertz spectroscopy: The renaissance of far infrared spectroscopy. Journal of Molecular Structure. 2010;964(1-3):1-4.

145.   Simmons DL, Ranz RJ, Gyanchandani ND, Picotte P. Polymorphism in Pharmaceuticals. II. Tolbutamide. Can J Pharm Sci. 1972;7:121-3.

146.   Simmons DL, Ranz RJ, Gyanchandani ND. Polymorphism in Pharmaceuticals. III. Chlorpropamide. Can J Pharm Sci. 1973;8(4):125-7.

147.   Taylor LS, Zografi G. The quantitative analysis of crystallinity using FT-Raman spectroscopy. Pharm Res. 1998;15(5):755-61.

148.   Paudel A, Raijada D, Rantanen J. Raman spectroscopy in pharmaceutical product design. Advanced Drug Delivery Reviews. 2015;89:3-20.

149.   Huang C, Powell CT, Sun Y, Cai T, Yu L. Effect of Low-Concentration Polymers on Crystal Growth in Molecular Glasses: A Controlling Role for Polymer Segmental Mobility Relative to Host Dynamics. J Phys Chem B. 2017;121(8):1963-71.

150.   Yao X, Huang CB, Benson EG, Shi CY, Zhang GGZ, Yu LA. Effect of Polymers on Crystallization in Glass-Forming Molecular Liquids: Equal Suppression of Nucleation and Growth and Master Curve for Prediction. Crystal Growth & Design. 2020;20(1):237-44.

151.   Bruce C, Fegely KA, Rajabi-Siahboomi AR, McGinity JW. Crystal growth formation in melt extrudates. Int J Pharm. 2007;341(1-2):162-72.

152.   Ye X, Patil H, Feng X, Tiwari RV, Lu J, Gryczke A, et al. Conjugation of Hot-Melt Extrusion with High-Pressure Homogenization: a Novel Method of Continuously Preparing Nanocrystal Solid Dispersions. AAPS PharmSciTech. 2016;17(1):78-88.

153.   Lauer ME, Grassmann O, Siam M, Tardio J, Jacob L, Page S, et al. Atomic force microscopy-based screening of drug-excipient miscibility and stability of solid dispersions. Pharm Res. 2011;28(3):572-84.

154.   Yuan X, Munson EJ, University of Kentucky. College of Pharmacy., University of Kentucky. Department of Pharmaceutical Sciences. A molecular-level view of the physical stability of amorphous solid dispersions. Available from: http://uknowledge.uky.edu/pharmacy_etds/51/.

155.   Skoog DA, Holler FJ, Crouch SR. Principles of instrumental analysis: Cengage learning; 2017.

156.   Aso Y, Yoshioka S, Kojima S. Molecular mobility-based estimation of the crystallization rates of amorphous nifedipine and phenobarbital in poly(vinylpyrrolidone) solid dispersions. J Pharm Sci. 2004;93(2):384-91.

157.   Marsac PJ, Li T, Taylor LS. Estimation of drug-polymer miscibility and solubility in amorphous solid dispersions using experimentally determined interaction parameters. Pharm Res. 2009;26(1):139-51.

158.   Knopp MM, Gannon N, Porsch I, Rask MB, Olesen NE, Langguth P, et al. A Promising New Method to Estimate Drug-Polymer Solubility at Room Temperature. J Pharm Sci. 2016;105(9):2621-4.

159.   Rabi II, Zacharias JR, Millman S, Kusch P. A New Method of Measuring Nuclear Magnetic Moment. Physical Review. 1938;53(4):318-.

160.   Purcell EM, Torrey HC, Pound RV. Resonance Absorption by Nuclear Magnetic Moments in a Solid. Physical Review. 1946;69(1-2):37-8.

161.   Bloch F. Nuclear Induction. Physical Review. 1946;70(7-8):460-74.

162.   Arnold JT, Dharmatti SS, Packard ME. Chemical Effects on Nuclear Induction Signals from Organic Compounds. The Journal of Chemical Physics. 1951;19(4):507-.

163.   Vogt FG. Evolution of solid-state NMR in pharmaceutical analysis. Future Med Chem. 2010;2(6):915-21.

164.   Geppi M, Mollica G, Borsacchi S, Veracini CA. Solid-state NMR studies of pharmaceutical systems. Applied Spectroscopy Reviews. 2008;43(3):202-302.

165.   Harris RK. Nuclear magnetic resonance spectroscopy: a physiochemical view. Essex, England: Longman; 1987. 260 p.

166.   Derome AE. Modern NMR Techniques for Chemistry Research. New York: Pergamon Press, Inc.; 1987. 280 p.

167.   Sharma RG. Other Applications of Superconducting Magnets. Superconductivity: Springer International Publishing; 2015. p. 359-404.

168.   Nick Pace C, Scholtz JM, Grimsley GR. Forces stabilizing proteins. FEBS Letters. 2014;588(14):2177-84.

169.   Andrew AR, Bradbury A, Eades RG. Removal of Dipolar Broadening of Nuclear Magnetic Resonance Spectra of Solids by Specimen Rotation. Nature. 1959;183(4678):1802 - 3.

170.   Harris RK, Olivieri AC. Spinning Sideband Analysis for Spin-1/2 Nuclei. Encyclopedia of Magnetic Resonance: John Wiley & Sons; 2007. p. 1-10.

171.   Dixon WT, Schaefer J, Sefcik MD, Stejskal EO, McKay RA. Total Suppression of Sidebands in CPMAS C-13 NMR. Journal of Magnetic Resonance. 1982;49(2):341-5.

172.   NMR   Relaxation   [Available   from: http://chem.ch.huji.ac.il/nmr/techniques/other/t1t2/t1t2.html.

173.   Wemmer DE. Some Double Resonance and Multiple Quantum NMR Studies in Solids: University of California, Berkeley; 1979.

174.   Pines A, Gibby MG, Waugh JS. Proton-enhanced NMR of Dilute Spins in Solids. J Chem Phys. 1973;59(2):569 - 90.

175.   Schaefer J, Stejskal EO. Carbon-13 nuclear magnetic resonance of polymers spinning at the magic angle. Journal of the American Chemical Society. 1976;98(4):1031-2.

176.   Slichter CP. Principles of Magnetic Resonance. New York: Harper & Row; 1990. 658 p.

177.   Kolodziejski W, Klinowski J. Kinetics of cross-polarization in solid-state NMR: a guide for chemists. Chem Rev. 2002;102(3):613-28.

178.   Paudel A, Geppi M, Van den Mooter G. Structural and Dynamic Properties of Amorphous Solid Dispersions: The Role of Solid-State Nuclear Magnetic Resonance Spectroscopy and Relaxometry. Journal of Pharmaceutical Sciences. 2014;103(9):2635-62.

179.   Lubach JW, Padden BE, Winslow SL, Salsbury JS, Masters DB, Topp EM, et al. Solid-state NMR studies of pharmaceutical solids in polymer matrices. Anal Bioanal Chem. 2004;378(6):1504-10.

180.   Clauss J, Schmidt-Rohr K, Spiess HW. Determination of domain sizes in heterogeneous polymers by solid-state NMR. Acta Polymerica. 1993;44(1):1-17.

181.	Bovey FA, Mirau PA. 1 - FUNDAMENTALS OF NUCLEAR MAGNETIC RESONANCE. In: Bovey FA, Mirau PA, editors. NMR of Polymers. San Diego: Academic Press; 1996. p. 1-115.

182.	Vanderhart DL. Proton Spin Diffusion as a Tool for Characterizing Polymer Blends. Makromolekulare Chemie-Macromolecular Symposia. 1990;34:125-59.

183.	Duan P, Lamm MS, Yang F, Xu W, Skomski D, Su Y, et al. Quantifying Molecular Mixing and Heterogeneity in Pharmaceutical Dispersions at Sub-100 nm Resolution by Spin Diffusion NMR. Mol Pharm. 2020;17(9):3567-80.

184.	Torchia DA. The measurement of proton-enhanced carbon-13 T1 values by a method which suppresses artifacts. J Magn Reson. 1978;30:613-6.

185.	Offerdahl TJ, Salsbury JS, Dong Z, Grant DJ, Schroeder SA, Prakash I, et al. Quantitation of crystalline and amorphous forms of anhydrous neotame using 13C CPMAS NMR spectroscopy. J Pharm Sci. 2005;94(12):2591-605.

186.	Jarrells TW, Zhang D, Li S, Munson EJ. Quantification of Monomer Units in Insoluble Polymeric Active Pharmaceutical Ingredients Using Solid-State NMR Spectroscopy I: Patiromer. AAPS PharmSciTech. 2020;21(3):116.

187.	Dempah KE, Lubach JW, Munson EJ. Characterization of the Particle Size and Polydispersity of Dicumarol Using Solid-State NMR Spectroscopy. Mol Pharm. 2017;14(3):856-65.

188.	Mistry P, Chakravarty P, Lubach JW. Probing the Distribution of Water in a Multi-Component System by Solid-State NMR Spectroscopy. Pharm Res. 2016;33(10):2470-80.

189.	Harris RK. Quantitative Aspects of High-resolution Solid-state Nuclear Magnetic Resonance Spectroscopy. Analyst. 1985;110:649 - 55.

190.	Zell MT, Padden BE, Paterick AJ, Hillmyer MA, Kean RT, Thakur KAM, et al. Direct Observation of Stereodefect Sites in Semi-crystalline Poly(lactide) Using 13-C Solid-State NMR. Journal of the American Chemical Society. 1998;120(48):12672 - 3.

191.	Sotthivirat S, Lubach JW, Haslam JL, Munson EJ, Stella VJ. Characterization of Prednisolone in Controlled Porosity Osmotic Pump Pellets using Solid-State NMR Spectroscopy. Journal of Pharmaceutical Sciences. 2007;96(5):1008-17.

192.	Lubach JW, Hau J. Solid-State NMR Investigation of Drug-Excipient Interactions and Phase Behavior in Indomethacin-Eudragit E Amorphous Solid Dispersions. Pharmaceutical Research. 2018;35(3).

193.	Li J, Yu F, Chen Y, Oupicky D. Polymeric drugs: Advances in the development of pharmacologically active polymers. J Control Release. 2015;219:369-82.

194.	Li J, Zhao J, Tao L, Wang J, Waknis V, Pan D, et al. The effect of polymeric excipients on the physical properties and performance of amorphous dispersions: Part I, free volume and glass transition. Pharm Res. 2015;32(2):500-15.

195.	Chourasia MK, Jain SK. Polysaccharides for colon targeted drug delivery. Drug Deliv. 2004;11(2):129-48.

196.	Duncan R, Vicent MJ, Greco F, Nicholson RI. Polymer-drug conjugates: towards a novel approach for the treatment of endrocine-related cancer. Endocr Relat Cancer. 2005;12 Suppl 1:S189-99.

197.	Torchilin VP. Structure and design of polymeric surfactant-based drug delivery systems. J Control Release. 2001;73(2-3):137-72.

198.   Kannan RM, Nance E, Kannan S, Tomalia DA. Emerging concepts in dendrimer-based nanomedicine: from design principles to clinical applications. J Intern Med. 2014;276(6):579-617.

199.   Uhrich KE, Cannizzaro SM, Langer RS, Shakesheff KM. Polymeric systems for controlled drug release. Chem Rev. 1999;99(11):3181-98.

200.   Bhugra C, Pikal MJ. Role of thermodynamic, molecular, and kinetic factors in crystallization from the amorphous state. J Pharm Sci. 2008;97(4):1329-49.

201.   Guo J, Skinner GW, Harcum WW, Barnum PE. Pharmaceutical applications of naturally occuring water-soluble polymers. Pharmaceutical Science & Technology Today. 1998;1(6):254-61.

202.   Connor EF, Lees I, Maclean D. Polymers as Drugs - Advances in Therapeutic Applications of Polymer Binding Agents. Journal of Polymer Science Part A: Polymer Chemistry. 2017;55:3146-57.

203.   Sterns RH, Rojas M, Bernstein P, Chennupati S. Ion-exchange resins for the treatment of hyperkalemia: are they safe and effective? J Am Soc Nephrol. 2010;21(5):733-5.

204.   Davidson MH. The use of colesevelam hydrochloride in the treatment of dyslipidemia: a review. Expert Opin Pharmacother. 2007;8(15):2569-78.

205.   Watson M, Abbott KC, Yuan CM. Damned if you do, damned if you don't: potassium binding resins in hyperkalemia. Clin J Am Soc Nephrol. 2010;5(10):1723-6.

206.   Rosenbaum DP, Holmes-Farley SR, Mandeville WH, Pitruzzello M, Goldberg DI. Effect of RenaGel, a non-absorbable, cross-linked, polymeric phosphate binder, on urinary phosphorus excretion in rats. Nephrol Dial Transplant. 1997;12(5):961-4.

207.   Mendonca PV, Serra AC, Silva CL, Simoes S, Coelho JFJ. Polymeric bile acid sequestrants - Synthesis using conventional methods and new approaches based on "controlled"/living radical polymerization. Progress in Polymer Science. 2013;38:445-61.

208.   Veltassa (Patiromer) [package insert]. Redwood City, CA: Relypsa, Inc.; May 2018.

209.   Renagel (Sevelamer hydrochloride) [package insert]. Cambridge, MA: Genzyme Corporation; February 2019.

210.   Renvela (Sevelamer carbonate) [package insert]. Cambridge, MA: Genzyme Corporation; June 2018.

211.   Welchol (Colesevelam hydrochloride) [package insert]. Basking Ridge, NJ: Daiichi Sankyo, Inc.; September 2019.

212.   Telwatte S, Moore K, Johnson A, Tyssen D, Sterjovski J, Aldunate M, et al. Virucidal activity of the dendrimer microbicide SPL7013 against HIV-1. Antiviral Res. 2011;90(3):195-9.

213.   Thoma LM, Boles BR, Kuroda K. Cationic methacrylate polymers as topical antimicrobial agents against Staphylococcus aureus nasal colonization. Biomacromolecules. 2014;15(8):2933-43.

214.   Ilker MF, Nusslein K, Tew GN, Coughlin EB. Tuning the hemolytic and antibacterial activities of amphiphilic polynorbornene derivatives. J Am Chem Soc. 2004;126(48):15870-5.

215.   Mowery BP, Lindner AH, Weisblum B, Stahl SS, Gellman SH. Structure-activity relationships among random nylon-3 copolymers that mimic antibacterial host-defense peptides. J Am Chem Soc. 2009;131(28):9735-45.

216.   Breslow DS. Biologically Active Synthetic Polymers. Pure & Applied Chemistry. 1976;46:103-13.

217.   Seymour L. Synthetic Polymers with Intrinsic Anticancer Activity. Journal of Bioactive and Compatible Polymers. 1991;6:178-216.

218.   Cheng HN, Smith TE, Vitus DM. Tacticity of Poly(N-vinyl Pyrrolidone). Journal of Polymer Science Polymer Letters Edition. 1980:29-31.

219.   Chavan RB, Rathi S, Sainaga Jyothi VGS, Shastri NR. Cellulose based polymers in development of amorphous solid dispersions. Asian Journal of Pharmaceutical Sciences. 2018;14(3):248-64.

220.   Pinto JMO, Leao AF, Riekes MK, Franca MT, Stulzer HK. HPMCAS as an effective precipitation inhibitor in amorphous solid dispersions of the poorly soluble drug candesartan cilexetil. Carbohydr Polym. 2018;184:199-206.

221.   Delaney SP, Nethercott MJ, Mays CJ, Winquist NT, Arthur D, Calahan JL, et al. Characterization of Synthesized and Commercial Forms of Magnesium Stearate Using Differential Scanning Calorimetry, Thermogravimetric Analysis, Powder X-Ray Diffraction, and Solid-State NMR Spectroscopy. J Pharm Sci. 2017;106(1):338-47.

222.   Zarmpi P, Flanagan T, Meehan E, Mann J, Fotaki N. Biopharmaceutical aspects and implications of excipient variability in drug product performance. Eur J Pharm Biopharm. 2017;111:1-15.

223.   Mansky P, Albrecht D, Burdick M, Chang HT, Charmot D, Connor EF, et al., inventors; Relypsa, Inc., assignee. Crosslinked Cation Exchange Polymers, Compositions and Use in Treating Hyperkalemia. United States of America2011.

224.   Anderson J, Bell C, Bishop J, Capila I, Ganguly T, Glajch J, et al. Demonstration of equivalence of a generic glatiramer acetate (Glatopa). J Neurol Sci. 2015;359(1-2):24-34.

225.   Zhang D, editor Demonstrating Complex API Sameness. Demonstrating Equivalence of Generic Complex Drug Substances and Formulations; 2017 October 6, 2017; Silver Spring, MD.

226.   Blanco M, Villarroya I. NIR spectroscopy: a rapid-response analytical tool. Trends in Analytical Chemistry. 2002;21(4):240-50.

227.   Mark J, Andre M, Karner M, Huck CW. Prospects for multivariate classification of a pharmaceutical intermediate with near-infrared spectroscopy as a process analytical technology (PAT) production control supplement. Eur J Pharm Biopharm. 2010;76(2):320-7.

228.   Bly RM, Kiener PE, Fries BA. Near-Infrared Method for Analysis of Block and Random Ethylene-Propylene Copolymers. Anal Chem 1966;38(2):217-20.

229.   Anderson CA, Drennen JK, Ciurczak EW. Pharmaceutical Applications of Near-Infrared Spectroscopy. In: Burns DA, Ciurczak EW, editors. Handbook of Near-Infrared Analysis. Boca Raton, FL: CRC Press; 2008. p. 834.

230.   Gies AP. Mass spectrometry of insoluble polymers: University of Alabama at Birmingham; 2004.

231.   Park J, Kataoka K. Precise Control of Lower Critical Solution Temperature of Thermosensitive Poly(2-isopropyl-2-oxazoline) via Gradient Copolymerization with 2-Ethyl-2-oxazoline as a Hydrophilic Comonomer. Macromolecules. 2006;39(19):6622-30.

232.   Montaudo MS. Mass spectra of copolymers. Mass Spectrom Rev. 2002;21(2):108-44.

233.   Montaudo G, Samperi F, Montaudo MS. Characterization of synthetic polymers by MALDI-MS. Progress in Polymer Science. 2006;31:277-357.

234.   Gorman EM. Solid-state Physical Form Detection and Quantitation of Pharmaceuticals in Formulations: University of Kansas; 2011.

235.   Li L, Harrison SD, Cope MJ, Park C, Lee L, Salaymeh F, et al. Mechanism of Action and Pharmacology of Patiromer, a Nonabsorbed Cross-Linked Polymer That Lowers Serum Potassium Concentration in Patients With Hyperkalemia. J Cardiovasc Pharmacol Ther. 2016;21(5):456-65.

236.   Peppas NA, Bures P, Leobandung W, Ichikawa H. Hydrogels in pharmaceutical formulations. Eur J Pharm Biopharm. 2000;50(1):27-46.

237.   Fung BM, Khitrin AK, Ermolaev K. An improved broadband decoupling sequence for liquid crystals and solids. J Magn Reson. 2000;142(1):97-101.

238.   Barich DH, Gorman EM, Zell MT, Munson EJ. 3-Methylglutaric acid as a 13C solid-state NMR standard. Solid State Nucl Magn Reson. 2006;30(3-4):125-9.

239.   Herzfeld J, Berger AE. Sideband Intensities in NMR Spectra of Samples Spinning at the Magic Angle. J Chem Phys. 1980;73(12):6021-30.

240.   Demco DE, Johansson A, Tegenfeldt J. Proton spin diffusion for spatial heterogeneity and morphology investigations of polymers. Solid State Nucl Magn Reson. 1995;4(1):13-38.

241.   Slichter CP. Spin Temperature in Magnetism and in Magnetic Resonance. Principles of Magnetic Resonance. Berlin, Heidelberg: Springer Berlin Heidelberg; 1990. p. 219-46.

242.   Lubach JW, Xu D, Segmuller BE, Munson EJ. Investigation of the effects of pharmaceutical processing upon solid-state NMR relaxation times and implications to solid-state formulation stability. J Pharm Sci. 2007;96(4):777-87.

243.   Charmot D, Chang HT, Fordtran J, Klaerner G, Buysse JM, Alpern R, et al., inventors; Relypsa, Inc., assignee. Ion Binding Polymers and Uses Thereof. United States of America2012.

244.   Albrecht D, Burdick M, Chang HT, Charmot D, Chidambaram R, Connor EF, et al., inventors; Relypsa, Inc., assignee. Linear Polyol Stabilized Polyfluoroacrylate Compositions. United States of America2012.

245.   Huang Y, Dai WG. Fundamental aspects of solid dispersion technology for poorly soluble drugs. Acta Pharm Sin B. 2014;4(1):18-25.

246.   Lin X, Hu Y, Liu L, Su LL, Li N, Yu J, et al. Physical Stability of Amorphous Solid Dispersions: a Physicochemical Perspective with Thermodynamic, Kinetic and Environmental Aspects. Pharmaceutical Research. 2018;35(6).

247.   Hate SS, Reutzel-Edens SM, Taylor LS. Absorptive Dissolution Testing: An Improved Approach to Study the Impact of Residual Crystallinity on the Performance of Amorphous Formulations. J Pharm Sci. 2020;109(3):1312-23.

248.   Moseson DE, Taylor LS. The application of temperature-composition phase diagrams for hot melt extrusion processing of amorphous solid dispersions to prevent residual crystallinity. International journal of pharmaceutics. 2018;553(1-2):454-66.

249.   Haser A, Cao T, Lubach J, Listro T, Acquarulo L, Zhang F. Melt extrusion vs. spray drying: The effect of processing methods on crystalline content of naproxen-povidone formulations. European Journal of Pharmaceutical Sciences. 2017;102:115-25.

250. Purohit HS, Trasi NS, Sun DD, Chow EC, Wen H, Zhang X, et al. Investigating the impact of drug crystallinity in amorphous tacrolimus capsules on pharmacokinetics and bioequivalence using discriminatory in vitro dissolution testing and physiologically based pharmacokinetic modeling and simulation. Journal of pharmaceutical sciences. 2018;107(5):1330-41.

251. Trasi NS, Purohit HS, Taylor LS. Evaluation of the Crystallization Tendency of Commercially Available Amorphous Tacrolimus Formulations Exposed to Different Stress Conditions. Pharmaceutical Research. 2017;34(10):2142-55.

252. Que C, Gao Y, Raina SA, Zhang GG, Taylor LS. Paclitaxel crystal seeds with different intrinsic properties and their impact on dissolution of paclitaxel-HPMCAS amorphous solid dispersions. Crystal Growth & Design. 2018;18(3):1548-59.

253. Purohit HS, Trasi NS, Osterling DJ, Stolarik DF, Jenkins GJ, Gao W, et al. Assessing the impact of endogenously derived crystalline drug on the in vivo performance of amorphous formulations. Molecular pharmaceutics. 2019;16(8):3617-25.

254. Knopp MM, Wendelboe J, Holm R, Rades T. Effect of amorphous phase separation and crystallization on the in vitro and in vivo performance of an amorphous solid dispersion. European Journal of Pharmaceutics and Biopharmaceutics. 2018;130:290-5.

255. Lappalainen M, Karppinen M. Techniques of differential scanning calorimetry for quantification of low contents of amorphous phases. J Therm Anal Calorim. 2010;102:171-80.

256. Van den Mooter G, Wuyts M, Blaton N, Busson R, Grobet P, Augustijns P, et al. Physical stabilisation of amorphous ketoconazole in solid dispersions with polyvinylpyrrolidone K25. European Journal of Pharmaceutical Sciences. 2001;12(3):261-9.

257. Takahashi H, Chen R, Okamoto H, Danjo K. Acetaminophen particle design using chitosan and a spray-drying technique. Chem Pharm Bull (Tokyo). 2005;53(1):37-41.

258. Hermans P, Weidinger A. X-ray studies on the crystallinity of cellulose. Journal of Polymer Science. 1949;4(2):135-44.

259. Chen X, Bates S, Morris KR. Quantifying amorphous content of lactose using parallel beam X-ray powder diffraction and whole pattern fitting. Journal of Pharmaceutical and Biomedical Analysis. 2001;26(1):63-72.

260. Stueber D, Dance ZEX. Component Quantification in Solids with the Mixture Analysis Using References Method. Analytical Chemistry. 2020;92(16):11095-102.

261. Windig W, Antalek B. Direct exponential curve resolution algorithm (DECRA): A novel application of the generalized rank annihilation method for a single spectral mixture data set with exponentially decaying contribution profiles. Chemometrics and Intelligent Laboratory Systems. 1997;37(2):241-54.

262. Asada M, Nemoto T, Mimura H, Sako K. Advanced New Relaxation Filter-Selective Signal Excitation Methods for 13C Solid-State Nuclear Magnetic Resonance. Analytical Chemistry. 2014;86(20):10091-8.

263. Gunn E, Guzei IA, Cai T, Yu L. Polymorphism of Nifedipine: Crystal Structure and Reversible Transition of the Metastable β Polymorph. Crystal Growth & Design. 2012;12(4):2037 - 43.

264. Kaplan DS. Structure-Property Relationships in Copolymers to Composites: Molecular Intrepretation of the Glass Transition Phenomenon. J Appl Polym Sci. 1976;20(10):2615-29.

265.   Krause S, Iskander M. Phase Separation in Styrene-α-Methyl Styrene Block Copolymers. Polym Sci Technol. 1977;10:231-43.
266.   Aso Y, Yoshioka S. Molecular mobility of nifedipine-PVP and phenobarbital-PVP solid dispersions as measured by C-13-NMR spin-lattice relaxation time. Journal of Pharmaceutical Sciences. 2006;95(2):318-25.
267.   Ishida H, Wu TA, Yu LA. Sudden rise of crystal growth rate of nifedipine near T-g without and with polyvinylpyrrolidone. Journal of Pharmaceutical Sciences. 2007;96(5):1131-8.
268.   Triggle AM, Shefter E, Triggle DJ. Crystal structures of calcium channel antagonists: 2,6-dimethyl-3,5-dicarbomethoxy-4-[2-nitro-, 3-cyano-, 4-(dimethylamino)-, and 2,3,4,5,6-pentafluorophenyl]-1,4-dihydropyridine. J Med Chem. 1980;23(12):1442-5.
269.   Apperley DC, Forster AH, Fournier R, Harris RK, Hodgkinson P, Lancaster RW, et al. Characterisation of indomethacin and nifedipine using variable-temperature solid-state NMR. Magn Reson Chem. 2005;43(11):881-92.
270.   Thomas LC. Modulated DSC Paper #7 Characterization of Pharmaceutical Materials. TA Instruments Technical Paper. 2005;TP 012:1-9.
271.   Ostwald W. Studien über die Bildung und Umwandlung fester Körper. Zeitschrift für Physikalische Chemie. 1897;22U(1):289-330.
272.   Otun S, Blade H, Meehan E, Qi S, Craig D. Overcoming dissolution effects: the use of hyper differential scanning calorimetry to detect drug melting in solid dispersion systems. Journal of Pharmacy and Pharmacology. 2009;61:63.
273.   Amharar Y, Curtin V, Gallagher KH, Healy AM. Solubility of crystalline organic compounds in high and low molecular weight amorphous matrices above and below the glass transition by zero enthalpy extrapolation. Int J Pharm. 2014;472(1-2):241-7.
274.   Mathers A, Hassouna F, Klajmon M, Fulem M. Comparative Study of DSC-Based Protocols for API–Polymer Solubility Determination. Molecular Pharmaceutics. 2021;18(4):1742-57.
275.   Alexander L, Klug HP. Basic Aspects of X-ray Absorption In Quantitative Diffraction Analysis of Powder Mixtures. Anal Chem. 1948;20(10):886 - 9.
276.   Bergese P, Colombo I, Gervasoni D, Depero LE. Assessment of the X-ray diffraction-absorption method for quantitative analysis of largely amorphous pharmaceutical composites. Journal of Applied Crystallography. 2003;36:74-9.
277.   Mahieu A, Willart JF, Dudognon E, Danede F, Descamps M. A new protocol to determine the solubility of drugs into polymer matrixes. Mol Pharm. 2013;10(2):560-6.
278.   Shen X, Hu W, Russell TP. Measuring the Degree of Crystallinity in Semicrystalline Regioregular Poly(3-hexylthiophene). Macromolecules. 2016;49(12):4501-9.
279.   Gustafsson C, Lennholm H, Iversen T, Nyström C. Comparison of solid-state NMR and isothermal microcalorimetry in the assessment of the amorphous component of lactose. International Journal of Pharmaceutics. 1998;174(1-2):243-52.
280.   Nývlt J. Kinetics of nucleation in solutions. Journal of Crystal Growth. 1968;3-4:377-83.
281.   Kalepu S, Nekkanti V. Insoluble drug delivery strategies: review of recent advances and business prospects. Acta Pharm Sin B. 2015;5(5):442-53.
282.   Mistry P, Suryanarayanan R. Strength of Drug-Polymer Interactions: Implications for Crystallization in Dispersions. Crystal Growth & Design. 2016;16(9):5141-9.

283.   Yoshioka M, Hancock BC, Zografi G. Crystallization of indomethacin from the amorphous state below and above its glass transition temperature. J Pharm Sci. 1994;83(12):1700-5.

284.   Yoshioka M, Hancock BC, Zografi G. Inhibition of indomethacin crystallization in poly(vinylpyrrolidone) coprecipitates. J Pharm Sci. 1995;84(8):983-6.

285.   Konno H, Taylor LS. Ability of different polymers to inhibit the crystallization of amorphous felodipine in the presence of moisture. Pharm Res. 2008;25(4):969-78.

286.   Wegiel LA, Zhao YH, Mauer LJ, Edgar KJ, Taylor LS. Curcumin amorphous solid dispersions: the influence of intra and intermolecular bonding on physical stability. Pharmaceutical Development and Technology. 2014;19(8):976-86.

287.   Bhardwaj SP, Arora KK, Kwong E, Templeton A, Clas SD, Suryanarayanan R. Correlation between Molecular Mobility and Physical Stability of Amorphous Itraconazole. Molecular Pharmaceutics. 2013;10(2):694-700.

288.   Xiang TX, Anderson BD. Effects of Molecular Interactions on Miscibility and Mobility of Ibuprofen in Amorphous Solid Dispersions With Various Polymers. Journal of Pharmaceutical Sciences. 2019;108(1):178-86.

289.   Bhugra C, Rambhatla S, Bakri A, Duddu SP, Miller DP, Pikal MJ, et al. Prediction of the onset of crystallization of amorphous sucrose below the calorimetric glass transition temperature from correlations with mobility. J Pharm Sci. 2007;96(5):1258-69.

290.   Caron V, Bhugra C, Pikal MJ. Prediction of Onset of Crystallization in Amorphous Pharmaceutical Systems: Phenobarbital, Nifedipine/PVP, and Phenobarbital/PVP. Journal of Pharmaceutical Sciences. 2010;99(9):3887-900.

291.   Bhardwaj SP, Arora KK, Kwong E, Templeton A, Clas SD, Suryanarayanan R. Mechanism of Amorphous Itraconazole Stabilization in Polymer Solid Dispersions: Role of Molecular Mobility. Molecular Pharmaceutics. 2014;11(11):4228-37.

292.   Greco S, Authelin JR, Leveder C, Segalini A. A Practical Method to Predict Physical Stability of Amorphous Solid Dispersions. Pharmaceutical Research. 2012;29(10):2792-805.

293.   Konishi T, Tanaka H. Possible origin of enhanced crystal growth in a glass. Physical Review B. 2007;76(22).

294.   Wu T, Yu L. Origin of enhanced crystal growth kinetics near Tg probed with indomethacin polymorphs. J Phys Chem B. 2006;110(32):15694-9.

295.   Wu T, Yu L. Surface crystallization of indomethacin below Tg. Pharm Res. 2006;23(10):2350-5.

296.   Pomposo JA, Eguiazabal I, Calahorra E, Cortázar M. Glass transition behaviour and interactions in poly(p-vinyl phenol)polymethacrylate blends. Polymer. 1993;34(1):95-102.

297.   Trask AV, Shan N, Jones W, Motherwell WDS. Indomethacin methyl ester. Acta Crystallographica Section E Structure Reports Online. 2004;60(4):o508-o9.

298.   Surwase SA, Boetker JP, Saville D, Boyd BJ, Gordon KC, Peltonen L, et al. Indomethacin: new polymorphs of an old drug. Mol Pharm. 2013;10(12):4472-80.

299.   Van Scoik KG, Carstensen JT. Nucleation phenomena in amorphous sucrose systems. International Journal of Pharmaceutics. 1990;58(3):185-96.

300.   Burnett D, Thielmann F, Sokoloski T, Brum J. Investigating the moisture-induced crystallization kinetics of spray-dried lactose. International Journal of Pharmaceutics. 2006;313(1-2):23-8.

301.   Kissinger HE. Variation of peak temperature with heating rate in differential thermal analysis. Journal of research of the National Bureau of Standards. 1956;57(4):217-21.

302.   Kistenmacher TJ, Marsh RE. Crystal and molecular structure of an antiinflammatory agent, indomethacin, 1-(p-chlorobenzoyl)-5-methoxy-2-methylindole-3-acetic acid. Journal of the American Chemical Society. 1972;94(4):1340-5.

303.   Andronis V, Zografi G. The molecular mobility of supercooled amorphous indomethacin as a function of temperature and relative humidity. Pharm Res. 1998;15(6):835-42.

304.   Angell CA. Perspective on the glass transition. Journal of Physics and Chemistry of Solids. 1988;49(8):863-71.

305.   Crowley K, Zografi G. The use of thermal methods for predicting glass-former fragility. Thermochimica Acta. 2001;380(2):79 - 93.

306.   Theil F, Milsmann J, Kyeremateng SO, Anantharaman S, Rosenberg J, van Lishaut H. Extraordinary Long-Term-Stability in Kinetically Stabilized Amorphous Solid Dispersions of Fenofibrate. Molecular Pharmaceutics. 2017;14(12):4636-47.

307.   Sun Y, Zhu L, Wu T, Cai T, Gunn EM, Yu L. Stability of Amorphous Pharmaceutical Solids: Crystal Growth Mechanisms and Effect of Polymer Additives. Aaps Journal. 2012;14(3):380-8.

308.   Musumeci D, Powell CT, Ediger MD, Yu L. Termination of Solid-State Crystal Growth in Molecular Glasses by Fluidity. The Journal of Physical Chemistry Letters. 2014;5(10):1705-10.

309.   Stevenson JD, Wolynes PG. The ultimate fate of supercooled liquids. J Phys Chem A. 2011;115(16):3713-9.

310.   Caroli C, Lemaitre A. Ultrafast spherulitic crystal growth as a stress-induced phenomenon specific of fragile glass-formers. J Chem Phys. 2012;137(11):114506.

311.   Tanaka H. Possible resolution of the Kauzmann paradox in supercooled liquids. Phys Rev E Stat Nonlin Soft Matter Phys. 2003;68(1 Pt 1):011505.

312.   Hasebe M, Musumeci D, Powell CT, Cai T, Gunn E, Zhu L, et al. Fast Surface Crystal Growth on Molecular Glasses and Its Termination by the Onset of Fluidity. J Phys Chem B. 2014;118(27):7638-46.

313.   Sun Y, Zhu L, Wu T, Cai T, Gunn EM, Yu L. Stability of amorphous pharmaceutical solids: crystal growth mechanisms and effect of polymer additives. AAPS J. 2012;14(3):380-8.

314.   Bates S, Zografi G, Engers D, Morris K, Crowley K, Newman A. Analysis of amorphous and nanocrystalline solids from their X-ray diffraction patterns. Pharm Res. 2006;23(10):2333-49.

315.   Xiang TX, Anderson BD. Molecular dynamics simulation of amorphous indomethacin-poly(vinylpyrrolidone) glasses: solubility and hydrogen bonding interactions. J Pharm Sci. 2013;102(3):876-91.

316.   Woldt E. The relationship between isothermal and non-isothermal description of Johnson-Mehl-Avrami-Kolmogorov kinetics. Journal of Physics and Chemistry of Solids. 1992;53(4):521-7.

317.   Jacobs PWM. Formation and Growth of Nuclei and the Growth of Interfaces in the Chemical Decomposition of Solids: New Insights†. The Journal of Physical Chemistry B. 1997;101(48):10086-93.

318.   Tian B, Gao W, Tao X, Tang X, Taylor LS. Impact of Polymers on the Melt Crystal Growth Rate of Indomethacin Polymorphs. Crystal Growth & Design. 2017;17(12):6467-76.

319.   Schmidt-Rohr K, Kulik A, Beckham H, Ohlemacher A, Pawelzik U, Boeffel C, et al. Molecular Nature of the. beta. Relaxation in Poly (methyl methacrylate) Investigated by Multidimensional NMR. Macromolecules. 1994;27(17):4733-45.

320.   Hancock BC, Shamblin SL, Zografi G. Molecular mobility of amorphous pharmaceutical solids below their glass transition temperatures. Pharm Res. 1995;12(6):799-806.

321.   Sojitra C, Tehare A, Dholakia C, Sudhakar P, Agarwal S, Singh KK. Development and validation of residual solvent determination by headspace gas chromatography in Imatinib Mesylate API. SN Applied Sciences. 2019;1(3).

322.   Sykes C. Time-and temperature-controlled transport: supply chain challenges and solutions. Pharmacy and Therapeutics. 2018;43(3):154.

323.   Lieberman H, Vemuri NM. Chemical and Physicochemical Approaches to solve formulation problems. The Practice of Medicinal Chemistry: Elsevier; 2015. p. 767-91.

324.   Poozesh S, Lu K, Marsac PJ. On the particle formation in spray drying process for bio-pharmaceutical applications: Interrogating a new model via computational fluid dynamics. International Journal of Heat and Mass Transfer. 2018;122:863-76.

325.   Oksanen CA, Zografi G. The relationship between the glass transition temperature and water vapor absorption by poly(vinylpyrrolidone). Pharm Res. 1990;7(6):654-7.

326.   Vehring R, Foss WR, Lechuga-Ballesteros D. Particle formation in spray drying. Journal of Aerosol Science. 2007;38(7):728-46.

327.   Guideline IHT. Impurities: guideline for residual solvents Q3C (R5). Current Step. 2005;4:1-25.

328.   Mugheirbi NA, Marsac PJ, Taylor LS. Insights into water-induced phase separation in itraconazole–hydroxypropylmethyl cellulose spin coated and spray dried dispersions. Molecular pharmaceutics. 2017;14(12):4387-402.

329.   Pantani R, De Santis F, Auriemma F, De Rosa C, Di Girolamo R. Effects of water sorption on poly (lactic acid). Polymer. 2016;99:130-9.

330.   Lamm MS, Simpson A, Mcnevin M, Frankenfeld C, Nay R, Variankaval N. Probing the Effect of Drug Loading and Humidity on the Mechanical Properties of Solid Dispersions with Nanoindentation: Antiplasticization of a Polymer by a Drug Molecule. Molecular Pharmaceutics. 2012;9(11):3396-402.

331.   Angell CA, Sare JM, Sare EJ. Glass transition temperatures for simple molecular liquids and their binary solutions. The Journal of Physical Chemistry. 1978;82(24):2622-9.

332.   Taylor LS, Langkilde FW, Zografi G. Fourier transform Raman spectroscopic study of the interaction of water vapor with amorphous polymers. Journal of Pharmaceutical Sciences. 2001;90(7):888-901.

333.   Xiang TX, Anderson BD. Molecular dynamics simulation of amorphous hydroxypropyl-methylcellulose acetate succinate (HPMCAS): polymer model development, water distribution, and plasticization. Mol Pharm. 2014;11(7):2400-11.

334.   Doppers L, Sammon C, Breen C, Yarwood J. FTIR-ATR studies of the sorption and diffusion of acetone/water mixtures in poly(vinyl alcohol). Polymer. 2006;47(8):2714-22.

335.   Kruk M, Jaroniec M, Guan S, Inagaki S. Adsorption and Thermogravimetric Characterization of Mesoporous Materials with Uniform Organic−Inorganic Frameworks. The Journal of Physical Chemistry B. 2001;105(3):681-9.

336.   Chen XD, Lin SXQ. Air drying of milk droplet under constant and time-dependent conditions. AIChE Journal. 2005;51(6):1790-9.

337.   Elversson J, Millqvist-Fureby A. Particle Size and Density in Spray Drying—Effects of Carbohydrate Properties. Journal of Pharmaceutical Sciences. 2005;94(9):2049-60.

338.   Purohit HS, Taylor LS. Phase Behavior of Ritonavir Amorphous Solid Dispersions during Hydration and Dissolution. Pharmaceutical Research. 2017;34(12):2842-61.

339.   Defrese MK, Farmer MA, Long Y, Timmerman LR, Bae Y, Marsac PJ. Approaches to Understanding the Solution-State Organization of Spray-Dried Dispersion Feed Solutions and Its Translation to the Solid State. Molecular Pharmaceutics. 2020;17(12):4548-63.

340.   Vehring R. Pharmaceutical particle engineering via spray drying. Pharm Res. 2008;25(5):999-1022.

341.   Paudel A, Loyson Y, Van den Mooter G. An investigation into the effect of spray drying temperature and atomizing conditions on miscibility, physical stability, and performance of naproxen-PVP K 25 solid dispersions. J Pharm Sci. 2013;102(4):1249-67.

342.   Ekdahl A, Mudie D, Malewski D, Amidon G, Goodwin A. Effect of Spray-Dried Particle Morphology on Mechanical and Flow Properties of Felodipine in PVP VA Amorphous Solid Dispersions. J Pharm Sci. 2019;108(11):3657-66.

343.   Prajapati P, Agrawal YK. Analysis and impurity identification in pharmaceuticals. Reviews in Analytical Chemistry. 2014;33(2).

344.   Kelly GM, O'Mahony JA, Kelly AL, O'Callaghan DJ. Water sorption and diffusion properties of spray-dried dairy powders containing intact and hydrolysed whey protein. LWT - Food Science and Technology. 2016;68:119-26.

345.   Rahman MA, Al-Abadleh HA. Surface Water Structure and Hygroscopic Properties of Light Absorbing Secondary Organic Polymers of Atmospheric Relevance. ACS Omega. 2018;3(11):15519-29.

346.   Smith L, Schmitz V. The effect of water on the glass transition temperature of poly(methyl methacrylate). Polymer. 1988;29(10):1871-8.

347.   Drake AC, Lee Y, Burgess EM, Karlsson JOM, Eroglu A, Higgins AZ. Effect of water content on the glass transition temperature of mixtures of sugars, polymers, and penetrating cryoprotectants in physiological buffer. PLOS ONE. 2018;13(1):e0190713.

348.   Crowley KJ, Zografi G. Water vapor absorption into amorphous hydrophobic drug/poly(vinylpyrrolidone) dispersions. J Pharm Sci. 2002;91(10):2150-65.

VITA

Travis Wayne Jarrells

Education
2012 – 2016   University of Kentucky
                            B.S., Chemical Engineering *summa cum laude*
                            Minor in Mathematics

Honors and Awards
Oct. 2018   2018 Pharmaceutical Sciences Graduate Program Student Travel Award

Oct. 2018   Peter G. Glavinos, Jr., Ph.D. Travel Award

Nov. 2017   2017 Pharmaceutical Sciences Graduate Program Student Travel Award

Sep. 2017   David E. Burgio and Thalia McMillen Endowed Graduate Pharmacy Scholarship

Publications
Jarrells, T.W., Zhang, D., Li, S., and Munson, E.J. *Quantification of Monomer Units in Insoluble Polymeric Active Pharmaceutical Ingredients using Solid State NMR Spectroscopy I. Patiromer*. AAPS PharmSciTech **21**, 116 (2020).

Hancock, M.L., Yokel, R.A., Beck, M.J., Calahan, J.L., **Jarrells, T.W.**, Munson, E.J., Olaniyan, G.A., and Grulke, E.A. *The Characterization of Purified Citrate-Coated Cerium Oxide Nanoparticles Prepared Via Hydrothermal Synthesis*. Appl. Surf. Sci., **535**, 147681 (2021).

Jarrells, T.W. and Munson, E.J. *Comparison of Differential Scanning Calorimetry, Powder X-ray Diffraction, and Solid-State Nuclear Magnetic Resonance Spectrometry for Measuring Crystallinity in Amorphous Solid Dispersions – Application to Drug-in-Polymer Solubility*. Journal of Pharmaceutical Sciences. (2022).